



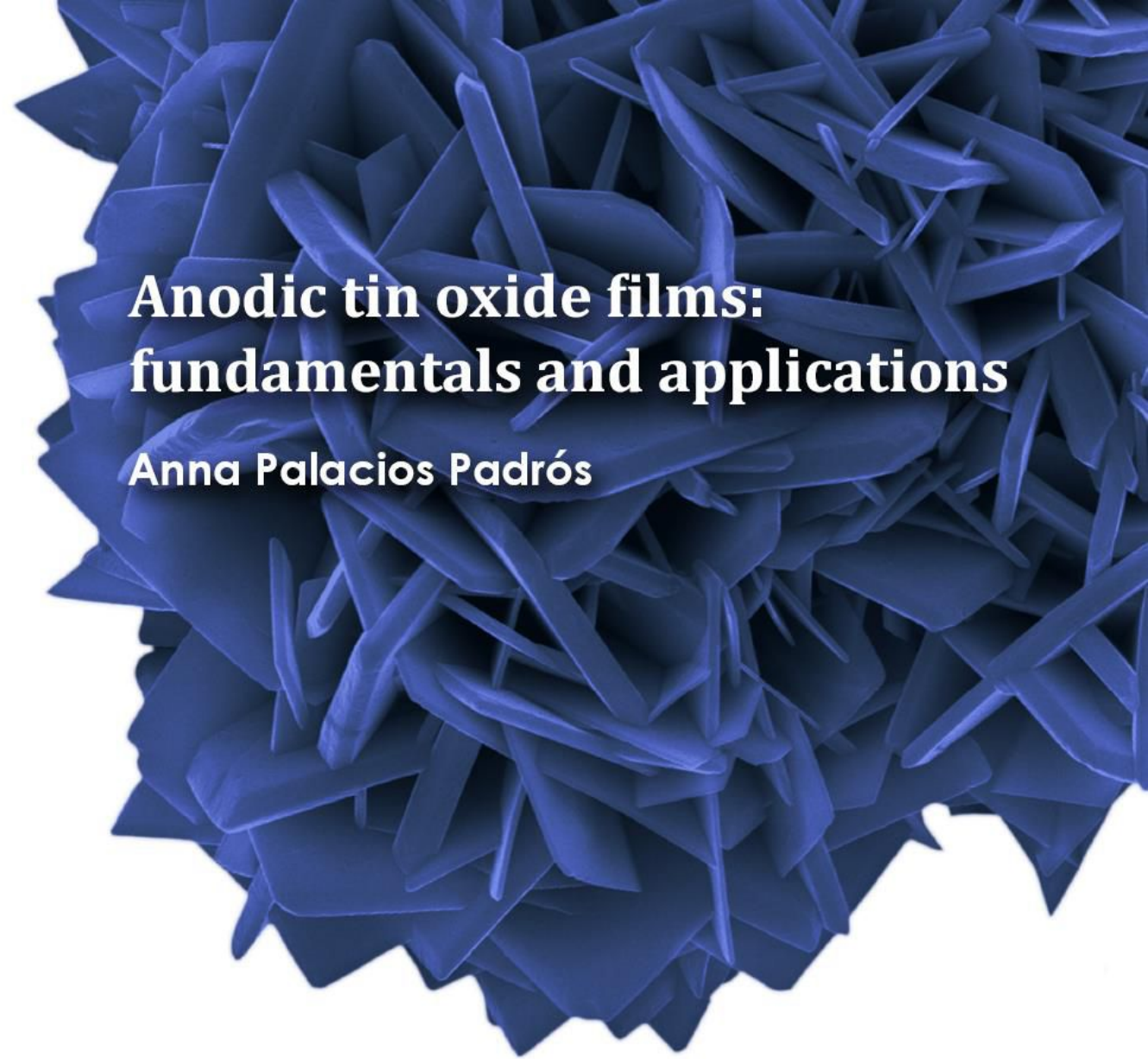
Anodic tin oxide films: fundamentals and applications

Anna Palacios Padrós

ADVERTIMENT. La consulta d'aquesta tesi queda condicionada a l'acceptació de les següents condicions d'ús: La difusió d'aquesta tesi per mitjà del servei TDX (www.tdx.cat) i a través del Dipòsit Digital de la UB (diposit.ub.edu) ha estat autoritzada pels titulars dels drets de propietat intel·lectual únicament per a usos privats emmarcats en activitats d'investigació i docència. No s'autoritza la seva reproducció amb finalitats de lucre ni la seva difusió i posada a disposició des d'un lloc aliè al servei TDX ni al Dipòsit Digital de la UB. No s'autoritza la presentació del seu contingut en una finestra o marc aliè a TDX o al Dipòsit Digital de la UB (framing). Aquesta reserva de drets afecta tant al resum de presentació de la tesi com als seus continguts. En la utilització o cita de parts de la tesi és obligat indicar el nom de la persona autora.

ADVERTENCIA. La consulta de esta tesis queda condicionada a la aceptación de las siguientes condiciones de uso: La difusión de esta tesis por medio del servicio TDR (www.tdx.cat) y a través del Repositorio Digital de la UB (diposit.ub.edu) ha sido autorizada por los titulares de los derechos de propiedad intelectual únicamente para usos privados enmarcados en actividades de investigación y docencia. No se autoriza su reproducción con finalidades de lucro ni su difusión y puesta a disposición desde un sitio ajeno al servicio TDR o al Repositorio Digital de la UB. No se autoriza la presentación de su contenido en una ventana o marco ajeno a TDR o al Repositorio Digital de la UB (framing). Esta reserva de derechos afecta tanto al resumen de presentación de la tesis como a sus contenidos. En la utilización o cita de partes de la tesis es obligado indicar el nombre de la persona autora.

WARNING. On having consulted this thesis you're accepting the following use conditions: Spreading this thesis by the TDX (www.tdx.cat) service and by the UB Digital Repository (diposit.ub.edu) has been authorized by the titular of the intellectual property rights only for private uses placed in investigation and teaching activities. Reproduction with lucrative aims is not authorized nor its spreading and availability from a site foreign to the TDX service or to the UB Digital Repository. Introducing its content in a window or frame foreign to the TDX service or to the UB Digital Repository is not authorized (framing). Those rights affect to the presentation summary of the thesis as well as to its contents. In the using or citation of parts of the thesis it's obliged to indicate the name of the author.



Anodic tin oxide films: fundamentals and applications

Anna Palacios Padrós



B Universitat de Barcelona

Doctorat en Ciència i Tecnologia de Materials

Universitat de Barcelona

Departament de Química Física

Anodic tin oxide films: fundamentals and applications

Memòria presentada per **Anna Palacios Padrós** per optar al títol de
Doctora per la Universitat de Barcelona

Directors:

Dr. Fausto Sanz Carrasco

Catedràtic del Departament de Química Física de la Universitat de
Barcelona

Dr. Ismael Díez Pérez

Investigador Ramón y Cajal de la Universitat de Barcelona

Barcelona, 22 de gener de 2015



Universitat de Barcelona

Universitat de Barcelona

Facultat de Química

Departament de Química Física

Anodic tin oxide films: fundamentals and applications

Anna Palacios Padrós

PhD Thesis

A la meva família,
el meu pilar.

Però també a aquells que ja no hi són...

Al Joan, a qui considero tiet per mèrits propis,
per tot el que podia haver estat i no va arribar a ser mai.

A la meva àvia Divina,
perquè em dol tenir-ne tan pocs records.

Al meu avi Vicens,
que és qui més feliç seria de poder veure aquesta tesi.

Al meu avi Anastasio,
perquè no ho podrem celebrar a ritme de "Pasodoble".

*No deixis de caminar
Encara que et fallin les forces
No deixis de caminar*

*Avançant aquí allà
dins teu parla la revolta
no t'aturis mai
encara que et fallin les forces*

*Sent el cor va bategant
cal seguir caminant
viatger de l'esperança
no deixis de caminar*

**No deixis de caminar, Txarango
(Benvinguts al llarg viatge, 2012)**

Contents

Preface	1
State of the art of metal Anodization	1
Motivation: Why tin?	2
Objectives	3
Structure	4

PART A: FUNDAMENTALS

Introduction	9
A.1 Fundamentals of passivity	10
A.1.1 Thermodynamic and kinetic aspects of passivity	10
A.1.2 Mechanisms of passive film growth	11
A.1.2.1 Layer pore resistance model (LPRM): dissolution-precipitation	12
A.1.2.2 High field mechanism (HFM): solid state ion migration	13
A.1.3 Properties of passive oxide films	16
A.1.3.1 Structure and chemical composition	16
A.1.3.2 Electronic properties	17
A.2 The semiconductor electrolyte interface	20
A.2.1 Electrical double layer at the metal electrolyte interface	20
A.2.2 Electrical double layer at the semiconductor electrolyte interface	21
A.2.2.1 The semiconductor electrolyte interface under electrochemical control	23
A.2.2.2 Capacitance measurements of the SCL: Mott-Schottky plots	24
A.3 <i>In situ</i> nanoscale studies of anodic oxide growth	26

A.3.1 Electrochemical scanning tunnelling microscopy (EC-STM) principles	26
A.3.2 EC-STM in the study of metal oxide growth, passivation and corrosion	28
A.4 State of the art of tin passivation	31
Chapter 1: Tin electrochemistry in alkaline media	33
1.1 Specific goals of this chapter	33
1.2 Results and discussion	34
1.2.1 Primary passive layer ($E < -0.9$ V)	35
1.2.2 Surface etching and SnO crystals growth (-0.9 V $< E < -0.7$ V)	41
1.2.3 Final electrode passivation ($E > -0.7$ V)	44
1.3 Summary	48
1.4 Further work	49
1.5 Experimental details	50
1.5.1 Sample preparation	50
1.5.2 Characterization techniques	50
Chapter 2: Nanoscale insight into the early stages of tin anodic oxidation	53
2.1 Specific goals of this chapter	53
2.2 Results and discussion	54
2.2.1 Preparation of atomically flat Sn surfaces	54
2.2.2 Early stages of Sn anodic oxidation by in situ EC-STM	58
2.3 Summary	62
2.4 Further work	63
2.5 Experimental details	63
2.5.1 Surface preparation	63
2.5.2 Surface characterization	64
2.5.3 Preparation of W EC-STM tips	64
2.5.4 EC-STM measurements	65
 PART B: APPLICATIONS	
Introduction	69
B.1 Self-ordered anodization	69
B.1.1 Principles of self-ordering anodization	70
B.1.2 Geometry control in self-ordered oxide layers	74
B.1.2.1 Pores vs. tubes	74

B.1.2.2 Length and diameter	76
B.1.2.3 Advanced geometries: bamboo, nanolaces, and branched tubes	77
B.1.3 Poor state-of-the-art of Sn self-ordered anodization	78
B.2 Application of metal oxides in gas sensing	80
B.2.1 SnO ₂ in gas sensing: on the potential of nanostructures	80
B.2.2 Gas sensing measurements: setup and sensing response	82
B.3 Photoelectrochemistry in anodic oxides: clean H ₂ production	82
B.3.1 Fundamentals of semiconductor photoelectrochemistry	85
B.3.1.1 Photoexcitation of electrons by light absorption in semiconductors	85
B.3.1.2 Photoelectrochemistry at the semiconductor electrode electrolyte interface	84
B.3.2 Applications of photoelectrochemistry: photoelectrochemical water splitting	86
B.3.3 Photoelectrochemical characterization: measurement configurations and setup	89
B.3.3.1 Photocurrent at variable wavelength	89
B.3.3.2 Photoelectrochemical performance: measurements under simulated sunlight ...	91
Chapter 3: Development of anodic self-ordered tin oxide nanochannelled structures	93
3.1 Specific goals of this chapter	93
3.2 Results and discussion	93
3.2.1 Phosphoric-acid based solutions	94
3.2.2 Ammonium nitrate in ethylene glycol	96
3.2.3 Alkaline electrolytes: ammonia and sodium carbonate	98
3.2.3 Sodium sulphide and ammonium fluoride solutions	99
3.3 Summary	105
3.4 Further work	106
3.5 Experimental details	106
3.5.1 Sample preparation	106
3.5.2 Characterization techniques	107
Chapter 4: Application of self-ordered nanochannelled SnO₂ structures in H₂ gas sensing	109
4.1 Specific goals of this chapter	109
4.2 Results and discussion	110
4.2.1 Characterization of the nanochannelled SnO ₂ /Si films	110
4.2.2 H ₂ sensing performance of self-ordered anodic SnO ₂ layers	112

4.3 Summary.....	117
4.4 Further work	117
4.5 Experimental details	118
4.5.1 Sample preparation.....	118
4.5.2 Characterization techniques	118
Chapter 5: Photoelectrochemical properties of self-ordered tin oxide structures	121
5.1 Specific goals of this chapter	122
5.2 Results and discussion	122
5.2.1 Effect of annealing in morphology, structure and composition	122
5.2.2 Photoelectrochemical characterization	126
5.2.2.1 Photocurrent at variable wavelength.....	126
5.2.2.2 Photoelectrochemical performance: measurements under simulated solar light.....	128
5.3 Summary.....	130
5.4 Further work	130
5.5 Experimental details	131
3.5.1 Sample preparation.....	131
3.5.2 Characterization techniques	131
Chapter 6: Self-ordered SnO₂ as hematite host for photoelectrochemical water splitting	133
6.1 Specific goals of this chapter	134
6.2 Results and discussion	135
6.2.1 Photoanode build-up process	135
6.2.2 Structure, morphology and composition	135
6.2.3 Photoelectrochemical performance	138
5.3 Summary.....	142
5.4 Further work	142
5.5 Experimental details	142
3.5.1 Sample preparation.....	142
3.5.2 Characterization techniques	143
CONCLUSIONS	
Conclusions	147

APPENDICES

Appendix a: SnO electrosynthesis: effect of electrochemical conditions on the growth of microcrystals	153
Introduction	153
Results and discussion	153
Effect of temperature and NaOH concentration	153
Effect of organic solvents: limiting the etching rate	158
Summary	162
Experimental details	162
Sample preparation	162
Characterization techniques	163
Appendix b: First steps towards the further improvement of self-ordered tin oxide structures: pulsed anodization and indented Sn surfaces	165
Introduction	165
Results and discussion	165
Potential pulses	165
Patterning with Ni mould: indented Sn surfaces	167
Summary	169
Experimental details	170
Appendix c: Symbols and acronyms	171
Appendix d: Publications and Meetings (2010-2014)	175
Resum en català	181
Acknowledgements / Agraïments	205
References	211

Preface

State-of-the-art of metal Anodization

Anodizing or anodization can be defined as an electrochemical process for producing stable oxide films on the surface of metals. The name comes from the process itself: the metal to be oxidized acts as the anode electrode in the electrochemical cell and transfers its electrons to the cathode through the external circuit [1].

First patent on anodic treatment dates back to 1923, when Bengough and Stuart developed a procedure to protect against corrosion the aluminium parts of the Duralumin seaplane exposed to salt water [2,3]. Since then, the use of anodic films has widely spread in the metal finishing industry because they confer corrosion and wear resistance to the metals, improve the adhesion for paints or glues and can even give a coloured appearance for decorative purposes. Due to their protective character, these oxide layers are also referred to as passive oxides. Given the technological implications of metals such as aluminium, titanium, magnesium or zinc, their anodization is nowadays a well-known standardized industrial process. Most of these metals are part of our everyday life. For instance, anodized aluminium is used in aircraft parts, architectural materials like window frames, and consumer products (cookware, smartphones, cameras, *etc.*) whereas anodized titanium is employed mainly in dental implants or jewellery.

Aside from protective purposes, anodic oxide layers have proved by far their potential in biomedical, photoelectrochemical, electrical and sensing devices. Under most experimental conditions, randomly porous or compact oxide layers are formed. However, in 1995 Fukuda and Masuda first reported the formation of perfectly ordered nanopore arrays on aluminium by a process that was named self-organizing or self-ordered anodization [4]. Few years later,

in 1999, the growth of self-ordered nanotubes on titanium was demonstrated [5]. The possibility of developing nanostructures like nanotubes or nanopores with enhanced properties compared to the bulk opened a prominent field of research that generates a significant amount of scientific contributions (~ 1000 documents since 1995 among articles, reviews or communications). Self-ordering anodization of many other metals (Ta, Nb, Fe, Sn, W, Hf or Zr) and alloys (TiZr, TiAl, TiTa, *etc.*) has been achieved up to now [6].

Motivation: Why tin?

Tin is one of the oldest metals known to mankind. Historically, it had a direct impact on the technological development of human civilizations. The discovery of copper-tin alloys marked the beginning of the Bronze Age and enabled prehistoric societies to create harder and more durable tools, weaponry and decorative elements. To face the increasing demand, it was one of the first metals to be mined.

Nowadays, the most relevant applications of Sn are in soldering or as coating of other metals to prevent corrosion, such as food cans, which are made of tin-coated steel. For both applications, understanding the passivation and corrosion behaviour is of outmost importance. Generally, Sn resists well corrosion from water but can be attacked by strong acids and alkalis. In the 1980s, many research works tackled this issue but the complexity in identifying the exact composition of tin passive films, the dependence of their structure on the environmental conditions (electrolyte, pH, potential, *etc.*) and the multiple electrochemical pathways and possible species in solution led to a scattered set of results. In our research group, Raul Díaz examined the electrochemical behaviour of Sn in borate buffer solutions at neutral pH and first applied electrochemical scanning tunnelling microscopy (EC-STM) to follow *in situ* its oxidation process [7]. In such neutral conditions, the stability of the passive tin oxide layers is greater than in alkaline media and in consequence thinner films are obtained, which makes its characterization rather complicated. Also, the electrochemical activity is less obvious. So, based on our previous experience on tin and the passivation and corrosion of other metals [7–14], we decided to carry out a systematic study on the passivating behaviour of Sn in alkaline media. For this, we have used our knowledge on common electrochemical tools such as voltammetry or electrochemical impedance spectroscopy available in our laboratory in combination to *ex situ* characterization by scanning electron microscopy, atomic force microscopy, X-ray diffraction, Raman spectroscopy and X-ray photoelectron spectroscopy or *in situ* EC-STM. By combining all these measurements, new processes like the hydroxyl etching and SnO electrocrystallization could be identified, as well as surface modifications prior to the first oxidation peak when studying the morphology evolution at the nanoscale level with EC-STM.

Although the idea to shed light in understanding the passive behaviour of Sn in alkaline solutions is a motivation by itself, the possibility of exploiting the electrochemical oxidation

or anodization to prepare functional tin oxides is even more stimulating. According to its oxidation states, the feasible stoichiometric oxides are SnO and SnO₂, both showing radically different electronic properties. The first one is known to be a p-type semiconductor with a band gap of 0.7 eV and a pronounced anisotropic character arising from its layered tetragonal structure. On the contrary, SnO₂ is a wide band gap n-type semiconductor ($E_g = 3.6$ eV). Additionally, tin has a very rich defect nature and can easily form intermediate oxides with mixed valence giving rise to a variety of oxide materials with new optical and electronic properties, such as visible optical absorption or enhanced conductivity. Among this family of tin-related oxides, SnO₂ has been particularly defined as a material with “an abundance of uses” that range from transparent conductive oxides (TCO’s) to solid state gas sensors, Li-batteries, supercapacitors, UV-detectors, field-effect-transistors or solar cells. In many of these applications, the exploitation of nanostructured porous or tubular SnO₂ layers offering a high surface to volume ratio could really signify an important breakthrough.

Objectives

There are initially two main goals in this PhD thesis: on one hand, we intend to get a quantitative picture of the anodization/passivation mechanisms of tin in alkaline solution, and from the other hand, we pretend to use that knowledge to develop nanostructured anodic tin oxide films that could be exploited in real life applications.

Regarding the fundamental study of Sn passivation, a preliminary electrochemical characterization is required to identify the different regions of potential where each electrochemical reaction takes place. Then, it is essential to develop the oxide layers in both the active and passive range and *ex situ* characterize their topography and composition. With all these results, a global view of the different processes involved in tin passivation can be deduced. Next stage is to *in situ* characterize at the nanoscale the very early stages of the anodic process by EC-STM to get an exact picture on how tin passivation is initiated. Despite our experience in the EC-STM field, this part of the PhD was done in collaboration with the group of Prof. Philippe Marcus, one of the leading laboratories on the study of oxidation processes at the atomic level.

The knowledge gained while attaining this first goal is used for the design of protocols to develop self-ordered anodic tin oxide structures that can be subsequently applied in real devices. To this aim, we closely collaborated with the laboratory of Prof. Patrik Schmuki, a reference lab in self-ordering anodization of titanium as well as many other different metals and alloys. First, electrochemical conditions need to be optimized to reach the desired porous structures. Once structures with appropriate morphology are obtained, they are thermally treated to improve the crystallinity and tune their properties for applications in gas sensors and/or photoelectrochemical water splitting. The final results demonstrate the capabilities of our layers in real devices. However, this goal is so ambitious that I am sure this thesis is just the tip of the iceberg. There is still plenty of room and I just hope to have

opened a new door with this work to understand how to fine-tune the growth and preparation of complex semiconducting oxides for their use in practical applications.

Structure

The structure of this PhD thesis has been divided into two separated parts, to distinct those chapters dealing with the fundamental electrochemical studies of tin passivation and reaction mechanisms (Part A) from those addressing the development of nanostructured anodic tin oxide layers and its final application in sensing and photoelectrochemical water splitting (Part B). At the beginning of each part there is an introductory chapter that settles the necessary background concepts required to understand the results in the Chapters therein. Each results Chapter is organized in sections, namely, the specific goals, the results and discussion where all the experimental data is collected, a brief summary with all the important findings, a section proposing further experiments to clarify points that deserve further study or interesting aspects of the system that could be explored, and finally, the experimental details where the measurement conditions and the equipment used are specified.

PART A: FUNDAMENTALS

- **Introduction:** is intended to contain the indispensable concepts of passivity, growth mechanisms of passive films and semiconductor electrochemistry required for the interpretation of results in Chapters 1 and 2. Additionally, the transcendence of *in situ* techniques such as electrochemical scanning tunnelling microscopy (EC-STM) in the passivation and corrosion studies of metals such as Cu, Ni and Fe is discussed in order to provide some hints on the interpretation of our EC-STM results. Finally the chapter includes an overview on the state-of-the-art of tin passivation, with emphasis on the reaction pathways proposed to date and the suggested structures of the passive layer.
- **Chapter 1:** the results on a detailed study of the electrochemical behaviour of tin in alkaline solution are presented. The oxides formed within the active and passive regimes are characterized by microscopy and spectroscopy techniques and a mechanism for the different electrochemical reactions is proposed. Interestingly, in a certain region of potentials the formation of SnO microcrystals by hydroxyl induced etching of the Sn substrate and subsequent precipitation is identified. This process has been scarcely described in Sn passivation up to date. Most of the results contained in this chapter are published in *Electrochimica Acta 111 (2013) 837-845*.
- **Chapter 2:** begins with the optimization on the chemical polishing and etching conditions to achieve atomically flat surfaces on polycrystalline Sn discs. Pyramidal hillocks exhibiting flat terraces at the pyramidal faces were obtained. Early stages of

anodic oxidation were followed in these terraces by EC-STM. Results show changes in the morphology before the onset of the primary passivation that suggest a dissolution and precipitation mechanism. The results are currently in preparation for publication.

PART B: APPLICATIONS

- **Introduction:** includes the basic principles of self-organized anodization highlighting the plusses of this technique: metal oxide structures with tuneable morphologies ranging from nanochannels to nanopores can be obtained in many different metals in a straightforward and cost effective way. The current status of self-ordered structures on Sn and the urgent need to find new electrolytes is also revised. Subsequent sections are focused on the applications that will be tackled in Chapters 4 to 6. First, a general view on the operation of metal oxide chemiresistive gas sensors and the best results on SnO₂-based H₂ sensors are given. Afterwards, photoelectrochemical properties at the electrode | electrolyte interface and the build-up and material requirements for efficient photoanodes in photoelectrochemical water splitting are introduced.
- **Chapter 3:** presents the results from the wide screening of electrolytes and electrochemical conditions attempted in order to achieve self-ordered tin oxide structures with a top-opened morphology free of cracks on its cross-section. Some of the results presented here are gathered in the supplementary material of *J. Mater. Chem. A* 2 (2014) 915-920.
- **Chapter 4:** approaches directly the application of the self-ordered structures developed in Chapter 3 in H₂ gas sensing. The effect of parameters such as the annealing temperature, the operating temperature of the sensor or the film thickness is studied. To assess the superior properties of our anodic layers, their performance is compared to the ones developed on non-optimized conditions or even using other electrochemical conditions described in the literature. The sensing results from this chapter were published in *J. Mater. Chem. A* 2 (2014) 915-920.
- **Chapter 5:** is devoted to study the influence of annealing temperature on the composition, structure and photoelectrochemical properties of tin oxide self-ordered structures. Also, the effect of the annealing atmosphere is examined. By controlled annealing, tin oxide structures showing absorption in the visible range were found and then were tested in photoelectrochemical water splitting. Some of the data gathered here is available in *ChemElectrochem* 1 (2014) 1133-1137.
- **Chapter 6:** focuses on the preparation of host-guest systems for high efficiency photoelectrochemical water splitting. The systems combine self-ordered

nanochannelled tin oxide layers as scaffold and hematite nanoparticles as light absorber. In this chapter, the improvement of the electrical properties of tin oxide nanostructures by effective antimony doping is of great importance. This step is the key for a high efficiency water splitting performance. The effect of Sb loading, the hematite deposition time or the SnO₂ thickness is assessed. The results from this chapter are published in *ChemSusChem* 7 (2014) 421-424.

CONCLUSIONS

Corresponds to the general conclusions of this PhD Thesis

APPENDICES

- **Appendix a:** shows the effect of both temperature and NaOH concentration on the morphology of SnO microcrystals. Also, preliminary experiments on the effect of organic solvents in the etching process and the final SnO morphology are included.
- **Appendix b:** includes the first experiments towards the improvement of self-organized tin oxide nanochannel structures by using advanced approaches such as potential pulses or indented Sn surfaces.
- **Appendix c:** Symbols and acronyms
- **Appendix d:** Publications and meetings during the Thesis period (2010-2014)

PART A:

Fundamentals

Introduction

The passivation of a metallic electrode is understood as “the hindering, under certain conditions, of a thermodynamically expected metal dissolution reaction” [15]. In other words, the passivation of a metal anode kinetically retards its spontaneous dissolution, so it becomes chemically inactive or less affected by environmental factors such as air or water. Most metals, aluminium, titanium or tin for example, are generally self-passivating: in a specific environment they readily react to form a thin oxide layer that protects them against further oxidation. On the contrary, others like iron suffer uniform corrosion and need to be coated or alloyed with other metals to create a protective shell.

Fundamental studies on metal passivity and corrosion in aqueous environment have been originally approached from the Electrochemistry discipline. Basic electrochemical techniques have provided insight in the thermodynamic and kinetic aspects of passivity. In these sense, (electro)chemical reaction pathways of electrode passivation for a huge variety of metal electrodes in contact to different solution environments have been suggested. Many efforts have been concentrated too in the elucidation of the chemical and crystalline structure of the passive oxide films, as its atomic organization and structural defects often determine the electrical properties that finally control its protecting or passivating character. To better understand the electronic properties of these passivating oxide surfaces, electrical models of the metal | passive film | electrolyte interface are of outmost importance.

In the following sections, we will discuss the fundamental aspects of passivity, from the thermodynamic and kinetic points of view. A very brief sketch on the models of passive film growth and the main parameters affecting the final properties of the film (composition, thickness or electronic properties) will be provided. The electronic properties of a semiconducting oxide film and the behaviour of the metal | oxide | electrolyte interface under equilibrium or applied potential are examined to understand the Mott-Schottky relation derived from electrochemical impedance spectroscopy (EIS) measurements. Finally, *in situ* nanoscale studies of oxide growth and the state-of-the-art of tin passivation will be addressed.

A.1 Fundamentals of passivity

For a metal exposed to a solution or air, thermodynamic stability is only observed on noble metals due to their high reduction potentials. For non-noble metals, the difference in redox potentials between the metal and a second phase in contact to it leads to a driving force ($\Delta G < 0$) for metal oxidation [15]. The environmental conditions can either favour the dissolution of the oxidized metal cations (active dissolution) or the formation of an insoluble oxide film (passivation), so both processes are somehow competing. For all chemical processes, the two aspects have to be considered: equilibrium and kinetics [15-17].

A.1.1. Thermodynamic and kinetic aspects of passivity

The first consideration when studying a passive oxide layer is its chemical stability in the electrolyte medium where it is being formed. The thermodynamic stability of the different species as a function of pH and electrochemical potential are represented in Pourbaix diagrams [15-17]. Fig. A.1a gives the Pourbaix diagram of tin in aqueous solution [18]. The diagram provides regions of existence, for example, for a particular combination of pH and potential it can be predicted whether it is thermodynamically favourable for Sn to be inert (immunity), to actively dissolve (corrosion) or to form an oxide/hydroxide layer (passivation). However, it must be noticed that these diagrams do not provide neither kinetic information nor the exact composition and structure of the final passive layer [15]. This limits the use of these diagrams to a mere qualitative guidance. In the particular case of tin, it can be observed that passive layers are generally formed at pH values lower than 13 and at

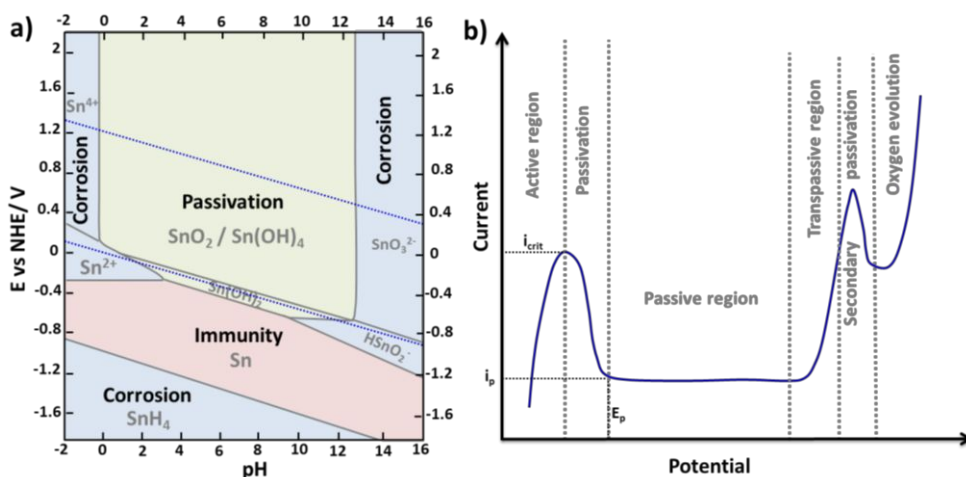


Figure A.1 a) Potential - pH equilibrium diagram (Pourbaix diagram) of the tin-H₂O system at 25°C and theoretical conditions of corrosion, immunity and passivation. Adapted from ref. [18]. b) Ideal anodic polarization curve for a metal electrode exhibiting passivation.

potentials above -0.4 V vs SHE. Here, a SnO_2 or Sn(OH)_4 layer is expected.

Anodic polarization curves are very instructive to examine the combined thermodynamic and kinetic aspects of metal passivation [16]. In polarization experiments, the electrode potential is linearly changed while monitoring the current given by the reactions occurring at the electrode | electrolyte interface (Fig. A.1b). Information on the different oxidation states and active/passive transitions can be extracted. A polarization curve can be perceived as a cross-section through the Pourbaix diagram at a fixed pH [15].

Starting with a cathodic current in the range of hydrogen evolution, when the potential of the bare metal electrode is raised it starts to oxidise and an increase in the current response is observed (Fig. A.1b). This region where current is boosted is known as the active region. By further increasing the potential to the passivation potential, E_p , the current decreases sharply resulting in surface passivation. A measure of the easiness of passivation is the critical current density (i_{crit}), which corresponds to the maximum current density in the active/passive transition [15]; the lower the i_{crit} the easiest the metal passivates. During passivation the electrode is covered with the oxidation product, normally an oxide film that blocks the surface against further oxidation. After this, the current reaches a minimum plateau over a large potential range. Depending on the passivation nature, whether it is a physical or an electronic barrier, such potential range can be related to the oxide semiconducting properties. The current flow in the passive range (i_p) is a measure of the protectiveness or the quality of the oxide film [15].

If potential is swept to higher anodic values, transpassive oxidation begins. In this potential region metal cations are oxidised to higher valences, which implies that depending upon environmental conditions, the surface of the electrode may either passivate again (secondary passivation) or dissolve to higher valence soluble species leading to electrode corrosion. There are metals that are not prone to transpassivation and remain stable even if the potential is anodically increased to tens or even hundreds of volts. In such case, metal activation occurs due to the electric breakdown of the passive film. The electrochemical stability of the oxide film is related to its energy band structure: the electric breakdown upon anodic potentials begins when the Fermi level of the metal becomes lower than the valence band edge of the oxide [19]. Under these conditions, electron tunnelling is possible and, in consequence, the dissolution rate of metal ions is considerably increased [19]. It must be noticed that here the presence of aggressive ions has been neglected. If species such as chlorides, nitrates or perchlorates are present in solution, Sn and other metals like Fe or Cu would experiment localized corrosion or pitting phenomena and the potential range of stability of its passive film would be shortened.

A.1.2. Mechanisms of passive film growth

The *electrochemical passivation* has been usually described by using two models: the layer-pore resistance model and the solid-state migration model.

A.1.2.1. Layer pore resistance model (LPRM): dissolution-precipitation

The Layer-pore resistance model was first proposed by Müller and later on extended by Calandra *et al.* in the 1970s [20,21]. It assumes that the surface passivation results from a dissolution-precipitation process; the metal is dissolved until a critical concentration is reached in the vicinity of the anode and then a low conductivity oxide layer is precipitated blocking the metal surface. The precipitated layer usually presents a poor electrical contact to the metal substrate underneath, so it merely acts as a physical barrier.

Initially, the randomly formed precipitates spread over the electrode at a constant thickness until only small pores in the layer remain as the only access to the reactive metal surface. After this, the increase in the oxide film thickness proceeds with a constant pore area. Under these circumstances, the current flow is controlled by the resistance of the layer-pore system. If the total area of the electrode is A_0 , θ the surface coverage, the resistance of the pores threading the layer, $R(\theta)$, can be expressed as in equation (A.1) [20]:

$$R(\theta) = \frac{\delta}{\kappa A_0 (1-\theta)} \quad (\text{A.1})$$

where δ is the film thickness, and κ the specific conductivity of the electrolyte solution in the pores. When an external potential is applied, E , the resulting current, I , depends on the total resistance given by the resistance of layer-pore system and the ohmic resistance of the system in the absence of the oxide layer:

$$I(R(\theta) + R_0) = E \quad (\text{A.2})$$

If a potential sweep is applied, both E and θ change with time. By assuming that E changes linearly with time, δ is independent on the potential sweep rate, v , and that the E/I curve exhibits a maximum current, I_m , at a potential E , which is determined from the condition $\partial^2 \theta / \partial t^2 = 0$ the following expression (A.3) is derived:

$$I_m = \left(\frac{z F \rho \kappa A_0}{M} \right)^{1/2} (1 - \theta_m) v^{1/2} \quad (\text{A.3})$$

where ρ is the specific gravity of the grown film and M its molecular weight. The whole mathematical derivation can be found in [20]. According to equation (A.3), if θ_m is independent of v , the current peak height should increase linearly with the square root of the potential sweep rate, the slope depending on the properties and thickness of the film.

At a constant R_0 , the potential at I_m , E_m , should also increase linearly with the square root of the potential sweep as deduced from equations (A.2) and (A.3), by following equations in (A.4) and (A.5):

$$E_m = \left[R_0 + \frac{\delta}{\kappa A_0 (1 - \theta_m)} \right] \left(\frac{z F \rho \kappa A_0}{M} \right)^{1/2} (1 - \theta_m) v^{1/2} \quad (\text{A.4})$$

$$E_m = E_0 + \left(\frac{z F \rho \kappa}{M} \right)^{1/2} \left[\left(\frac{\delta}{\kappa} \right) + R_0 A_0 (1 - \theta_m) \right] v^{1/2} \quad (\text{A.5})$$

It should be noted that the nuclei of the precipitated material will always be three-dimensional so this mechanism is not expected to lead to epitaxial or compact layers but to porous films with a relatively low surface protectiveness.

A.1.2.2. High field mechanism: solid state ion migration

The high field mechanism is used to describe the growth of a compact or barrier-type oxide film on a metal electrode surface. In such case, the film is assumed to grow thanks to the migration of ionic species (M^{n+} and O^{2-}) through the oxide film [22,23] and accordingly the oxide layer develops preferentially either at the inner metal | oxide or the outer oxide | electrolyte interface [6,24] as shown in Fig. A.2. In a qualitative way, one can assume that reactions (A.6) and (A.7) occur at the metal | oxide interface, the first corresponding to the formation of metallic ions and the latter to the growth of the oxide by reaction with the incoming O_2^- [6,22–24].



Conversely, reactions (A.8)-(A.11) are given at the oxide | electrolyte interface. Reaction (A.8) is the dissociation of water molecules to supply the oxygen ions required for the oxide growth. Reaction (A.9) is associated to the oxide formation at the oxide | electrolyte

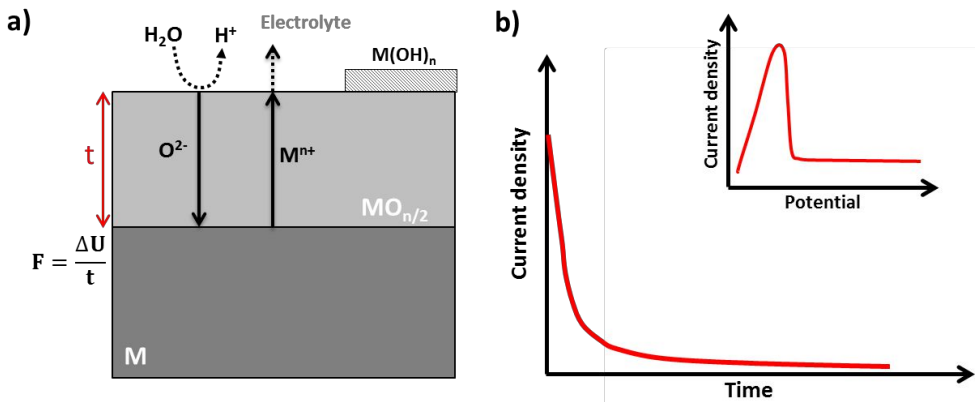
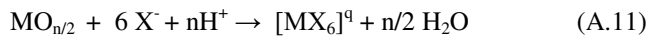


Figure A.2 a) Schematic representation of the high field mechanism involved in the formation of a compact or barrier-type oxide layer. This process is given when the metal is anodized in the absence of an agent that dissolves the oxide. b) Typical current-time curve after the application of a potential step for the growth of a compact oxide layer. The inset shows the linear sweep voltammogram. Adapted from reference [25].

interface. Reaction (A.10) corresponds to the complexation of field-assisted ejected M^{n+} into the electrolyte. If these ejected M^{n+} ions are not solubilized or complexed as $[MX_6]^q$ (where q is a charge that depends on the oxidation state of the metal and the nature of X^-), a hydroxide layer $(M(OH)_n)$ is likely to precipitate [6,22,25]. This hydroxide layer is typically not well attached and has a porous nature, so it just induces a certain delay in the diffusion of species. Also, dissolution of the grown oxide can take place following reaction (A.11) [6,25].



Commonly, anodization is carried out under potentiostatic conditions (constant applied voltage more positive than the thermodynamically reversible potential for the formation of the oxide phase). In these conditions, the current response decays exponentially with time as displayed in Fig. A.2b. Several models have been developed to explain the ion migration mechanism through the oxide film and the observed behaviour of the current response. These models provide a quantitative perception of the overall process. The first high field model was proposed by Verwey in 1935 [26] and later modified by Cabrera and Mott [27] and by Fehlner and Mott [28]. In all cases, the film is assumed to grow thanks to the migration of interstitial atoms of at least one of the ionic species through the oxide film [29,30]. The model was further revised by Macdonald *et al.* in 1981 [31,32] to include the dissolution of the oxide film and the role of other defects such as anion and cation vacancies, the so-called Point Defect Model (PDM). The main characteristics of these models are summarized in Table A.I and will be discussed in the following lines.

- (i) *Cabrera-Mott model*: it assumes that the oxide growth is due to the transport, via interstitial positions, of cations (I_M) across the oxide film to the oxide | solution interface where they react with species from the electrolyte (reaction d in Fig. A.3). In weak field conditions, the migration of cations is the rate limiting step, but under strong fields this migration is fast and then the limiting step is the injection of cations species at the metal | oxide interface [27,29,30]. The current during the oxide growth takes the expression (A.12)

$$i = Ae^{\beta F} = Ae^{\beta \frac{\Delta U}{t}} \quad (A.12)$$

where F is the electric field strength (typically $\sim 10^6$ - 10^7 Vcm^{-1}) on a barrier layer with thickness t and A and β are temperature-dependent parameters characteristic of the oxide. The model is not valid to describe steady state conditions where current and

Table A.I. Comparative summary of the main characteristics of the kinetic models used to describe the electrochemical growth of a compact oxide layers on a metal surface. From reference [29].

	Cabrera-Mott (air formation)	Fehlner-Mott (air formation)	Point Defect Model or Macdonald (electrochemical formation)
Growth mechanism	Migration of interstitial cations	Migration of interstitial anions	Migration of anion vacancies
Limiting step	<u>Weak electric field</u> transport of cations <u>Strong electric field</u> injection of cations at the metal oxide interface	Anion transport through the film	<u>Transport control</u> oxygen vacancies <u>Interface control</u> anion vacancies injection at the metal oxide interface
Electric field	Function of layer thickness ($F=\Delta U/t$)	Independent of thickness	Independent of thickness
Dissolution	No	No	Dissolution of oxide Dissolution of metal
Interfacial potential	No	No	Function of pH and applied E

thickness do not change with time. Moreover, there are important points that are not taken into consideration such as the possible growth through anion migration, the presence of vacancies, the dissolution of the oxide, and the potential drops at the metal | oxide and oxide | electrolyte interfaces [29].

- (ii) *Fehlner-Mott model*: was intended as an evolution of the Cabrera-Mott model and is based on similar assumptions. Their main difference is the fact that here the transport of interstitial anions across the oxide film is considered the source of the oxide growth and therefore its transport is the rate limiting step [28–30]. Also, the electric field is assumed to be constant, and then it is the activation energy of the rate-limiting step the one depending on the oxide thickness. The model gives a similar expression for the current response and presents the same weaknesses as the Cabrera-Mott model. However, its physical description is questionable because the electric field cannot remain constant during the oxide growth and the migration of anions via interstitial positions is difficult due to the steric hindrance of the oxide network, though it could be valid at the intergranular boundaries [29].
- (iii) *Point Defect Model*: it considers that the transport of anionic vacancies (V_o) across the oxide film to the oxide | electrolyte interface is responsible for the growth and acts as the rate-limiting step [29,31,32]. The diffusion of interstitial cations and/or cation vacancies results only in metal dissolution following reactions f and h in Fig. A.3. The dissolution of the oxide film is also considered (reaction i in Fig. A.3) and then a

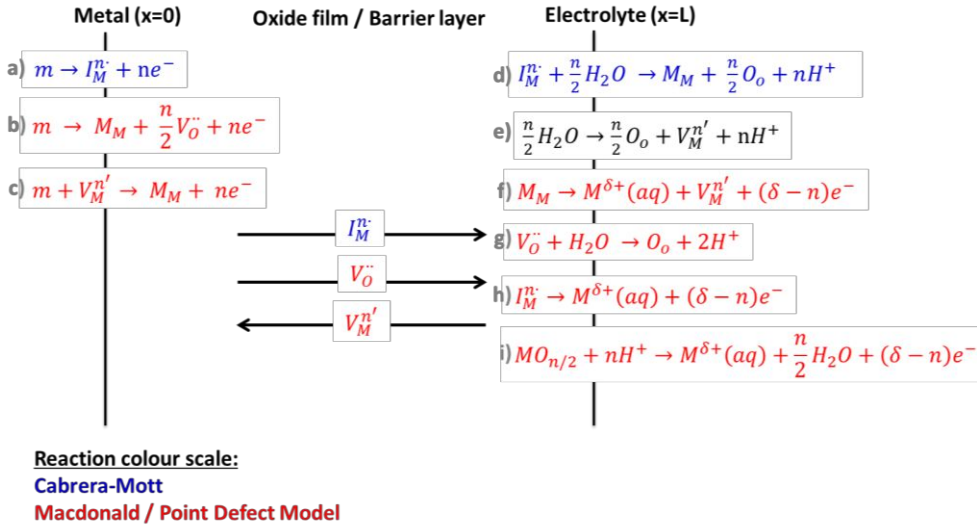


Figure A.3 Scheme describing the reaction and transport processes involved in the system metal | oxide | electrolyte during the growth of a compact oxide layer. Oxygen vacancies (V_O) metallic vacancies (V_M) and metallic interstitials (I_M) are implied and the dissolution of the oxide is also taken into account. The reactions correspond to a) cation injection in interstitial position of the oxide at the metal | oxide interface, b) oxygen vacancy formation at the metal | oxide interface, c) cation injection into vacancy position of the oxide at the metal | oxide interface, d) growth of the oxide via interstitial positions at the oxide | electrolyte interface, e) formation of cation vacancies at the oxide | electrolyte interface, f) cation dissolution through the generation of cation vacancies at the oxide | electrolyte interface, g) injection of an oxygen vacancy position at the oxide | electrolyte interface, h) cation dissolution via interstitial positions at the oxide | electrolyte interface, i) dissolution of the oxide. Adapted from references [29,32].

stationary state can be reached when the oxide growth rate and the dissolution rate are equal. This model was the first one to take into consideration the interfacial potential drops, which become functions of the pH and the applied potential. Although it is one of the most complete and quantitative models, there are also limitations such as the omission of oxide growth by cation migration via interstitial or vacancy positions, the assumption of a constant electric field and the consideration that the metal | oxide interface is also pH dependent [29].

A.1.3. Properties of passive oxide films

A.1.3.1. Structure and chemical composition

Passive oxide films are often amorphous or have a nanocrystalline nature. They are usually non-stoichiometric so they contain a high number of defects that can act as doping levels in their electronic structure and assist in the kinetic diffusion of vacancies across the oxide layer. There are many parameters influencing the composition and thickness of a passive oxide film, apart from the base metal, such as the passivation potential, time, electrolyte composition or temperature. In addition, it should not be considered as a rigid layer, but as a

system in dynamic equilibrium so its composition and thickness can be adjusted to changing environmental factors. For example, the “aging” or alteration with time of composition, structure, degree of hydration and ionic or electronic conductivity are well documented [15]. All these factors make the study of both structure and accurate composition of passive films really challenging, and highlight the need of characterization studies under electrochemical conditions.

First *in situ* investigations were carried out on passive iron oxide films by photoelectrochemical [33] or ellipsometric [34] techniques to gain insight on the electronic structure or layer thickness. Later on, more sensitive measurements such as *in situ* Surface Enhanced Raman Spectroscopy (SERS) were performed to provide chemical information. However, iron as well as tin shows a poor Raman scattering, so measurements were complicated because the signal was close to the noise level [35–37]. For iron, SERS investigations found that at low anodic potentials the passive film is composed mainly of a ferrous hydrated oxide [35,38] while at high potentials within the passive range it corresponds to a spinel type Fe_2O_3 [36,39]. Similar work done by Huang *et al.* on tin electrodes just allowed to detect the formation of $\text{Sn}(\text{OH})_4$ in the passive region and its associated reduction peak [37]. On other systems with a more SERS active surface like Cu, valuable information has been obtained for a wide electrochemical range *i.e.* OH adsorption is found at very negative potentials, followed by Cu_2O formation and then $\text{Cu}_2\text{O}/\text{Cu}(\text{OH})_2$ [40]. *In situ* far IR spectroscopy studies have corroborated the SERS measurements and propose that at high anodic potentials the final passive layer is composed of a duplex layer $\text{Cu}_2\text{O} | \text{CuO}, \text{Cu}(\text{OH})_2$ [41].

Quantitative evidence on the passive film composition can be acquired by *in situ* X-Ray absorption near-edge spectroscopy (XANES) and X-Ray diffraction (XRD) performed using synchrotron radiation. On iron passive films, XANES spectra revealed that at the onset of passivation the oxide layer is mainly composed of Fe (III) with a 10 - 20 % content of Fe (II) in its structure [42]. The percentage of Fe (II) doping gradually decreases with the applied potential up to 4 - 10 %, confirming the model of a final Fe(II)-doped passive film [42]. *In situ* XRD measurements confirmed the formation of a highly defective Fe_2O_3 spinel phase showing a fully occupied oxygen lattice with a different cationic occupancy in octahedral, tetrahedral and octahedral interstitial sites [43,44]. Analogous XRD studies have been reported for passive nickel indicating an inner crystalline NiO structure covered with an hydrated top $\text{Ni}(\text{OH})_2$ layer [45]. For Sn, only *in situ* XANES measurements have been attempted but given the difficulty on achieving flat surfaces, the small grazing angle and the low quality of the spectra any relevant conclusion could be drawn [46].

A.1.3.2. Electronic properties

The electronic properties of passive oxide films are very important because they determine, in many cases, the mechanism of film formation and passivity breakdown, as these processes involve diffusion of charge carriers through the layer. Most of the anodically grown oxide

films present a semiconducting nature [15]. Some of the electronic parameters characterizing these films are gathered in table A.II.

From the point of view of solid state physics, the band models of metals and semiconductors are considerably different. In periodic systems (bulk materials), the overlap between the discrete atomic orbitals of all the constituent atoms form bands of allowed energies. These bands are filled up with electrons up to a certain level, the Fermi level (E_F). In metals, the E_F lies inside an energy band, which is only partially filled (Fig. A.4a). These neither empty nor completely filled bands allow the free movement of electrons and contribute to their good conducting properties. In semiconductors, the filled and empty energy states do not overlap, so they are separated into the valence band (VB) and conduction band (CB) by the energy band gap (E_g) as shown in (Fig. A.4b). In this case, the E_F level virtually lies right within the energetically forbidden band gap. Although thermal excitation at room temperature provides charge carriers available for conduction, their amount is significantly lower than in metals [47]. Interestingly, conductivity can be increased by light driven excitation of electrons from the VB to the CB.

Table A.II. Main parameters corresponding to the electronic properties of bulk oxide semiconductor | electrolyte interfaces. ϵ_{ox} is the dielectric constant of the oxide layer. Data extracted from refs [15,48].

Metal or alloy	Conduction		E_g / eV	N_D / cm^{-3}	E_{FB} / eV	VB edge / eV	CB edge / eV	ϵ_{ox}
	type	(n, p, i)						
Al	i		4.5 - 9.0	-	-	-	-	7 - 20
Cr	p (n)		2.5 - 3.5	10^{20}	-	-	-	10 - 50
Cu	p		0.6 - 1.8	-	0.5	-	-	7 - 18
Fe	n		1.6 - 2.2	10^{20}	-0.1 / 0.15	2.2	0.2	10 - 35
Fe/Cr	n		1.9 - 2.1	10^{20} - 10^{21}	-	-	-	10 - 30
Fe/Cr/Ni	n		1.9 - 2.3	10^{20} - 10^{21}	-	-	-	10 - 30
Fe/Cr/Ni/Mo	n		2.3 - 2.8	10^{21}	-	-	-	10 - 30
Fe/Ni	n		1.9	10^{20}	-	-	-	10 - 35
Nb	n		3.4	-	-0.75	-	-	-
Ni	p (n)		2.2 - 3.7	10^{20}	1.2	-	-	30
Pb	n		2.8	-	0	-	-	-
Sn	n		3.5 - 3.7	10^{19} - 10^{20}	-0.45 / -0.3	3.8	0.1	10
Ti	n		3.2 - 3.8	10^{20}	-0.6	2.7	-0.3	7 - 114
V	n		2.75	-	0.9	-	-	-
W	n		2.7 - 3.1	10^{17} - 10^{18}	-0.5 / 0	-	-	23 - 57
Zn	n		3.2	10^{18}	-0.4 / -0.85	2.6	-0.6	8.5
Zr	i (n)		4.6 - 8	-	-1.8	2.5	-1.4	12 - 31

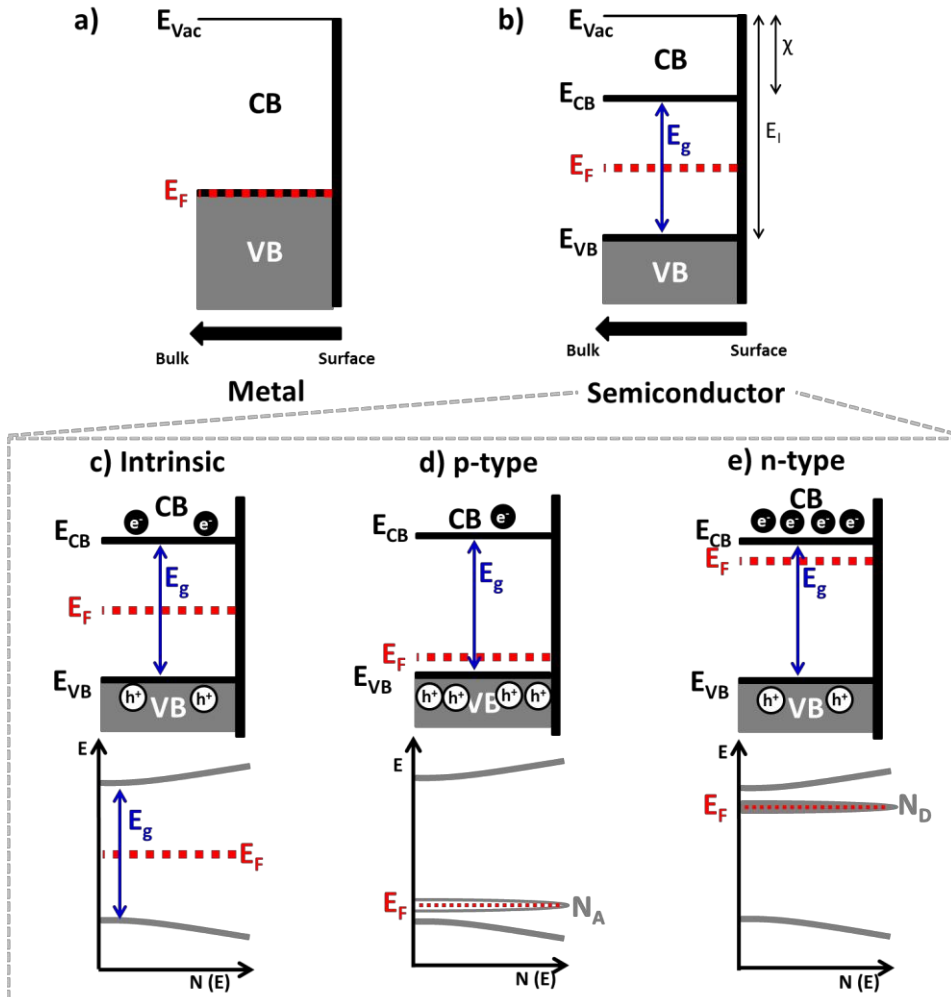


Figure A.4 Band diagrams for a) metal and b) semiconductor. E_{CB} and E_{VB} are conduction and valence band respectively. E_F denotes the Fermi energy level and E_g is the forbidden band gap between the bottom of the conduction band (CB) and the top of the valence band (VB). The electron affinity and ionization energy are χ and E_I respectively. All energies are given versus the vacuum level $E_{vac}=0$. Band diagram and density of states for a c) intrinsic, d) p-type and e) n-type semiconductor.

The energy band diagram represented in Fig. A.4c corresponds to an *intrinsic* semiconductor in the absence of any source of doping levels near the energy bands. Typically, chemically pure semiconductors such as Si, Ge, *etc.* present this behaviour [47]. However, passive films, whose structure and chemical composition are rather complex, tend to have impurities, vacancies, interstitials, dislocations or grain boundaries that generate additional energy levels near either the VB or CB leading to *doped* or *extrinsic* semiconductors. The presence of these new levels within the band gap, acceptor states near the valence band or donor levels close to the conduction band, increase the conductivity of the material. Since

the E_A -VB and E_D -CB differences are typically a few tens of meV, electrons will flow at room temperature from the valence band to the acceptor level (h^+ injection) or from the donor level to the conduction band (e^- injection). The enhancement in conductivity will then be proportional to e^- or h^+ concentrations. The standard terminology in solid-state physics is that if a semiconductor is dominated by acceptor impurities, so h^+ in the valence band outnumber the e^- in the CB, the material behaves as a p-type semiconductor (Fig. A.4d) [47]. On the contrary, it is called n-type semiconductor when e^- act as the majority charge carriers (Fig. A.4e). In an intrinsic semiconductor the amount of h^+ and e^- is equal (Fig. A.4c) [47].

A.2 The semiconductor | electrolyte interface

The electronic properties of the semiconducting passive layers can be studied by techniques derived from the semiconductor electrochemistry field such as photoelectrochemistry and capacitance measurements [15]. To understand both, some of the basic aspects of the semiconductor | electrolyte interface need to be introduced.

A.2.1. Electrical double layer at the metal | electrolyte interface

Upon immersion of a metal electrode in an electrolyte, rearrangement of surface charges takes place. Electrons are transferred from the higher E_F phase (either metal, E_F , or electrolyte, $E_{F,redox}$) towards the lower until an equilibrium condition is reached ($E_F = E_{F,Redox}$). At the equilibrium, the charge in the metal surface is balanced by an opposite charge in the electrolyte, giving rise to the region called electrochemical double layer (EDL). Such interface is represented as a capacitor in an equivalent electronic circuit due to its particular structure of two charged planes.

The existence of an EDL was first postulated by Helmholtz in 1879. That first theoretical model assumed the presence of a compact layer of ions in contact with the charged metal surface (Fig. A.5a). In 1910 and 1913, respectively, Gouy and Chapman proposed the formation of a diffuse double layer in which the accumulated ions, following a Boltzmann distribution, extended to some distance from the electrode surface (Fig. A.5b). In further developments, Stern (1924) suggested that the electrified solid-liquid interface included both the rigid Helmholtz and the diffuse layer of Gouy and Chapman (Fig. A.5c). Specific adsorption of ions at the metal surface was pointed out by Graham in 1947 (Fig. A.5d) and in consecutive developments, the role of polar solvents solvating the ions in the electrolyte, was introduced in the EDL model (Bockris, Devanathan and Muller, 1963, Fig. A.5e).

Experimentally, the presence of the EDL is manifested as an electrical capacitance at the interface. The total capacitance of the electrical double layer (C_{dl}) is a composition of the in series capacitance of the two charged regions: the Helmholtz (C_H) and diffuse (C_d , Gouy-Chapman) electrical layers, as represented in equation (A.13).

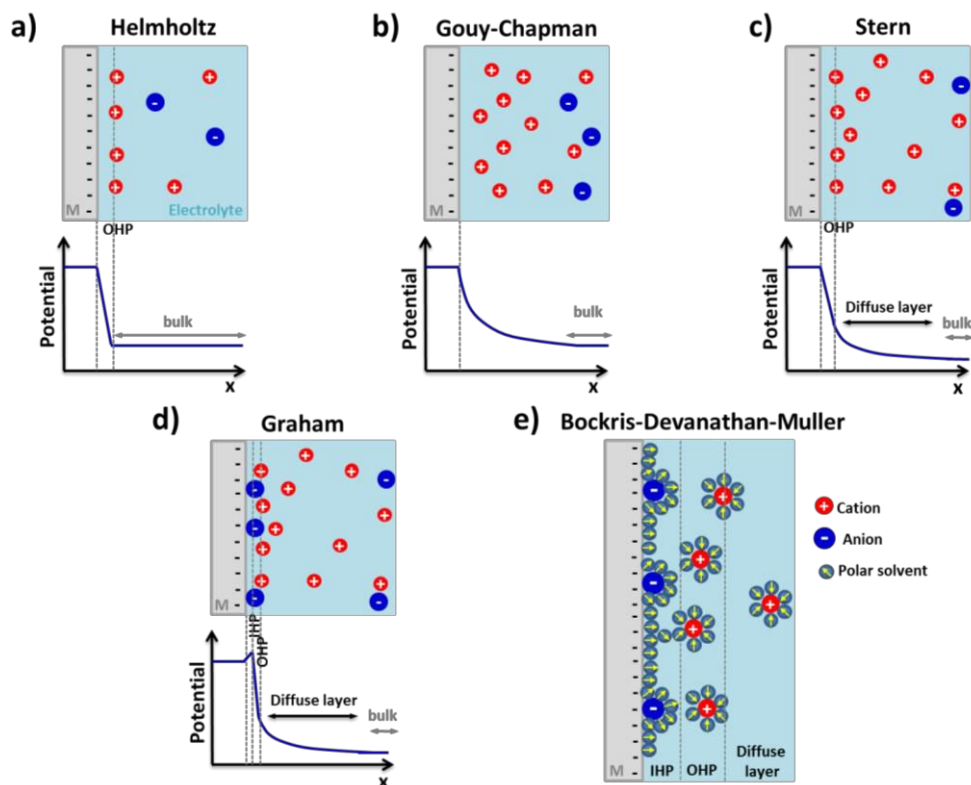


Figure A.5 Double layer models for a metal | electrolyte interface, considering a negatively charged metal: a) Helmholtz, b) Gouy-Chapman or diffuse layer, c) Stern, d) Graham, assuming specific adsorption of anions and e) Bockris-Devanathan-Muller, considering adsorption of anions and the effect of a polar solvent. At the top the charge distribution vs the distance is given and at the bottom the potential vs distance.

$$\frac{1}{C_{el}} = \frac{1}{C_H} + \frac{1}{C_d} \quad (\text{A.13})$$

Further discussion on the characteristics of the Helmholtz and diffuse layer will not be given because they are beyond our scope but can be found in references [47,48].

A.2.2. Electrical double layer at the semiconductor | electrolyte interface: the space charge region

The metal | electrolyte interface displays the simplest electrochemical interface because the charge carrier density in the metal electrode is concentrated just below the surface. However, semiconductors have smaller charge carrier density ($\sim 10^{17} \text{ cm}^{-3}$ vs $\sim 10^{22} \text{ cm}^{-3}$ in metals) and the spatial distribution of the charge can extend over a considerable distance at the electrode side of the semiconductor | electrolyte interface. This phenomenon originates the so-called space charge region or space charge layer (SCL), which makes the semiconductor |

electrolyte interface particularly more complex given that both capacitive components, SCL and EDL, may now play a role in the electron transfer processes at such interfaces. In absence of a current flow, each of these individual layers has an associated stored charge that can be expressed as a differential capacitance (in μFcm^{-2}) like in (A.14)

$$C = \frac{dQ}{dV} = \frac{A\epsilon\epsilon_0}{s} \quad (\text{A.14})$$

where A and s are the area and the separation of the charge being stored, respectively, and ϵ the dielectric constant. The whole semiconductor | electrolyte interface can be represented as a composition of capacitors (Fig. A.6) in series as in expression (A.15)

$$\frac{1}{C_{\text{Total}}} = \frac{1}{C_{\text{SC}}} + \frac{1}{C_{\text{el}}} = \frac{1}{C_{\text{SC}}} + \frac{1}{C_{\text{H}}} + \frac{1}{C_{\text{d}}} \quad (\text{A.15})$$

where the smallest capacity predominates in determining the overall capacity ($1/C_{\text{Total}}$). Usually, the smallest capacity occurs in the compact layer (C_{H}) for metal electrodes and in the space charge layer (C_{sc}) for semiconducting ones [47].

Fig. A.6 also sketches the complete charge distribution generated when a semiconducting electrode and an electrolyte are placed into contact. For a n-type semiconductor at open circuit potential, the Fermi level is typically higher than the Fermi redox level of the electrolyte (*i.e.* the Fermi redox potential of an electrolyte is the average between the energy of the oxidized and reduced form of the electro-active species in solution, which can be directly related to the redox potential) and, hence, electrons will flow from the electrode into the solution leading to a positive charge at the electrode surface that will conform the SCL [49]. This process is represented as an upward band bending in the band diagram representation of the semiconductor (Fig. A.6). Since the majority charge carriers of the semiconductor have been removed from this region, it is also referred to as a depletion layer.

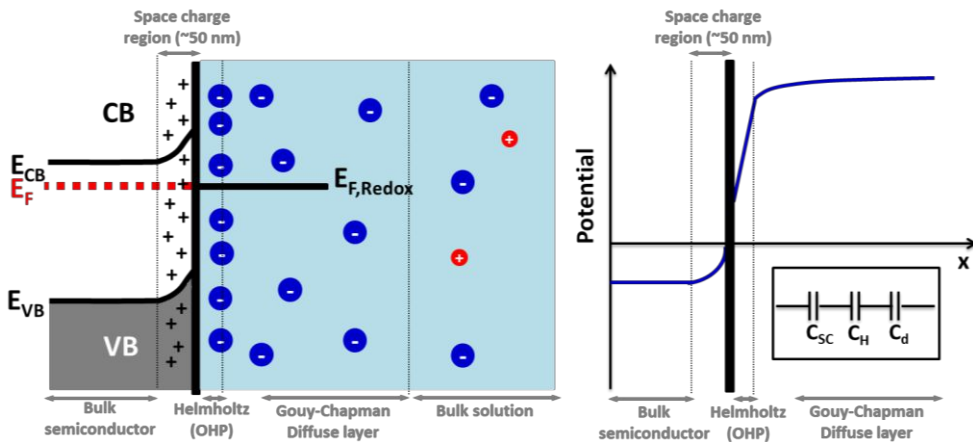


Figure A.6 Schematic representation of the double layer created in a semiconductor electrode in contact with an electrolyte solution.

For a p-type semiconductor, the Fermi level is generally lower than the redox potential, and therefore electrons must transfer from the solution to the semiconducting electrode to reach the equilibrium [49]. This generates a negative charge in the space charge region, which causes a downward band bending. As the holes at the SCL are removed, this region is again the depletion layer.

A.2.2.1. The semiconductor | electrolyte interface under electrochemical control

Modifying the electrochemical potential in a metal electrode implies controlling its E_F energy position, thus supplying or removing charge carriers to/from the electrode surface that will be ready to be transferred to/from redox species in solution. If the same concept is applied to a semiconducting electrode and E_F is shifted, this will affect the energy position of the semiconductor band edges and in consequence directly modify the extension of the SCL at the electrode surface due to the supply/removal of charge carriers. The applied electrochemical potential introduces then overall modifications in the magnitude and direction of band bending [47]. There are three different situations to be considered (Fig. A.7):

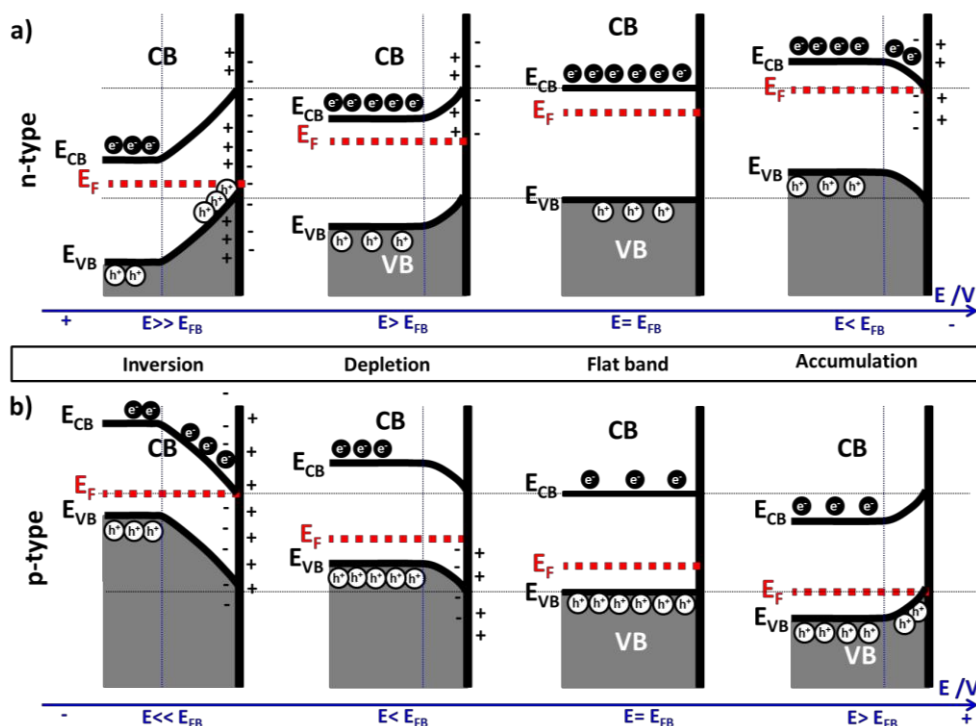


Figure A.7 Band diagrams showing the space charge layer profiles of a) n-type and b) p-type semiconductor electrodes at different applied potentials (E). Four different situations are described in each case: inversion, depletion, flat band (E_{FB}) and accumulation.

- I) At a certain potential, the charge due to fixed ions within the solid lattice is balanced by the free charges at the surface, so there is no potential drop across the SCL of the semiconductor. Then, the electron energy at the semiconductor surface is the same as in the bulk; so bands are represented like flat bands as shown in Fig. A.7. This potential is referred to as the flat band potential, E_{FB} . In this situation, the charge at the interface is zero, $Q_{SC} = Q_{el} = 0$, which is somehow analogous to the potential of zero charge in metals.
- II) Depletion regions arise at electrochemical potentials more positive than the E_{FB} for an n-type semiconductor ($E > E_{FB}$) and at potentials more negative than the E_{FB} for a p-type semiconductor ($E < E_{FB}$). Here, the majority charge carriers are extracted from the surface, producing an insulating layer represented by an upward bending in n-type or downward for p-type.
- III) At potentials negative than the E_{FB} for an n-type semiconductor, there is an excess of the majority charge carrier (electrons) in the SCL, thus the semiconductor is in accumulation conditions and the bands are bended downwards. Accumulation conditions arise in a p-type semiconductor at potentials more positive than the E_{FB} and cause an upward bending.

The charge transfer abilities of a semiconductor electrode depend on whether it is under accumulation or depletion conditions. If there is an accumulation layer, the behaviour of a semiconductor electrode is similar to that of a metal, since there is an excess of the majority charge carriers available for charge transfer. In contrast, if there is a depletion layer, then the surface is depleted of charge carriers producing an insulating layer that will hinder the electron transfer reactions.

A.2.2.2. Capacitance measurements of the SCL: Mott-Schottky plots

Mott-Schottky analysis of capacitance measurements can be used to determine properties such as E_{FB} , the semiconductor type and the number of charge carriers of a passive oxide layer. The derivation of the Mott-Schottky equation used to fit the data involves several steps. As in any study of an electrified interface, the problem starts by solving the one-dimension Poisson's equation that describes the relationship between charge density and the electric potential:

$$\frac{d^2E}{dx^2} = -\frac{\rho}{\epsilon\epsilon_0} \quad (\text{A.16})$$

where ρ corresponds to the charge density at a position x away from the semiconductor surface, ϵ is the dielectric constant of the semiconductor and ϵ_0 the permittivity of vacuum. Using the Boltzmann distribution to describe the distribution of electrons in the SCL and the

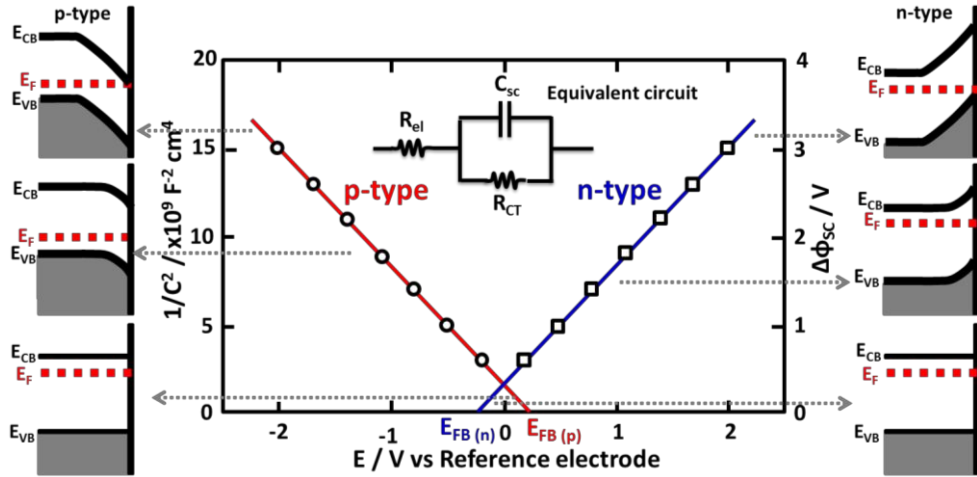


Figure A.8 Mott-Schottky representation of the capacitance data for both n-type and p-type semiconductors under depletion conditions. Schemes at the lateral sides represent the sequence of band bending as the potential is decreased (p-type) or increased (n-type) from the flat band situation (E_{FB}). Inset in the graph details the equivalent circuit used to fit the impedance data: R_{el} accounts for the resistance of the electrolyte solution, R_{CT} the resistance of the passive layer to the charge transfer and C_{sc} the capacitance of the semiconductor. If the semiconductor capacitance does not show ideal capacitance behavior, C_{sc} can be replaced by a constant phase element (CPE).

Gauss' Law relating the electric field through the interface to the charge contained within that region, equation (A.16) can be solved to obtain the Mott-Schottky equation:

$$\frac{1}{C_{Total}^2} = \frac{2}{\epsilon\epsilon_0 e N_D} \left(E - E_{FB} - \frac{k_B T}{e} \right) \quad (A.17)$$

where C_{Total} is the interfacial capacitance of the semiconductor | electrolyte interface, N_D the donor density, E the applied electrochemical potential, k_B the Boltzmann's constant, T the absolute temperature and e the electron charge ($k_B T/e = 0.025$ V). For the whole derivation of the Mott-Schottky equation the reader is referred to [49].

Experimentally, the total capacitance C_{Total} can be measured by electrochemical impedance spectroscopy (EIS). The impedance data as a function of frequency is fitted to an equivalent circuit (Fig A.8) to extract the capacitance values of the electrode | electrolyte interface. In the absence of other forms of interfacial stored charge than the SCL, C_{Total} can be approximated to the semiconductor capacitance C_{sc} . Subsequently, capacitance vs potential measurements are performed at a constant frequency within the region where the capacitive behaviour is maximized, *i.e.* the phase response is close to 90° . The capacitance data is then represented in the form $1/C^2$ vs E , the so-called Mott-Schottky plot. The slope of the linear trend provides a measurement of the carrier density (N_D or N_A values for n- or p-type respectively), and the intercept $1/C^2=0$ stands for the E_{FB} (see Mott-Schottky plot in Fig.

A.8). Note also that the slope sign determines the kind of doping species; n-dopants give a positive slope while p-dopants give a negative slope.

More complex capacitance behaviours can be found if other capacitive elements are also present at the interface, *e.g.* adsorbed anions, effective surface states or other sources of charge carriers. For more details on the contribution of surface states or adsorbed anions check on reference [47].

A.3 *In situ* nanoscale studies of anodic oxide growth

In situ characterization at the oxide | electrolyte interface has gained interest in passivation studies as it offers the possibility to measure directly the properties of the oxide and avoids the contribution of the changes it may suffer when transferred from the solution to the measurement chamber. There are many technical difficulties on these experiments that make them really challenging, namely, the implementation of an electrochemical cell in the measuring system to accurately control the potential, the strong technical constrictions to resolve the structure and the composition of the passive oxide film and the low signal to noise ratio arising from the presence of the liquid medium.

Electrochemical scanning tunnelling microscopy (EC-STM), sometimes referred to as *in situ* STM, is a powerful technique to study nanoscale structural and electronic changes on a metal | electrolyte interface under electrochemical control [50]. Relevant electrochemical processes such as corrosion, passivation, electro-deposition, molecular adsorption, surface reconstruction or surface dissolution reactions can be studied *in situ* [51,52,53].

In the following sections we will describe the fundamentals of the EC-STM approach and its relevance in the study of passivation and corrosion processes of transition metals like Cu, Ni or Fe.

A.3.1. Electrochemical scanning tunnelling microscopy (EC-STM) principles

The scanning tunnelling microscope (STM) was first developed by Gerd Binnig and Heinrich Rohrer in 1981 [54]. Since then, the STM has become a key tool in surface science as it provides surface images with resolution at the atomic level. The operation mode is based on the quantum mechanical tunnelling phenomenon occurring between a sharp metallic tip placed very close to a conducting surface (metal or semiconductor). Under the application of a small bias between the surface and the tip, electrons can flow between both through the insulating vacuum or air gap (Fig. A.9a). The simplest equation that relates the applied bias (E_{bias}), the tunnelling current (I_T) and the insulating gap distance (S) yields [55]:

$$I_T = I_0 \frac{E_{bias}}{S} e^{-k\sqrt{\phi_{bias}} S} \quad (\text{A.18})$$

Basically, an STM microscope can image the studied surface using two different modes: the constant current or the constant height. In the constant current mode, the tip scans the surface by keeping the tunnelling current constant, so that the vertical position of the tip is adjusted by the feedback system through a precise piezo-positioner. On the contrary, in the constant height mode the distance between tip and sample is fixed and the changes in the tunnelling current are recorded. This mode can only be used in extremely flat surfaces; otherwise the tip can easily crash against the irregularities.

The electrochemical scanning tunnelling microscope (EC-STM) is an extended technique of the standard STM developed to study the electrode | electrolyte interface. It uses the imaging principles of STM but operated in a three-electrode electrochemical cell in which the substrate acts as a working electrode, and a reference and a counter electrode complete the electrochemical configuration (Fig. A.9b). This setup is the same as a standard electrochemical cell coupled to a potentiostat to control the potential of the working electrode with respect to the reference electrode, while the current flows through the counter electrode. In the EC-STM configuration, the tip becomes a second working electrode under the same potentiostatic conditions. A bipotentiostat is introduced to independently control the potential of tip and sample with respect to the same reference electrode [55].

In conventional STM, tips are made by sharpening the edge of a metallic wire, being gold, platinum or tungsten the most commonly used. As the edge is very sharp, just the atoms at the very apex of the tip contribute to the tunnelling current. However, the incorporation of

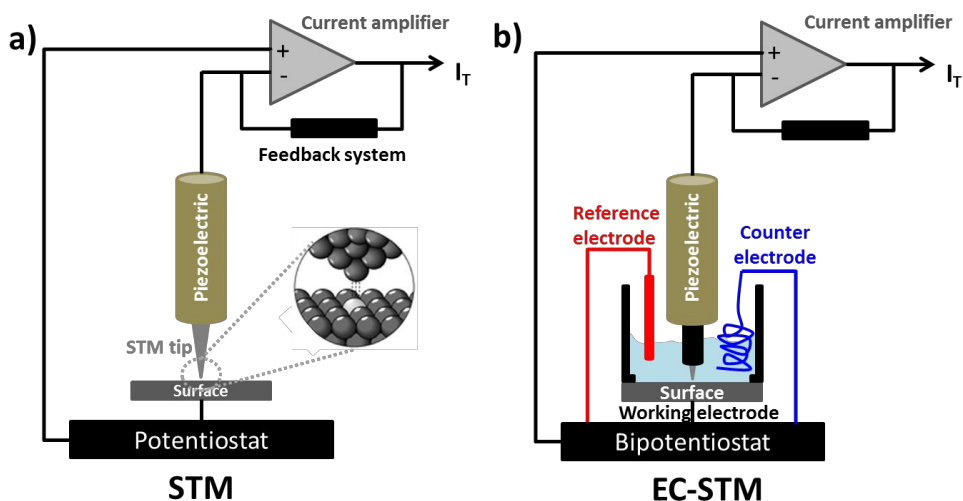


Figure A.9 Schematic diagram of a) a scanning tunneling microscope (STM) and b) an electrochemical scanning tunneling microscope (EC-STM). In b) the bipotentiostat controls the potential of the tip and sample with respect to reference electrode.

the liquid medium introduces other sources of current, such as Faradaic currents from electrodic reactions at the tip surface. These additional current sources strongly influence the overall measured STM current and cause instabilities that affect the imaging capability of the technique. In order to reduce the Faradaic contribution to the STM tunnelling current down to affordable values (< 10 % of the total tunnelling current), the tips used for EC-STM are coated with an insulating layer, which leaves only its very apex exposed to the solution. Moreover, the coating of the tip results also in a decrease of the EDL capacitance associated with the interface between the tip and the electrolyte, which also contributes as capacitive current noise to the tunnelling current [50].

Another critical issue in STM techniques is the preparation of the surface under study. Most of the EC-STM works require atomically flat surfaces with well-defined exposed crystallographic planes [50]. Usually single crystalline surfaces are employed, but its preparation is not straightforward and can require specific polishing and even annealing treatments. In the following section, a brief overview on EC-STM studies of the early stages of anodic oxidation in Cu and Ni single crystalline surfaces will be given. Also similar works on iron polycrystalline surfaces will be discussed.

A.3.2. EC-STM in the study of metal oxide growth, passivation and corrosion

Understanding the mechanisms of electrochemical metal passivation and localized corrosion at the nanoscale is a challenging issue. In this context, several EC-STM studies in transition metals such as Cu [51,53,56–60], Ni [52, 61,62], Ag [63,64] or Fe [10,11] have been reported.

Marcus *et al.* have carried out extensive EC-STM studies in single crystalline Cu (111) and (001) surfaces to understand the early stages of oxidation in alkaline media, the growth of Cu₂O, the structure of the whole duplex passive layer and the effect of Cl⁻ species in the passivation process [51,53,56–60]. At potentials more cathodic than the first oxidation process (Cu → Cu₂O, A1 in Fig. A.10b), the appearance of OH adlayers has been observed [51,53,57]. This surface hydroxylated regions present lower apparent height in the EC-STM image, nucleate preferentially at the step edges and grow laterally until the whole surface is covered (Fig. A.10a) [57]. In high-resolution EC-STM images, a hexagonal lattice has been obtained for the OH-adlayer phase (see Fig. A.10c) [53,57]. The incorporation of chlorides in the alkaline media competes with the OH adsorption, notably affecting the formation of the OH-adlayer. In fact, in presence of low Cl⁻ concentrations, thread-like structures of Cu-chloride containing compounds are formed [51]. Also interesting works have compared the structural characteristics of the Cu₂O layer formed in Cu (111) and Cu (001) and the tilt on the orientation of the oxide lattice with respect to the Cu lattice [53]. From these measurements epitaxial relationships between oxide and metal substrate were derived, *i.e.* there is a 45° direction tilt between Cu (001) and Cu₂O (001) that leads to the following

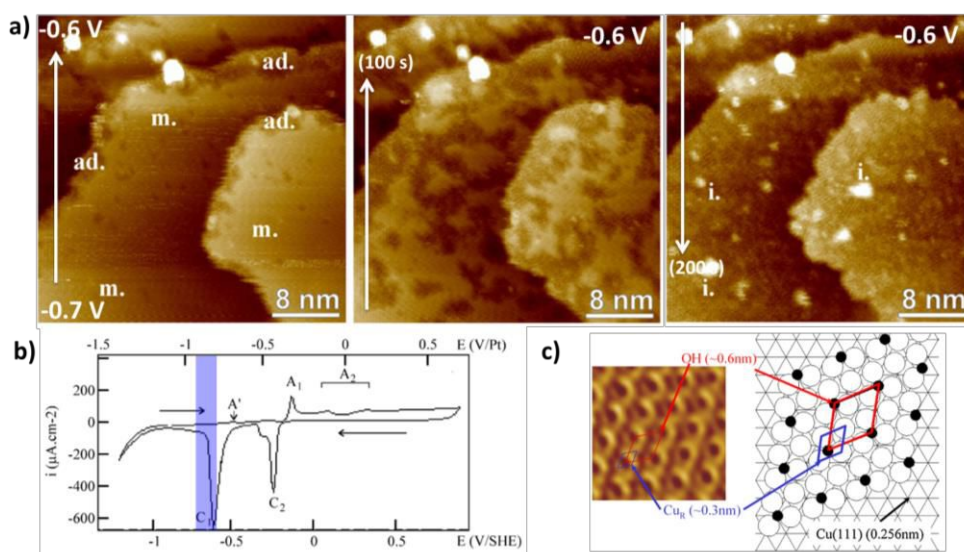


Figure A.10 a) EC-STM $40 \times 40 \text{ nm}^2$ recorded during the adsorption of hydroxide on Cu (111) surfaces, $I_t = 2 \text{ nA}$ and $E_{ip} = -0.4 \text{ V}$ ($\Delta z = 1.08 \text{ nm}$, 1.15 nm and 1.18 nm). The potential is scanned from -0.7 V to -0.6 V vs NHE (left image) and kept subsequently at -0.6 V vs. NHE where the adlayer (ad.) grows and the formation of Cu adislands (i.) occurs (middle and right). b) Cyclic voltammogram on Cu (111) in 0.1 M NaOH solution at 0.02 Vs^{-1} . c) High resolution EC-STM image of the OH-adlayer and model of the ordered structure. Data from references [53,56,57].

relationship $\text{Cu}_2\text{O}(001)[\bar{1}\bar{1}0] \parallel \text{Cu}(001)[100]$, while in Cu (111) Cu_2O can be oriented parallel or antiparallel to the substrate direction and therefore $\text{Cu}_2\text{O}(111)[\bar{1}\bar{1}0] \parallel \text{Cu}(111)[\bar{1}\bar{1}0]$ or $[\bar{1}10]$ [60].

Similar studies have been carried out for Ni (111) surfaces. An equivalent mechanism to that described for the early passivation stages of Cu (111) has been reported [62]. Additionally, 3D localized corrosion by competitive dissolution and re-passivation of the surface has been observed upon prolonged polarization in the active/passive potential region [61]. The dissolved or corroded regions show depressions of several monoatomic steps, whereas the uncorroded terraces that remain in between are covered by a 2D-passivating OH adlayer [61]. Interestingly, stripped patterns have been detected in some terraces and ascribed to a superstructure derived from the co-adsorption of H_2O and OH groups on a $\text{Ni}(\text{OH})_2$ monolayer [61]. In the presence of chlorides, the formation of these superstructures also occurs but requires longer polarization times due to the competitive adsorption of both OH^- and Cl^- anions [51]. Important effect of Cl^- has been observed during the growth of the final passive layer. For high Cl^-/OH^- ratios, the 2D growth of the crystalline passive film is blocked and then 3D nuclei and nanograin clusters are formed [51].

Díez-Pérez *et al.* studied the first oxidation stages of a polycrystalline Fe surface by EC-STM in borate buffer solutions [10]. Given the polycrystalline nature of the substrates, the

3D growth of the passive layer was the focus. The transition from a metallic surface to the first $\text{Fe}(\text{OH})_2$ nuclei by a dissolution-precipitation mechanism was followed at very low anodic potentials. The nuclei were found to grow laterally till their coalescence resulting in the coverage of the entire surface and passivating the electrode surface. When the passive film was fully developed, instabilities in the tunnelling current appeared and the EC-STM imaging was lost. These Fe passivation studies extended the EC-STM capabilities to understand the electronic properties of the passive layer [8,11] and its changes during the passivity breakdown process by Cl^- [9]. Conductance maps within the whole studied electrochemical potential range were derived from EC-STM spectroscopic measurements to determine the regions where tunnelling and, consequently, imaging was possible. From this data a quantitative energy diagram of the Fe | passive film | electrolyte interface was derived as well as key electronic parameters of the semiconducting passive film [8].

Although tin passivation has been widely addressed from the fundamental electrochemical point of view (see the following discussion in Section A.4), only Díaz *et al.* have followed the early stages of the oxidation process at the atomic level by EC-STM. Experiments were performed in borate buffer solutions at $\text{pH}=7.5$ [7]. In such conditions, a non-uniform $\text{Sn}(\text{II})$ -based thin oxide layer was formed and could be reversibly reduced if formed at potentials below the appearance of $\text{Sn}(\text{IV})$ -related oxide species (Fig. A.11). This film had a clustered structure typical of a film formed by a dissolution-precipitation process. Similar studies in strong alkaline media are not available up to date in the literature.

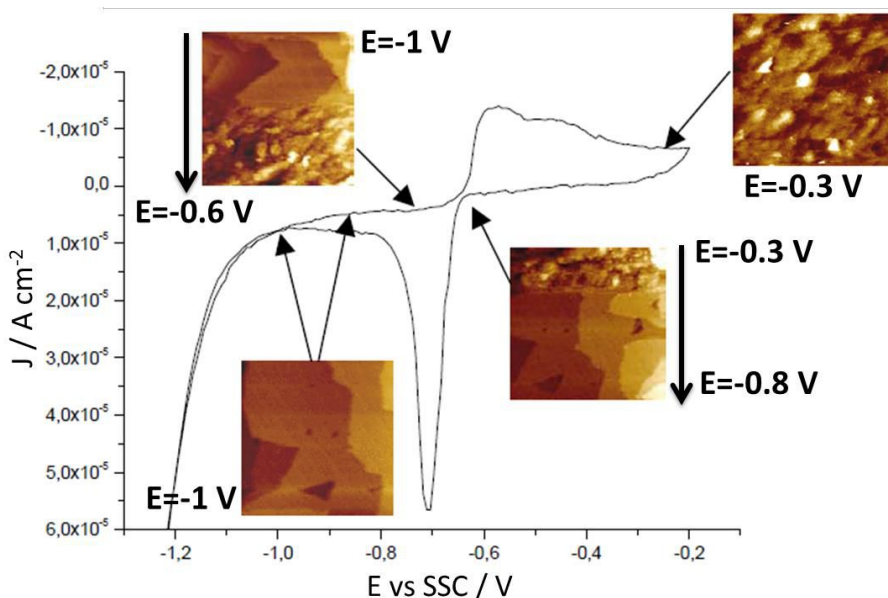
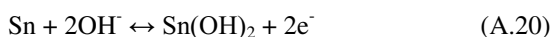
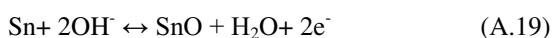


Figure A.11 *In situ* EC-STM images of the tin oxide layer formed in borate buffer at $\text{pH}=7.5$. Potentials were reached by scanning at 0.005 Vs^{-1} . At -1 V the initial metallic surface can be observed. Image size: $300 \times 300 \text{ nm}^2$. Z scale: 2 nm . From reference [7].

A.4 State-of-the-art of tin passivation

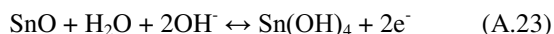
Passivation of non-transition metals such as Sn [7,65–78], Pb [79,80], *etc.* has been proven to be a more complex process as compared to their transition counterparts. Tin electrochemical behaviour in alkaline or slightly alkaline solutions has always been a matter of concern, given its technological implications [7,66,68,76]. Tin is mainly used as protective coating in food packaging (tin plated stainless steel) or as a soldering material. In the first case it is obvious that its passivation and corrosion behaviour need to be well understood, but also in the latter, since corrosion is one of the causes contributing to tin whiskering problem that leads to shortcuts in the electrical contacts [81]. In this view, special interest has emerged to understand its anodic behaviour, both within the corrosion [82–84] and passivation [65–78] regimes. Despite the amount of literature available on the subject, the electrochemical pathways and composition of the oxidation products are still a subject of debate.

Up to now, most contributions agree that, upon anodic polarization, the first electrochemical process corresponds to the active Sn dissolution as divalent tin ions in the stannite form (HSnO_2^- or $[\text{Sn}(\text{OH})_3]^-$) and subsequent formation of $\text{Sn}(\text{OH})_2$ or SnO surface passivating species [7,65–76] according to reactions (A.19) - (A.21). Irrespective of the employed electrolyte (NaOH, borate, citrate or bicarbonate), it is generally accepted that this process follows a dissolution-precipitation mechanism [7, 65–72]. Recently, the formation of SnO nanostructured microspheres has been reported within this active potential region in strongly alkaline media and ascribed to an anodic electrocrystallization process [85].



The mechanism of the final tin electrode passivation has always been more controversial. It is widely accepted that this process involves the formation of SnO_2 , but the route through which it is formed is not clear yet. A solid-state oxidation process from the early $\text{SnO}/\text{Sn}(\text{OH})_2$ primary passive film [70], detailed in reactions (A.22) and (A.23), or from the bare metallic Sn to a $\text{Sn}(\text{OH})_4$ phase [86] (in reaction (A.24)) has been generally proposed. More specific studies suggest that it proceeds through the contribution of two reaction paths: the oxidation of soluble Sn^{2+} species to Sn^{4+} and the direct oxidation of Sn to Sn^{4+} [65,66,68,69]. Despite the differences among these studies, it is accepted that the final passive film is initially a hydrated oxide [7, 68,70,71], $\text{Sn}(\text{OH})_4$, which gradually dehydrates with increasing time and potentials to a more stoichiometric SnO_2 layer [68,71] as shown in reaction (A.25). Once the surface is totally covered by a continuous insulating SnO_2 film, the growth proceeds by an ionic-conduction mechanism driven by the applied high electric field

across the film [72,86]. This behaviour has been compared to that of other valve metals such as Ti [72,73].



The composition of the final electrochemically grown passive film is also under discussion. The main disparities stem from its strong composition dependency on the working pH and electrolyte composition [71]. In strong alkaline media, Stirrup *et al.* proposed a duplex structure composed of a porous SnO and/or Sn(OH)₂ outer film and a continuous Sn(OH)₄ film at the metal/oxide interface [65] (Fig. A.12a). Contrarily, the X-ray photoelectron spectroscopy (XPS) measurements of samples prepared in similar conditions by Ansell *et al.* revealed the presence of SnO₂ or Sn(OH)₄ species only [74] (Fig. A.12b). Comparable results were obtained in neutral electrolytes such as borate [75]. In citrate buffer, Gervasi *et al.* performed galvanostatic electroreduction and EIS measurements and proposed a multilayered film structure with an inner SnO layer, a thick intermediate SnO₂ and an outer Sn(OH)₄ layer (Fig. A.12c) [76].

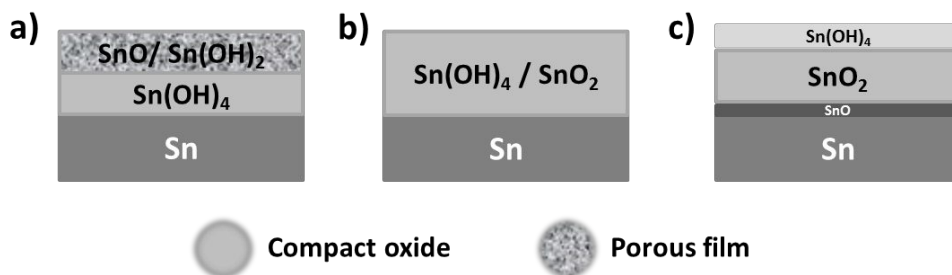


Figure A.12 Schematic representation of the structures proposed by a) Stirrup *et al.* [65], b) Ansell *et al.* [74] and c) Gervasi *et al.* [76] for passive films electrochemically formed on metallic tin.

Chapter 1

Tin electrochemistry in alkaline media

This chapter focuses on the study of the electrochemical processes occurring during the anodic oxidation of a metallic tin electrode in an alkaline solution. The actual knowledge on Sn passivation and the proposed reactions and mechanisms of oxide growth were discussed in section A.4. The lack of clear reaction pathways as well as its relevance in applied materials justifies the need of a consistent study.

The background concepts required for the interpretation of the results were provided in sections A.1 and A.2. Section A.1 deals with the important concepts in passivity and the two main oxide growth mechanisms while A.2 addresses the formation of the space charge layer and capacitance measurements (Mott-Schottky plots) that will be used during the results discussion.

1.1. Specific goals of this chapter

- Characterize the evolution of the chemical composition, structure and electronic properties of tin oxide layers formed within the active and passive electrochemical ranges by means of microscopic and spectroscopic techniques.
- Propose a complete mechanism for the electrochemical passivation of tin in alkaline media.

1.2. Results and discussion

Fig. 1.1a shows a representative cyclic voltammogram taken at 0.01 V s^{-1} for a freshly polished tin electrode in the -1.7 V to $+2.0 \text{ V}$ potential range. The anodic scan displays similar behaviour as reported previously in the literature [65,74,87]: two anodic peaks (labelled as I and II) in the potential range between -1.2 V and -0.4 V , followed by a large plateau (labelled as III) that extends up to the onset of the oxygen evolution reaction at $+1.4 \text{ V}$. As discussed in the introductory Section A.4, peak I has been always assigned to the oxidation of Sn to Sn^{2+} , while peak II has been ascribed to the generation of Sn(IV) species to produce either a passive $\text{Sn}(\text{OH})_4$ or a dehydrated SnO_2 layer in region III [68,71]. However, when the anodic voltammetric signal is taken at a reduced potential scan rate, namely 0.001 V s^{-1} (Fig. 1.1a, inset), a more complex behaviour is revealed, especially in the peak II region where several voltammetric peaks can be identified.

To come out with a first chemical identification of the main oxide compounds formed during the slow potential scan, the voltammetric reduction method described by Nakayama *et al.* [88] was used. Briefly, the Sn electrode surface is passivated in the working alkaline medium, removed under anodic potentiostatic conditions, washed with MilliQ water and electrochemically reduced in an ammonia buffer composed by $0.5 \text{ M NH}_4\text{Cl}$ and $0.5 \text{ M NH}_4\text{OH}$. In such medium, the cathodic reduction of reference SnO , $\text{SnO}_2 \cdot n\text{H}_2\text{O}$ and SnO_2 powders have been identified at clearly separated potentials of -1.2 , -1.5 and -1.7 V vs SSC, respectively. The method has been proven to be a feasible strategy to identify air formed tin oxide products [88]. In this vein, a set of Sn oxide layers were prepared in 0.1 M NaOH by anodically sweeping the potential from -1.3 V to -1 V , -0.8 V , -0.7 V , -0.5 V and -0.3 V . These potentials correspond to the different observed electrochemical processes in the voltammetric signal (A–E respectively in Fig. 1.1a, inset). The corresponding voltammetric reductions in the ammonia buffer are shown in Fig. 1.1b. The oxide grown at -1 V (A in Fig.

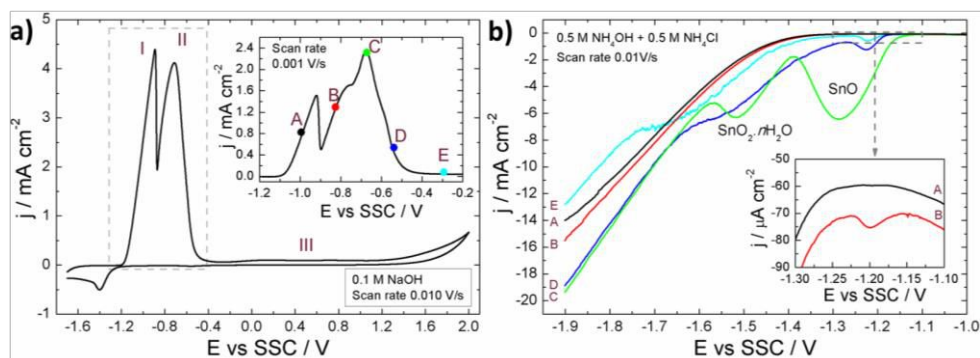


Figure 1.1 a) Cyclic voltammetry in 0.1 M NaOH of a freshly polished Sn electrode at a scan rate of 0.01 V s^{-1} . The inset shows a detail of the regions I and II recorded at a lower scan rate of 0.001 V s^{-1} . The potentials labelled as A–E were used to anodize the electrodes studied in panel b. b) Voltammetric reduction curves in ammonia buffer ($0.5 \text{ M NH}_4\text{Cl} + 0.5 \text{ M NH}_4\text{OH}$) of samples prepared in 0.1 M NaOH by sweeping potential at 0.001 V s^{-1} to different end potentials of -1 V , -0.8 V , -0.7 V , -0.5 V and -0.3 V corresponding to A, B, C, D and E, in panel a inset, respectively. The inset shows a zoom of samples A and B in the -1.1 V to -1.3 V range.

1.1a, inset) presents no noticeable reduction peaks within the studied potential range, either due to the high reversibility of the surface process [7] or because the cathodic reduction occurs simultaneously with the hydrogen evolution reaction (HER), as it has also been observed in Fe passive films [8]. If the anodic film formation potential is increased to -0.8 V (B in Fig. 1.1a, inset), a cathodic peak at -1.2 V in the ammonia buffer shows up (Fig. 1b, inset). The potential of this peak is in agreement with the reported cathodic reduction of stoichiometric SnO [88]. For the oxide film grown at -0.7 V (C in Fig. 1.1a, inset), the cathodic signal of the stoichiometric SnO becomes more pronounced. Moreover, the cathodic peak assigned to a $\text{SnO}_2 \cdot n\text{H}_2\text{O}$ phase is now evident (Fig. 1.1b). Applying a more anodic formation potential of -0.5 V (D in Fig. 1.1a, inset) results in a slight cathodic shift of the $\text{SnO}_2 \cdot n\text{H}_2\text{O}$ peak, most likely due to the formation of a more stoichiometric SnO_2 layer [88]. A substantial decrease in the SnO phase is also observed at this formation potential. At a more anodic potential of -0.3 V (E in Fig. 1.1a, inset), the cathodic $\text{SnO}_2 \cdot n\text{H}_2\text{O}$ signal shifts to even more negative values, close to the stoichiometric SnO_2 value (-1.7 V). The large width of this cathodic peak may be due to the known amorphous nature of the passive film. The HER appears significantly inhibited after passivation at -0.3 V, which could stem from the incomplete reduction of the SnO_2 during the reduction potential sweep [7,66,68]. The decrease in the intensity of the cathodic peak corresponding to the SnO phase from C to E indicates that its formation rate decreases as the anodic end potential increases.

The amphoteric nature of Sn prompts a large variety of Sn oxidized species (see Sn Pourbaix diagram in Fig. A.1a from the Introduction [18]) that will be potentially involved in the passivation process. As a result, Sn passivation is expected to be a more complex process as compared to other studied passivation processes for transition metals such as Fe, Ni or Cu. In this sense, the observed fast SnO growth occurring within the potentials B–D foresees a complex dynamic process for the final Sn electrode passivation in an alkaline medium, and evidences the need for a more detailed study. In the following sections, the voltammetric curve is analysed in depth for the important electrochemical ranges: primary passivation ($E < -0.9$ V), surface etching and SnO formation (-0.9 V $< E < -0.7$ V) and secondary passivation ($E > -0.7$ V).

1.2.1. Primary passive layer ($E < -0.9$ V)

Here, the passive layer formed within the potential region of peak I is characterized. The primary passive layer is grown by slowly sweeping the potential from -1.3 V to -1 V (A in Fig. 1.1a, inset). The potential was held for 1800 s at -1 V to ensure that the resultant oxide layer is fully developed (Fig. 1.2a). Fig. 1.2b and c show the field emission scanning electron microscopy (FESEM) images and the corresponding atomic force microscopy (AFM) detail of a freshly polished tin surface and the same surface after passivation at -1 V, respectively. The morphology of the polished Sn substrate presents a flat surface with $R_{\text{RMS}} = 17.5$ nm and typical non-preferentially oriented scratches from the polishing process. In contrast, the oxidized sample in Fig. 1.2c shows a rougher surface with a porous white oxide film of random distribution (R_{RMS} of 170 nm). XRD measurements of such films show no

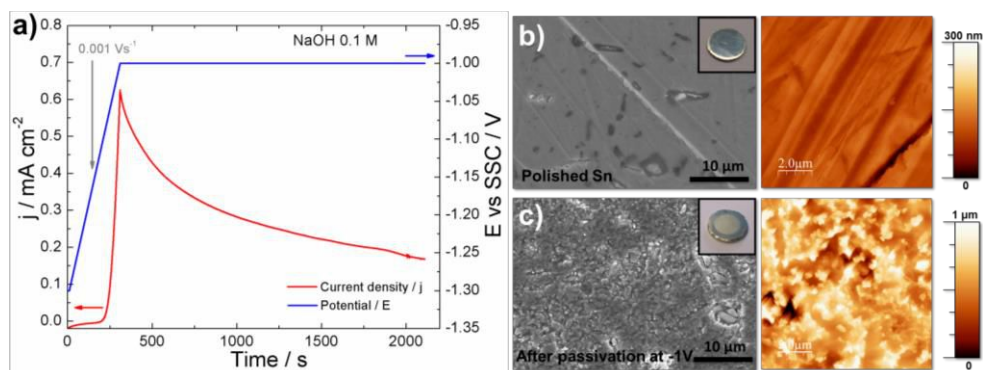


Figure 1.2 a) Current response during the growth of the primary passive layer in by sweeping the potential at 0.001 V s^{-1} to -1 V plus a 1800 s hold in 0.1 M NaOH . b) FESEM (left) and $10 \mu\text{m} \times 10 \mu\text{m}$ AFM (right) images of a) a freshly polished tin electrode and b) a tin electrode anodized as described in panel a). Photographs of the samples are shown as insets in the upper-right corner of the FESEM images.

appreciable crystalline orientation, which evidences its amorphous or nanocrystalline nature. The polishing lines of the substrates are no longer appreciable, which manifests the formation of an oxide film of considerable larger thickness compared to Sn oxide films prepared in more acidic electrolytes, such as borate buffer [68,75,77].

Raman spectroscopy measurements of the surfaces presented in Fig. 1.2b and 1.2c are displayed in Fig. 1.3a together with the reference spectra for SnO and $\text{Sn}_6\text{O}_4(\text{OH})_4$ powders. $\text{Sn}_6\text{O}_4(\text{OH})_4$ is a crystalline form of the hydrated Sn(II) oxide of the form $6\text{SnO} \cdot 2\text{H}_2\text{O}$ that was synthesized by incorporating a certain amount of SnCl_2 into a NaOH solution (see Experimental details). An image of the white solid and its XRD pattern are given in Fig. 1.3b. Tin hydroxide, $\text{Sn}(\text{OH})_2$, was not considered because it is reported to exist solely in aprotic solvents [89,90]. In contrast to the featureless Raman spectrum for the metallic Sn surface, the primary passive layer grown at -1 V potential presents a peak at 124 cm^{-1} that matches well with the Raman peak position of the $\text{Sn}_6\text{O}_4(\text{OH})_4$ reference. After careful noise subtraction, a small band at around 250 cm^{-1} and a broad band in the $400 - 650 \text{ cm}^{-1}$ range are also identified and located in positions where the $\text{Sn}_6\text{O}_4(\text{OH})_4$ powder spectrum presents peaks. The broadening of the peaks and its manifestation as weak bands could be caused by the distortion of the vibrational modes due to the lack of crystallinity. A possible explanation for the absence of the A_{1g} Raman signal in the primary passive film, as compared to the $\text{Sn}_6\text{O}_4(\text{OH})_4$ spectrum, arises from the anisotropy of the Raman modes in layered tetragonal solids such as SnO, analogue to PbO [91–93], and $\text{Sn}_6\text{O}_4(\text{OH})_4$ [94]. This anisotropy results in strong differences on the relative intensity of the Raman modes along the c axis (A_{1g} band) and ab planes (E_{1g} band) [91] when the material is constrained in a thin film. The above results point towards an amorphous hydrated Sn(II) oxide layer, $\text{SnO} \cdot n\text{H}_2\text{O}$, as the main component of the primary passive layer. Rapid formation of amorphous $\text{SnO} \cdot n\text{H}_2\text{O}$ is known to occur when $\text{Sn}^{2+}(\text{aq})$ is present in an alkaline medium [90]. Given the low reported

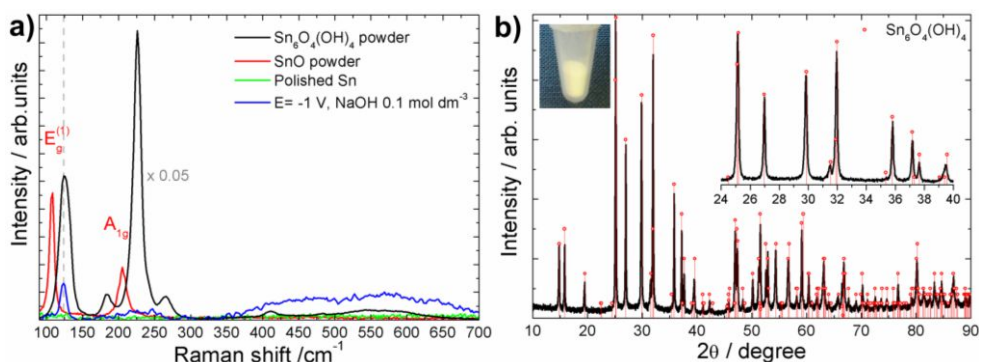


Figure 1.3 a) Raman spectra of a polished Sn electrode and the oxide film formed in 0.1 M NaOH solution by potential sweep from -1.3 V to -1 V at 0.001 Vs^{-1} plus a 1800 s hold at -1 V, together with the spectra of SnO and $\text{Sn}_6\text{O}_4(\text{OH})_4$ powder references. d) XRD pattern of the synthesized $\text{Sn}_6\text{O}_4(\text{OH})_4$ powder and photograph of the white powder.

K_{SP} values for $\text{Sn}(\text{OH})_2$ ($K_{\text{SP}} = 5 \times 10^{-26}$ [71]), precipitation of $\text{SnO} \cdot n\text{H}_2\text{O}$ is a plausible mechanism for the primary passivation of Sn [90].

The semiconducting properties of the primary passive layer are evaluated by EIS. Such information provides additional clues on its composition and passivation mechanisms [11,12,95,96]. As discussed in the introductory section A.2.2, EIS data is fitted to an equivalent circuit that corresponds to the electrical interpretation of the electrode | electrolyte interface. In the case of compact passive oxide films, a capacitive behaviour that can be fitted to a simple $R_{\text{sol}}(\text{RQ})$ circuit [72,86,95] has been commonly observed, where R_{sol} is the electrolyte resistance, R is the oxide charge transfer resistance and Q is a constant phase element (CPE) that accounts for the non-ideal capacitive behaviour due to film inhomogeneities [95]. The Nyquist and bode plot of our primary passive layer are shown in Fig. 1.4a and Fig. 1.4b, respectively. The behaviour is far from the standard $R_{\text{sol}}(\text{RQ})$ as two loops are shown in the Nyquist plot, meaning that a more complex equivalent circuit needs to be used to describe this particular interface. The two possible equivalent circuits employed to fit the passive layer | electrolyte interface are given in Fig. 1.4c and Fig. 1.4d. The $R_{\text{sol}}(\text{R}_1\text{Q}_1)(\text{R}_2\text{Q}_2)$ circuit used to fit the data in Fig.1.4a and Fig. 1.4b has been also applied to describe oxide films on titanium [97,98] or oxide coatings in stainless steel [99] having a duplex structure, an inner barrier layer and an outer porous layer. So, Q_1 and R_1 correspond to the capacitance and resistance of the porous outer film and Q_2 and R_2 the corresponding parameters for the inner compact oxide film. The second circuit, $R_{\text{sol}}(\text{Q}_1[\text{R}_1(\text{R}_2\text{Q}_2)])$, in Fig. 1.4d, is typical of defective coatings, *i.e.* oxide films where the electrolyte solution can penetrate and further react at the metal | oxide interface [99,100]. Here, Q_1 is the capacitance of the compact oxide layer, R_1 the inner oxide resistance to the ionic current, and Q_2 and R_2 account for the capacitance of the interface between the solution in the pores and the bare metal in parallel with the resistance of the electrolyte inside the pores [97]. The parameters of both fittings are given in Table I.1. The two models seem to fit

with comparable accuracy, given by the order of magnitude of χ^2 , so it is difficult to discern

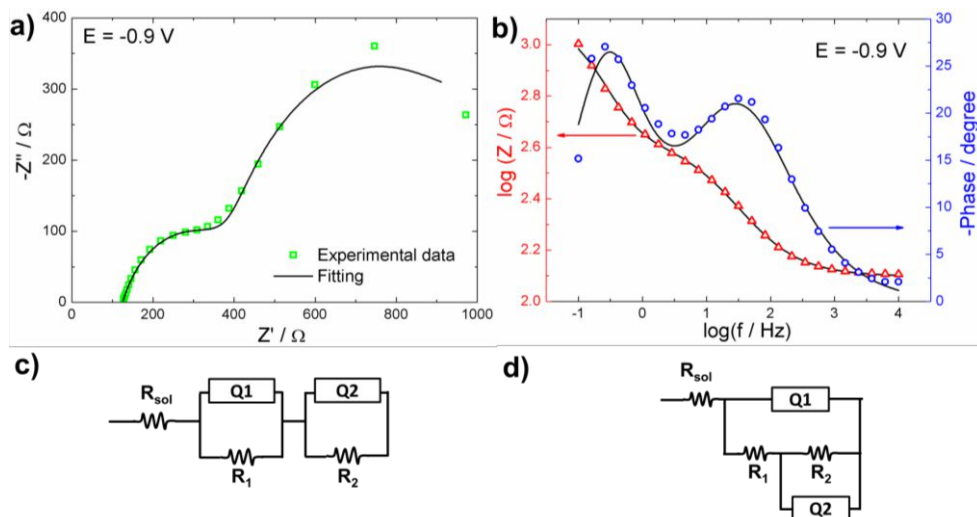


Figure 1.4 a) Nyquist plot and b) Bode plot representations of the impedance data recorded in 0.1 M NaOH for a film prepared by anodizing a tin electrode in 0.1 M NaOH using a potential sweep at 0.001 Vs^{-1} to -1 V plus a 1800 s hold. Open symbols correspond to the experimental data and the fitting to $R_{\text{sol}}(R_1Q_1)(R_2Q_2)$ is given in solid line. c) and d) show the representation of the equivalent circuits used for the fitting $R_{\text{sol}}(R_1Q_1)(R_2Q_2)$ and $R_{\text{sol}}(Q_1[R_1(R_2Q_2)])$, respectively.

Table 1.1 Parameters derived from the fitting of the EIS data in Fig. 1.4.

Circuit element	Fitting $R_{\text{sol}}(R_1Q_1)(R_2Q_2)$ (1.4c)	Fitting $R_{\text{sol}}(Q_1[R_1(R_2Q_2)])$ (1.4d)
R_{sol}	125 Ω	125 Ω
R_1	729 Ω	312 Ω
Q_1	$y=1.36 \times 10^{-3} \text{ F}, n=0.937$	$y=1.46 \times 10^{-4} \text{ F}, n=0.704$
R_2	286 Ω	750 Ω
Q_2	$y=1.53 \times 10^{-4} \text{ F}, n=0.698$	$y=1.18 \times 10^{-3} \text{ F}, n=0.906$
χ^2	1.35×10^{-2}	1.95×10^{-2}

which one is more adequate in our particular case. Apparently the more compact a layer is, the higher should be its resistance and its n parameter in the CPE [98]. With this assumption, the $R_{\text{sol}}(R_1Q_1)(R_2Q_2)$ seems to describe more accurately our system because it has higher R_1 and Q_1 values than the $R_{\text{sol}}(Q_1[R_1(R_2Q_2)])$ equivalent circuit. In any case, the final conclusion drawn from the EIS data is that the oxide layer is permeable to the electrolyte, porous, and does not act as a good passive barrier [100]. For such complex equivalent circuits, a more detailed analysis of the capacitance behaviour versus potential using the

Mott-Schottky relationship is difficult, which prevent us to gather semiconducting properties of the primary passive layer.

As discussed in the introductory Section A.1.2, porous passive films are usually formed by a dissolution-precipitation mechanism described by the Layer-Pore Resistance model [20]. To further corroborate this model for our primary passive Sn oxide layer, the film was formed by anodically scanning the potential at different scan rates (see Fig. 1.5a). When the scan rate increases, both the current (I_m/J_m) and the electrode potential (E_m) of the main peak monotonically increase. The observed linear dependence of I_m and E_m values versus the square root of the scan rate (see Fig. 1.5b) evidences that the electrochemical oxide film formation follows the behaviour described by equations (1.1) and (1.2) derived from the Layer-Pore Resistance model (LPRM) (see Section A.1.2 in the Introduction)[20].

$$I_m = \left(\frac{zF\rho\kappa A_0}{M} \right)^{1/2} (1-\theta_m) v^{1/2} \quad (1.1)$$

$$E_m = E_0 + \left(\frac{zF\rho\kappa}{M} \right)^{1/2} \left[\left(\frac{\delta}{\kappa} \right) + R_0 A_0 (1-\theta_m) \right] v^{1/2} \quad (1.2)$$

The results in Fig. 1.5 are in agreement with the morphology, the observed impedance behaviour and the previous reported data for Sn anodization [67–70]. A value of $E_0 = -0.954$ V, the spontaneous film formation potential [69], can be extracted directly from the linear regression in Fig. 1.5b, and is close to the formal reduction potential of -1.1 V corresponding to the Sn/Sn(OH)₂ electrochemical reaction [67,101].

The electrochemical response of the primary passive film formation process at different NaOH concentrations was also analysed. The intensity of the critical current (as defined in Section A.1.1) is an indication of the “easiness” of passivation (see Fig. 1.6). The intensity of peak I ($I_{p,I}$) increases with OH concentration denoting enhanced metal oxidation or, in other words, a less favoured passivation. Similar behaviour has been also observed when

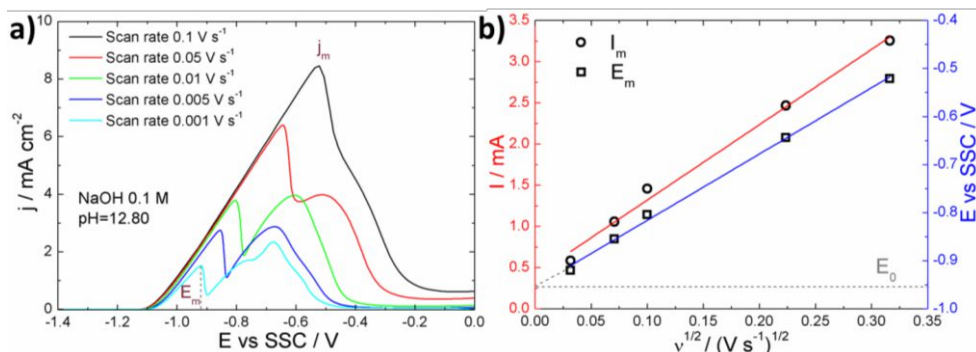


Figure 1.5 a) Effect of the potential scan rate (v) on the linear sweep voltammograms at 0.001 V s^{-1} of a freshly polished Sn electrode immersed in a 0.1 M NaOH solution. b) Representation of I_m and E_m vs. the square root of the scan rate and its fitting to the LPR model.

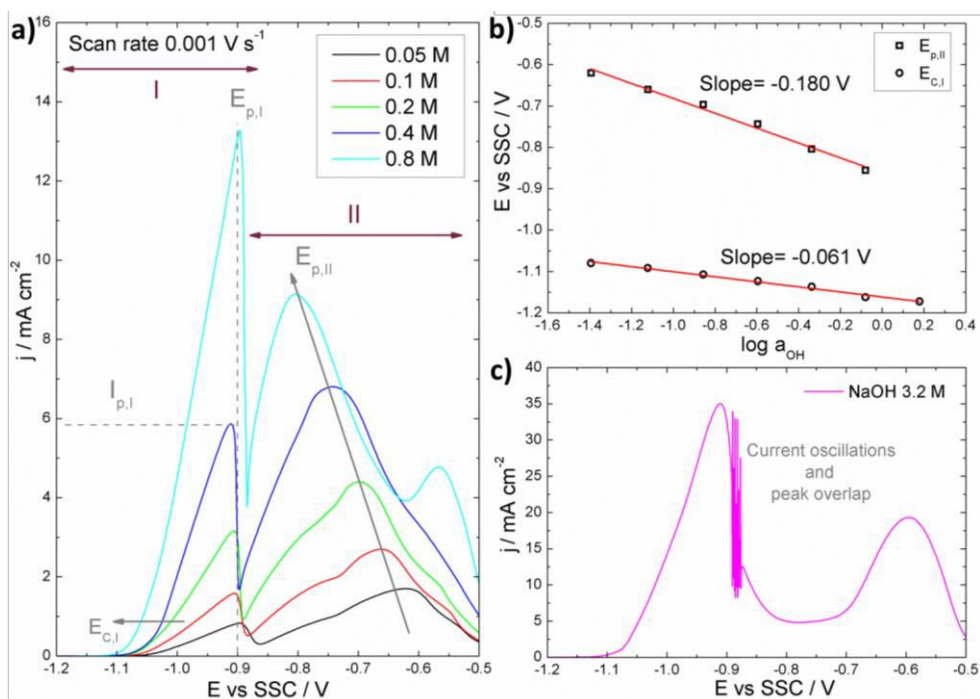
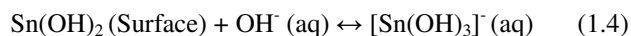


Figure 1.6 a) Effect of NaOH concentration on the linear sweep voltammograms taken at 0.001 V s^{-1} on a freshly polished Sn electrode. b) Corrosion potential (E_C) and second peak potential ($E_{p,II}$) vs logarithm of the OH^- activity. c) Linear sweep voltammogram at 0.001 V s^{-1} of freshly polished Sn electrode in 3.2 M NaOH solution (it is placed separately due to the change in scale).

complexing agents like Ethylenediaminetetraacetic acid (EDTA) or 2,2-bipyridine are present during the electrochemical passivation of an Fe electrode [38,102]. From the $K_{sp}(\text{Sn}(\text{OH})_2)$ value, one might expect faster passivation at higher NaOH concentration, which would result in a decrease in the $I_{p,I}$ [10]. The opposite behaviour observed for the Sn primary passivation is explained by the amphoteric nature of $\text{SnO} \cdot n\text{H}_2\text{O}$ that makes it less stable in highly acidic or alkaline conditions [89,90]. The onset potential of peak I, so-called corrosion potential ($E_{C,I}$), is also shifted to more negative potentials as the OH^- concentration is increased (Fig. 1.6b). The slope of the $E_{C,I}$ vs. OH^- activity semilog plot gives a slope of 0.061 V/pH unit, very close to the expected value for a Nernst potential shift per pH unit considering a second order on the OH^- species and 2-electron exchange. Accordingly, the following reactions for the formation of the Sn primary oxide layer are proposed:



The proposed steps agree with both the Nernst slope in Fig. 1.6b, reaction in (1.3), and the dissolution–precipitation mechanism (LPRM), reactions (1.4) and (1.5).

1.2.2. Surface etching and SnO crystals growth ($-0.9\text{ V} < E < -0.7\text{ V}$)

After the primary passivation, if the electrochemical potential is scanned to more anodic values, the current increases again and the surface turns black denoting new electrochemical processes occurring at the primary passivated interface (see *in situ* photographs of the electrode in Fig 1.7). So, again, passive films were grown within this electrochemical potential range by slowly sweeping the potential at 0.001 V s^{-1} and a 1800 s hold to let the oxide layer to fully develop. Details on the surface topography by electron microscopy of the sample oxidized at -0.8 V (B in Fig. 1.1a inset and in the voltammogram in Fig. 1.7) reveal that the sparse black areas correspond to associations of $\sim 10\text{ }\mu\text{m}$ platelet crystals appearing concurrently with visible pyramidal pits (Fig. 1.8a). Upon increasing the potential to -0.7 V (C in Fig. 1.1a inset or Fig. 1.7) the surface becomes totally black and the electrode is fully covered by the platelet crystals (Fig. 1.8b), presenting a length distribution of $2\text{--}5\text{ }\mu\text{m}$. The reduced size of the platelet crystals at higher anodic potentials is most likely due to a larger crystals nucleation.

The film composed of platelet crystals was characterized by XRD (Fig. 1.8d). The black microcrystals correspond to tetragonal SnO, known as romarchite, a layered Sn-O material [91,92] whose calculated low indirect band gap transition at 0.7 eV is responsible for its black colour [92]. Raman spectroscopy results (Fig. 1.8e) further confirm the presence of stoichiometric SnO. The two main Raman modes at $113\text{ and }211\text{ cm}^{-1}$ correspond respectively to the characteristic E_{1g} and A_{1g} modes for SnO polarized along the ab planes in the layers and along the c axis of the tetragonal cell, respectively [92]. Additionally, two weak modes are detected at $350\text{--}370\text{ cm}^{-1}$ and $460\text{--}494\text{ cm}^{-1}$. These weak modes are rarely observed [91] and have been assigned to B_{1g} and E_{2g} modes of oxygen vibrations. No SnO_2 signal was detected in both XRD and Raman spectroscopy measurements within this electrochemical potential range.

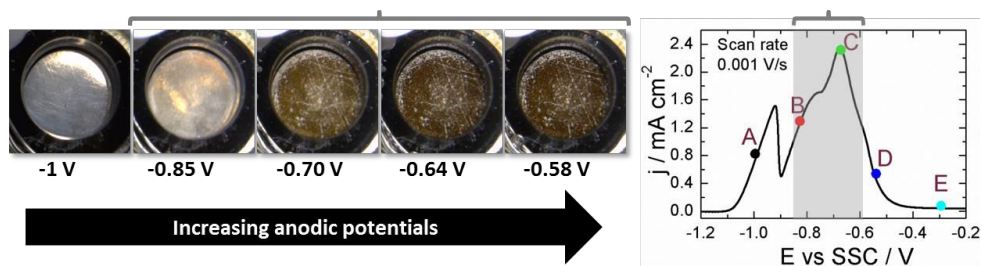


Figure 1.7 *In situ* photographs of the Sn electrode upon potential increase from -1 V to -0.58 V at 0.001 V s^{-1} in 0.1 M NaOH solution. The black/brown areas develop in the region of potentials marked in grey in the linear sweep voltammogram (right).

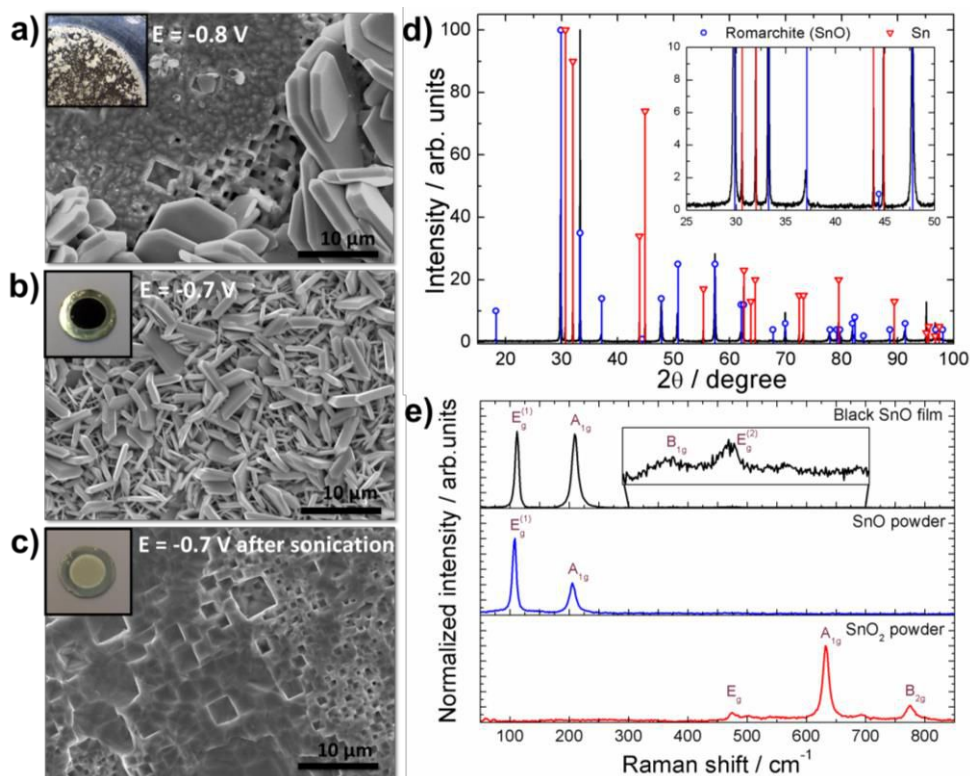
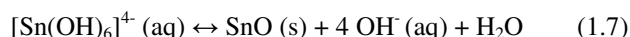


Figure 1.8 FESEM image of a tin electrode passivated in 0.1 M NaOH by applying a potential sweep at 0.001 V s⁻¹ and a 1800 s hold to a) -0.8 V, b) -0.7 V and c) -0.7 V vs SSC after sonication to remove the SnO crystals. Photographs of the electrodes are shown in the upper left corners. d) X-ray diffraction pattern (PDF cards: 060395 (SnO) and 040673 (Sn)) and e) Raman spectroscopy measurements of the black film formed in the same conditions as in panel b). Raman signals for the standard SnO and SnO₂ powders are included.

The SnO crystals formed on the tin electrode surface are poorly attached and fail against the standard Scotch tape test. The 3-dimensional growth of the crystals and their weak interaction with the substrate suggest that they are formed through a chemical crystallization stage in solution. The electrode surface after sonication is shown in Fig. 1.8c and reveals pyramidal etching pits of different sizes all over the Sn/SnO interface. The well-defined pit geometry evidences a preferential etching. Similar pyramidal pits are observed on etched Sn single crystals [103]. The simultaneous appearance of the pits and the SnO crystals supports the hypothesis that the SnO crystals are formed by a crystallization reaction of the supersaturated Sn²⁺(aq) etching product in the alkaline medium near the electrode surface. The presence of Sn²⁺(aq) in this potential range is also evidenced by the precipitation of a black-brown product, identified as SnS, after the addition of Na₂S to the electrolyte solution at an applied -0.7 V potential ($K_{sp}(\text{SnS}) = 1 \times 10^{-26}$, [104]).

The effect of NaOH concentration on the electrochemical etching process linked to peak II is studied in detail in Fig. 1.6a. The peak maximum ($E_{p,II}$) shifts to more negative potentials as

the OH⁻ concentration is increased. At NaOH concentrations > 3.2 M, primary passivation is not achieved and peaks I and II overlap (Fig. 1.6c). This effect has been previously reported for tin anodization in strong alkaline media [65,67] and possible explanations such as film breakdown and recrystallization or alternate dissolution and deposition have been proposed [67]. The E_{p,II} evolution with the logarithm of OH⁻ activity (Fig. 1.6b) displays a linear dependence with a calculated value for the slope of 0.180 V/pH unit, which strongly deviates from the previous reactions (1.3) - (1.5) in the primary passivation region. Note that direct comparison between E_{p,II} and E_{c,I} is approximated here due to the fact that E_{c,II} cannot be properly determined given the peak overlap. The obtained higher slope here suggests a sharp increase in the electrochemical reaction order on the OH⁻ species for the electrochemical Sn etching process, which is explained by the formation of highly coordinated Sn(II) hydroxo-complexes in a 2-electron exchange process:



The formation of hexacoordinate stannite complexes in (1.6) agrees with the observed Nernst potential shift per pH unit under the E_p ≈ E_c approximation. This reaction has been described in the literature in strong alkaline conditions [105]. The slow decomposition of these complexes would lead to the crystallization of the SnO microcrystals (reaction (1.7)).

A part from the abovementioned concentration effect, the temperature was found to have also a strong influence in the current response of the processes related to Sn etching and consequently in the rate of SnO growth. Here, the temperature effect in both processes, primary passivation (peak I) and electrochemical etching (peak II) is compared. Fig. 1.9a and 1.9b shows the linear sweep voltammetry scans taken at 0.001 V s⁻¹ for a tin electrode immersed in NaOH solutions with different concentrations and working temperatures. For a given NaOH concentration an increase in temperature leads to an augment in the current, more pronounced in the case of peak II. The effect of temperature was further analysed in Fig. 1.9c and 1.9d by plotting log |j| vs 1/T according to the Arrhenius equation in (1.8):

$$\log(|j|) = A + \frac{E_a}{k_B T} \quad (1.8)$$

where k_B is the Boltzmann constant, E_a the apparent activation energy and A is a constant. The apparent activation energies were calculated from the slopes of the straight lines [106,107]. For the process linked to peak I, the apparent activation energy seems to depend on the concentration of NaOH in solution: the apparent E_a increases from 0.084 eV to 0.177 eV when decreasing the NaOH concentration from 0.3 M to 0.05 M. This suggests that the process is facilitated at high NaOH concentrations. In the case of peak II values range from 0.151 eV to 0.206 eV but without a clear trend with the NaOH concentration. The higher activation energies for the etching process in peak II indicate that the process has a stronger dependence on temperature. The values of activation energy obtained are in line with those

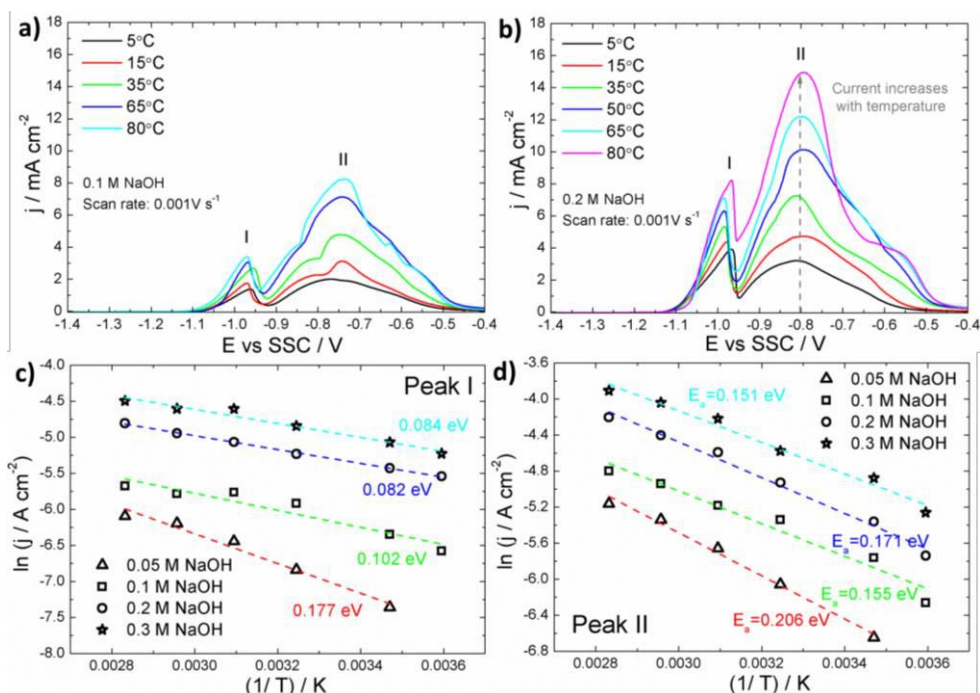


Figure 1.9 Linear sweep voltammetry curves acquired at different temperatures (5, 15, 35, 50, 65, 80 °C) for a freshly polished Sn electrode immersed in a) 0.1 M NaOH and b) 0.2 M NaOH (Scan rate = 0.001 Vs⁻¹). Representation of the current density of the peak vs. the inverse of the temperature (Arrhenius plot) for the process in c) peak I and d) peak II.

reported for Silicon etching in NaOH (~ 0.345 eV [107]). Usually activation energies below 20 KJ/mol are related to diffusion controlled processes while those larger than 40 KJ/mol correspond to processes limited by charge transport or surface controlled processes [108–110]. In the present case, all values were found to be below 17 KJ/mol so the limiting step in both cases seems to be the diffusion of reactants. For peak I, the diffusion controlled behaviour has been previously described in rotating disk electrode experiments [69]. However, the reason why peak I is influenced by concentration and not peak II is still unclear. Further experiment would be required to completely understand the present results. The temperature effect as well as the influence of NaOH concentration on the growth rate of SnO crystals and their morphology has been omitted here as it is not relevant for the mechanism of tin passivation but a detailed analysis and further discussion can be found in Appendix a.

1.2.3. Final electrode passivation ($E > -0.7$ V)

The maximum rate of surface etching and stoichiometric SnO formation is achieved at a potential of -0.7 V. Further potential increase, *e.g.* at -0.5 V (indicated as D in Fig. 1.1a

inset), results in a second current drop. The etching rate is significantly reduced and, consequently, the final surface passivation begins. The large passivation plateau starts beyond -0.3 V (E in Fig. 1.1a inset). The last peak before the plateau at -0.5 V is ascribed to the formation of Sn(IV) species, *i.e.* SnO_2 or $\text{SnO}_2 \cdot n\text{H}_2\text{O}$, as supported by the results gathered from the voltammetric reduction experiments of Fig. 1.1b. The peak at -0.5 V becomes more noticeable at high OH concentrations (>0.8 M), as observed in Fig. 1.6a. This rise in the current density of the Sn(IV) formation process at higher pHs may be due to an increase in the effective electrode area available for passivation as the OH etching becomes more severe and the surface is increasingly roughened. Along the passive plateau, up to $+1.5$ V, no further changes on the electrode surface are appreciated, which suggests an effective electrode passivation by the Sn(IV) layer. Given the poorly adherent nature of the SnO crystals, it is clear that they do not play a role in the passivation process and that the actual passive layer develops at the Sn/SnO interface. This is verified by performing experiments with the electrode under stirring conditions, as shown in Fig. 1.10a. Under continuous agitation, the black SnO crystals are not developed on the electrode surface due to the

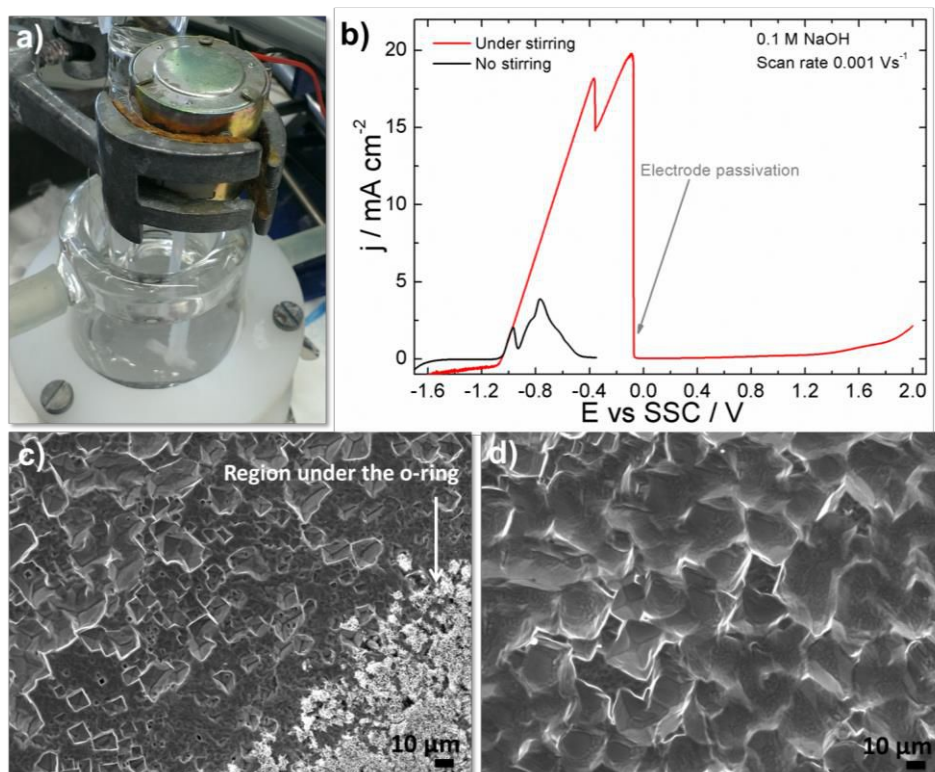


Figure 1.10 a) Photograph of the experimental setup used to perform experiments under stirring conditions. A PTFE stirring bar was introduced in the electrochemical cell and controlled with a motor. b) Linear sweep voltammetry in 0.1 M NaOH of a tin electrode under stirring conditions compared to the same voltammogram in non-stirred conditions. c) and d) FESEM images of the electrode surface after a potential scan up to -2 V under stirring. SnO crystals are not formed because stirring prevents supersaturation of Sn^{2+} but passivation is achieved anyway at $E > -0.2$ V.

applied hydrodynamic conditions. The SnO crystals are only visible in the regions below the O-ring junction of the electrochemical cell (Fig. 1.10c). The rest of the electrode surface is considerably damaged by the strong etching/dissolution of the Sn metal surface. The increase in the anodic current response (approximately five times larger) explains these aggressive etching observed in the FESEM images (Fig. 1.10d). However, as can be seen in the linear voltammogram in Fig. 1.10b, even though SnO crystals are not formed, the electrode passivation still occurs. The passivation potential is shifted to higher values because of the stirring effect.

Given the poor crystallinity of the final passive layer, no XRD peaks were found and therefore the Sn(IV) oxide layers were analysed by performing depth chemical profiles of the Sn $3d_{5/2}$ and O1s XPS signals (Fig. 1.11a). In order to minimize the formation of SnO crystals on the electrode surface for this particular analysis, the Sn(IV) passive film is prepared by sweeping the potential to +1.5 V at a larger scan rate. The binding energy (BE) values reported in the literature for the Sn species are 484.5 eV for Sn 0 , 486.2 eV for Sn(II) and 486.9 eV for Sn(IV) [111]. The O1s BE signal is simultaneously recorded (Fig. 1.11b) for its correlation with the Sn oxide state. Although XPS oxygen signals of both Sn(II) and Sn(IV) oxides cannot be well differentiated [71,111], the signals corresponding to the Sn O lattice, OH groups and H $_2$ O at 530.4 eV [62,74], 531.5 eV [62,74,111] and 533.8 eV [111] respectively can be analysed to gather information on the hydration degree of the film. In the spectra prior to the first Ar $^+$ sputtering, presumably Sn(IV) species dominate the Sn XPS spectrum. A combination of the three oxygen types can be also observed at the XPS O1s energy region, being the OH signal predominant with a visible contribution of H $_2$ O signal. The presence of a more hydrated layer at the oxide/electrolyte interface is expected [7,62,68,70]. Sn(II) XPS signal seems to be the Sn dominant signal after the 3 rd Ar $^+$

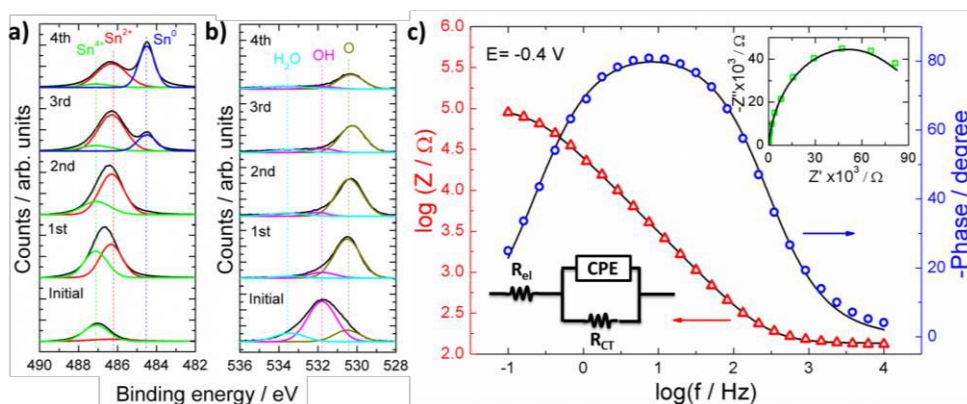


Figure 1.11 XPS spectra of the a) Sn $3d_{5/2}$ and b) O1s regions for a film prepared by potential sweep to +1.5 V at 0.01 Vs $^{-1}$. Initial spectrum corresponds to the 0th Ar $^+$ sputtering cycle. The estimated sputtering rate is approximately 1.5 - 2 nm per cycle. c) Experimental (open symbols) and simulated Bode plot (solid line) representations of the impedance data recorded in 0.1 M NaOH for a film prepared by applying a potential sweep at 0.001 Vs $^{-1}$ to -0.4 V. The inset shows the experimental (open symbols) and simulated (solid line) Nyquist plots (top right) and the R $_{el}$ (RQ) equivalent circuit (bottom left) used for the simulation.

sputtering cycle (Fig. 1.11a), which roughly corresponds to ~ 5 nm of the oxide film thickness (see calibration in the Experimental details, Section 1.5). After the 4th cycle (~ 8 nm in depth) and successive ones, the Sn XPS spectrum is mostly composed by metallic Sn⁰ with a small percentage of remaining Sn(II). As for the O1s signal along all subsequent cycles, the dominant signal corresponds to Sn-O and experiences a progressive decrease as the Sn(IV)/Sn(II) signal ratio is reduced. The in-depth chemical Sn speciation found in the XPS spectra indicates that the Sn passive layer has a duplex Sn(II)/Sn(IV) structure similar to other passive films. For instance passive films formed on Fe at high anodic potentials, exhibit an outermost part with the highest oxidation state and traces of the lower oxidation state acting as the n-dopant [11,95] that overall results in an effective electronic passivation of the surface electrode.

Electronic passivation has been reported in a number of passive oxide films on metals displaying semiconducting properties such as Fe, Cu, Ni, etc. [11,12,95,96]. The space charge layer of the semiconducting oxide builds up a surface electronic barrier, which is responsible for the observed electrode passivation. Access to the semiconducting properties can be obtained through the oxide capacitance behaviour by means of EIS. Fig. 1.11c shows EIS results for a Sn oxide film formed at $E > -0.4$ V. Contrarily to what was obtained for the primary passive layer, the oxide | electrolyte interface here can be described by a simple $R_{sol}(RQ)$ circuit, which evidences that a compact oxide film is formed in this potential range. The parameters obtained from the fitting of the Bode plot are gathered in Table I.2. The $R_{sol}(RQ)$ model is then used to study the oxide layer capacitance as a function of the applied potential at a fixed frequency, and the results are represented in the form of Mott-Schottky plots (Fig. 1.12b). The frequency used is 10 Hz, a value obtained from the Bode plot in Fig. 1.11c close to the maximum phase to guarantee a quasi-ideal capacitive behaviour. To ensure a complete electrode passivation and strong depletion conditions of the semiconducting oxide, the Mott-Schottky plot is performed on a sample oxidized at 0.6 V, where surface passivation is fully developed. We assume that 0.6 V is an appropriate value because at potentials lower than this value, the anodic peak within the region -0.85 V $< E < -0.7$ V can be appreciated during both anodic and cathodic sweep (Fig. 1.12a). At potential values higher than 0.6 V, the anodic process is no longer observed during the cathodic wave due to complete surface passivation. The Mott-Schottky plot of the anodized sample at 0.6 V is shown in Fig. 1.12b. It presents a positive slope in agreement with an n-type

Table I.2 Parameters derived from the fitting of the EIS data in Fig. 1.11c.

Circuit element	Fitted parameters
R_{sol}	143 Ω
R_{CT}	100 k Ω
Q_{sc}	$y=1.35 \times 10^{-5}$, $n=0.913$
χ^2	9.0×10^{-2}

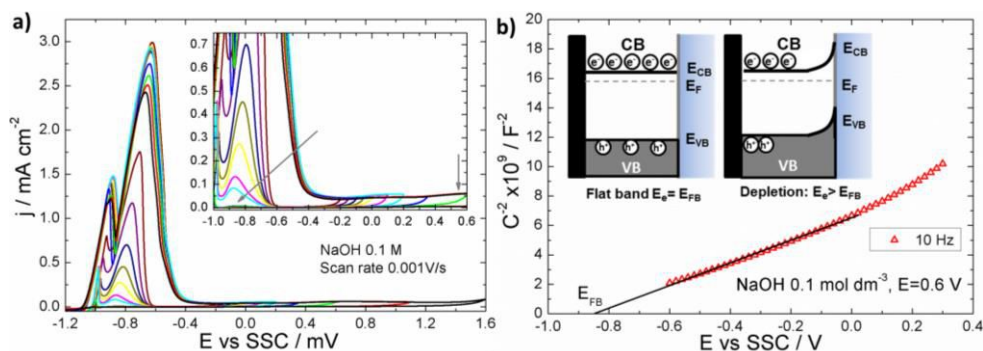


Figure 1.12 a) Cyclic voltammograms of a tin electrode immersed in 0.1 M NaOH solution taken at 0.001 V s⁻¹ using different end potential. The inset shows a zoom of the region between -1 V and 0.6 V. b) Mott-Schottky representation of the interfacial capacitance of a sample prepared by potential sweep at 0.001 V s⁻¹ to 0.6 V in a 0.1 M NaOH solution.

semiconductor and a calculated N_D in the order of 10^{21} cm⁻³ (taking $\epsilon = 10$ [86]). The n-type character of SnO₂ [72,86] has been extensively described in the literature and the estimation of N_D obtained here is in the order of measured values for other semiconducting passive layers [11,12,86]. The extracted E_{FB} of -0.85 V is close to the onset of the first cathodic process (Fig. 1.1a), in agreement with a transition of the semiconductor space charge layer from an electron depletion situation to an accumulation at the surface, giving rise to the cathodic oxide reduction. Although the exact Sn(II)/Sn(IV) duplex film structure requires more advance crystallographic determinations, here we propose the different plausible electrochemical routes for the passive film formation according to the obtained experimental observations:



Note that the exact stoichiometry of the Sn(IV)-based oxide film is not known and a good estimation of the Sn(II) content from the N_D values can be extracted.

1.3. Summary

The electrochemical passivation process of a Sn electrode in alkaline medium has been described within a large potential range covering the active regime and both the primary and final passive electrochemical potential ranges. New processes such as the formation of SnO microplatelets have been identified. The electrochemical range has been divided in different potential regions according to the involved processes (see Fig. 1.13). At potentials lower than -0.9 V, a white primary passive SnO·nH₂O film is formed on the electrode surface by a dissolution-precipitation mechanism. The formation is favoured at neutral-to-high pHs due

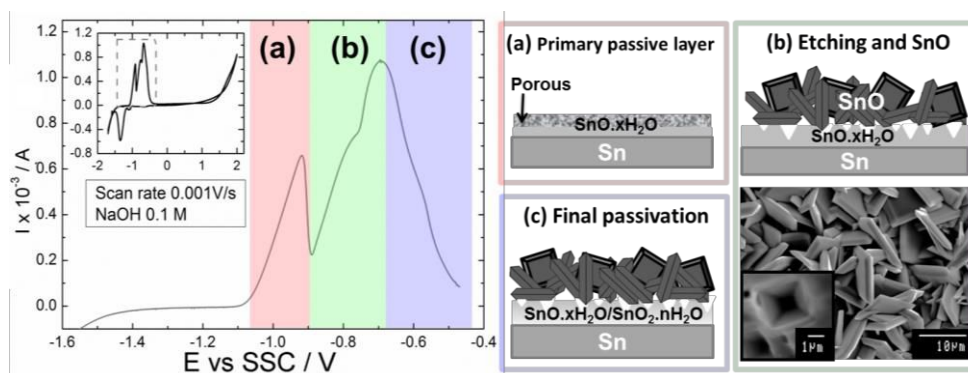


Figure 1.13 Summary of the electrochemical regions discussed in the results section and scheme of oxide layer composition at those potentials.

to its low solubility product. At very high pH, dissolution of Sn(II) species occurs due to its amphoteric nature. This hydrated primary passive layer is amorphous and porous and it does not effectively passivate the electrode surface.

At potentials more anodic than -0.9 V, black SnO micro-sized crystals are formed corresponding to a tetragonal SnO romarchite phase. The three-dimensional SnO crystals originate from the supersaturation of Sn^{2+} species close to the electrode vicinity generated as a result of a severe etching process at the Sn surface. Surface etching is evidenced by the pyramidal pits found at the metal/SnO interface. In our experimental conditions, the SnO crystals present a platelet shape. The etching process is strongly dependent on NaOH concentration; the potential is markedly shifted to negative values with increasing OH⁻ concentrations, which suggests the formation of soluble Sn(II) hydroxocomplexes of high coordination number. At the same time, a strong dependence with the working temperature was observed. The data followed Arrhenius behaviour and an estimate of the activation energy of ~ 0.17 eV was obtained.

From the observed current drop at potentials larger than -0.7 V and the suppression of SnO crystals formation, we conclude that the etching process ceases within this electrochemical potential range and the final electrode passivation takes place as a result of a Sn(IV)-based film formation. Results presented indicate that the SnO crystals do not play a role in the passivation process and that the actual Sn(IV)-based passive layer develops at the Sn/SnO interface. The Sn(IV)-based film displays marked n-type semiconducting behaviour which results in an effective electronic passivation of the electrode surface.

1.4. Further work

- It would be interesting to compare the behaviour of the Sn in 0.1 M NaOH with a more neutral solution where passive films are more stable. The most common strategy is to

use buffer solutions but, for instance, the use of borate buffers has always been controversial because they tend to adsorb on metallic surfaces. In this case, the hindering of the anodic processes is difficult to interpret because it might be influenced by both adsorbed anions and the enhanced stability of tin passive layers in neutral pH. Other buffers such as phosphates form phosphate species when Sn is dissolved and the system becomes more complex. An alternative approach would be to dilute the NaOH solution with a solution of an inert salt to ensure that it is conductive enough. However, typical salts such as NaNO_3 , NaCl or NaClO_4 are discarded since their anions induce pitting corrosion on Sn. For this, an appropriate salt that does not contribute to any pitting or corrosion phenomena should be found.

- In this work we used polycrystalline tin electrodes, but as the etching of the electrode is highly preferential, one would expect to see differences if single crystalline surfaces are employed. For instance, it would be reasonable to see changes in the current of the anodic peaks and the appearance or not of SnO crystals. Moreover, in single crystalline surfaces synchrotron radiation *in situ* studies could be performed. *In situ* X-ray absorption and diffraction could provide quantitative information on the oxide composition and structure in electrochemical ranges such as the primary passivation.
- Study the effect of NaOH concentration, temperature or presence of organic solvents in the morphology of the SnO crystals and the etching process itself. Some preliminary experiments are gathered in Appendix a.

1.5. Experimental details

1.5.1. Sample preparation

Polycrystalline Sn disks (99.999 %, Goodfellow) of 1 cm dia. were used as substrates. Prior to electrochemical studies and film growth, the substrates were mechanically polished down to 3 μm with Al_2O_3 polishing disks, rinsed with MilliQ water and N_2 blown. The experiments were performed in an electrochemical glass cell in a standard three-electrode configuration using an Ag/AgCl/KCl(sat) (SSC from herein, E^0 vs NHE = 0.222 V) reference electrode and a platinum auxiliary electrode. The voltammetric curves, the film growth and the impedance measurements were carried out in 0.1 M NaOH (Riedel-de Haën, 99 %) electrolyte using a PGSTAT302N Autolab potentiostat (Metrohm Autolab). The electrolyte was purged with Ar (99.999 %) prior to measurements to remove the dissolved oxygen.

1.5.2. Characterization techniques

XRD measurements were done in a PANalytical X'Pert PRO MPD Alpha1 diffractometer using $\text{Cu K}\alpha$ ($\lambda = 0.15418$ nm) radiation in the Bragg-Brentano geometry. The phases were identified with the JCPDS database. Surface morphology was characterized in a H-4100

FESEM (Hitachi High-Technologies Corporation), and in a Multimode I Atomic Force Microscope (Bruker) controlled with a Nanoscope IIIA electronics using tapping mode with Si cantilevers of 35 N m^{-1} nominal spring constant. The AFM images were processed with the WSxM software [112].

Raman scattering analysis was performed in a LabRAM HR 800 (Horiba Jobin Yvon) using the backscattering configuration and the 532 nm line of a solid-state laser as excitation source. To avoid sample damage by laser heating, measurements were taken at the minimal power density of 0.5 mW. As powder references for the Raman measurements, SnO (Strem Chemicals, 98 %), SnO₂ (Strem Chemicals, 99.9 %) and Sn₆O₄(OH)₄ synthesized following the procedure is described in [113]. Briefly, 0.64g of SnF₂ (Sigma Aldrich, 99 %) were added to 20 mL of 0.25 M NaOH (Riedel-de-Haën, 99 %). Then mixture was stirred at room temperature during 1 h. The white powder formed was removed from the solvent by filtration and dried in the desiccator for 1 day.

Chemical identification by voltammetric reduction was performed in ammonia buffer (0.5 M NH₄OH + 0.5 M NH₄Cl) using a method described by Nakayama *et al.* [32]. XPS measurements were performed in a PHI 5500 Multitechnique System (Physical Electronics) with a monochromatic X-ray source (Al K α line of 1486.6 eV and 350 W), placed perpendicular to the analyser axis. The analysed area was a circle of 0.8 mm diameter, and the selected resolution for the spectra was 58.7 eV of pass energy and 0.25 eV/step. In-depth measurements for composition profiles were obtained by sputtering the surface with an Ar⁺ ion source (4 keV). Sputtering time was 0.3 min, the lowest that could be achieved with our system and the estimated surface removed in these conditions is around 1.5-2 nm per cycle (estimation in Si₃N₄ on Si). All Measurements were made in an ultra-high vacuum chamber with a base pressure $\sim 5 \times 10^{-9}$ Torr.

Chapter 2

Nanoscale insight into the early stages of tin anodic oxidation

In this chapter, the first stages of tin anodization in alkaline solution are followed *in situ* by electrochemical scanning tunnelling microscopy (EC-STM). Here, direct information on the growth mechanism of the oxide has been extracted by observing the morphological changes occurring at the atomic level. Surface structures or processes that could not be detected macroscopically have been identified. All these phenomena will be discussed in relation to the results reported for other metals and the description of the process given in Chapter 1.

A brief overview on how an EC-STM works and its possibilities in metal passivation studies was given in the Introduction Section A.3. A helpful summary on the observations derived from previous EC-STM works on Cu and Ni can be found in Section A.3.2.

2.1 Specific goals of this chapter

- Optimize the chemical polishing and etching procedure to achieve the atomically flat Sn surfaces needed for EC-STM imaging.
- Follow the early stages of anodic oxidation of a Sn surface in 0.05 M NaOH solution by EC-STM.
- Relate the observed phenomena to previously studied metals and propose a plausible mechanism for the process.

2.2 Results and discussion

2.2.1 Preparation of atomically flat Sn surfaces

The surface preparation procedure we used for our Sn polycrystals is based on the work reported by Honda [114] and Hirokawa *et al.* [103,115,116], and consists of 3 steps:

1. Chemical cleaning in 3 parts of concentrated nitric acid and 2 parts of water.
2. Chemical polishing in 1 part of HNO₃, 1 part of glacial acetic acid and 4 parts of glycerol.
3. Chemical etching in 10 g of NH₄NO₃, 10 mL HCl and 50 mL water. Sometimes a small amount of CuSO₄ is added in this solution because when used in low concentrations it leads to bigger pyramidal hillocks as compared to a CuSO₄ free solutions [116]. Despite larger terraces would be desirable, the use of CuSO₄ was discarded to avoid the presence of Cu impurities that may affect the corrosion behaviour in the EC-STM experiments.

During the chemical cleaning an oxide layer is quickly formed on the Sn surface upon dipping. Although it is easily removed by washing, the remaining metallic surface is considerably roughened and, in consequence, to achieve totally flat surfaces very long chemical polishing times are required and the Sn polycrystals are rapidly consumed. To make the process less aggressive, lower nitric acid percentage was attempted, but it prevented the detachment of the oxide layer during the washing step and then the following stages were not effective. Considering this, we decided to omit the first stage of chemical cleaning.

The chemical polishing step was found to be the key for the success of the whole process: if there is oxide remaining in the surface after polishing, the subsequent etching process is not effective and leads to non-oriented surfaces containing oxide particles. Longer etching times in the presence of a whitish oxide veil also fail in revealing the oriented surfaces. As starting point, Sn surfaces were dipped for 10 min in the chemical polishing solution and subsequently etched. The surface morphology after the whole treatment is shown in Fig. 2.1a. The surfaces do not present perfectly defined planes and contain oxide particles. For larger polishing times, 15 min, oxide grains covered the entire surface (Fig. 2.1b). Contrarily, if very short times are employed the surface cannot be properly flattened and scratches from the mechanical polishing remain. To overcome this issue, the surface was repeatedly subjected to polishing/washing cycles, in which the polishing step never exceeded 2 min. These surfaces, after the final chemical etching process, show mirror-like and iridescent regions upon illumination (inset in Fig. 2.2a). The regions were examined by FESEM to get an overall picture. The iridescent regions correspond to the oriented surfaces as a result of the preferential etching. Depending on the orientation of the Sn grain, as our

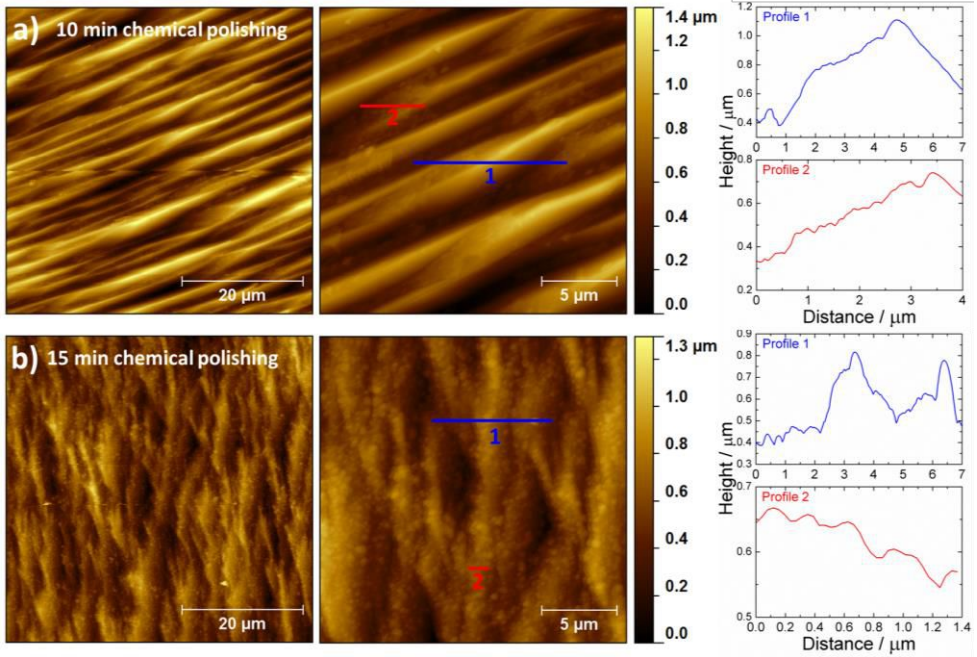


Figure 2.1 AFM topographic image of $50 \times 50 \mu\text{m}^2$ (left) and $20 \times 20 \mu\text{m}^2$ (right) and profile of the sections for Sn polycrystals chemically polished in a solution containing 1 part of HNO_3 , 1 part of glacial acetic acid and 4 parts of glycerol for a) 10 min and b) 15 min and subsequently etched in a mixture of 10 g of NH_4NO_3 , 10 mL HCl and 50 mL water for 2 min.

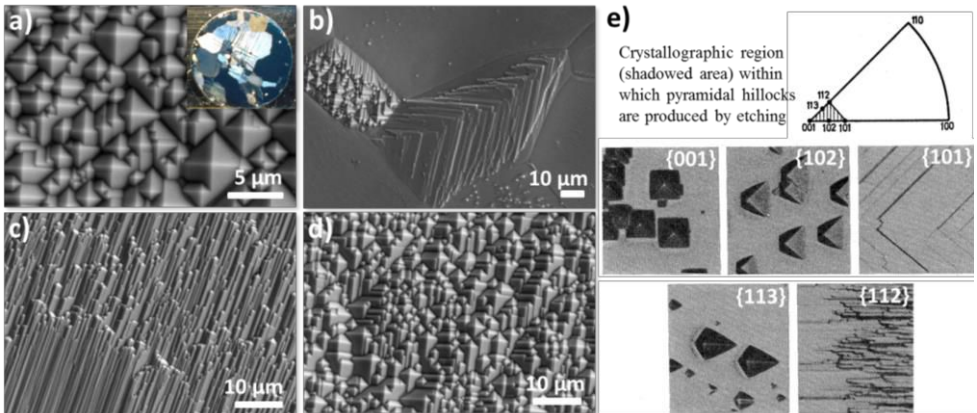


Figure 2.2 a-d) FESEM images of the iridescent regions on the Sn polycrystal after several polishing/washing cycles in a solution containing 1 part of HNO_3 , 1 part of glacial acetic acid and 4 parts of glycerol and subsequently etched in a mixture of 10 g of NH_4NO_3 , 10 mL HCl and 50 mL water for 2 min. The inset in a) shows a photograph of the corresponding polycrystal. e) Scheme of the crystallographic region within which the pyramidal hillocks are produced and morphologies obtained as function of the substrate orientation. Data from reference [116].

sample is polycrystalline in nature, morphologies can evolve from perfect pyramidal hillocks (Fig. 2.2a) to flat triangular planes (Fig. 2.2b) or distorted pyramids (Fig. 2.2c and 2.2d). The results are comparable to the ones obtained by Honda *et al.* [116] in single crystalline surfaces (Fig. 2.2e). In the mirror-like regions, no preferential etching can be observed because the orientation of the grains is not located within the crystallographic planes indicated in the shadowed area of the inverse pole figure in Fig. 2.2e.

The reason behind the different morphologies and the lack of oriented surfaces for certain grain orientations lies in the anisotropic nature of the etching process at the different Sn crystalline planes. Overall, the close packed planes of the {101} family exhibit lower dissolution rates [103] compared to the rest. Metallic tin crystallizes in a body centred tetragonal structure, space group: I41/amd (space group number: 141), with cell parameters $a = 5.832 \text{ \AA}$ and $c = 3.182 \text{ \AA}$ as shown in Fig. 2.3a. The position of the 4 tin atoms located inside the cell is fixed by symmetry and lie in the (x,y,z) positions of (0, 1/4, 3/8), (0, 3/4, 5/8), (1/2, 3/4, 7/8) and (1/2, 1/4, 1/8). The {101} family of planes for the Sn tetragonal cell are given in Fig. 2.3b. In (001) surfaces, the intersection of these planes leads to pyramidal hillocks having the edges of the base in the [100] direction. The values of the angles can be calculated from the unit cell parameters of metallic Sn. The angle between two {101} faces on opposite sides is 122.5° , while the angle between the basal plane and the {101} plane yields 28.7° [103]. If the orientation of the surface is inclined with respect to the (001) plane the hillocks appear deformed in shape as predicted in Fig. 2.3c for the {101}, {102}, {112} and {113} orientations [103,116]. As we work in polycrystalline surfaces, all these distorted pyramidal features are likely to be formed.

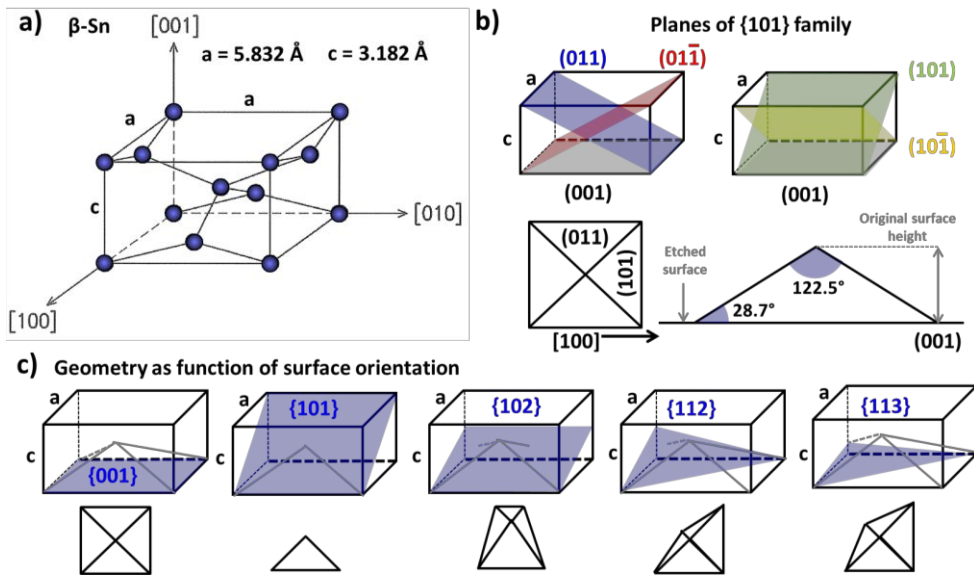


Figure 2.3 a) Unit cell of metallic tin. b) Schematic representation of the {101} planes in the tin unit cell that leads to the pyramidal hillocks due to their slower etching rate (top), top view of the hillocks and calculated angles (bottom) [103]. c) Evolution of the hillock geometry as the as function of the surface orientation.

The morphology of the etched Sn polycrystal was further characterized by AFM (Fig. 2.4). Similarly to FESEM images, several morphologies were encountered at different surface locations. The pyramids were assigned to (001) grains in accordance to Honda's results, but further confirmation is currently under investigation. From the topographical profile, the pyramids were found to have a height $\sim 1.4 \mu\text{m}$ and an angle between the base and the {101} plane of 30° , in close agreement to the expected value of 28.7° (Fig. 2.4a). The profile along the {101} plane of a hillock facet reveals also a completely flat surface, though tilted, free of oxide particles or grains (Fig. 2.4a). These {101} facets are atomically flat so they are an appropriate substrate to study the early stages of Sn passivation by EC-STM. In general,

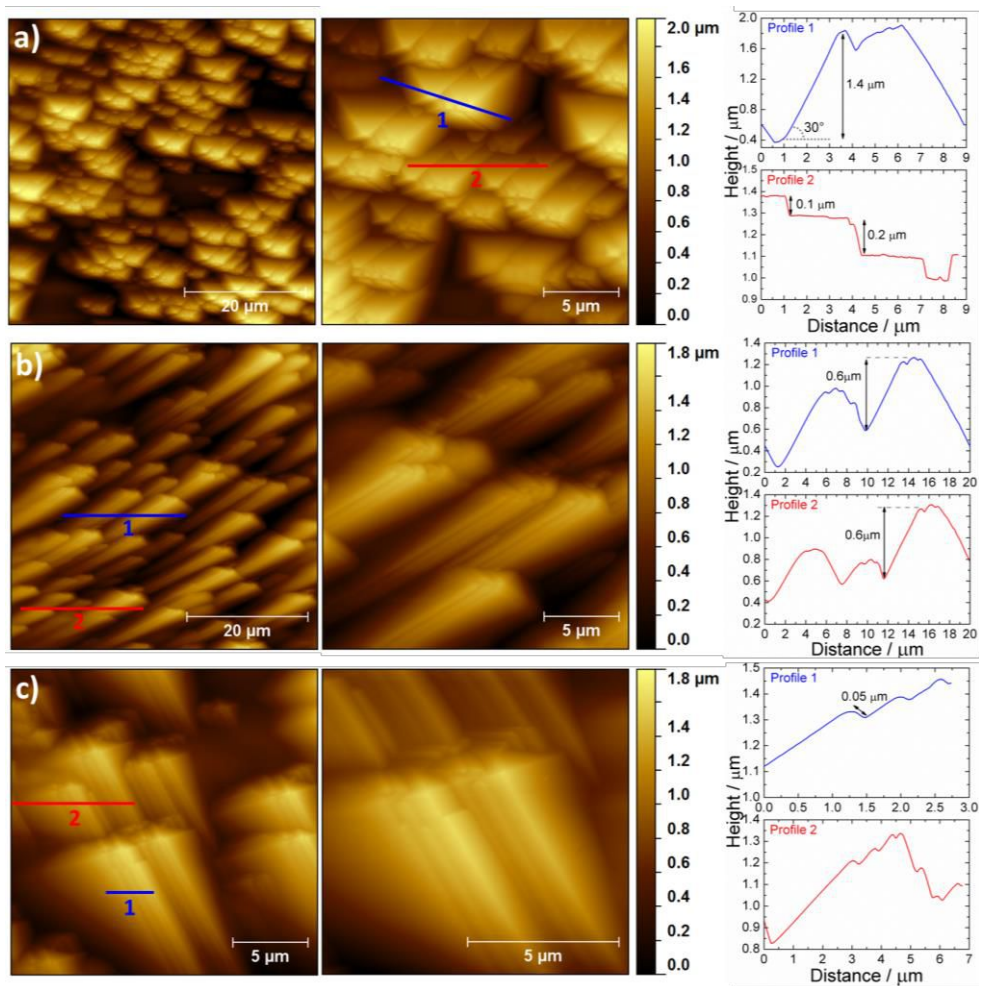


Figure 2.4 Topographical AFM images and profiles for different the orientations of a Sn polycrystal after several polishing/washing cycles in a solution containing 1 part of HNO_3 , 1 part of glacial acetic acid and 4 parts of glycerol and subsequently etched in a mixture of 10 g of NH_4NO_3 , 10 mL HCl and 50 mL water for 2 min. a) shows pyramidal hillocks in (001) surfaces while b) and c) correspond to distorted shapes due to the different grain orientations. The faces of the pyramidal hillocks are perfectly flat and will be used for the EC-STM experiments.

these structures are more abundant in the polycrystal and relatively easier to locate compared to the other morphologies in Fig. 2.4b and 2.4c.

2.2.2 Early stages of Sn anodic oxidation by *in situ* STM

Fig. 2.5a shows the EC-STM image of the pyramidal regions of the Sn polycrystal taken at a potential of -1.3 V, where apparently no anodic reaction takes place and hydrogen evolution is kept at low rates. The corresponding profile of some of the pyramids is given in Fig. 2.5c. The height of the pyramids can range from 0.5 μm to 1.5 μm and the angle was found to be $\sim 28.8^\circ$ in agreement with the AFM images in Fig. 2.4a and the expected value for the pyramidal hillocks formed in (001) oriented Sn grains. In the facets of the pyramids, monoatomic terraces were observed (Fig. 2.5b). The height of the monoatomic steps is ~ 3.6 \AA as extracted from the topographic profiles in Fig. 2.5d. The value is close to 3.182 \AA , the c cell parameter of Sn. This seems to corroborate that the crystallographic planes at the pyramid facets correspond to the $\{101\}$ family.

In the terraces shown in Fig. 2.5b brighter islands can be appreciated. These islands are mainly located at the step edges, although some of them can also be found in the inner terrace regions. The islands can be appreciated in the detail in Fig. 2.6a. They have a size ranging from ~ 20 to 50 nm and a height of ~ 0.05 nm (Fig. 2.6c). Higher resolution images were attempted as shown in Fig. 2.6d. There, some diagonal striped patterns seem to be present in the islands but the quality of the image is not good enough to confirm whether this is really atomic resolution or not. At such negative potentials (-1.3 V) the presence of these

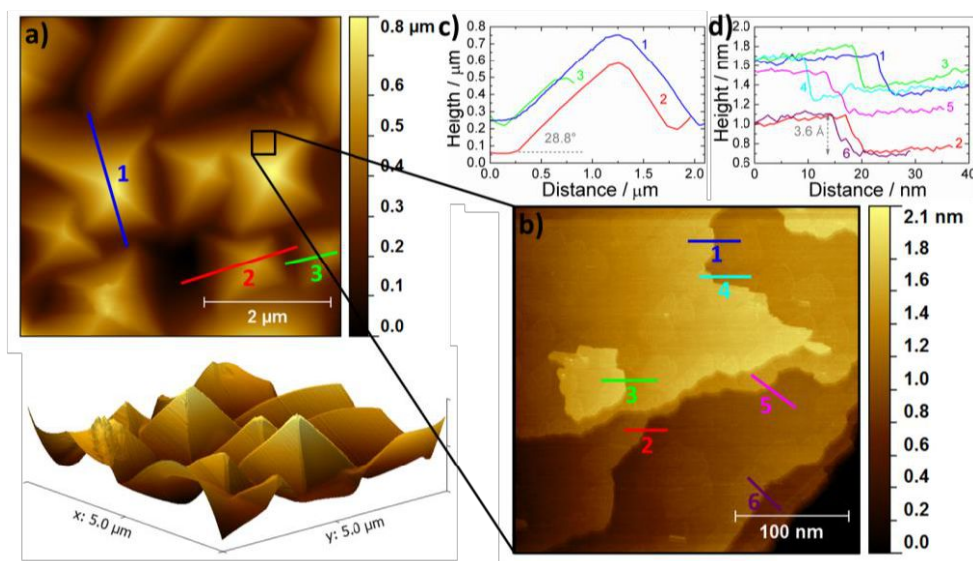


Figure 2.5 a) EC-STM image ($5 \times 5 \mu\text{m}^2$) of the Sn polycrystal taken at $E_S = -1.3$ V ($E_{\text{tip}} = -0.9$ V, $E_{\text{bias}} = 0.4$ V) and b) zoom in one of the terraces ($300 \times 300 \text{nm}^2$) taken in the same conditions. At the bottom the 3D view of the $5 \times 5 \mu\text{m}^2$ is given. c) and d) are profiles detailed in the EC-STM images from panel a) and b), respectively.

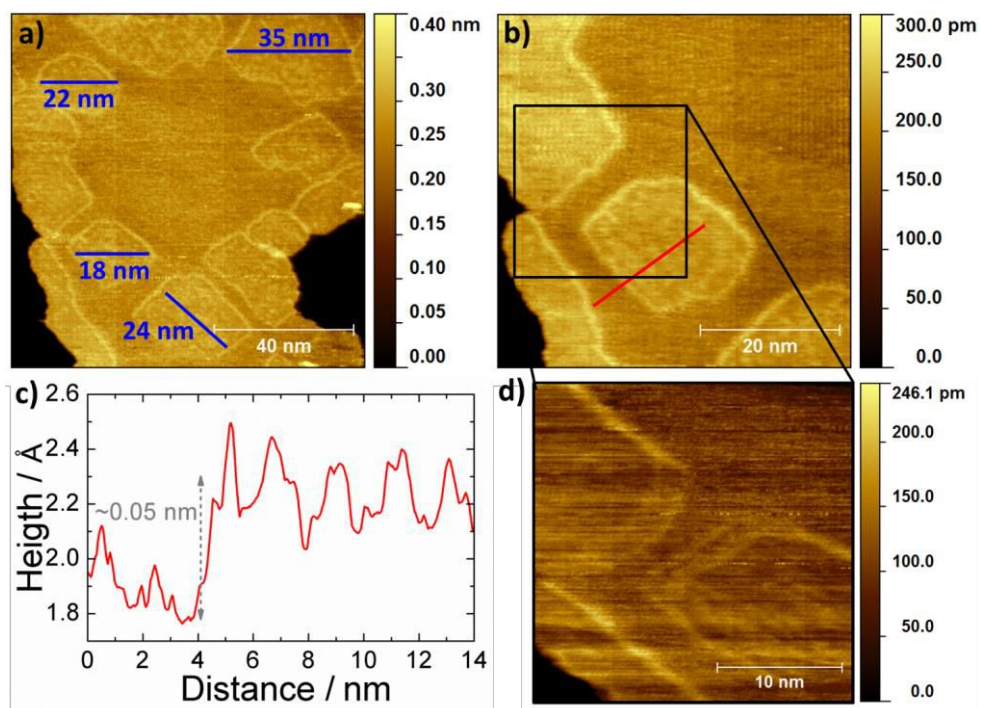


Figure 2.6 a) EC-STM image ($100 \times 100 \text{ nm}^2$) of a terrace in the Sn polycrystal taken at $E_S = -1.3 \text{ V}$ ($E_{\text{tip}} = -0.9 \text{ V}$, $E_{\text{bias}} = 0.4 \text{ V}$) and b) zoom in the bright islands ($50 \times 50 \text{ nm}^2$) taken at $E_S = -1.3 \text{ V}$ ($E_{\text{tip}} = -0.7 \text{ V}$, $E_{\text{bias}} = 0.6 \text{ V}$). c) Profile of the red line in panel b. d) $25 \times 25 \text{ nm}^2$ image of the islands acquired at $E_S = -1.3 \text{ V}$ ($E_{\text{tip}} = -0.7 \text{ V}$, $E_{\text{bias}} = 0.6 \text{ V}$), linear patterns are observed in the middle of the islands.

islands is surprising because no electrochemical processes were expected within this range. A possible explanation for this phenomenon could be (i) the formation of an OH adlayer as described in other systems such as Cu [51,53,57] or Ni [62], (ii) surface reconstruction processes or (iii) impurities of the Sn polycrystal at the surface. This will be discussed more in depth later on, after studying the evolution of the surface morphology with increasing anodic potentials.

Fig. 2.7 shows $200 \times 200 \text{ nm}^2$ EC-STM images of the same region upon application of increasing anodic potentials. The linear voltammetry sweep is given in Fig. 2.7a as a visual guidance. At -1.3 V , as shown in Fig. 2.5 and Fig. 2.6, Sn terraces of $\sim 50 \text{ nm}$ width can be observed. The height of the monoatomic steps extracted from the topographic profiles in Fig. 2.8c and was found to be $\sim 3.8 \text{ \AA}$ in accordance to the values measured in Fig. 2.5d and the reticular distance of the $\{101\}$ planes. As discussed previously, the terraces are decorated with bright islands mainly located at the step edges. At increasing anodic potentials, these bright islands do not grow laterally and remain static, so no coalescence between them is appreciated. Some changes, though, can be observed at the step edges due to shift of Sn atoms as indicated by the blue arrows. This is a usual phenomenon as the surface is in a dynamic equilibrium and atoms in the edges can move to positions with lower energy. At a

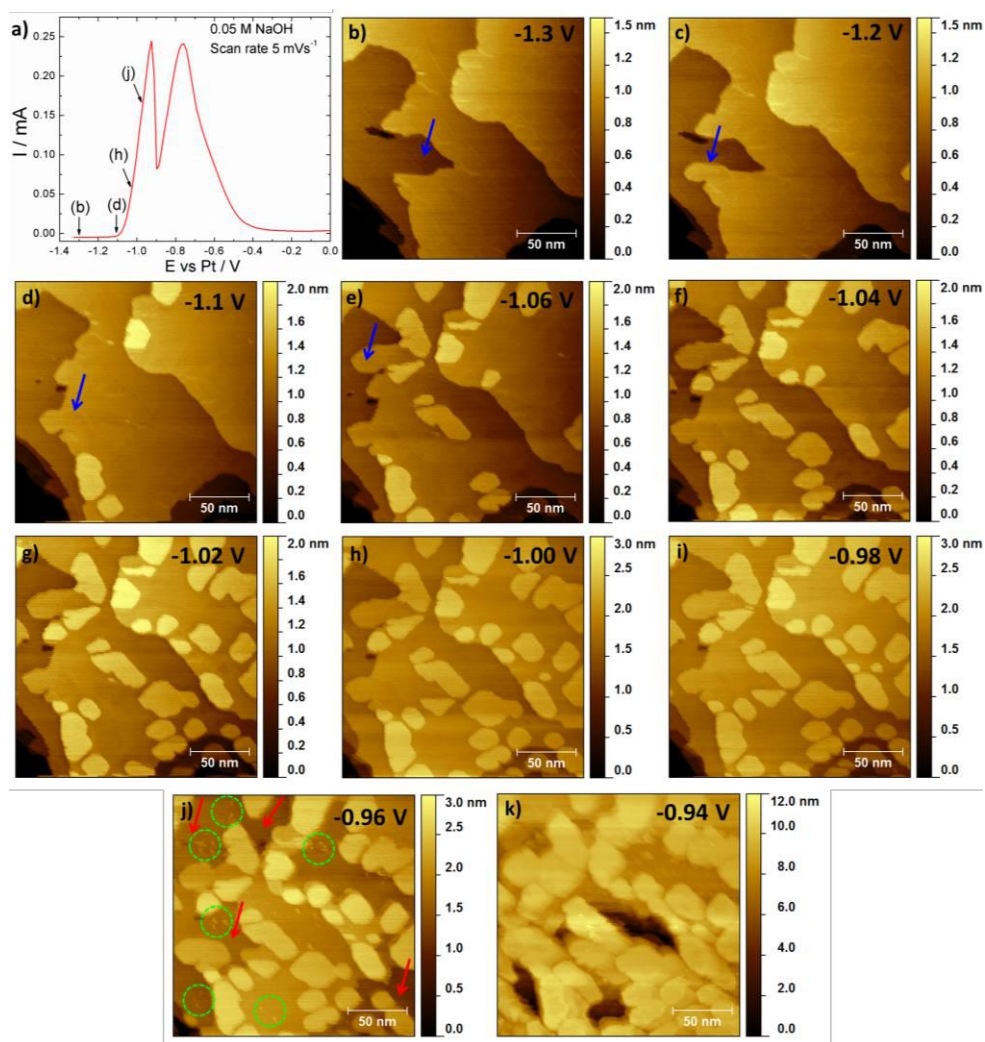


Figure 2.7 a) Cyclic voltammogram at 0.005 Vs^{-1} for a Sn single crystal immersed in a 0.05 M NaOH solution. The voltammogram was taken in the STM cell using a Pt pseudoreference electrode, but the values of potential are comparable to those attained in Chapter 1 with a SSC reference electrode. From b) to k) EC-STM images ($200 \times 200 \text{ nm}^2$) acquired at increasing anodic potentials. The region of potential of some of the images is indicated in the voltammogram in panel a). Blue and red arrows indicate changes in the step edges or the terraces, respectively whereas the green circles correspond to the first precipitates. All images were taken using $E_{\text{tip}} = -0.7 \text{ V}$, except for k) where $E_{\text{tip}} = -0.5 \text{ V}$ was used.

potential of -1.1 V , we observe the deposition of a new crystallographic plane on top of the islands located at the step edges. The height of these new atomic planes was determined to be $\sim 3.8 \text{ \AA}$ from the topographic profiles in Fig. 2.8d. The height matches well with that of the Sn monoatomic steps. Upon potential increase, the amount of islands gradually increases also occupying regions in the middle of the terraces. It is worth to notice that this new phase

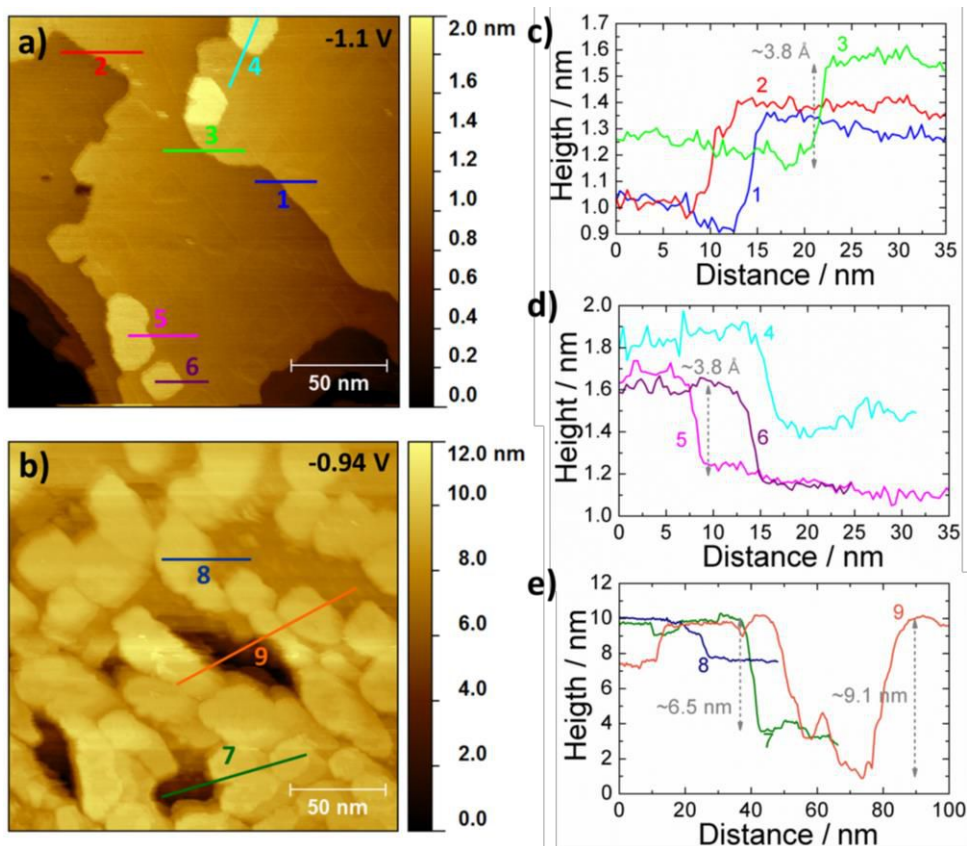


Figure 2.8 EC-STM images ($200 \times 200 \text{ nm}^2$) acquired at a) $E_S = -1.1 \text{ V}$ ($E_{\text{tip}} = -0.7 \text{ V}$, $E_{\text{bias}} = 0.4 \text{ V}$) and b) $E_S = -0.94 \text{ V}$ ($E_{\text{tip}} = -0.5 \text{ V}$, $E_{\text{bias}} = 0.44 \text{ V}$). Colour lines denote the topographic profiles gathered in panels c) to e).

does not grow laterally and only appears in the areas where the islands were previously located. At -0.96 V , parts of the terraces not covered by this new phase disappear (red arrows in Fig. 2.7j) and small bright spots randomly distributed appear (green circles in Fig. 2.7j). The concurrent observation of precipitates and disappearance of parts of the terraces suggests a dissolution and precipitation mechanism for the early formation of the primary passive layer as had already been proposed in Chapter 1. If the potential is further increased to -0.94 V , dissolution results in the formation of pits of several nanometres (see profiles in Fig. 2.8e) followed by the massive precipitation of a non-conducting oxide/hydroxide-related phase. After this, the EC-STM image is lost. The pitting events observed indicate that etching is also present within the primary passive region, but the process can be hindered by the porous 3D layer developed on top.

Considering the above-mentioned observations, we will discuss the possible hypothesis for the nature of the initial islands:

- (i) *Adsorbed OH islands*: this could be the most intuitive explanation; however, the observed behaviour in Fig. 2.7 cannot be explained by this model. OH adlayers widely reported in other metals such as Cu [51,53,57] or Ni [62] have a lower apparent height of ~ 0.05 nm while our islands present a higher apparent height. Moreover, in Cu and Ni these OH adlayers start to develop at the step edges and gradually grow, coalesce and finally cover the whole surface upon potential increase or time. In our case, the islands remain frozen, no matter if we assume that the OH covered region is the one with lower or higher apparent height, since there is no evolution with either potential or time. For Ni, superstructures with OH and water have been identified as bright stripes [61], but these structures change again with both time and potential.

- (ii) *Surface reconstruction*: this phenomenon has been observed in metals such as Au [117] or even Cu, the latter under hydrogen evolution conditions [118,119]. Surface reconstructions on metals tend to rearrange the atoms from the top layer to relax the structure and decrease its surface energy. In the present case, the islands could correspond to reconstructed surface regions, but if so their development should be potential dependent and at some point they should cover the whole surface. The redeposition of Sn on them could be understandable.

- (iii) *Impurities or alloys at the surface*: the idea of surface localized impurities is in agreement with the observed kinetic behaviour of the islands, which keep motionless under potential application. Moreover, the preferential redeposition of Sn in these regions could be also explained. To fully confirm this, grazing angle XPS or even X-ray absorption near edge spectroscopy (XANES) would be required to analyse the surface composition.

2.3 Summary

The first stages of anodic oxidation in Sn were followed by EC-STM. For this, we first optimized the procedure to prepare atomically flat Sn surfaces by a chemical polishing and etching process. With this method, pyramidal hillocks were formed in (001) Sn grains exhibiting flat {101} facets. In these facets flat terraces with monoatomic steps were found.

At very negative potentials (-1.3 V), the surface of the Sn electrode is covered by islands having ~ 20 to 50 nm in width and a height of ~ 0.05 nm. The nature of these islands is not well understood yet and further work is required in this line. These islands are preferentially located at the step edges, remain frozen with the increasing anodic potential and have a positive apparent height. This overall seems to contradict the usual features described for OH adsorbed layers in transition metals such as Cu or Ni. Other possible explanations such as surface reconstruction or accumulation impurities at the surface have been proposed. Surface reconstruction phenomena are usually potential dependent processes, so it does not

fully match with the observed trends. The presence of impurities better fits our observations and must be confirmed with further experiments such as XPS or XANES. At higher anodic potentials of -1.1V , a new phase starts to develop on these bright islands. The height of this new phase is in agreement with the interplanar distance of metallic Sn suggesting that a step edge dissolution and a redeposition process on top of the surface islands are taking place. At more anodic potential, dissolution of terraces begins together with the formation of precipitates randomly distributed on the surface. By increasing the potential to -0.94V , the process is accelerated and dissolution pits of several nanometers along with the precipitation of a non-conducting oxide 3D phase are observed. This causes the complete loss of the EC-STM image. Results denote that etching/ dissolution processes are also predominant in tin electrodes even at the very early stages of the first passivation stage.

2.4 Further work

- Characterize in detail the different orientation of the Sn grains and relate the morphology achieved with its crystalline orientation, this to corroborate that the terraces where we carry out the EC-STM measurements correspond to the $\{101\}$ planes.
- EC-STM images at more negative potentials would be interesting to see if the islands start to develop at some point or are permanently in the surface. Also solutions of higher NaOH concentration could be used to see if there is a relationship between the amount of islands and OH content.
- XPS surface analysis or XANES to determine if the Sn polycrystal presents relevant impurities that remain in the surface after the polishing and etching processes.
- Find an explanation for the nature and composition of the islands in Fig. 2.6.

2.5 Experimental details

2.5.1 Surface preparation

Polycrystalline Sn disks (99.999%, Goodfellow) of 1 cm dia. were used. Previous to the chemical attack, the substrates were mechanically polished with 2400 and 4000 SiC discs. Chemical polishing was performed by repeatedly dipping the Sn disk in a freshly prepared solution containing 1 part of HNO_3 (Normapur, 68%), 1 part of glacial acetic acid (Normapur, 100%) and 4 parts of glycerol (Normapur, 99.5%). The mirror-like surface obtained was thoroughly washed with running MilliQ water and immediately immersed in the cold etching solution ($\sim 5\text{ }^\circ\text{C}$). The chemical etching solution was prepared by mixing 10 g of NH_4NO_3 (Sigma Aldrich, 99%), 10 mL HCl (Normapur, 37%) and 50 mL MilliQ water.

The oriented areas were revealed after 2-3 min. The sample was then removed from the etching solution and washed thoroughly with running water. To make sure that all the components from the polishing and etching process were washed out, especially glycerol, subsequent cleaning was carried out in hot trichloroethylene (Merck, >99.5%), acetone, ethanol and water under, this three last steps under sonication.

2.5.2 Surface characterization

The morphology of the tin polycrystals was characterized in a field-emission scanning microscope (Hitachi FESEM S4800, Japan) and a PicoSPM AFM microscope (Molecular Imaging, USA) in intermittent contact mode.

2.5.3 Preparation of W EC-STM tips

The tungsten (W) EC-STM tips were prepared from a 0.25 mm diameter wire (99.95 %, Goodfellow) electrochemically etched in 3 M NaOH. A piece of about 2 cm was cut. First a rough etching was carried out by vertically dipping the very end of the wire piece and completely etching it at 10 V vs Pt (two-electrode setup). Then, 1-2 mm of the freshly etched wire end were dipped again in the 3 M NaOH and etched at 10 V. The wire was rapidly

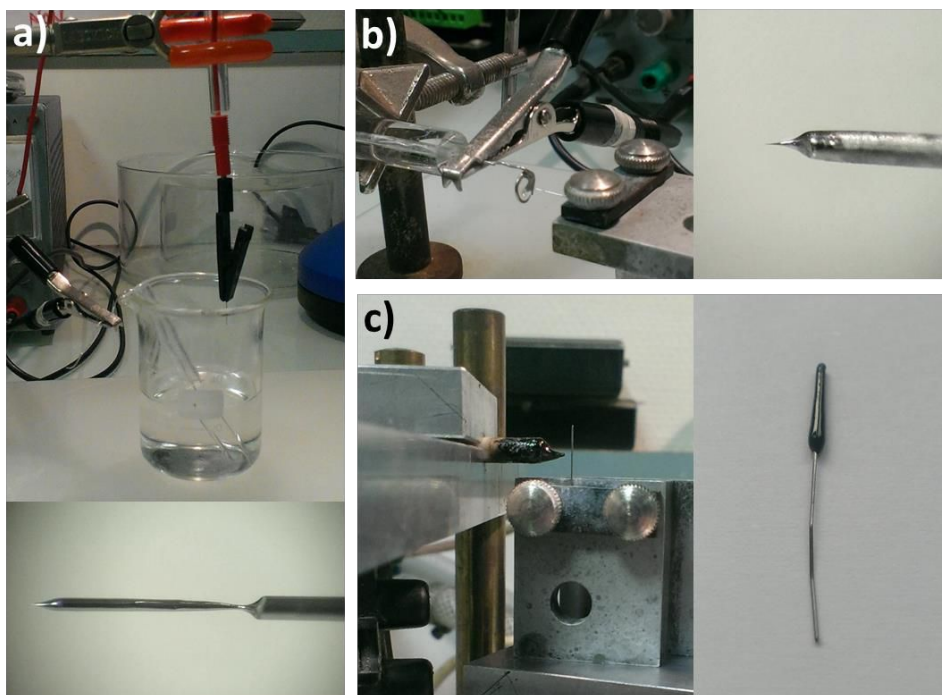


Figure 2.9 a) Experimental setup used to perform the electrochemical etching of W EC-STM tips and image of the wire edge after thinning of the 1-2 mm. b) Pt ring used to sharpen and cut the STM tip and photograph of the tip after the cutting. c) Setup used to cover the tip with Apiezon wax and image of a covered W EC-STM tip.

thinned out until a sharp long tip was left (Fig. 2.9a). Careful attention was taken to avoid the complete cut of the wire. Further thinning and the final cut of the tip were carried out in a Pt ring as shown in Fig 2.9b. A drop of the same 3 M NaOH solution was placed in the Pt ring and the sharpened edge of the wire was intermittently introduced under a potential of 3 V. This procedure allows us to carefully control the final geometry of the tip (length, diameter).

Finally, the tips were completely covered with Apiezon wax, until no current passed through them. A U-shaped heating device made of platinum wire was used (see Fig. 2.9c). The procedure involved two steps. First, the device was heated to the temperature needed for the wax to melt and the heating wire crotch was filled by a droplet of the wax. The tip was covered by passing 4-5 mm of the tip through the droplet. Prior to the EC-STM experiments the very end of the tip was uncovered by gently moving the covered tip towards the heater. To test if the insulation is satisfactory, the tip is mounted in the STM and dipped into Millipore water. The tunnelling current should be less than 1 nA.

2.5.4 EC-STM measurements

EC-STM measurements were performed using a PicoSPM base equipped with a STMA head, a PicoStat bi-potentiostat and a PicoScan 2100 controller (Molecular Imaging, USA). A modified electrochemical STM cell made of Teflon with a capacity of 240 μL and an exposed electrode area of 0.16 cm^2 was employed. The Sn polycrystal was placed at the bottom as working electrode and a Pt wire functioned as counter electrode. As reference electrode, a Pt wire was used (pseudoreference). All potentials will be given with respect to Pt reference (but it must be noticed from the voltammogram in Fig. 2.7a that potential values are comparable to those in Chapter 1 taken using an Ag/AgCl/KCl(sat) reference electrode).

Before the measurements, the EC-STM cell and the two Pt electrodes were cleaned in a 2:1 mixture of concentrated H_2SO_4 and H_2O_2 , in concentrated HNO_3 and finally thoroughly rinsed with MilliQ water. Afterwards, the sample was transferred in air to the electrochemical cell of the STM. The measurements were carried out in a 0.05 M NaOH solution. To remove possible native oxide on the Sn surface the sample was conveniently reduced before the experiment by sweeping the potential to -1.4 V. All images were obtained in the constant current topographic mode at set-point currents ranging from 1 to 2 nA and were corrected from the background plane using Gwyddion SPM software.

PART B:

Applications

Introduction

The part B of this PhD thesis is mainly focused on the preparation of functional nanostructured tin oxide layers by anodization and the study of their performance in real life applications such as gas sensing and photoelectrochemical water splitting for H₂ production. Keeping in mind the target of the following chapters, this introduction section will review the following topics: first, the principles of self-ordered anodization and the state-of-the art of Sn oxide structures obtained up to date using this approach; second, the application of metal oxide layers in gas sensing and the potential of SnO₂ nanostructures in this field; and finally, the basic principles of photoelectrochemical water splitting and the material requirements for their efficient performance.

B.1 Self-ordered anodization

Since the discovery of carbon nanotubes in 1991 by Iijima [120], intense research has been carried out to attain this kind of unusual geometries that present enhanced properties, such as quantum confinement effects, high electron mobility, high specific surface area, or high mechanical strength [6,25]. Although carbon nanotubes are still amongst the most explored nanomaterials, one-dimensional (1D) oxides or sulphides have attracted considerable attention due to their potential use in biomedical, photochemical, electrical, and sensing devices [6,22,25]. In fact, chemical and hydrothermal strategies for the synthesis of metal oxides with 1D geometries (nanowires, nanofibers or nanotubes) have been extensively reported [121,122]. However, in order to exploit these nanostructures in most devices, it is necessary to create ordered arrays [25,123]. In this sense, electron-beam, X-ray, or ion beam lithographic techniques have been investigated, as well as more elegant strategies that rely on self-alignment processes [25,123].

One of the cheapest, simplest, and most straightforward self-alignment processes to form nanostructures is anodization [6,25,123]. In the 1960s, researchers found that under certain anodic conditions random porous oxide films of several microns could be obtained, *i.e.* by anodizing aluminium in acidic environments such as sulphuric, phosphoric, or oxalic acid [23,123]. It was not until 1995 that the first work on a perfectly self-ordered anodic oxide was published. There, Masuda and Fukuda described the formation of arranged hexagonal

alumina nanopores [4]. The key to successfully achieve those ordered structures instead of the usual random pores was the proper optimization of the electrolyte composition in such a way that an equilibrium situation between oxide formation and dissolution rates was attained. These nanostructures opened a broad spectrum of possibilities because, aside from their own applications in photonic crystals [124], they could also be used as templates for the deposition of nanowires or nanotubes of other materials [125–127].

In 1999, Zwillling *et al.* grew the first self-ordered nanotubular TiO_2 structures by anodizing Ti in a diluted fluoride containing electrolyte [5]. From then on, many studies were focused on controlling the anodization parameters (temperature, potential, electrolyte composition and pH, viscosity, *etc.*) that strongly influence the diameter, length, and shape of the nanostructures. By the accurate conditions choice, the morphology was proved to evolve from a flat compact oxide to a disordered porous layer, a highly-organized porous layer or a self-organized nanotubular film [24]. Besides, self-ordered anodization was successfully applied to other valve metals such as Hf [128,129], Ta [130–134], W [135,136], Nb [137,138], Zr [139], V [140], or even alloys such as TiNb [138,141–143], TiZr [144,145], TiAl [146,147], and TiTa [148]. Some examples of these nanoporous or nanotubular structures are given in Fig. B.1.

B.1.1 Principles of self-ordering anodization

To understand the growth of nanotubular or nanoporous structures by self-ordering anodization, the development of a compact oxide layer also referred to as barrier-type oxide needs to be considered first. It is well-known that when valve metals are anodically polarized, a compact oxide irreversibly grows by a field-assisted migration of ions through the film [6,22,25,151]. Briefly, oxygen ions migrate inward from the oxide | electrolyte

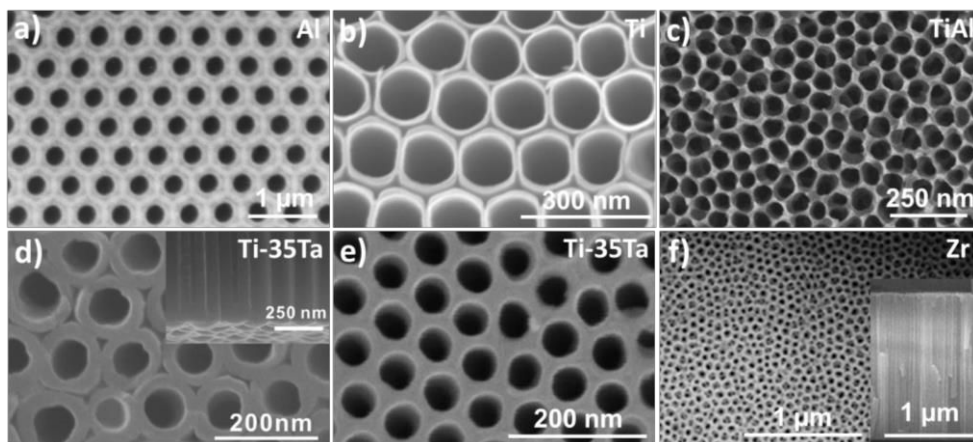


Figure B.1 FESEM micrographs of electrochemically grown self-ordered nanopores on a) Al [149] and b) Ti [150] or their alloy c) TiAl [146]. A special case where d) nanotubes or e) nanopores can be formed on Ti-35Ta alloys [148]. f) Nanotubular structures obtained by Zr anodization [139].

interface while metallic ions migrate outwards from the metal | oxide interface (see Fig. B.2a). The metallic ions (M^{n+}) reaching the oxide | electrolyte interface can either be used to contribute to the growth of the oxide film or be ejected to the electrolyte. The reader is referred to Section A.1.2. in the Part A Introduction for more details.

In order to develop self-ordered nanoporous or nanotubular structures, a process involving the dissolution of the as-formed oxide needs to be also taken into account. A general expression for the process is given in (B.1)



where $MO_{n/2}$ is the growing oxide, X^- the ionic species favouring the oxide dissolution and

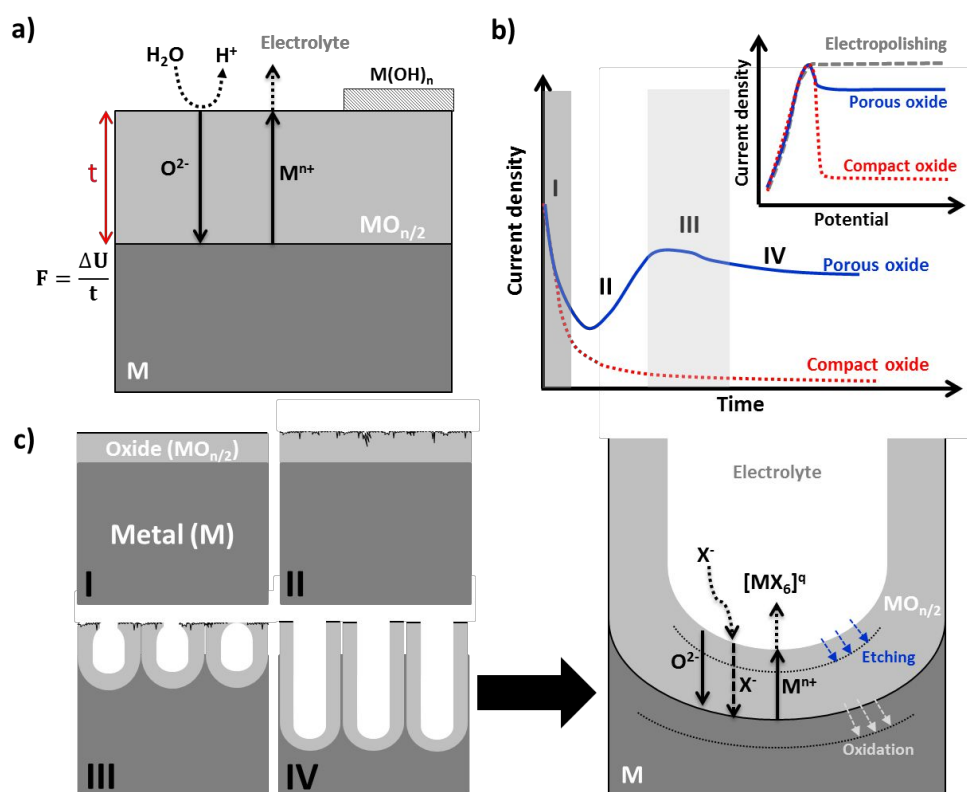


Figure B.2 a) Schematic representation of the high-field mechanism involved in the formation of a compact or barrier-type oxide layer. This process is given when the metal is anodized in the absence of an agent that dissolves the oxide. b) Typical current-time curve after the application of a potential step for the growth of a compact and a porous oxide layer. The inset shows the linear sweep voltammogram for increasing contents of the species promoting the oxide dissolution. c) Illustration of the different stages involved in the growth of an anodic porous/nanotubular oxide layer according to the different regions (I-IV) in the current-time curve. The anodization is carried out in the presence of a solubilizing agent (X^-) that promotes the tube growth. The soluble complex is indicated as $[MX_6]^q$, where q can be either positive or negative depending on the valence of M and the nature of X , which could be a cation like H^+ or an anion as F^- . Adapted from references [6,25,123].

$[\text{MX}_6]^\ominus$ the soluble complex. Solubility can be provided by incorporating certain ions such as F^- in the case of TiO_2 nanotubes [22,25] or by acidic/alkaline pH as occurs for Al_2O_3 nanopores [23].

Usually, compact anodic layers are formed in electrolytes where the oxide is poorly dissolved (in very low concentration or absence of X^-), meaning that it is chemically stable [22]. In such case, the current response exponentially decays (Fig. B.2b). However, when X^- ions are incorporated in the solution, two different scenarios can be given. If the concentration of the solubilizing agent X^- is very high, the field-assisted $\text{M}^{\text{n}+}$ ions arriving at the oxide | electrolyte interface are immediately complexed and the grown oxide is chemically attacked. Here, no current decrease due to oxide formation is observed at increasing potentials (Fig. B.2b inset) and the overall result is the electropolishing of the metal anode [6]. For intermediate X^- concentrations, a competition between oxide growth and solubilisation reactions occurs and this results in the formation of self-ordered porous or nanotubular structures [6,22,24,25]. A typical current-time curve in these conditions is shown in Fig. B.2b. The curve presents four different regions that can be related to the different stages of the self-organized nanotube/nanopore growth illustrated in B.2c:

- I) Stage I: in an initial step (first seconds after the anodic potential step), the current-time curve has the same behaviour as in the absence of X^- : after a certain thickness is reached, the surface is passivated and the current drops rapidly to the minimum value [23]. This owes to the development of a compact oxide layer by a field-assisted growth mechanism described in Fig. B.2a, the so-called initiation layer [6,22,24,25,123].
- II) Stage II: there is a slight increase in the current response as irregular nanoscale pores are formed and the reactive area increases. O'Sullivan and Wood [152] suggest that the pore initiation may occur at thinner oxide areas existing on the initial barrier layer. These irregularities appear due to the current concentration on local imperfections like defects, impurities, pits or ridges. Alternatively, Thompson and co-workers have proposed that the tensile stress may induce the local cracking of the initial barrier oxide and may settle the paths for electrolyte penetration [24,153–155]. The local increase in field strength at the penetration paths facilitates the field-assisted oxide dissolution and eventually leads to the development of embryo pores.
- III) Stage III: the early pores formed in Stage II start to increase in size by persistent merging with the adjacent ones [23] until an average size is reached. O'Sullivan and Wood proposed that the field-assisted dissolution at the base of the growing pores should occur to some different extents until the electric field across the barrier layers becomes the same for every pore [152]. The decrease in the total pore density causes a slight decrease in the current response.

- IV) Stage IV: pores start to grow longer and steady-current conditions are attained due to the equilibrium situation between the oxide growth at the metal | oxide interface of the pore and the oxide etching at its outer oxide | electrolyte interface (see the detailed scheme in Fig. B.2c) [6,22,24]. The current stabilizes at a value significantly higher than the one given when a compact oxide film is formed at the same voltage [6]. This current is diffusion controlled, so the rate limiting step is the diffusion of X^- species to the electrolyte region close to the tube bottom or the transport of reacted $[MX_6]^{q-}$ [25]. The final thickness of the entire nanotubular/porous oxide layer depends on the anodization time, though, at some point, the dissolution rate at the top of the oxide will equal the rate of tube/pore growth at the bottom and thickness will not increase anymore [6,25]. For most electrochemical conditions, anions from the electrolyte are incorporated to the film (F^- , SO_4^{2-} , PO_4^{3-} , etc.) [6,22,24,123].

The last stage of pore growth, which occurs under steady-current (stage IV in Fig. B.2b), involves several additional processes that have been omitted in the previous discussion for sake of simplicity and will be separately treated below:

- (i) *Joule's Heat-induced chemical dissolution*: the main contribution to heat generation in anodization is related to the current flow through the barrier oxide layer (bottom of the pore/tube, Fig B.2c) [156]. The production of Joule's heat is proportional to the square of the current density [156]. Apparently, this excessive heat promotes the chemical dissolution of the barrier oxide (usually an endothermic process) and enlarges the pores by assisting the dissolution of its walls [23,157]. However, recent *in situ* measurements of the anode temperature during anodization found that the maximum temperature change is $\sim 1^\circ\text{C}$ which seems to question the role of Joule Heat-induced dissolution at the pore base [158].
- (ii) *Field-assisted oxide dissolution*: it is accepted that the local oxide dissolution is assisted by the increased electric field due to the geometry of the pore base [23,24]. Some authors have proposed a physical mechanism for field-assisted chemical dissolution based on the effective polarization of M-O bonds along the field direction, which lowers the effective activation energy for bond dissociation [152].
- (iii) *Oxide dissolution by local acidity*: it has been suggested that the solubility of the oxide can be enhanced by the pH drop at the bottom of the pores. The local decrease in pH arises from the hydrolyzation of the cations formed during anodization [24].
- (iv) *Viscous flow*: a remarkable feature of anodic nanotubular/nanoporous structures is that they are generally longer/thicker than the value estimated assuming 100% current efficiency [6,23,159]. The expansion factor when the metal is converted into oxide, the so-called Pilling-Bedworth ratio (PBR), is given by the ratio of the molar volume of the grown oxide to the molar volume of the consumed metal [160]. In self-ordered

nanostructures this PBR is commonly larger than expected. For example, for anodic TiO_2 the PBR is 2.43, but TiO_2 nanotubes grow much larger than this expectation with an expansion factor of ~ 3 [159]. This additional lengthening of the tubes is caused by an upward plastic flow of the tube/pore walls [6,23,161–163] given the large compressive interfacial stress at the pore base [6,23,161–164]. This flow model has been validated by using tracers in the metallic substrate and following their evolution during the growth [162,163].

B.1.2 Geometry control in self-ordered oxide layers

Self-ordered anodization is by itself a very powerful strategy for the preparation of nanostructures because it offers the possibility to accurately control the morphology (either pores or tubes), the pore/tube diameter or the film thickness by providing a constant electric field in a certain electrolyte. Modifications of the tube geometry can be also achieved by altering the applied voltage during the growth [6,165].

B.1.2.1 Pores vs. tubes

Self-ordered anodization of Al in more or less acidic electrolytes is known to lead to porous oxide structures [24,123]. Self-organized anodic porous alumina can be represented schematically as a closed-packed array of hexagonally arranged cells containing pores at each cell centre (see Fig. B.3) [23,123]. Studies on the composition of these individual nanopores have shown that the chemistry of the inner and outer oxide parts is significantly different. At the cell boundaries, or inner oxide layer, almost pure Al_2O_3 is found, while the outer layer in direct contact with the electrolyte through the pores is rich in anions from the electrolyte [24]. Other metals like Ta or Nb were found to behave in a similar way [25,132,137].

Contrarily, Ti, Zr, or Hf present oxide structures with well separated individual tubes [25,128,139,150]. Although both self-organized oxide morphologies seem to be considerably different at first sight (see Fig. B.1a for Al pores and Fig. B.1b for Ti

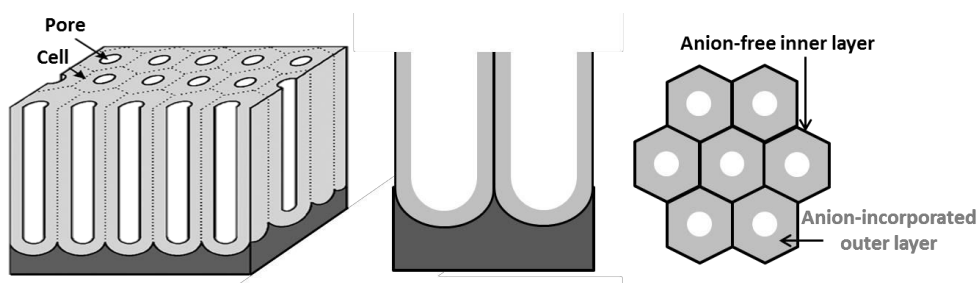


Figure B.3 Schematic structure of anodic porous alumina. A detail of the cross-section and top view is given, where the regions in a single pore having different composition are indicated. Adapted from [123].

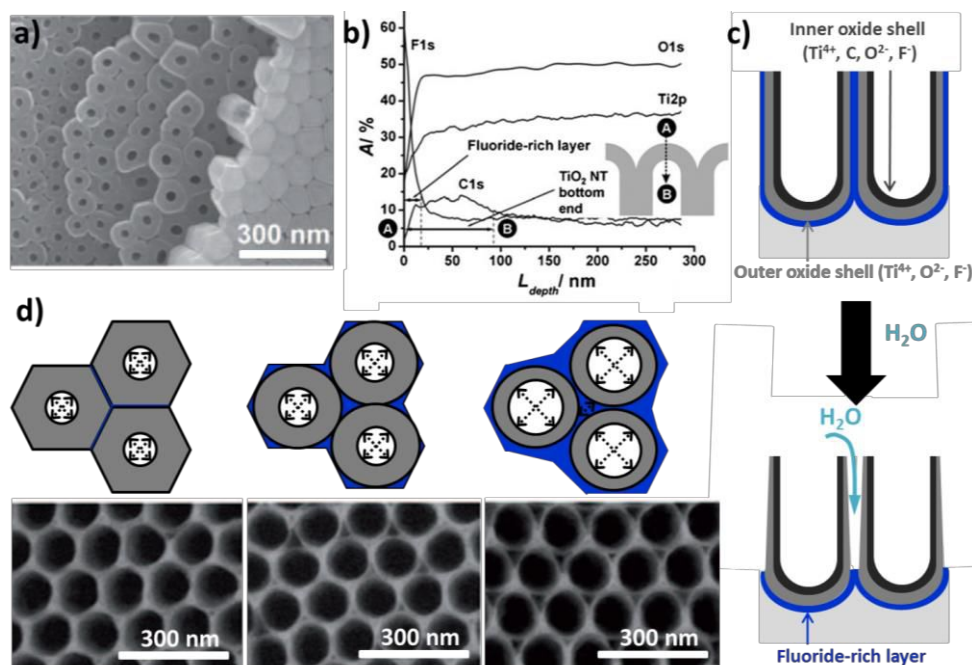


Figure B.4 a) SEM bottom view of a TiO₂ nanotube layer cracked off from the metallic substrate. The bottom of the tube layer consists of a closed-packed hexagonal pore layer that is gradually converted to tubes. b) XPS depth profile taken through the bottom of a lifted-off TiO₂ nanotube layer [6,166]. c) Representation of the formation of a tubular morphology from an originally porous morphology by selective dissolution of fluoride-rich layers and preferential etching at triple points by H₂O in the electrolyte. d) Transition from a porous to a tubular structure in Ti-54Al alloy (adapted from [6,146]).

nanotubes), a strong correlation between both nanostructures has been recently found [6]. Actually, the morphology at the bottom of a TiO₂ nanotube layer (Fig. B.4a) is identical to that of Al porous layers (Fig. B.1a) [6,24,150]. This suggests that the compact hexagonal oxide morphology is present at the early stages of nanotubular structure growth but it is gradually converted into the tubular shape as the oxide develops [6]. The structural change from nanopores to nanotubes seems to depend on the solubility properties of the cell boundaries [6,24,146]. XPS studies indicate that the inner part of the TiO₂ nanotubes is rich in electrolyte species such as F⁻, similar to the observed composition of the pore walls in Al₂O₃, however, Albu *et al.* [6,166] proved that a fluoride rich layer is also present at the bottom of the tubes (Fig. B.4b). This fluoride rich layer is presumably present in the tube walls too, so these regions are sensitized and more prone to chemical dissolution. The selective chemical dissolution of the fluoride-rich layer etches out the cell boundaries and leads to individual tube shapes [6,24].

Under comparable anodization conditions, an ordered porous oxide is obtained for Al₂O₃ but a tubular morphology is found for TiO₂. This can be ascribed to the higher solubility of Ti-F or Ti-O-F compounds in aqueous media as compared to Al-F species [6]. In other words,

separation into tubes and the height of the nanostructure where pore cells are split into separate tubes is determined mainly by the fluoride concentration and the water content, since it has a direct incidence in the solubility of the fluoride compounds (Fig. B.4c) [6,24]. Interestingly, transition from pores to tubes has been shown for TiO_2 and ZrO_2 by increasing the water content in the electrolyte (Fig. B.4c) [6,128] whereas for pure aluminium only porous structures can be obtained. To achieve Al_2O_3 tubular features, the metal is first anodized to form a porous layer and then the cell boundaries are attacked using a suitable etchant [167,168]. Pore to tube transitions have been shown for alloys like TiNb and TiAl [6,137,141,146] that contain typical tube-forming and pore-forming systems. For these alloys, oxide layers with distinct porous or tubular morphologies, or even transitional states, could be adjusted depending on the electrochemical conditions (Fig. B.4d).

B.1.2.2 Length and diameter

In general, the pore or tube diameter is, for many systems, reported to be linearly dependent on the applied voltage for a specific electrolyte and temperature, as represented in Fig. B.5a for TiO_2 self-ordered nanotubes [153,169–171]. Here, diameters ranging from 10 to 250 nm can be achieved by using potentials between 1 and 45 V in a glycerol- H_2O -based electrolyte. This level of diameter control bears significant potential for applications where the tube/pore

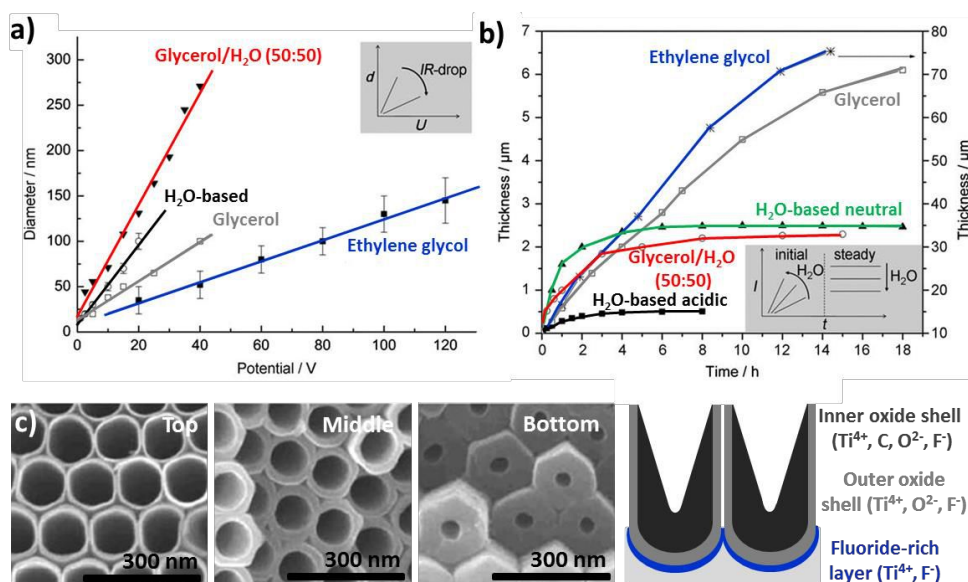


Figure B.5 a) Potential dependence of TiO_2 nanotube diameter for different electrolytes: Glycerol/ H_2O (50:50), H_2O -based, glycerol, and ethylene glycol [6]. b) TiO_2 nanotube-layer thickness dependence on anodization time in different electrolyte solutions (potential was fixed at 40 V, except for ethylene glycol that was held at 60 V). c) SEM images and of TiO_2 nanotubes prepared at long anodization times (6 h) taken at the top, from the fractures in the middle, and close to the bottom of a tube layer, illustrating the gradient in the tube-wall thickness of v-shaped nanotubes [150]. A schematic representation of as-grown v-shaped TiO_2 nanotube layer is also shown (adapted from [6,166]).

diameter needs to be tailored for specific use. Recently, it was shown that the linear relationship also holds for a variety of other transition metals. It was found by Yasuda *et al.* that in Ti and TiZr the nanopore/nanotube diameters correlate linearly with the growth factor of the metal oxide, that is to say with the compact oxide thickness grown at a specific voltage [153].

The duration of the anodization time, if the other electrochemical parameters are kept constant, controls the nanotube/pore layer thickness. As mentioned previously, this only holds for a certain time until the steady-state condition between dissolution at the top and growth at the bottom is reached (Fig. B.5b). For TiO₂ nanotubes grown with extended anodization times, the earlier formed walls of the tubes are longer exposed to the etching fluoride environment and become increasingly v-shaped in morphology: at the tops the tubes possess significantly thinner walls than at their bottoms (Fig. B.5c) [6,24,150]. If tube walls become too thin at the top to support their own weight or withstand capillary forces when drying, they tend to collapse and inhomogeneous needle or grass-like top structures are obtained. Hence, to grow long tubes, it is required to keep the fluoride concentration as low as possible along with a low acidity. As shown in Fig. B.5b, in H₂O-based acidic electrolytes the etching rate is so fast that the TiO₂ nanotube length is limited to ~500 nm, while using the same electrolytes at a neutral pH lead to 4 times thicker structures.

Chemical dissolution can be further decreased by anodizing in organic-based electrolytes since their viscous nature can strongly affect the diffusion-controlled tube/pore formation process [24]. As depicted in Fig. B.5b for self-ordered TiO₂ nanotubes grown in glycerol or ethylene glycol, the linear growth behaviour is extended and oxide thicknesses of ~70 μm can be achieved. These electrolytes can also enhance the self-ordering degree. For example, in electrolytes with low water contents (higher content of organic solvent) smooth tube walls are obtained [172,173], whereas side wall ripples are formed at higher contents (Fig. B.6a). The formation of ripples is ascribed to the continuous etching and passivation of the cell boundary regions as a result from the faster dissolution of the fluoride-rich layer between the tubes compared to the growth of the tubes in the underlying substrate [6].

B.1.2.3 Advanced geometries: bamboo, nanolaces, and branched tubes

Further modifications of the tube geometry can be achieved by altering the voltage during the growth [6,165], *i.e.* applying potential steps, interrupting the applied potential or decreasing it. For instance, if the voltage is lowered during anodization, the tube growth will be drastically slowed down, as the driving field across the bottom oxide is suddenly decreased. Given the permanent etching of the tube bottom in the fluoride environment, at some point, the oxide will be thinned down sufficiently to continue the growth process under low voltage conditions. Then, the tube diameter will decrease and tube branching may occur as shown in Fig. B.6b. Interestingly, if voltage cycling is carried out for an extended period of time 2D nanolace structures are formed as given in Fig. B.6c. This happens because the thinnest part of the tube wall formed at the higher voltage is etched off and only the

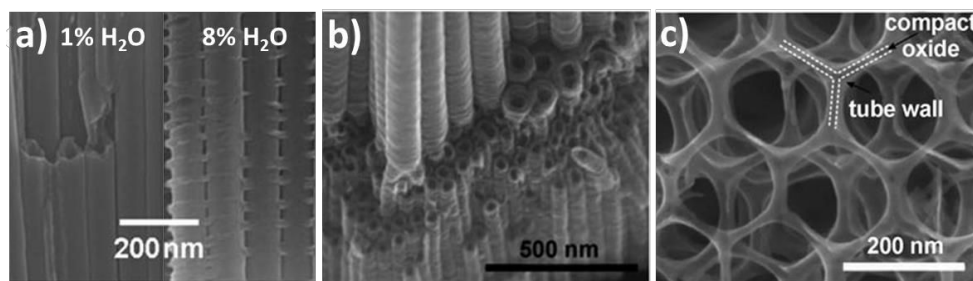


Figure B.6 a) SEM images of smooth TiO₂ nanotubes and with side wall ripples obtained by changing the water content [173]. SEM micrograph of b) branched nanotubes and c) a nanolace structure prepared by voltage stepping [165].

reinforced compact parts are left behind so the second tube layer will initiate in the space between the tubes (Fig. B.6c). By alternating potential steps during anodization, at an optimized step-width and step-time, a nanotube stacks or stratification layers (also referred as bamboo-like tubes) can be created. The structure has stratification layers connecting the tubes in a similar way as side wall ripples do when working in aqueous electrolytes (Fig. B.6a), but here the distance between the distinct bamboo rings can be altered by adjusting the holding times at the respective anodization potential. These bamboo type nanotubes show a higher surface area together with a higher mechanical stability as compared to the conventional ones.

Other advanced morphologies can be achieved through post-anodization modifications like specific heat treatments, selective dissolution and bottom opening, treatment with organic hydrophobic monolayers, among others [166,174].

B.1.3 Poor state-of-the-art of Sn self-ordered anodization

Although self-ordered anodization of Ti, Al, and other valve metals has been studied in detail, the preparation of self-ordered Sn oxide structures by anodization is still in a very preliminary stage. This is quite striking considering the interesting semiconducting properties of SnO₂ and its vast number of applications ranging from solid state gas sensors [175–182] to Li-batteries [183], supercapacitors [184], UV-detectors [185], field-effect-transistors [186], or solar cells [187]. Up to now, the possibility of preparing SnO₂ nanostructures (nanobelts, nanowires, or nanopores) with high surface area and enhanced properties compared to those of a bulk material has been mainly addressed by physical techniques such as thermal evaporation [181] and laser ablation [185], or by solution-based methods like hydrothermal synthesis [182] and template assisted electrodeposition [188].

In 2004, Shin *et al.* first reported the preparation of anodic porous SnO₂ by anodizing tin foils in aqueous oxalic acid electrolytes [189]. As can be observed in Fig. B.7a, those structures presented severe discontinuities along the channels due to the vigorous oxygen

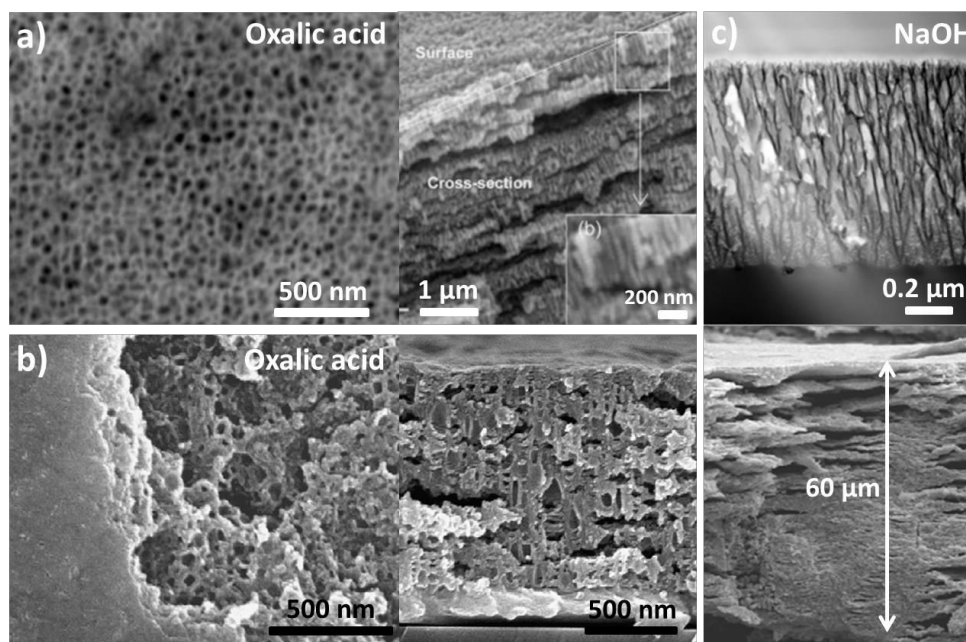


Figure B.7 a) SEM images of porous anodic tin oxide layers prepared a) by Shin *et al.* in a 0.5 M oxalic acid solution at room temperature [189], b) in 0.3 M oxalic acid at 5 °C and by applying a potential of 5 V as reported by Jeun and coworkers [175], and c) in NaOH at 5 V [191].

evolution during the film formation and its fast growth [175,189]. At first, the presence of these stacked layers may seem beneficial for gas or liquid transportation in catalytic applications [189] or as reservoir for active species [190], nevertheless, more homogeneous and robust layers are necessary for reliable long-term applications [190], especially when the anodic films are meant to be used for (photo)-electrochemical applications or gas sensing.

Posterior works, carried out by using similar oxalic acid electrolytes, explored the effects of the applied potential [184,189,190], the concentration [184], the working temperature [184], and the use of potential pulses [190] on the Sn oxide film structure, this in order to obtain crack-free films. All the attempts were of limited success; when either potential or temperature was decreased to avoid the formation of stacks, anodic layers presenting pores clogged at the top were obtained (Fig. B.7b) [184,190]. Ono *et al.* described the use of an alternative electrolyte and showed that porous tin oxide structures could also be attained in sodium hydroxide water-based solutions [191]. Yet, these studies ended up with results similar to those obtained for anodic films prepared in oxalic acid, as shown in Fig. B.7c.

So far, the changes in the anodization parameters for both electrolytes, oxalic acid and sodium hydroxide, have not resulted in a real improvement on both the film micro- and nanostructure. Hence, alternative electrolytes need to be investigated.

B.2 Application of metal oxides in gas sensing

Sensor technology has gained popularity as the demand for physical, chemical and biological recognition systems has increased. Gas sensors are used to detect gas, to discriminate odour, or generally to monitor changes in the ambient gas atmosphere [192]. Semiconducting metal oxides were identified as possible sensitive materials in the mid-1950s by Heiland *et al.*, Bielanski *et al.* and Seiyama *et al.* [193–195]. Since the 1970s, metal oxide-based gas sensor devices have been used, and among them, those based on conductivity changes have been the most frequently investigated [192,196]. Nowadays, there are many companies offering this type of sensors, *e.g.* Figaro, FIS, MICS, UST, CityTech, Applied-Sensors, NewCosmos, *etc.* Their applications span from “simple” explosive or toxic gases alarms to air intake control in cars or to components in complex chemical sensor systems.

Suitable metal oxides for detecting combustible, reducing, or oxidizing gases by conductive measurements are: ZnO, Cr₂O₃, Mn₂O₃, SnO₂, Co₃O₄, NiO, CuO, SrO, In₂O₃, WO₃, TiO₂, V₂O₃, Fe₂O₃, GeO₂, Nb₂O₅, MoO₃, Ta₂O₅, La₂O₃, CeO₂, Nd₂O₃. Among them ZnO, TiO₂ and SnO₂ have attracted much attention due to their low cost and flexibility in production; simplicity of their use; and large number of detectable gases and, consequently, possible application fields [196].

B.2.1 SnO₂ in gas sensing: the potential of nanostructures

With strong oxidizing power, high electron mobility, direct band gap, good chemical inertness, low cost, non-toxicity and unique optical properties, SnO₂ offers a great potential for gas sensing applications [192]. The basic detection principle of this sensor is the change of its surface resistance (or conductance) with gas adsorption [192,196]. The exact fundamental mechanisms are still controversial, but essentially, trapping of electrons from the conduction band by adsorbed oxygen species causes an upward band bending at the semiconductor surface and the formation of a space charge region (depletion layer) as shown in Fig. B.8a. This depletion layer lowers the charge carrier concentration and causes an overall decrease in conductivity. Reaction of the adsorbed oxygen species with reducing gases or a competitive adsorption and replacement of the adsorbed oxygen by other molecules releases the trapped electrons back to the conduction band and decreases the band bending (Fig. B.8b) [196]. This results in an increased conductivity.

SnO₂ has been widely used for gas-sensing applications, mainly as thin film made of polycrystalline nanoparticles because the Schottky barriers built up at the interfaces between grains add sensitivity to the device [177]. Moreover, these layers are usually produced with a certain degree of porosity to maximize the exposed area, as sensing phenomena takes place only at the oxide surface. This has aroused a growing interest on developing polycrystalline SnO₂ nanostructures with large surface-to-volume ratios or well-defined and uniform pore

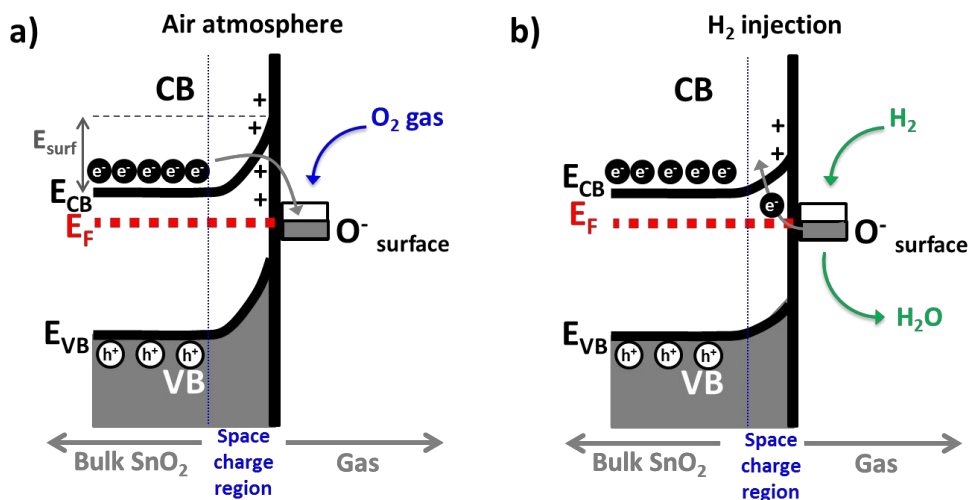


Figure B.8 a) Schematic diagram of band bending after chemisorption of charged species (here the ionosorption of oxygen) EC, EV, and E_F denote the energy of the conduction band, valence band, and the Fermi level, respectively, and E_{surf} denotes the potential barrier. b) Decrease in band bending after H_2 injection and its reaction with chemisorbed oxygen species to form water molecules. Adapted from reference [196].

structures to improve their sensing performance. Strategies based on physical methods such as thermal evaporation [177,178,197] or chemical vapour deposition [198] as well as solution routes, namely, sol-gel [179], nanocasting [199] or self-ordered anodization [175,176] have been proposed. In general, these SnO_2 nanostructures show improved sensitivity and reversibility (stability after several sensing cycles) together with lower operating temperatures if compared to compact films. This is attributed to their high surface area and directed charge transport [180]. In this view, SnO_2 nanowires [177,178,197,198], nanobelts [178], hollow spheres or mesoporous/nanoporous [180,199] films have been successfully applied in the detection of NO_x , CO, O_2 , H_2 and ethanol.

In the particular case of H_2 sensing, pristine SnO_2 nanowires were found to detect concentrations of H_2 as low as 10 ppm when operating at 300 °C [177], and up to 500 ppm under ambient conditions [179]. Improved responses were found by Huang *et al.*, sensing 100 ppm of H_2 in ambient conditions, although their optimal sensing temperature was found to be 200 °C [198]. SnO_2 is also used in combination to other materials such as doped with noble metals (being Pt or Pd the most common dopant [180,199]) or patterned with self-assembled monolayers [200]. Noble metal-decorated mesoporous SnO_2 layers or nanowires exhibit a better overall performance, *i.e.* 50 ppm of H_2 can be detected at room temperature [180] or 10 ppm when operating at 250 °C [199]. Despite the improved sensing performance, noble metal deposition dramatically increases the total cost of the device, so intensive research is still carried out to lower the operating temperatures and detection limits in a cost-effective way.

B.2.2 Gas sensing measurements: setup and sensing response

Gas sensors based on metal oxide nanostructures generally consist of three parts: the sensing film, the electrodes and the heater. The electrode pair is connected to a multimeter to register the changes in resistance occurring at the metal oxide film upon exposure to different concentrations of the target gas. Usually, gas sensors are equipped with a heater so that they are externally heated to reach an optimum working temperature. A scheme of a resistance versus time curve is given in Fig. B.9. In the presence of the reference gas the resistance is kept at a constant value, but upon injection of the target gas the resistance drops. The time required to achieve a new constant resistance value is the so-called response time. When the injection of the sensing gas is stopped, the resistance gradually returns to its original value and the time required to do so is the recovery time. From this plots, the sensor response for different concentrations of the target gas can be calculated using equation in Fig. B.9. Some of the important characteristics of a sensing device that can be deduced from the response curve are also indicated.

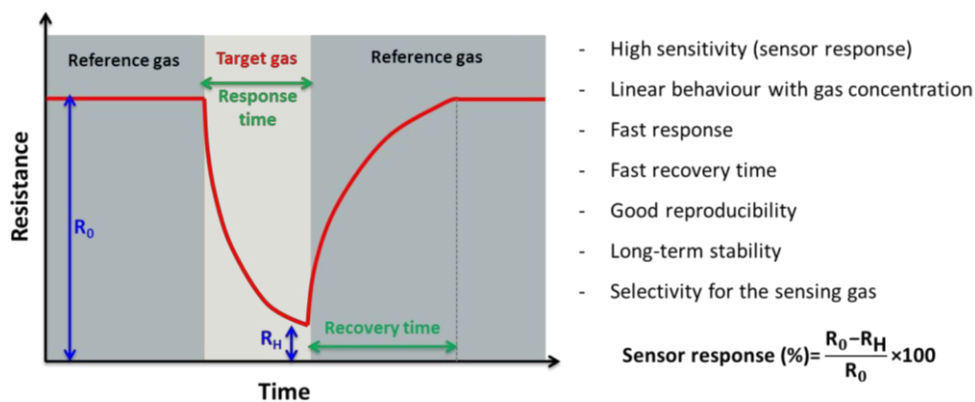


Figure B.9 Scheme of the resistance vs time curve for a sensing material when reference gas flows through the chamber and sudden injection of the target gas occurs. Important parameters in the sensing response are marked in the figure. On the right the formula used to calculate the sensor response and the important requirements a sensing device must meet are listed.

B.3 Photoelectrochemistry in anodic oxides: clean H₂ production

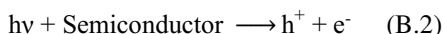
Photoelectrochemistry deals with the electrochemical current produced when one shines light onto a photo-responsive electrode in solution. There are two major interests in photoelectrochemistry studies [201]. The first concerns its fundamentals. The absorption of light is related to the energy gap in a semiconductor electrode; the incoming light must contain photons energetic enough to pump electrons up from the valence band to the conduction band. Photocurrent measurements as a function of the incident light wavelength

provide knowledge on the magnitude of the electrode energy gap (E_g) and its nature; direct or indirect. The second and most important aspect of photoelectrochemistry is its application in photoelectrochemical splitting of water for hydrogen and oxygen production. A clean way of hydrogen production to spread its use as fuel is now one of the main research topics to face the exhaustion of the fossil fuels and mitigate the release of gases contributing to the greenhouse effect [202,203].

B.3.1 Fundamentals of semiconductor photoelectrochemistry

B.3.1.1 Photoexcitation of electrons by light absorption in semiconductors

If light of a frequency ν , with $h\nu \geq E_g$, hits on a semiconducting material, it can promote an electron from the valence into the conduction band. This results in a delocalized electron in the CB, leaving behind a delocalized hole in the VB, so that an electron-hole pair is created [204] in agreement with reaction (B.2).



In the Introduction Chapter in Part A, we represented the bands of a semiconductor in a simplified way, only the vertical axis was labelled with energy but the horizontal one (spatial) remained unlabelled. Although the energy of a free electron is proportional to the square of its momentum, in real crystalline solids with a certain lattice periodicity, it is not simply proportional to the square of the momentum but also to the square of the wave vector, k . When bands of allowed energy are plotted against the wave vector, k , they are usually not flat and the valence and conduction bands present several minimum and maximum values. The top of the valence band and the bottom of the conduction band do not

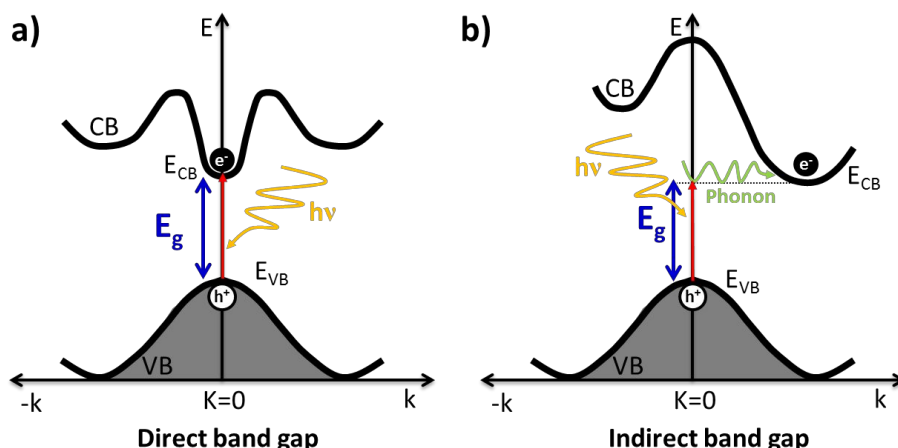


Figure B.10 Schematic representation of the band structure of a) direct band gap semiconductor and b) indirect band gap semiconductor, where transition of the electron from the VB to the CB is mediated by both a phonon and an electron. From reference [204].

lie necessarily at the same value of the electron momentum (k) [204]. If the top of the valence band and the bottom of the conduction band occur at the same value of momentum, the semiconductor has a direct band gap, as shown in Fig. B.10a. On the contrary, in an indirect band gap semiconductor, the maximum energy of the valence band occurs at a different value of momentum compared to the minimum in the conduction band. In this situation, to move an electron from the valence band to the conduction band, a photon and a phonon are required (Fig. B.10b), being a phonon a mechanical vibration that heats the crystal lattice. This process involves two steps so, in general, the chance to occur will be smaller than for a direct transition and in consequence, the efficiency of the light absorption will be lower and the penetration depth of the light ($1/\alpha$) larger [204]. This has important implications when semiconducting materials are meant to be used in photoelectrochemical water splitting or photovoltaic devices.

The absorption coefficient α near the band edge for these optical transitions depends on the photon energy according to:

$$(\alpha h\nu)^n = A'(h\nu - E_g) \quad (\text{B.3})$$

where A' is a constant of proportionality that depends on the transition probability and n takes a value of 2 for a direct band gap transition and $1/2$ for an indirect one [202,205].

B.3.1.2 Photoelectrochemistry at the semiconductor electrode | electrolyte interface

The band bending of a semiconductor | electrolyte interface in equilibrium with an electrolyte solution was described in section A.2 from the Introduction in Part A. For a n-type semiconductor at open circuit potential, the Fermi level is typically higher than the redox potential of the electrolyte, and hence electrons are transferred from the electrode into the solution [49]. Therefore, there will be a positive charge associated with the space charge region, and this is reflected in an upward bending of the band edges (Fig. B.11a).

If such semiconductor | electrolyte interface is illuminated, photons with energy larger than the band gap are absorbed and electron-hole pairs are generated, both in the bulk and in the space charge regions within the semiconductor as shown in Fig. B.11b. In the space charge region of the semiconductor, the pair can be separated by the electric field to prevent recombination. The direction of the electric field at the interface is such that the minority carriers (holes in this case) are driven towards the surface, where they can react with a suitable redox partner and generate a photocurrent, while the electrons migrate to the electronic circuit and afterwards to the counter electrode to contribute to the reverse redox reaction [205]. The migration of photoexcited electrons and holes induces in the electrode an inverse potential which reduces the potential across the space charge layer and retards the migration of electrons and holes in the opposite direction as shown in Fig. B.11b [47]. This inverse potential, induced by photoexcitation, is called the photopotential (ΔE_{photo}). Since the

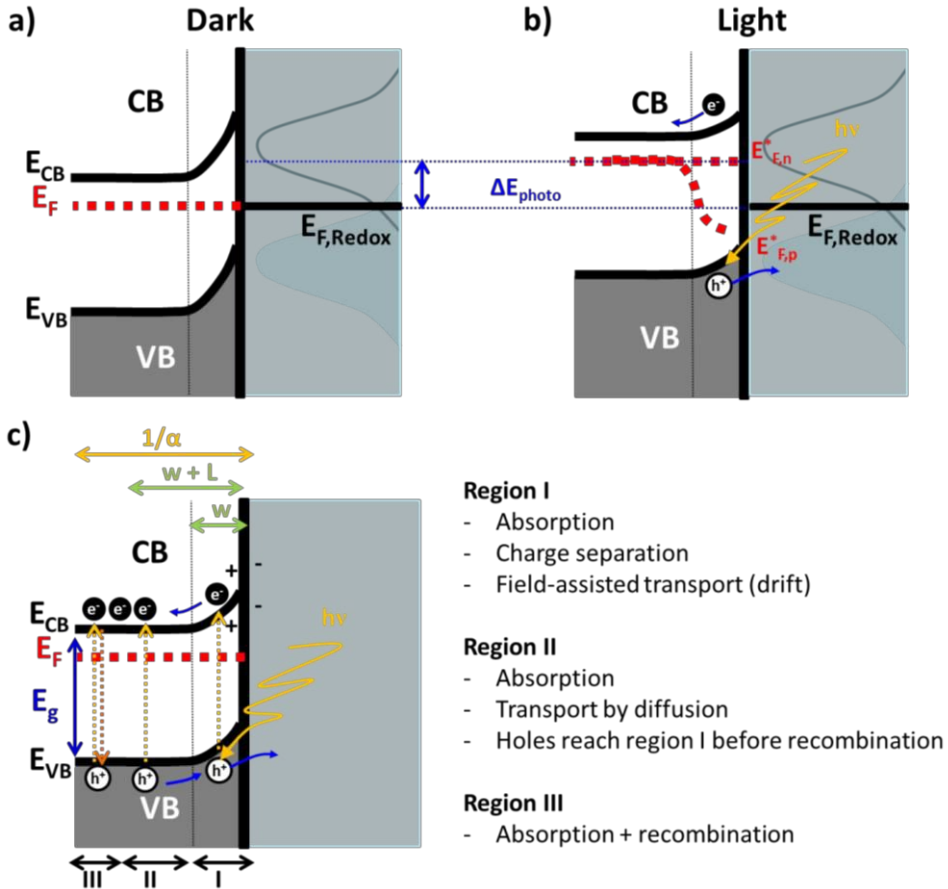


Figure B.11 Band diagram for a n-type semiconductor | electrolyte in equilibrium a) in the dark and b) under illumination. Illumination raises the Fermi level and decreases the band bending. Near the semiconductor/electrolyte interface, the Fermi level splits into quasi-Fermi levels for the electrons and holes. c) Schematic representation of the absorption regions in a semiconductor | electrolyte interface under illumination. L accounts for the diffusion length, w the thickness of the space charge region and $1/\alpha$ the penetration depth of the light. Adapted from references [203,204].

photopotential, reduces the potential across the space charge layer, the E_F of the semiconductor interior rises by an energy ΔE_{photo} . It must be noticed that in a photoexcited semiconductor there is no longer a thermal equilibrium, so the use of a single Fermi level is not appropriate. Instead, the concept of a quasi-Fermi level, E_F^* , is introduced. Under photoexcitation, the E_F^* of the majority charge carriers (e.g. electrons in n-type semiconductor) remains close to the original E_F but the E_F^* of the minority charge carriers (e.g. holes in n-type semiconductor) shifts away (Fig. B.11c). Since photoexcited electron-hole pairs are formed only within a limited depth from the semiconductor surface, the photon-induced split of the E_F into the E_F^* of electrons and holes occurs only in a surface layer of limited depth [47].

As already mentioned, the minority charge carriers are driven towards the semiconductor surface where they can react with a suitable redox partner and generate a photocurrent. This photocurrent is given by Eq. (B.4):

$$I_{ph} = eI_0 \left[1 - \frac{e^{-\alpha w}}{(1+\alpha L_p)} \right] \quad (\text{B.4})$$

where α is the absorption coefficient, w the length of the space charge region and L_p the diffusion length of holes (minority carriers) [47]. This equation presumes that each photon absorbed creates an electron-hole pair; if there are other absorption mechanisms, the right-hand side must be multiplied by the quantum efficiency [204].

The extent of collection of minority carriers from the region beyond the depletion layer is dictated by the diffusion length, L , defined in expression (B.5):

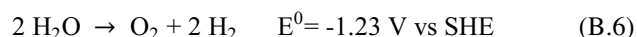
$$L_p = \sqrt{kT\mu_p\tau_p} \quad (\text{B.5})$$

where μ_p is the hole mobility and τ_p is the hole life-time [202]. The characteristic length L_p defines the region within which electron-hole pair generation is fully effective. Pairs generated at depths longer than the diffusion length will simply recombine (Fig. B.11c). Thus, the effective light-induced generation of charge carriers for a given interface will depend on the relative magnitudes of L_p and the light penetration depth, $1/\alpha$.

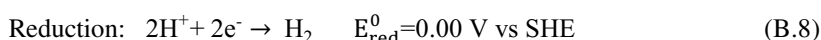
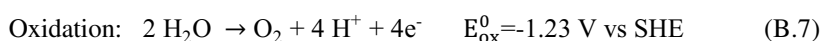
B.3.2 Applications of photoelectrochemistry: photoelectrochemical water splitting

Hydrogen is considered one of the most promising clean non-fossil fuels because when combined with oxygen in a fuel cell, electricity can be produced with water as the only final product [202,203,206,207]. However, many issues still need to be solved to spread its use as a common fuel. First, hydrogen needs to be generated in a cheap and environmentally-friendly manner, so that, the current method based on natural gas reforming, which is limited by the finite reserves of fossil fuels and leads to carbon dioxide as a side product, should be replaced by a cleaner strategy [202]. Second, given that its storage and transportation are not easy, more research is required to find safe ways to do it or develop *in situ* production methods to indirectly alleviate these limitations [202,207]. Among all the emerging hydrogen generation strategies, nowadays, photoelectrochemical water splitting is capturing most of the attention. The first report on photoelectrochemical water splitting dates back to the 1970s when Fujishima and Honda demonstrated that H_2 generation was possible by the illumination of a TiO_2 photo-anode connected to a platinum cathode [208]. After that initial work, several semiconductors have been explored and also new photoelectrochemical cell configurations.

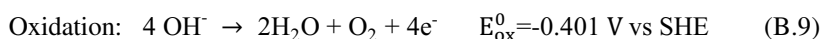
Photoelectrochemical water splitting, also called photoelectrolysis, uses the light collected at a semiconductor photoelectrode to provide the energy required to split water into H_2 and O_2 according to reaction (B.6). Under standard conditions (298 K, 1 bar and 1 mol/L), the process is thermodynamically endothermic ($\Delta G \sim 237.2$ KJ/mol) and requires a minimum potential of 1.23 V to proceed [202,203,206,207].



In an acid environment, the overall reaction can be separated into its corresponding oxidation and reduction half-cell reactions (B.7) and (B.8) [202].



Whereas for an alkaline electrolyte, the oxidation and reduction reactions can be written as (B.9) and (B.10) [203].



The most common photoelectrochemical cell configuration uses a n-type semiconductor as photoanode and a metal as cathode as described in the scheme in Fig. B.12a. Here, the photo-generated holes from the valence band react with water to form gaseous oxygen as described in equation (B.11). At the same time the photo-generated electrons in the conduction band travel through the external circuit to the counter electrode or cathode where protons are reduced to hydrogen (reaction (B.12)). Generally, the counter electrode is made

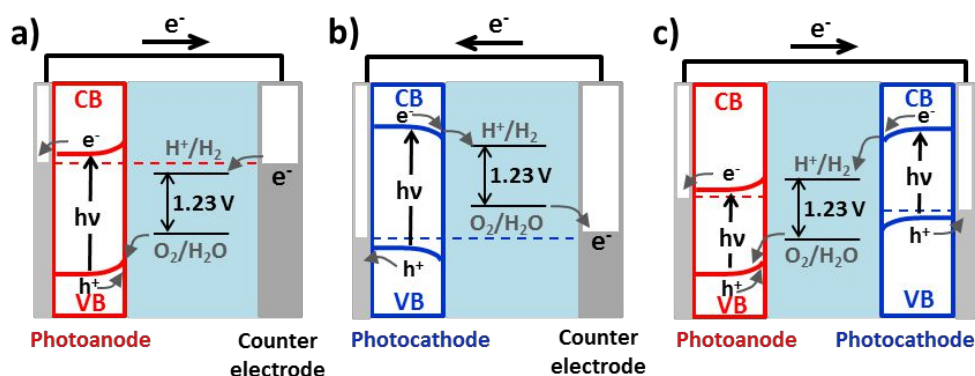
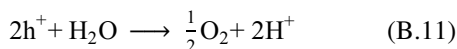


Figure B.12 PEC water splitting cells using a) a photoanode, b) photocathode and c) photoanode and photocathode in tandem configuration. From ref [206].

of a corrosion resistant metal like Platinum [203]. A reference electrode (not included in the scheme in Fig. B.12) is used to control the applied electrochemical potential.



Although this is the most standard PEC, other configurations are also possible. For instance, a p-type semiconductor photocathode that reduces H^+ into H_2 upon solar irradiation while oxygen is evolved at the metal anode (Fig. B.12b) or a cell that contains two photoactive semiconductors in a tandem arrangement (Fig. B.12c) [202,203,206].

Most of the requirements for a suitable water splitting photoanode or photocathode can be summarized as follows [203]:

- Good visible absorption: the spectral region in which the semiconductor absorbs is determined by the E_g of the material. The minimum E_g required to split water is 1.9 eV (considering losses and overpotentials) which corresponds to an onset at 650 nm [203]. Below 400 nm the intensity of the sunlight drops rapidly imposing an upper limit of 3.1 eV (see Fig. B.13a). Semiconductors with a direct E_g are preferred over indirect. In indirect band gap materials, recombination rates are much higher as most electron-hole pairs are generated far from the interface due to their low absorption coefficient.
- Chemical stability in the dark and under illumination: this is a critical requirement in nonoxide semiconductors as they either dissolve or form a thin oxide layer that hinders charge transfer across the semiconductor | electrolyte interface. Oxide semiconductors are more stable, but may be prone to anodic or cathodic decomposition. In general, the stability against (photo)corrosion increases at higher band gaps [203].
- Band edge positions that straddle the water reduction and oxidation potentials: A necessary condition for the spontaneous water splitting is that upon illumination the semiconductor conduction band edge should be more negative relative to the reduction potential of water, whereas the valence band edge needs to be more positive compared to the oxidation potential (Fig. B.13b) [202,203,206]. There are very few semiconductors that fulfil this requirement and usually the ones that do, have a very large band gap, like SiC, or are unstable in aqueous solution such as CdS [203]. In many semiconductor-electrolyte systems the conduction band edge is more positive than the reduction potential of water (see Fig. B.13b). In consequence, the generated photovoltage is less than 1.23 V and an external bias is necessary [202,203].
- Efficient charge transport in the semiconductor: here we can distinguish between intrinsic and extrinsic charge transport factors. Intrinsic factors depend on the electronic band structure of the material. For instance, the overlap between 3d orbitals

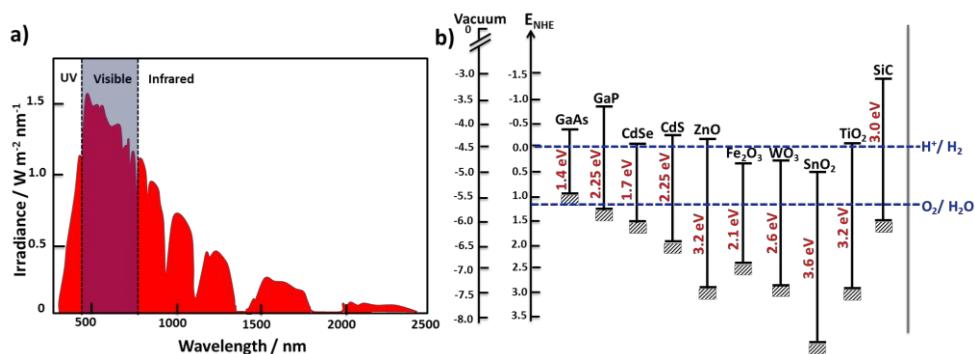


Figure B.13 a) Solar spectral irradiance (global AM1.5) and b) band edge position of several semiconducting materials in contact with an aqueous electrolyte at pH =1. Adapted from references [202,203].

usually leads to high electron mobility, whereas the overlap between O-2p orbitals determines the hole mobility in semiconductor oxides [202]. Extrinsic factors like shallow donors/acceptors and recombination centres are even more important. For example, in undoped Fe_2O_3 electron transport is the rate limiting step, while after donor doping with silicon it is the hole transport [202].

- Low overpotentials for reduction and oxidation of water: charge transfer across the semiconductor | electrolyte interface has to be fast to prevent corrosion and reduce the energy losses due to overvoltage [202,203]. Moreover, accumulation of charge carriers at the surface decreases the electrical field and favours electron-hole recombination.
- Low cost

B.3.3 Photoelectrochemical characterization: measurement configurations and setup

Photocurrent measurements are the main tool for investigating the properties and performance of photoelectrodes. Two main experimental configurations can be distinguished, based on the type of light source used: one for measuring wavelength-dependent properties using a monochromatic light source and the other for performance and stability measurements under high intensity white light [203].

B.3.3.1 Photocurrent at variable wavelength

By measuring the photocurrent as a function of wavelength, insights on the factors that limit the performance of a photoelectrochemical device or photoelectrode can be obtained. A

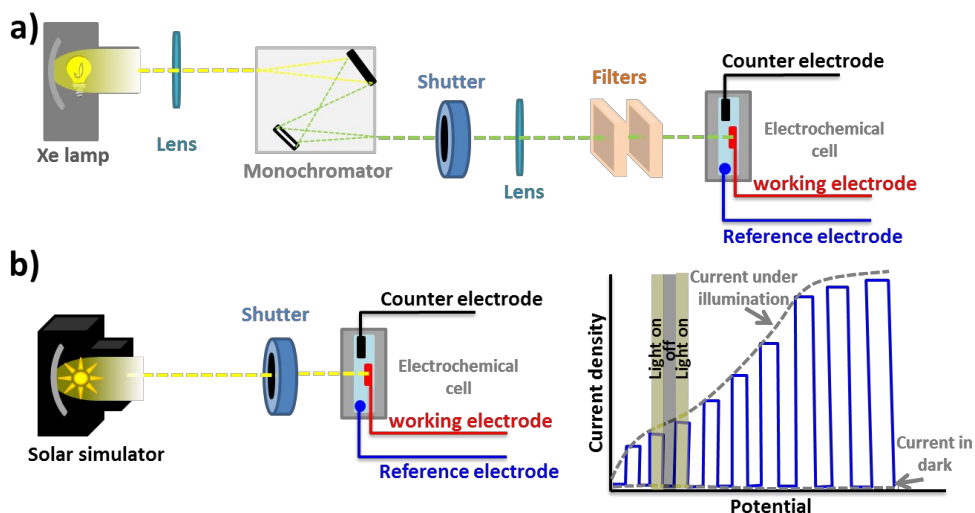


Figure B.14 Schematic representation of the setup required for a) wavelength dependent photoelectrochemical measurements and b) measurements under chopped light in a solar simulator and photoresponse under chopped light or constant illumination conditions for a n-type semiconductor.

typical setup for such measurements is shown in Fig. B.14a. The light source is a tungsten halogen or gas discharge (e.g., Xe) lamp, and a monochromator is used to filter out a narrow part of the spectrum centred on the wavelength of interest. An electromechanical shutter is used to control the exposure of the sample to the light, and optical lenses are used to properly focus the light onto the monochromator and the sample. It must be noticed that for this measurements the light intensities are 2-4 orders of magnitude lower than the $100 \text{ mW}\cdot\text{cm}^{-2}$ one gets with a solar simulator. The potential of the sample is controlled by a potentiostat, which also measures the current. The intensity of the incident light is measured with a calibrated photodiode and an internal calibration curve that reports the incident light intensity for a single wavelength is obtained. With this, it is possible to calculate the incident photon to current conversion efficiency (IPCE). The IPCE is the fraction of the incident photons that is converted to electrons. According to this, the expression used to calculate its value for a certain wavelength is given by (B.13):

$$IPCE_{\lambda} (\%) = \frac{I}{P} \times \frac{1240}{\lambda} \times 100 \quad (\text{B.13})$$

where I is the photocurrent density (A cm^{-2}), P is the power of the lamp ($\text{W}\cdot\text{cm}^{-2}$), and λ the wavelength (nm). For a direct band-gap semiconductor, the E_g can be obtained by plotting $(IPCE \text{ vs } h\nu)^2$ versus $(h\nu)$ and extrapolating the linear region of the plot to the energy axis at $(IPCE \text{ vs } h\nu)^2=0$. For an indirect band gap, the procedure is equivalent but using $(IPCE \text{ vs } h\nu)^{1/2}$.

B.3.3.2 Photoelectrochemical performance: measurements under simulated sunlight

The ultimate test for any photoelectrochemical device or individual photoelectrode is its performance under solar irradiation (100 mW cm^{-2} , which corresponds to 1 sun at AM1.5). Fig. B.14b shows an overview of the main components for a photoelectrochemical experimental test setup featuring simulated sunlight. A potentiostat is used to control the sample's potential and to measure the current, and an electromechanical shutter is used to block the light for chopped-light experiments. A calibrated solar cell or photodiode is used to verify that the intensity of the solar simulator at the sample position corresponds to the desired value.

Current-voltage characteristics are measured by sweeping the potential of the PEC cell and measuring the corresponding current. This is called dark current, and if the same experiment is carried out under illumination then the photocurrent is obtained. The current-voltage curve can be acquired also by alternatively illuminating the sample as shown in Fig. B.14b.

Chapter 3

Development of anodic self-ordered tin oxide nanochanneled structures

This chapter is devoted to the preparation of self-ordered tin oxide nanochanneled structures by anodization in a two-electrode configuration. The basic principles of this electrochemical approach together with state-of-the-art in the particular case of tin were discussed in Section B.1 from the Introduction. In the following chapters, these anodic layers will be further characterized and tested in applications such as H₂ gas sensing or as support material for photoelectrochemical water splitting anodes.

3.1 Specific goals of this chapter

- Find an alternative electrolyte to the conventional oxalic acid and NaOH-based solutions for the preparation of porous/nanotubular oxide structures on Sn.
- Optimize the composition of the newly developed electrolyte to attain nanostructures without inner cracks on its cross-section and top-open pores.

3.2 Results and discussion

Electrolytes commonly employed in self-ordering anodization of other metals like Ti, Al, Zn, *etc.* were tested for tin anodization. For each electrolyte, we carried out a fast screening of some critical parameters like the applied voltage, the temperature, and the concentration

of the species in order to determine their potential to achieve promising nanoporous or nanotubular structures.

3.2.1 Phosphoric acid-based solutions

Phosphoric acid (H_3PO_4) containing electrolytes are typically used to prepare self-ordered Al_2O_3 nanoporous structures [147,127,161]. Also, it has been exploited for the anodization of other metals like titanium but with the addition of a fluoride source such as sodium fluoride (NaF), ammonium fluoride (NH_4F), or hydrofluoric acid (HF) [209]. As a starting point, a solution containing 20 % wt. H_3PO_4 in ethylene glycol was employed. Under voltages of 10 and 30 V, a compact layer was observed. However, by applying higher potentials, as depicted in Fig. 3.1a for 50 V, rough surfaces that seem to be composed of either precipitates or cracked oxide layers were obtained. To avoid these cracked structures we decided to use voltages below 10 V, which were found to form compact layers, in combination with a potential driving force to induce the oxide dissolution required for the growth of self-ordered structures. In this view, two different strategies were followed: (i) increase the temperature or (ii) add an agent like fluorides, well-known promoters of the oxide dissolution.

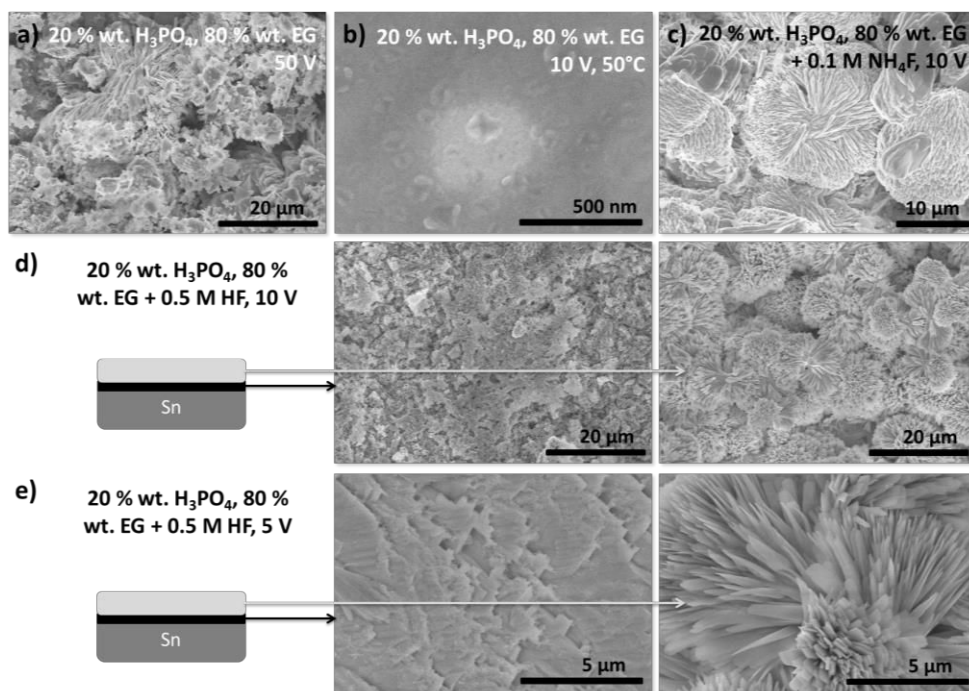


Figure 3.1 FESEM images of samples prepared by anodizing Sn foils in 20% wt. H_3PO_4 in ethylene glycol solution a) at room temperature and 50 V, b) 10 V and 50 °C, and c) at 10 V after adding 0.1 M NH_4F . d) and e) show the scheme of the layered structures formed in 20 % wt. H_3PO_4 solutions in ethylene glycol containing 0.5 M HF and the corresponding FESEM images for anodization potentials of d) 10 V and e) 5 V.

Fig. 3.1 b shows the morphology of a sample anodized at 10 V and 50 °C. In such conditions, a compact oxide layer is again formed, but presents several pyramidal pits due to its localized corrosion. Higher temperatures, up to 80 °C were attempted, but lead to comparable results. So, apparently an increase in the anodization temperature does not enhance the equilibrium situation required for the growth of self-organized structures. When a fluoride-containing species like ammonium fluoride was incorporated in the H_3PO_4 /Ethylene glycol solution, dissolution of the metal and subsequent formation of precipitates occurred (Fig. 3.1c). For other fluoride sources like HF, which lowers considerably the pH of the solution, the dissolution of the Sn electrode and the formation of precipitates becomes more evident (Fig. 3.1d). In fact, the as-formed layer on the Sn electrode clearly shows a dual structure. On the top, in close contact with the electrolyte, a whitish film composed of flower-like precipitates is found (right image in Fig. 3.1d). This layer can be easily detached from the rest of the substrate given its bad adhesion and the blackened surface underneath can be then examined by FESEM. This bottom surface is inhomogeneous and seems to be significantly roughened by the metal dissolution (left image in Fig. 3.1d). Defined dissolution planes and step edges resembling the teeth of a saw (left SEM image in Fig. 3.1e) could be distinguished when lower potentials (5 V) were used. At 5 V, the flower-like structures were also sharper probably because their growth rate is slowed

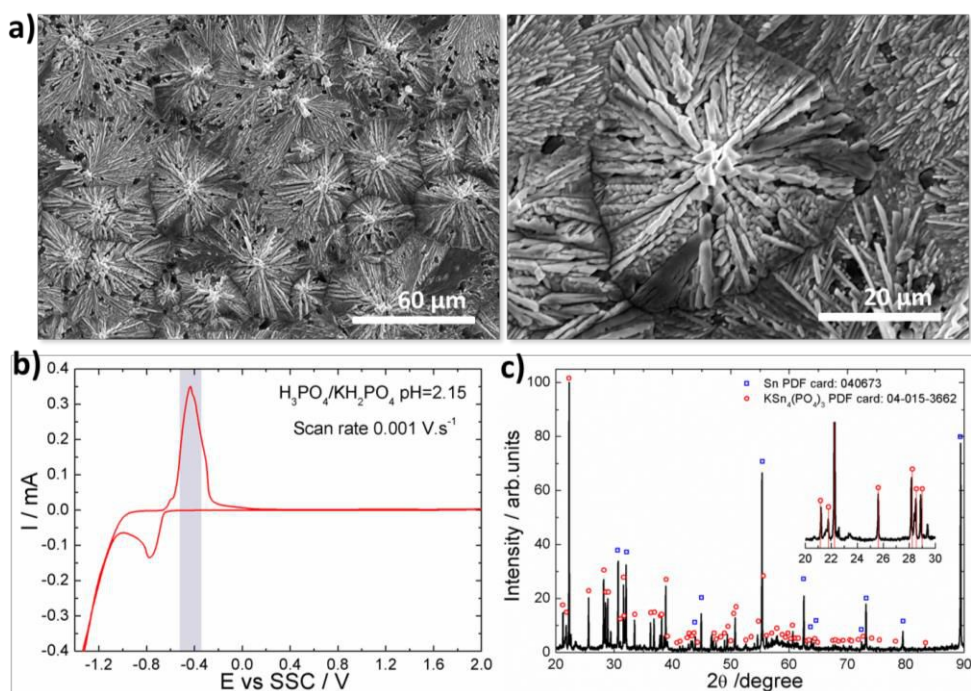


Figure 3.2 a) Low and b) high magnification FESEM images of samples prepared in a $\text{H}_3\text{PO}_4/\text{KH}_2\text{PO}_4$ buffer solution (pH=2.15) by applying a potential of -0.5 V vs SSC for 1800 s. b) Cyclic voltammetry of a tin electrode immersed in the phosphate buffer solution. The grey region indicates the range of potentials where samples with the morphology shown in a) and b) are obtained. c) XRD diffraction pattern of samples in a). The crystalline peaks are associated to the $\text{KSn}_4(\text{PO}_4)_3$ phase.

down (right image in Fig. 3.1e). The composition of these flower-like structures was not studied in detail, but they resemble the tin phosphate species precipitated when studying tin electrochemistry in acidic phosphate buffer (see Fig. 3.2 for comparison).

In these phosphoric-acid based electrolytes, no equilibrium between passivation and dissolution could be achieved, which is the key for the preparation of self-ordered oxide structures. Furthermore, the appearance of precipitates, probably tin phosphates, which accumulate at the electrode surface, is a major drawback. Considering the above-mentioned facts, other electrolytes were investigated.

3.2.2 Ammonium nitrate in ethylene glycol

Organic-based ammonium nitrate (NH_4NO_3) electrolytes have shown to provide highly aligned pore channels in many metals like W, Ta, Ti, Nb and alloys such as TiNb [134,136,138]. As a first approach for tin anodization in this kind of electrolytes, we used a solution of 0.2 M NH_4NO_3 in ethylene glycol. Fig. 3.3 shows the micrographs of Sn substrates anodized in this solution during 3600 s at increasing anodic potentials. At 5 V, no oxide layer was formed and just metallic Sn with the scratches from the original rolling process could be observed (Fig. 3.3a). On the contrary, at 10 V a random porous network could be noticed under an inhomogeneous top structure (Fig. 3.3b and higher magnification in Fig. 3.4b), analogous to the grass in TiO_2 long-duration anodization experiments. If anodization time is reduced to 1800 s, the porous structures become more evident (Fig. 3.4a). At larger potentials (20-50 V), the films showed significant cracks caused by physical breakdown of the oxide film (Fig. 3.3c-f). The cross-sectional view of these broken parts revealed an obvious nanochanneled structure as given in Fig. 3.3e.

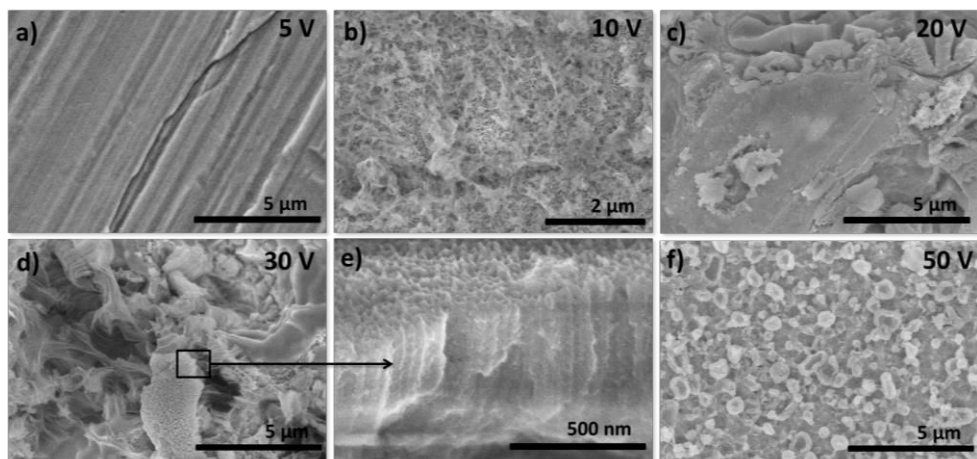


Figure 3.3 FESEM micrographs of anodized tin substrates in a 0.2 M NH_4NO_3 in ethylene glycol solution for 3600s at a) 5 V, b) 10 V, c) 20 V, d) and e) 30 V, and f) 50 V.

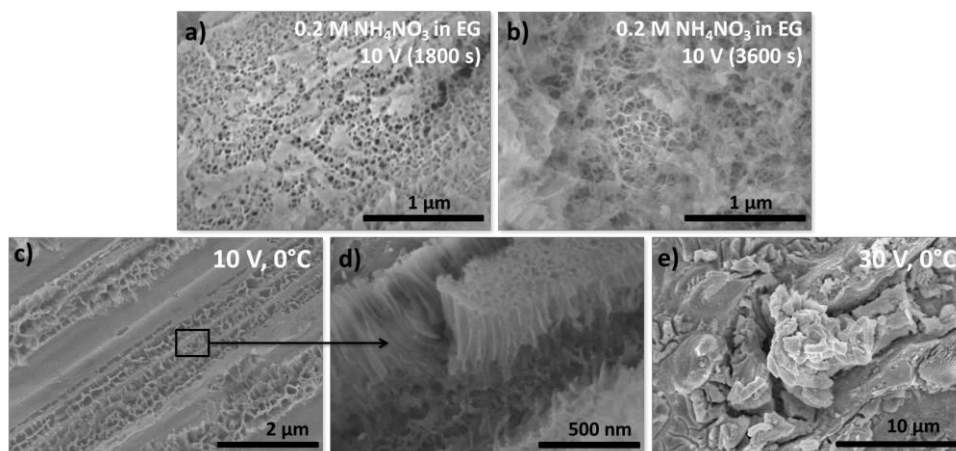


Figure 3.4 FESEM micrographs of tin substrates anodized at 10 V in a 0.2 M NH_4NO_3 in ethylene glycol solution for a) 1800 s and b) 3600 s. At lower anodization times the porous structures can be better appreciated because the presence of this inhomogeneous top structure is reduced. FESEM images of Sn foils anodized in the same electrolyte by cooling down the substrate at 0 °C. c) and d) were anodized at 10 V for 17 h, while e) at 30 V for 3600 s.

A possible way to reduce the cracking phenomena would be to decrease the anodization temperature. This should not only slow down the oxide formation process and consequently reduce the stress in the film, but also prevent Joule heating. In Fig. 3.4c-e, the morphologies of the oxide films prepared in a 0.2 M NH_4NO_3 in ethylene glycol solution by cooling down the Sn substrate at 0 °C are displayed. At 10 V, inhomogeneous layers that alternate porous areas showing tubular-like structures with compact regions are grown even for very long anodization times, *i.e.* ~ 17 h (Fig. 3.4c and 3.4d). If the potential is raised to 30 V, cracked layers are formed at anodization times of 3600 s, as occurred when anodizing at room temperature (Fig. 3.4e). Hence, at 30 V, lower temperature do not prevent the oxide cracking.

Addition of ethanol during aluminium anodization in H_3PO_4 has proven to be useful to reach well-defined structures because it accelerates the diffusion of heat generated at the oxide layer and lowers the local acidity [210]. Based on these assumptions, increasing amounts of ethanol were added to the ammonium nitrate solution when anodizing tin at 30 V (Fig. 3.5). Apparently, the incorporation of ethanol reduced the presence of cracks, although they could not be completely avoided. At 5 % ethanol, it can be seen that the cracking phenomena seems to begin by dissolution at the grain boundary regions, also referred to as intergranular corrosion (Fig. 3.5b). Samples containing 10 % ethanol (Fig. 3.5e and 3.5f) showed less cracks and a top open porous morphology.

Further experiments were carried out by (i) incorporating a percentage of water in the electrolyte, as in some metals a certain amount of water in the electrolyte is essential for the development of the ordered nanostructures; (ii) decreasing the concentration of ammonium

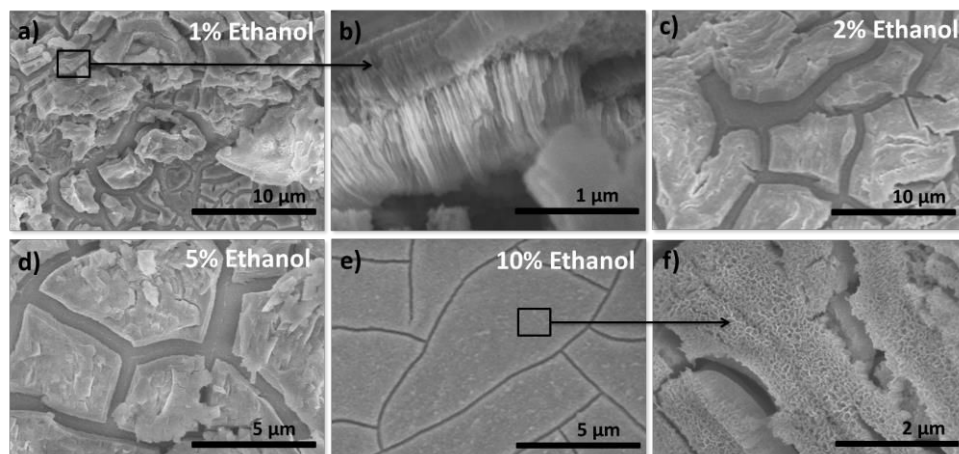


Figure 3.5 FESEM micrographs of tin substrates anodized at 30 V in a 0.2 M NH_4NO_3 in ethylene glycol solution for 1800 s containing different percentage of ethanol: a) and b) 1 %, c) 2 %, d) 5 % and e) and f) 10 %.

nitrate to slow down the growth rate; or even (iii) using galvanostatic conditions to limit the maximum current. None of them led to promising self-ordered structures and all the films showed cracks from breakdown phenomena. Given that the strategies proposed to avoid it were not successful, we decided to try other possible anodizing solutions.

3.2.3 Alkaline electrolytes: ammonia and sodium carbonate

Ono *et al.* reported that tin nanoporous structures could be achieved by anodizing tin foils in sodium hydroxide (NaOH) solutions [191]. Based on the hypothesis that alkaline media favours the growth of tin oxide but at the same time promotes its dissolution and self-organized structures are totally possible, other alkaline electrolytes such as ammonia (NH_3) or sodium carbonate (Na_2CO_3) were assessed. Fig. 3.6a shows the top and cross-sectional view of a tin foil anodized in 0.1 M NH_3 solution in water at a potential of 5 V. Although channels can be clearly distinguished in the cross-sectional view, the top of the oxide is totally clogged. At 10 V, again compact top surfaces were obtained though the channels seemed to be more defined (Fig. 3.6b and 3.6c). Unfortunately, if higher potentials were applied to reach top-open pores, then numerous inner cracks appeared leading to undesired discontinuities in the cross-section.

Sodium carbonate solutions also present an alkaline pH, so anodization of tin foils in 0.1 M of such solutions was attempted (Fig. 3.6d-f). At low potentials, 5 V, surfaces did not reflect exposed pores despite the channels observed in the cross-sectional view (Fig. 3.6d). At 10 V, a comparable trend was observed together with some localized pitting corrosion on the oxide surface (Fig. 3.6e). At potentials of 20 V, the oxide surface was still clogged but totally full of corrosion pits (Fig. 3.6f).

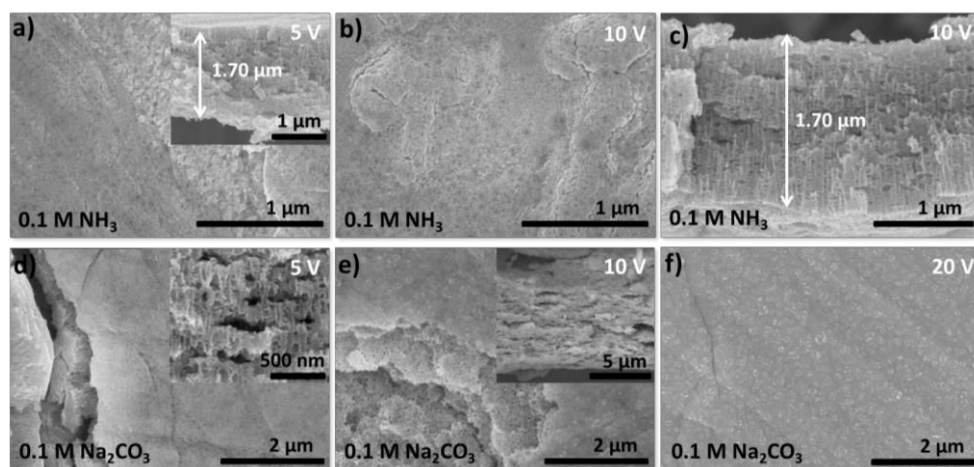


Figure 3.6 FESEM images of the top morphology of Sn foils anodized in 0.1 M NH_3 solutions for 600 s at a) 5 V and b) 10 V. Inset in a) and c) correspond to the cross-sectional views of both samples. d) FESEM top-view and cross-section (inset) of Sn foils anodized in 0.1 M Na_2CO_3 solutions for 600 s at d) 5 V, e) 10 V and f) 20 V.

Of course, these two electrolytes could still offer a lot of possibilities and parameters to play with, namely, concentration, temperature, organic content, *etc.* However, they are based in the same principle as NaOH (alkaline dissolution) and they do not introduce any real novelty. Moreover, from the experiments shown in Fig. 3.6 we can infer that equivalent problems as in NaOH are encountered: either clogged top morphologies are obtained in soft conditions (low potentials) or cracks in the cross-sections for higher potentials and concentrations. There seems to be no real intermediate point where one can reach top open pores without inner cracks.

3.2.4 Sodium sulphide and ammonium fluoride solutions

An electrolyte based on sodium sulphide (Na_2S) and ammonium fluoride (NH_4F) has been recently reported to effectively form self-ordered ZnO structures upon anodization of Zn foils [211]. Shrestha *et al.* used compositions ranging from 0.0125 M – 0.025 M for NH_4F and 0.1 M – 0.2 M for Na_2S and potential of 30 V. As a first attempt, we used a solution of 0.2 M Na_2S and 0.1 M NH_4F in water and a potential of 10 V, because, as seen for other electrolytes, usually very high potentials do not work well for Sn and induce too much cracking on the final oxide film. Fig. 3.7 shows the morphology of the as-anodized layer in this electrolyte. The surface displays random top-open pores (Fig. 3.7a), something that could not be completely achieved in the case of ammonia or sodium carbonate electrolytes. The cross-sectional view depicted in Fig. 3.7b, however, still presents stacked layers and cracks due to the fast oxide growth and not very well-defined channels (detail in Fig. 3.7c). In order to reduce the growth speed and reach the desired self-organized structures, we properly tuned the electrochemical conditions as will be discussed in the following lines.

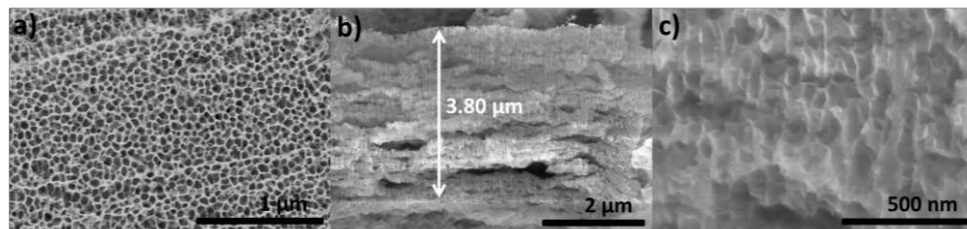


Figure 3.7 FESEM a) top-view and b) cross-section images of Sn foils anodized at 10 V in a 0.2 M Na_2S and 0.1 M NH_4F solution in water for 300 s. Image in c) shows a higher magnification image of the cross-section.

The key to the success of this sulphide-based anodization approach is the fact that sulphides provide an initial passivation layer, which consists of a compact tin-sulphide layer, during the early stages of the anodization process [211]. Such a compact layer is an essential precursor state in triggering an anodic self-organization process. In Fig. 3.8a the top morphology of a porous tin oxide structure formed just in the presence of Na_2S can be observed. This suggests that the Na_2S not only induces passivation of the metallic tin but also provides an alkaline medium where hydroxyl ions contribute to a controlled dissolution of the formed oxide. In the absence of sulphides, no self-organization and complete absence of an oxide layer is observed (Fig. 3.8c).

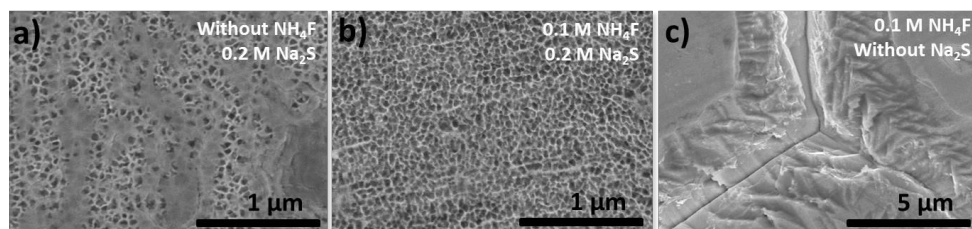


Figure 3.8 Top view FESEM micrograph of as-formed samples anodized at 5 V in a 20 vol. % ethylene glycol - 80 vol. % water mixture containing 0.2 M Na_2S and a) no NH_4F and b) 0.1 M NH_4F . Sample c) was obtained in the same conditions but in absence of Na_2S . Anodization time was 30 min.

The concentration of both Na_2S and NH_4F was firstly optimized to reach equilibrium between passivation and dissolution rates. We found that an increase of the NH_4F concentration up to 0.1 M (by keeping constant the Na_2S concentration around 0.2 M) allows the formation of more open and defined pores at the top of the layer (see Fig. 3.8a and 3.8b, where anodic layers in presence and absence of NH_4F are shown, respectively). Interestingly, other fluoride sources or even chlorides were found to be also successful for achieving self-organization and enhancing opened and defined top-morphologies (FESEM images included in Fig. 3.9). On the other hand, with lower Na_2S concentrations (at constant ~ 0.1 M NH_4F) a black precipitate was formed at the top of the tin substrate.

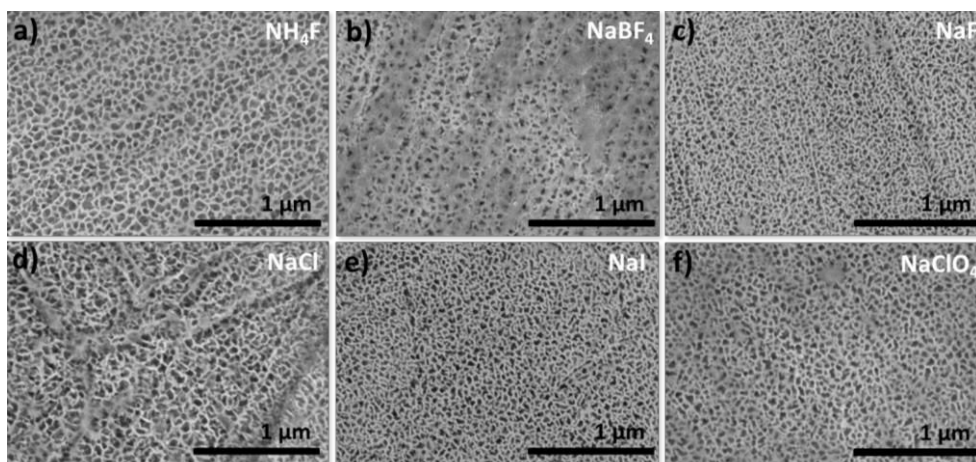


Figure 3.9 Top view FESEM micrograph of as-formed samples after anodization at 5 V in a 20 vol. % ethylene glycol - 80 vol. % water electrolyte containing 0.3 M Na_2S and 0.1 M NH_4F , a) NH_4F , b) NaBF_4 , c) NaF , d) NaCl , e) NaI , and f) NaClO_4 . Anodization time was 30 min.

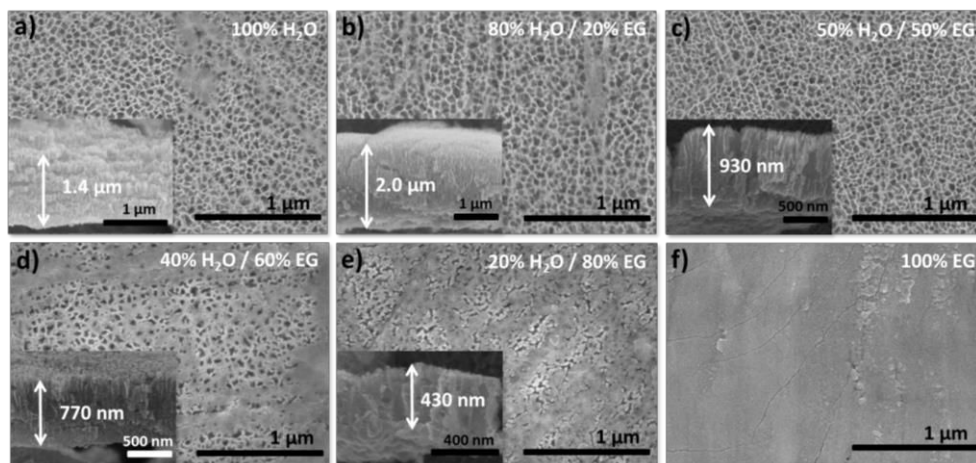


Figure 3.10 FESEM micrographs for the top and cross-sectional (inset) views for samples prepared by anodizing a tin foil at 5 V in 0.2 M Na_2S and 0.1 M NH_4F dissolved in a) 100 vol. % H_2O , b) 80 vol. % H_2O - 20 vol. % ethylene glycol, c) 50 vol. % H_2O - 50 vol. % ethylene glycol, d) 40 vol. % H_2O - 60 vol. % ethylene glycol, e) 20 vol. % H_2O - 80 vol. % ethylene glycol and f) 100 vol. % ethylene glycol. Anodization was performed for 10 minutes.

Anodization in electrolytes with increasing contents of organic solvent was attempted in order to reduce the growth rate and achieve a higher degree of self-ordering together with smoother walls of the channels (see Fig. 3.10). A content of organic solvent around 50 % was shown to be the most optimized percentage (Fig. 3.10c). In fact, with contents of the organic solvent between 60 and 80 %, the pores resulted clogged at the top and the channels were found to be less defined (Fig. 3.10d and 3.10e). On the other hand, only a thin compact oxide film was attained with electrolytes containing an organic content above 80 %

(Fig.3.10f). So, the effect of water in this case is somehow two-fold: on the one side, it is required for the oxide formation (at least 50 % vol.), and on the other, it accelerates too much the process and enhances the evolution of oxygen, both contributing to the formation of stacked layers (Fig. 3.10a). This behaviour is significantly different to other metals like titanium, where anodization with water contents as low as 1 % results in well-defined nanostructures.

Experiments for the optimization of the organic solvent/water content ratio were performed using ethylene glycol as the organic fraction, because it is highly miscible with water and very high percentages can be incorporated without phase separation, yet many other organic solvents are available for this purpose. A screening of the most frequently used organic solvents in self-ordered anodization, *i.e.* glycerol, dimethyl sulfoxide, diethylene glycol, acetonitrile, *etc.* was done (see FESEM images in Fig. 3.11). Amongst them, 2-methyl-1,3-propanediol and acetonitrile seemed to be the most promising since the films presented considerably less inner cracks (Fig. 3.11e and 3.11f, correspondingly).

Fig. 3.12a shows a top-view FESEM image for tin oxide nanochannels attained after 1 min of anodization at 10 V in a 50 % acetonitrile and 50 % water electrolyte containing 0.2 M Na_2S and 0.1 M NH_4F . In this optimized electrolyte composition, the growth of straight and vertically aligned nanochannels with fully open pores can be clearly observed (Fig. 3.12). The channels have a diameter of ~ 100 nm and present a bottom that resembles that of other self-ordered nanotubular or nanoporous structures like in Ti or Al (see detail in the bottom image in Fig. 3.12a). Several ripples along the inner cross-section can be appreciated, most probably induced by the high water content of the electrolyte as occurs in TiO_2 . As discussed previously, lower water contents cannot be used in the particular case of tin. In the presence of 50 % of acetonitrile, the oxide formation rate is significantly reduced in comparison to

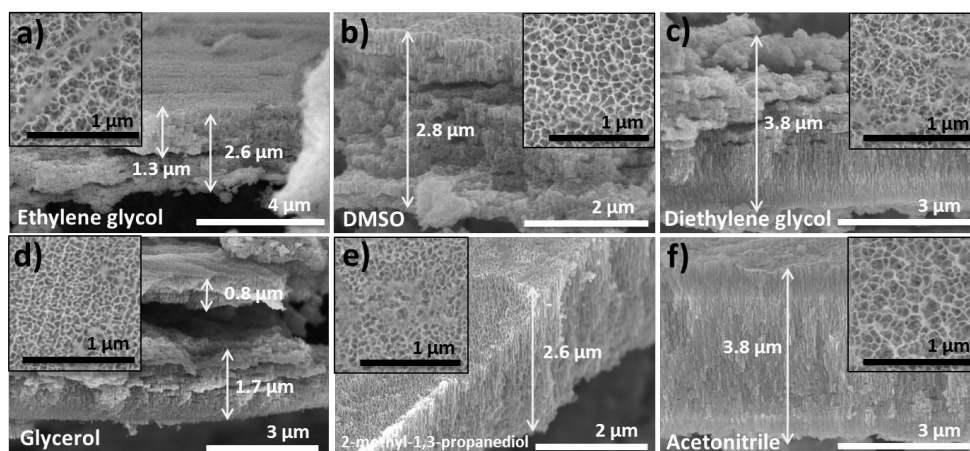


Figure 3.11 Top (inset) and cross-sectional view of as-formed tin oxide samples prepared by anodizing a tin foil at 10 V in 0.2 M Na_2S and 0.1 M NH_4F dissolved in 50 % water and 50 % of a) ethylene glycol, b) dimethyl sulfoxide (DMSO), c) diethylene glycol, d) glycerol, e) 2-methyl-1,3-propanediol, and f) acetonitrile. Anodization time was 600 s.

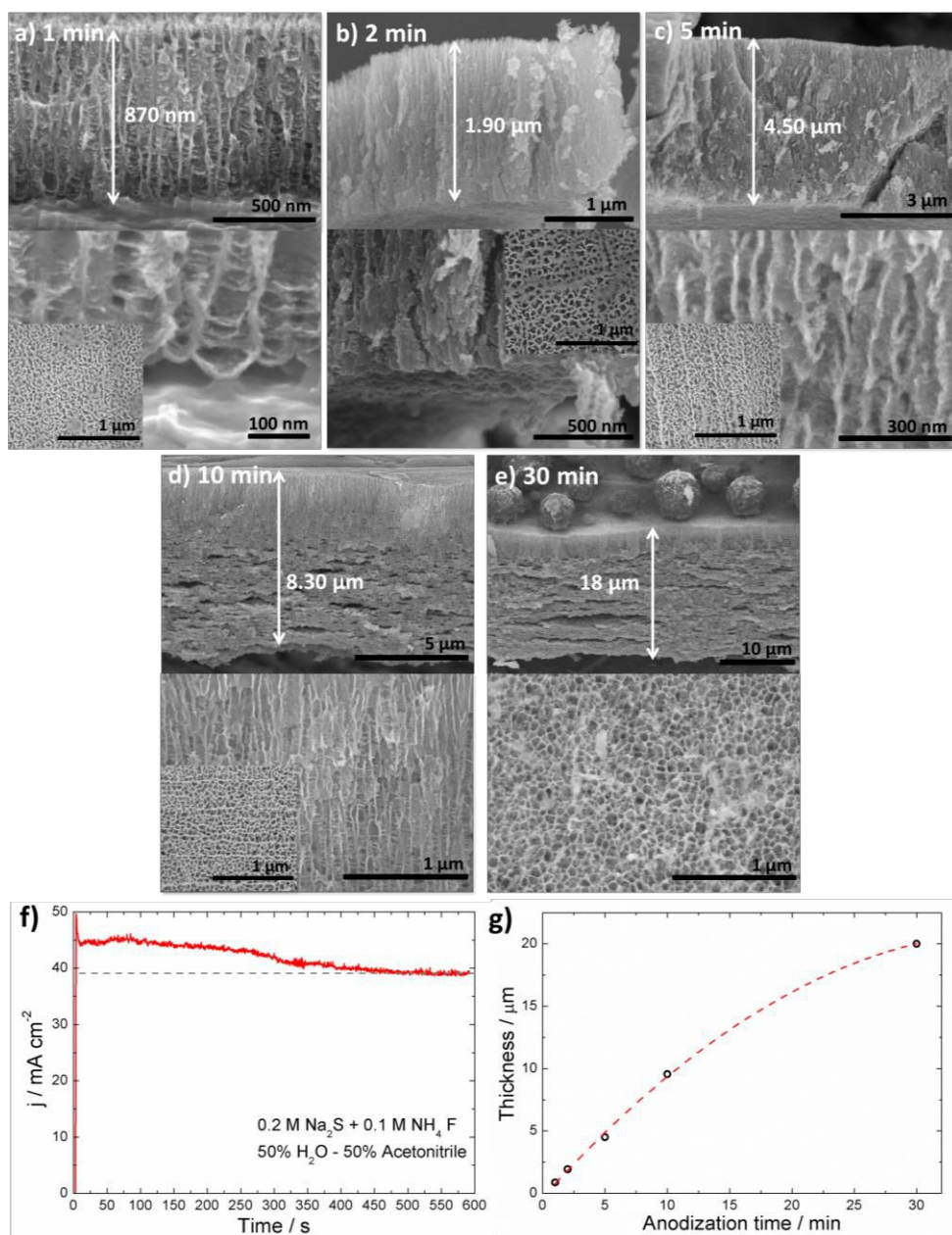


Figure 3.12 FESEM images of the cross-sectional view (left), details of the channels (right) and the top view (inset) of as-formed samples anodized at 10 V in an electrolyte composed of 50 vol. % acetonitrile and 50 vol. % water, containing 0.2 M Na_2S and 0.1 M NH_4F . Anodization experiments were carried out for a) 1 min, b) 2 min, c) 5 min, d) 10 min, and e) 30 min. f) Current density profile for a sample anodized for 10 min at 10 V in an electrolyte composed of 50 vol. % acetonitrile and 50 vol. % water, containing 0.2 M Na_2S and 0.1 M NH_4F . g) Evolution of film thickness over the anodization time in the same conditions.

that recorded for 100 % water-based electrolytes. However, the growth rate is still relatively high (steady state current density values of $\sim 40 \text{ mA cm}^{-2}$, as shown in Fig. 3.12f) if compared, for instance, to anodic TiO_2 nanotubes ($\sim 1 \text{ mA cm}^{-2}$ under steady state conditions), but still 5 times lower than for the anodization of tin in oxalic acid- or NaOH -based electrolytes, where the current density values are reported to be around 200 mA cm^{-2} [190,212]. The relatively slow growth rate achieved in our working electrolyte might be the reason for a more defined structure free of stacked layers and inner cracks.

The effect of the anodization potential was studied as it also has an important influence on the speed of the oxide formation (Fig. 3.13). At 5 V, the oxide growth rate is considerably reduced ($\sim 0.1 \mu\text{m min}^{-1}$) but the nanochanneled structures are no longer well-defined as for 10 V (Fig. 3.13a and 3.13b). On the contrary, a potential of 20 V leads to the delamination of the films (Fig. 3.13c). So, 10 V was found to be the most optimized potential. The thickening of the anodic oxide under optimized conditions (10 V) follows a parabolic trend with the anodization time (Fig. 3.12g). For 10 min, a layer of $\sim 8 \mu\text{m}$ thickness with nanochannels of 100 nm diameter is formed (Fig. 3.12d) but it presents inner cracks at the

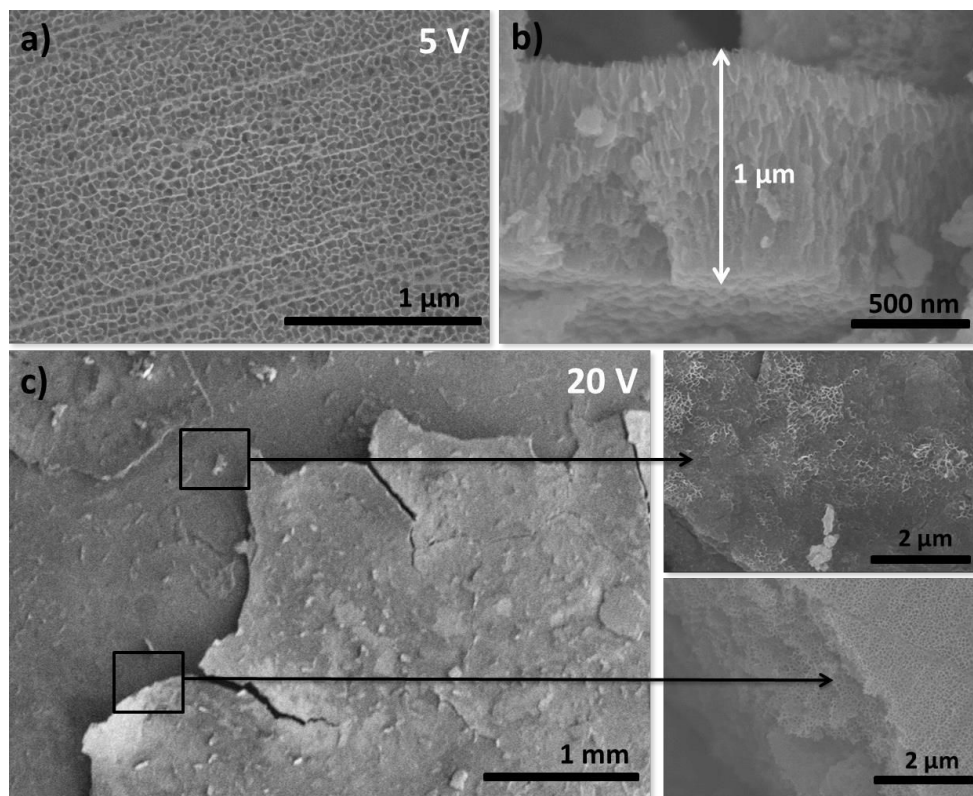


Figure 3.13 FESEM micrograph of a) top and b) cross-sectional views of a sample prepared by anodizing a Sn foil at 5 V for 10 minutes in 0.2 M Na_2S and 0.1 M NH_4F dissolved in a 50 vol.% acetonitrile – 50 vol.% water solvent. c) Top view FESEM micrograph of a sample prepared in the same electrolyte by applying a potential of 20 V showing the delamination of the oxide layer.

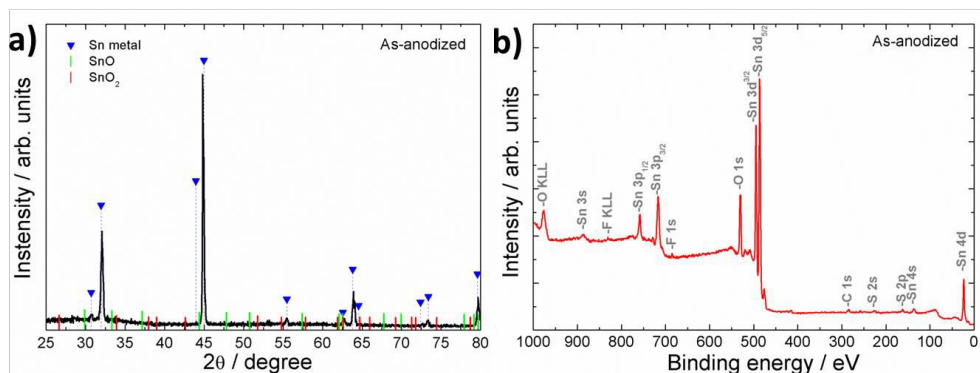


Figure 3.14 a) XRD pattern of an as-grown sample prepared by anodizing a tin foil at 10 V in 0.2 M Na₂S and 0.1 M NH₄F dissolved in 50 vol. % H₂O - 50 vol. % acetonitrile solution. b) General XPS survey spectrum for a sample prepared by anodizing a tin foil at 10 V in 0.2 M Na₂S and 0.1 M NH₄F dissolved in 80 vol. % H₂O - 20 vol. % ethylene glycol solution. From the spectrum compositional analysis was extracted.

bottom of the channels. Cracks along the structure of the anodic oxides start to form in long-lasting anodization processes (> 10 min), most likely owing to a more difficult removal of the O₂ bubbles from the nanochannels as the anodic layer becomes much thicker than just few microns. The maximum thickness we can achieve free of stacks is ~ 4.5 μm (Fig. 3.12c).

The as-anodized layers were found to be amorphous, as evidenced from XRD patterns in Fig. 3.14a. The chemical composition was derived from XPS analysis (Fig. 3.14b). The as-grown tin oxide layers consist of 45 at. % of tin and 54 at. % of oxygen. Small amounts of adventitious carbon together with sulphur and fluorine uptake from the electrolyte (~ 3 at.%) were also observed. The effect of annealing in the crystallinity and the conversion of the as-formed structures to SnO₂ will be addressed in the following chapters.

3.3 Summary

In order to achieve self-ordered porous tin oxide structures with top-open pores and free of stacks, a screening of possible electrolytes and electrochemical conditions was carried out. Ultimately, self-organized tin oxide nanostructures were successfully obtained by a new anodization approach in a Na₂S-based organic electrolyte. With an optimized electrolyte and by applying the proper potential (50:50 vol. % water-acetonitrile containing 0.2 M Na₂S and 0.1 M NH₄F and an applied potential 10 V), nanochannel structures, free of inner cracks, and characterized by top-open pores were attained with thicknesses of the layers up to ~ 4.5 μm. The as-formed structures are amorphous in nature and contain ~ 3 at. % of impurities incorporated from the electrolyte (fluorine, sulphur or carbon).

3.4 Further/Future work

- The structures developed are still far from the perfectly smooth and ordered nanotubular or nanoporous structures attained for titanium or aluminium. Further research is required in this sense. Other conditions that could be explored for our newly developed Na_2S and NH_4F electrolyte are for example the incorporation of ethanol, the use of potential pulses or the anodization of pre-patterned metallic surfaces. In this line, some preliminary experiments are gathered in Appendix b.
- Although we focused on this sulphide-based electrolyte as seemed more promising and it offered more perspectives to tune the electrochemical conditions, the potential of ammonia and sodium carbonate electrolytes cannot be obviated. A more detailed study could be carried out considering factors such as the incorporation of a fluoride/chloride source to enhance the pore opening, the use of higher potentials when an organic fraction is added, higher anodization temperatures, *etc.*

3.5 Experimental details

3.5.1 Sample preparation

Polycrystalline tin foils (99.95 %, Advent Ltd.) were ultrasonically cleaned in acetone, ethanol and deionized water ($\sim 18.2 \text{ M}\Omega\cdot\text{cm}$), and then dried in N_2 stream. Substrates (working electrodes) were mounted at the bottom of a two-electrode electrochemical cell equipped with a Pt foil as counter electrode, as shown in Fig. 3.15a. Anodization was performed in a circular area of 1 cm in diameter by applying a constant potential with a LAB-SM1500 (ET System, Germany) potentiostat in the different electrolyte solutions. After anodization films were rinsed with deionized water and N_2 blown.

Anodization at low temperatures was performed by cooling down the substrates using a

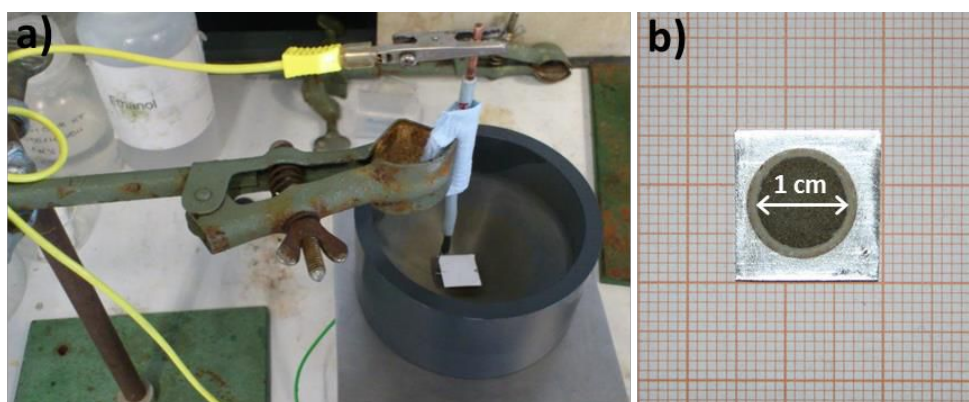


Figure 3.15 a) Photograph of the two-electrode electrochemical cell used for Sn anodization and b) a Sn foil after anodization. Size of the substrates was $1.5 \times 1.5 \text{ cm}^2$ and the diameter of the anodized area 1 cm.

Peltier element (quick cool, Conrad Electronics) and pumping out the heat with a thermostat (Huber Badthermostat-K6-NR, Germany).

3.5.2 Characterization techniques

The morphology of the as-anodized samples was characterized with a S4800 field-emission scanning electron microscope (FESEM, Hitachi High-Technologies Corporation, Japan). X-ray diffraction measurements were performed with a X'pert Philips MPD diffractometer equipped with a Panalytical X'celerator detector using graphite monochromized Cu K α radiation ($\lambda = 1.54056 \text{ \AA}$). Chemical characterization was carried out by X-ray photoelectron spectroscopy in a PHI 5600 Multitechnique System (Physical Electronics, USA) using a monochromatic X-ray source (AlK α line of 1486.6 eV).

Chapter 4

Application of self-ordered nanochanneled SnO₂ structures in H₂ gas sensing

In order to assess potential applications for the self-ordered anodic oxide structures developed in Chapter 3, the layers prepared under optimized conditions (50:50 vol. % water-acetonitrile electrolyte containing 0.2 M Na₂S and 0.1 M NH₄F and an applied potential of 10 V) were used in H₂ gas sensing devices. Their advanced structure offers a high surface area and an interconnected morphology that can be beneficial for the sensitivity and the reversibility of the sensor as discussed in the introductory Section B.2.

The as-formed anodic oxide structures reported in Chapter 3 were found to be amorphous which may seriously harm the device efficiency. To convert them into crystalline SnO₂, typically much more efficient for sensing [180], thermal treatments at temperatures higher than 500 °C are required. At these temperatures, melting of the tin substrate occurs ($T_{m,Sn} \sim 230$ °C) leading to the collapse of the oxide structure [175] along with the loss of the metallic back-contact.

4.1 Specific goals of this chapter

- Develop nanochanneled tin oxide structures on Si/SiO₂ wafers to solve the problem of the low melting point of metallic tin.
- Test the nanochanneled structures for H₂ gas sensing and adjust parameters like the annealing temperature, the sensing temperature or the thickness of the SnO₂ layer.

- Compare the H₂ gas sensing capabilities of our optimized self-ordered anodic nanochanneled SnO₂ films to other anodic structures prepared in non-optimized conditions or in other electrolytes, as reported in the literature (*i.e.* oxalic acid).

4.2 Results and discussion

4.2.1 Characterization of the nanochanneled SnO₂/Si films

Self-ordering anodization was carried out at 10 V in a 0.2 M Na₂S and 0.1 M NH₄F electrolyte solution in 50 vol. % acetonitrile - 50 vol. % water mixture (optimized conditions in Chapter 3). The surface reveals a porous structure composed of nanochannels having ~ 50 nm in diameter (Fig. 4.1a). Both the as-anodized and the layers annealed at temperatures below 200 °C were found to be amorphous as evident from XRD patterns in Fig. 4.2a.

As expected, temperatures higher than the melting point of tin (*ca.* 230 °C) were required to induce the conversion of the amorphous anodic oxide into a crystalline SnO₂ phase. For this, thin tin films were evaporated on silicon substrates, then completely anodized and finally annealed in air at T > 500 °C. Anodization was carried out onto Sn layers of different

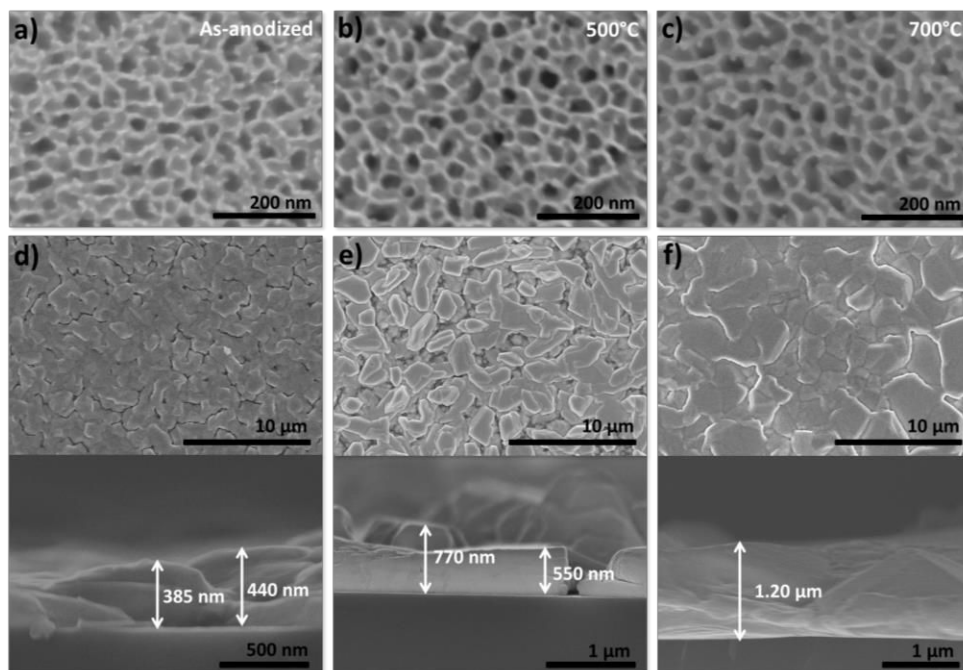


Figure 4.1 FESEM top-view images of samples prepared by anodizing an evaporated Sn layer (thickness ~ 600 nm) on p-type silicon wafer at 10 V in 0.2 M Na₂S and 0.1 M NH₄F electrolyte solution in 50 vol.% acetonitrile-50 vol.% water mixture: a) as-formed, b) annealed at 500 °C and c) annealed at 700 °C. FESEM images of the top (top) and the cross-sectional view (bottom) of e-beam evaporated Sn layers on p-type silicon substrates with different thicknesses: d) ~ 400 nm, e) ~ 600 nm and f) ~ 1.20 μm.

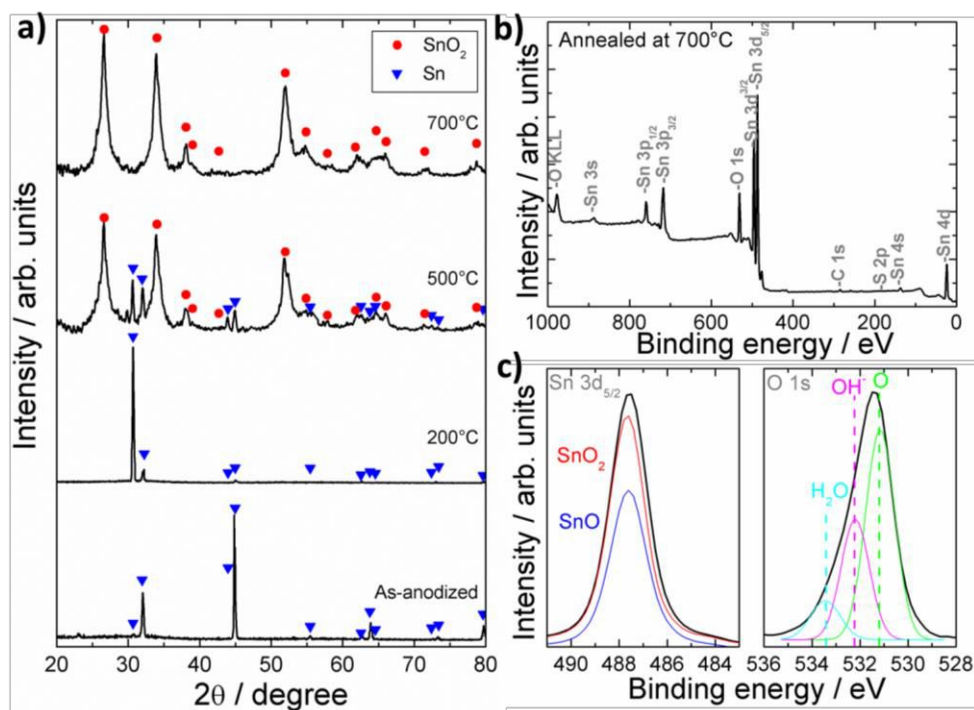


Figure 4.2 a) XRD patterns of an as-formed sample and of samples annealed at 200, 500 and 700 °C (all the layers were prepared by anodizing at 10 V in 50 : 50 vol. % acetonitrile - H₂O solution containing 0.2 M Na₂S and 0.1 M NH₄F; PDF cards: 040673 for Sn and 411445 for SnO₂). b) General XPS survey spectrum and c) high-resolution XPS spectra of Sn 3d_{5/2} and O 1s peaks for the nanochanneled tin oxide sample annealed at 700 °C. In the Sn 3d_{5/2} spectra, the reference SnO (Sigma Aldrich, 97 %) and SnO₂ (Sigma Aldrich, 99.9 %) peaks are included for comparison in blue and red, respectively. For the O 1s peak, deconvolution of the spectrum in different contributions is indicated: oxide-related oxygen (O), adsorbed OH species (OH) and adsorbed water molecules (H₂O).

thicknesses as shown in the FESEM images gathered in Fig. 4.1d-f. Upon annealing at such high temperatures, the porous structure was maintained and only a slight thickening of the nanochannel walls was observed (see Fig. 4.1b and 4.1c). Most importantly, the XRD patterns of these samples (Fig. 4.2a) confirmed the formation of tetragonal SnO₂. The elemental composition of the annealed films was further studied by XPS. A representative survey spectrum is presented in Fig. 4.2b. High-resolution XPS peaks of O 1s and Sn 3d_{5/2} are shown in Fig. 4.2c. The Sn 3d_{5/2} peak is located at 487.5 eV, in agreement with values reported for Sn in tin oxide materials [71]. The O 1s peak, located in the region between 530 eV and 534 eV, presents a shoulder at a higher binding energies denoting different contributions in addition to that of the oxide at around 531 eV [213]. The other contributions at 532.2 eV and 533.5 eV can be ascribed to adsorbed hydroxyl groups and to adsorbed water molecules [71], respectively. The contents of sulphur and fluorine impurities after annealing at 700 °C are below 0.6 at. %.

4.2.2 H₂ sensing performance of self-ordered anodic SnO₂ layers

A preliminary set of gas sensing measurements was performed on samples annealed at different temperatures to identify the optimal thermal treatment. As shown in Fig. 4.3a, samples annealed at 200 °C presented very low resistance values ($\sim 25 \Omega$) in the presence of the reference stream (N₂ + O₂ mixture) and no response was found when H₂ was introduced in the sensing chamber. Samples annealed at 500 °C exhibited higher resistance values ($\sim 470 \Omega$) and a slight decrease in resistance for H₂ concentrations in the range between 16 and 50 ppm (Fig. 4.3b), however, the sensor response was relatively low (*ca.* 15 %) and did not increase linearly with the increment in H₂ concentration (Fig. 4.3d). Best response was measured for samples annealed at 700 °C (Fig. 4.3c). In fact, annealing at this high temperature induced a full conversion of the amorphous anodic oxide into crystalline SnO₂, as previously shown by XRD measurements. Also, low temperature processing may allow a

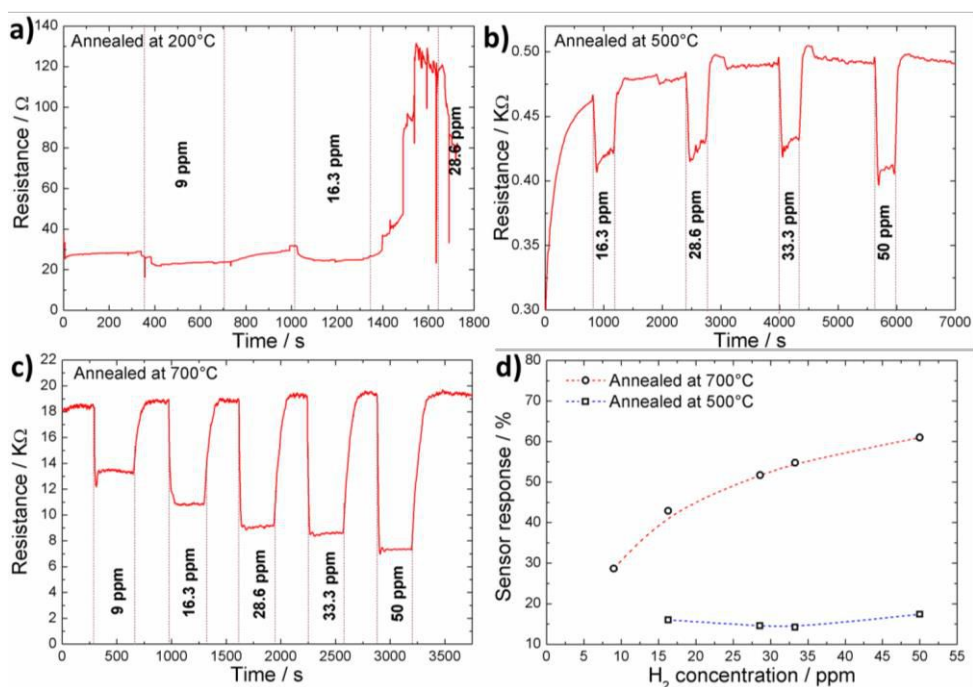


Figure 4.3 a) Change in the resistance for the nanochanneled anodic oxide film when exposed to H₂ concentrations ranging from 9 to 50 ppm (operating temperature = 120 °C). These films were prepared by anodizing a tin foil at an applied potential of 10 V for 10 minutes in a 50 vol.% acetonitrile - 50 vol.% H₂O solution containing 0.2 M Na₂S and 0.1 M NH₄F. The layer was annealed at 200 °C for 1 h in air atmosphere. b) Change in the resistance at 120 °C for a film prepared by anodizing a ~ 600 nm thick tin layer evaporated onto a Si wafer in the same electrolyte as for a) and annealed at 500 °C. c) Change in the resistance at 120 °C for an oxide film prepared by anodizing ~ 600 nm thick tin layer evaporated onto a Si in the same experimental conditions and then annealed at 700 °C. d) Sensor response of samples presented in b) and c) plotted as a function of the H₂ concentration. Notice that this was a control measurement and less strict purging conditions were employed. Consequently, results shown here for the sample annealed at 700 °C are not comparable to those shown in the rest of this chapter where long purging times were used.

high content of Sn²⁺ defects in the structure, which could be a detrimental factor for the sensing performance. Consequently, all the samples in further investigations were annealed at 700 °C. Notice that the resistance values shown in Fig. 4.3 are slightly different to the ones reported in the subsequent figures of this Chapter, so the values of the sensing response are not comparable. This is due to a change in the measurement conditions, *i.e.* purging time of the sensing chamber, as detailed in Fig. 4.3 caption.

The effect of the SnO₂ layer thickness was studied too. Fig. 4.4a shows the changes in the resistance for a 600 nm thick layer when exposed to H₂ concentrations in the range of 9 to 50 ppm and by operating at different sensing temperatures (80, 100, 120, 140, 160, 200, and 250 °C). Fig. 4.4 b shows the corresponding sensor response calculated according to the expression (4.1) in the Experimental details (see also section B.2 from the Introduction). The magnitudes of the sensor response calculated from the R₀/R_H ratio are gathered in table IV.1. Although the sensor exhibits a fast and sensitive response at temperatures as low as 80 °C (the sensor response was ~ 45 % and the magnitude of the response was ~ 1.8), the best response was found at 160 °C. Here, the resistance drastically decreased from 22 to 7 kΩ upon injection of 9 ppm of H₂ (the sensor response was ~ 68 % whereas the magnitude of

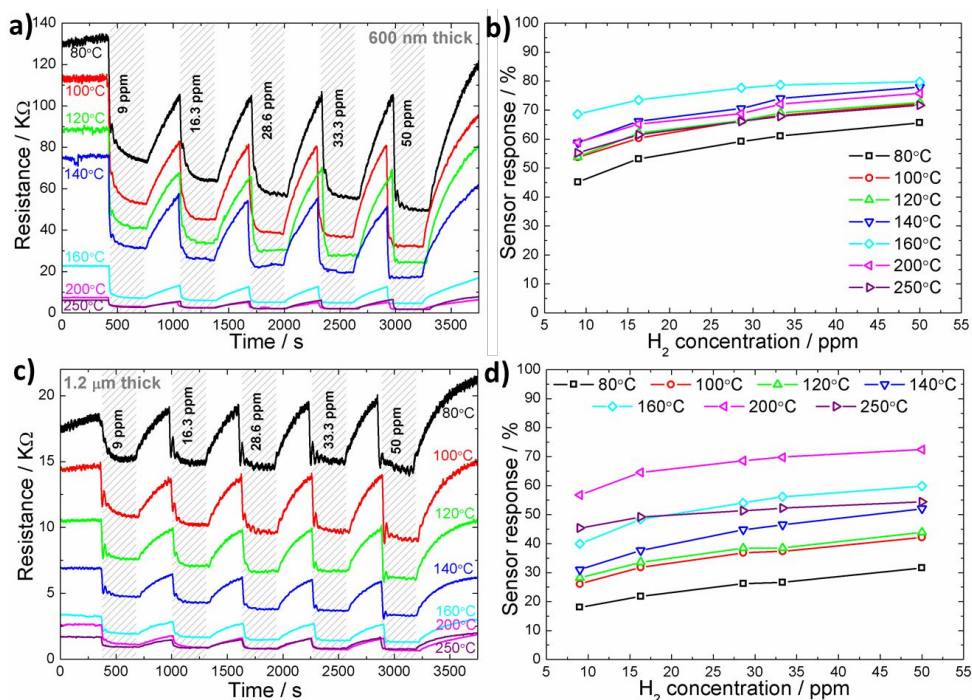


Figure 4.4 a) Change in the resistance measured for a SnO₂-based sensor prepared by anodizing a 600 nm thick tin film evaporated on Si wafers when exposed to H₂-containing streams in the gas-sensing chamber (H₂ concentration: 9, 16.3, 28.6, 33.3 and 50 ppm; chamber operating temperatures: 80, 100, 120, 140, 160, 200 and 250 °C). b) Sensor response vs. H₂ concentration at different operating temperatures for the sample shown in a). c) Change in the resistance measured for a SnO₂-based sensor obtained by anodizing a 1.2 μm thick tin film (concentrations of H₂: 9, 16.3, 28.6, 33.3 and 50 ppm; operating temperatures: 80, 100, 120, 140, 160, 200 and 250°C). d) Sensor response vs. H₂ concentration at different operating temperatures for the film presented in c).

Table IV.1 Magnitude of the sensor response (R_0/R_H) at the indicated operating temperatures for the different H_2 concentrations (in ppm).

SnO₂ thickness	9 ppm H₂	16.3 ppm H₂	28.6 ppm H₂	33.3 ppm H₂	50 ppm H₂
600 nm, 80 °C	1.80	2.05	2.28	2.37	2.66
600 nm, 160 °C	3.15	3.75	4.43	4.61	4.91
1.2 μm, 80 °C	1.20	1.25	1.30	1.31	1.38
1.2 μm, 160 °C	1.65	1.95	2.15	2.32	2.5

the signal was ~ 3.15). Moreover, the sensor response for this layer showed a linear trend in the 16.3 to 50 ppm of the H_2 range (Fig. 4.4b). For lower H_2 concentrations, a slight deviation from this behaviour was observed. The results are in line with other works where SnO_2 nanostructures were shown to detect H_2 in a concentration range of 10 to 50 ppm. In spite of this, the observed magnitude of their sensor response is much lower than what we found (~ 0.2 at 200 °C or ~ 0.4 at 300 °C for a concentration of 10 ppm of H_2 [177]). Additionally, much higher sensing temperatures were required in those studies [177]. Comparable operating temperatures and levels of sensitivity have been only reported when using individual SnO_2 nanorods [198] or SnO_2 films doped with noble metal (Pt and Pd) nanoparticles [180,199]. Thinner oxide layers of ~ 400 nm were also tested but they exhibited slow recovery times, especially at 80 °C. Fig. 4.4c shows the change in resistance observed for thicker SnO_2 layers, ~ 1.2 μm, exposed to different H_2 concentrations and sensing temperatures. The resistance values for the thicker layers were one order of magnitude lower than the values obtained for 600 nm thick films (22 vs 3 kΩ at 160 °C). The sensor response changed linearly when increasing the H_2 concentrations from 9 to 50 ppm, as shown in Fig. 4.4d, but in general, their responses were lower, especially when operating at low temperatures (see Table IV.I). So, its best sensing response was achieved when operating at 200 °C.

In order to compare the sensing response of our layers, obtained in optimized conditions, to other anodic tin oxide films, samples in non-optimized conditions and in oxalic acid electrolyte were prepared. As non-optimized conditions, a 100% water solution containing 0.2 M Na_2S and 0.1 M NH_2F and a potential of 10 V was used. For the samples in oxalic acid, the procedure described in [212] was employed. Fig. 4.5a-c shows the corresponding FESEM images after anodizing the Sn foils using the three different conditions: optimized, non-optimized and oxalic acid. Here, the formation of inner cracks and stacked layers can be clearly observed for samples obtained in non-optimized conditions (Fig. 4.5b) and oxalic acid-based electrolytes (Fig. 4.5c).

The resistance of the films was calculated from I-V curves taken at room temperature and in ambient atmosphere. In these conditions, resistance (R) values might differ from the ones

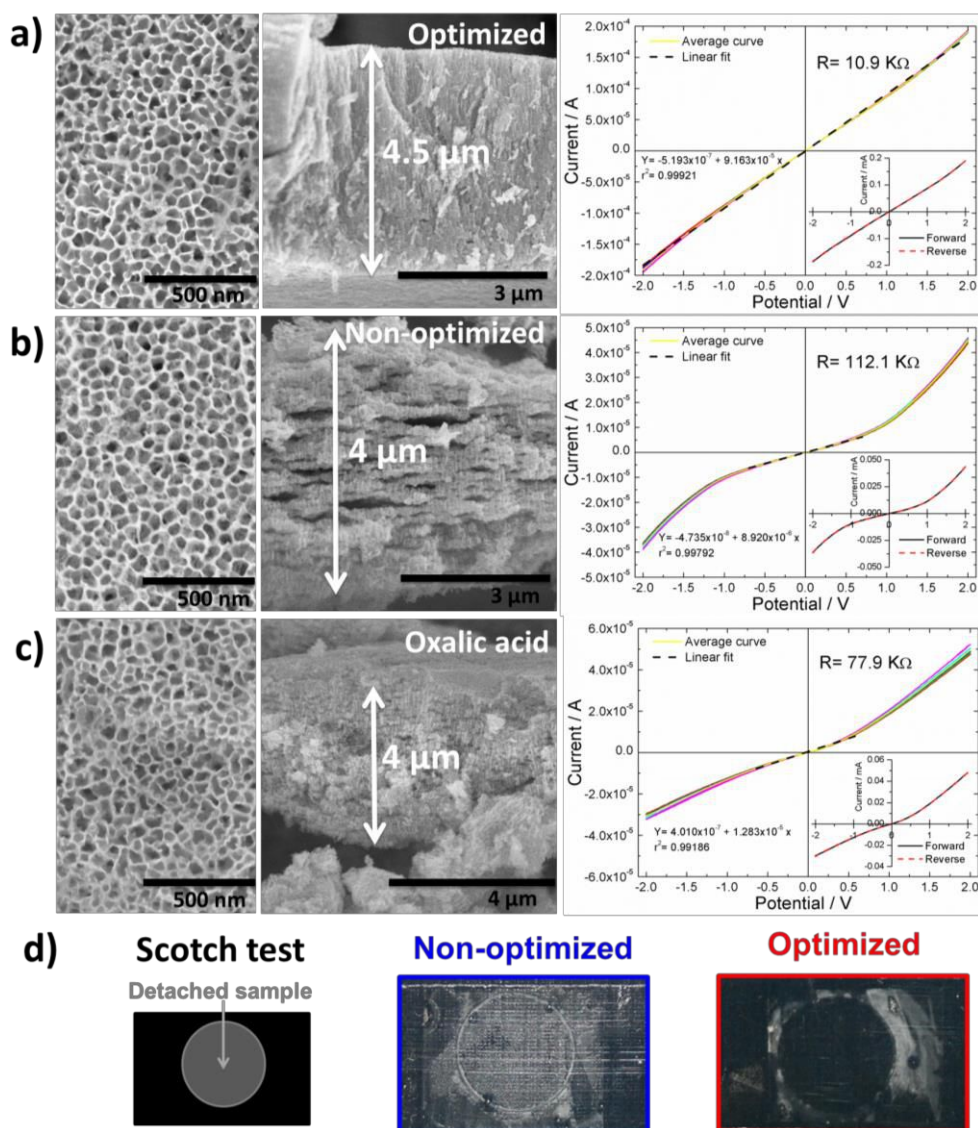


Figure 4.5 FESEM image of anodic layers prepared on Sn foil (top surface and cross-section view) and I-V curves (right) for samples were prepared in different forms: a) in optimized conditions, using 50 vol. % acetonitrile - 50 vol. % H₂O solution containing 0.2 M Na₂S and 0.1 M NH₄F at 10 V, b) in non-optimized conditions by employing a 100 % H₂O solution containing 0.2 M Na₂S and 0.1 M NH₄F at 10 V and c) 0.3 M oxalic acid at 8 V as detailed in the literature [212]. I-V curves were performed on anodic SnO₂ films of ~ 600 nm thick prepared by anodizing evaporated tin layers and subsequently annealed at 700 °C. d) Photograph of the detached film after performing the Scotch tape test in samples prepared in optimized (a) and non-optimized conditions (b).

obtained when samples were mounted in the sensing setup due to the humidity of the air. We found resistance values of 112.1 kΩ and 77.9 kΩ for the samples prepared in non-optimized conditions in contrast to the 10.9 kΩ for films under optimized anodization parameters.

Their higher resistance values may be attributed to the inner cracks observed in the FESEM images. Mechanical stability of the films was qualitatively studied by the so-called Scotch test. As shown in Fig. 4.5d, samples prepared under optimized conditions resist the test, while those grown in water-based solutions containing Na_2S and NH_4F are easily detached. The higher mechanical stability of the films may also arise from the crack-free structure.

The H_2 sensing response of the films is evaluated in Fig. 4.6. All films exhibit substantial changes in resistance for H_2 concentrations as low as 9 ppm. As has already been discussed,

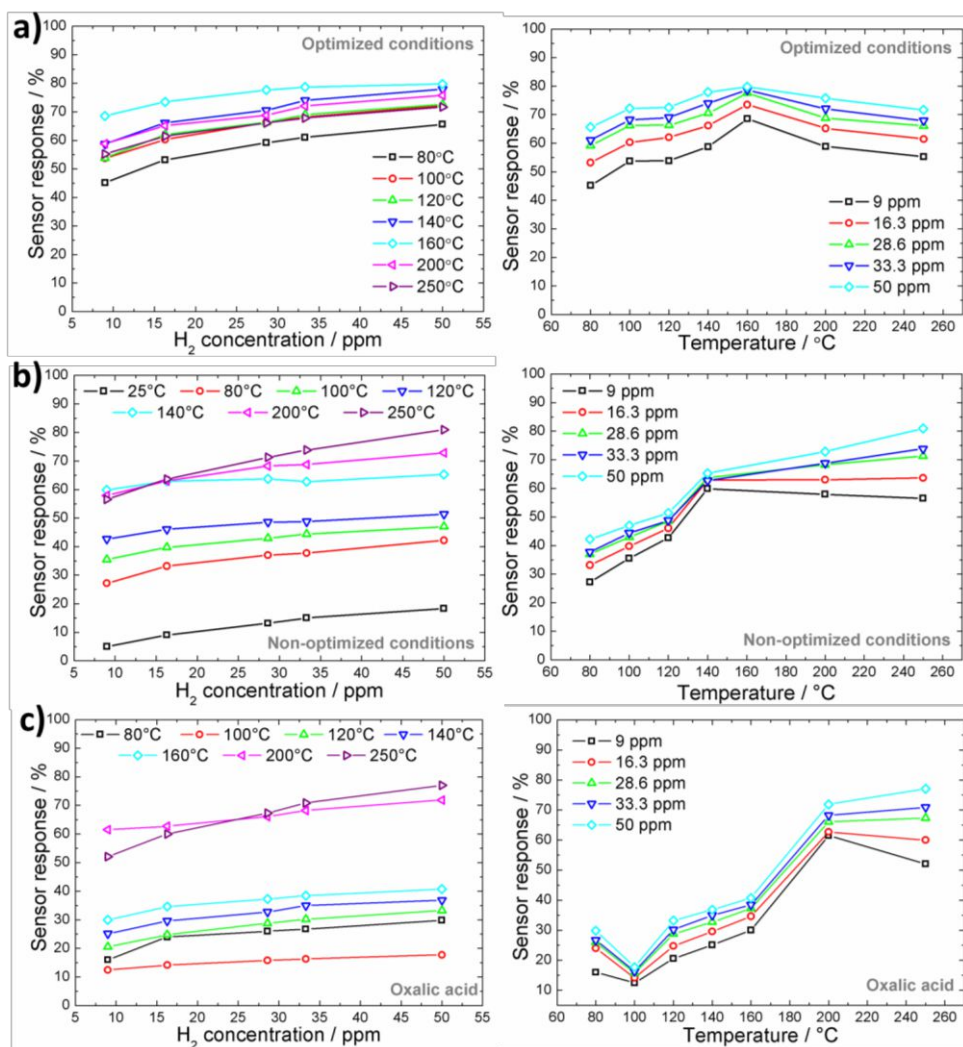


Figure 4.6 Sensor response at different H_2 concentrations (left) and sensor response at different temperatures (right) for samples prepared in different forms: a) in optimized conditions, using 50 vol.% acetonitrile - 50 vol.% H_2O solution containing 0.2 M Na_2S and 0.1 M NH_4F at 10 V, b) in non-optimized conditions by employing a 100 % H_2O solution containing 0.2 M Na_2S and 0.1 M NH_4F at 10 V and c) 0.3 M oxalic acid at 8V as detailed in the literature [212]. All samples were prepared on ~ 600 nm evaporated Sn layers and subsequently annealed at 700 °C.

layers prepared under optimized conditions show a linear response with increasing H₂ concentration and an optimal operating temperature of 160 °C (Fig. 4.6 a). The porous SnO₂ layers grown by the other methods (non-optimized or oxalic acid electrolyte) also denote a linear trend with increasing target gas injections in the sensing chamber; however, their performance is better at 200 - 250 °C (Fig. 4.6b and 4.6c). At these temperatures, the sensor response can be raised to values of ~ 70 %. While at high temperature the differences between the three layers are not remarkable, at temperatures below 160 °C they become more evident. Samples prepared under optimized conditions display sensor responses ~ 40 % for 9 ppm of H₂ against the 15 - 25 % for those non-optimized. So, overall films anodized under optimized conditions seem to present a more stable response through all the temperature range under study. The improved response at low temperatures could come from the lack of discontinuities in the structure, which may hinder electron mobility. As temperature is raised, the conductivity of the material is improved and the effect of the cracks in the structure becomes less noticeable.

4.3 Summary

Self-organized tin oxide nanostructures following the optimized conditions in Chapter 3 were successfully prepared onto Sn layers evaporated on Si/SiO₂ wafers. The as-formed structures were converted into crystalline SnO₂ by annealing at 700 °C and then tested for H₂-sensing. The best sensing performance was achieved for 600 nm thick SnO₂ layers at an operating temperature of 160 °C, although a good response could be obtained at temperatures as low as 80 °C. The sensor response is not only extremely fast but also exhibits a linear increase when the H₂ concentration is raised from 9 to 50 ppm. The response is also better than that of layers prepared using other self-ordering anodization approaches, especially at low operating temperatures. The sensitivity and the fast sensing and recovery abilities of the here prepared sensor can be attributed to the high surface area of the nanochannel geometry and to its superior conduction properties given by fully open pores and crack-free structures, respectively.

4.4 Further work

- It would be interesting to carry out sensing measurements against other target gases such as NO_x or CO. This would give an idea of the selectivity of the grown structures. In principle for small pore sizes, the diffusion of CO is lower than that of H₂ [192].
- Although one of the strong points of our sensor is that without noble metal decoration very good sensitivities and low operating temperatures are reached, it would be interesting to see if sensor performance can be pushed up by metal decoration.

4.5 Experimental details

4.5.1 Sample preparation

Given the low melting point of metallic tin, anodization was performed in e-beam evaporated tin layers on p-type silicon wafers. Tin evaporation was carried out with a PLS 500 evaporation system (Balzers-Pfeiffer, Germany) using 2-4 mm tin granules (99.999 %, Chempur) as metal source. Deposition was done at a rate of 0.1 nm s^{-1} and a pressure between 1×10^{-6} and 6×10^{-6} mbar. Different thicknesses of the tin layers were prepared, namely 400 nm, 600 nm and 1.2 μm . The substrates (working electrodes) were mounted at the bottom of a two-electrode electrochemical cell equipped with a Pt foil as counter electrode. Anodization was performed by applying a constant potential of 10 V with a LAB-SM1500 power source (ET System, Germany) and by using an electrolyte solution composed of acetonitrile (99.8 %, Sigma Aldrich) and deionized H_2O (volume ratio 50:50), containing 0.2 M $\text{Na}_2\text{S}\cdot x\text{H}_2\text{O}$ (Sigma-Aldrich) and 0.1M NH_4F (≥ 98.0 %, Sigma-Aldrich) [214]. Anodization time was adjusted to the thickness of the evaporated Sn layers to convert approximately the entire metallic layer into anodic oxide. For 400 nm, 600 nm and 1.2 μm , anodization times of 2.5, 3 and 4 minutes were employed. The as-formed films were annealed in a furnace (ZEW 1450-4, Heraeus, Germany) in air for 1h.

Alternatively, samples in non-optimized conditions were prepared by anodization in a 100% H_2O solution containing 0.2 M Na_2S and 0.1 M NH_4F at 10 V. For sake of comparison also layers in 0.3 M oxalic acid at 8 V were assessed following the procedure detailed by Zaraska *et al.* in reference [212].

4.5.2 Characterization techniques

The morphology of the anodized samples was characterized with a S4800 field-emission scanning electron microscope (FESEM, Hitachi High-Technologies Corporation, Japan). X-Ray diffraction measurements (XRD) were performed with a X'pert Philips MPD diffractometer equipped with a PANalytical X'celerator detector using the $\text{Cu K}\alpha$ ($\lambda = 1.5418 \text{ \AA}$) radiation in the Bragg-Brentano geometry. The phases were identified by using the JCPDS database. X-ray photoelectron spectroscopy (XPS) measurements were performed in a PHI 5600 Multi-Technique System (Physical Electronics, USA) with a monochromatic X-ray source (Al $\text{K}\alpha$ line of 1486.6 eV).

For the gas-sensing measurements, four circular-shaped 200 nm thick Pt contacts were sputtered on the samples with an EM SCD500 plasma-sputter equipment (Leica Microsystems, Germany), operating at 16 mA in vacuum conditions (10^{-2} mbar in Ar) and with a deposition rate of 0.1 nm s^{-1} . Electrical contact was established by connecting two Au wires to the top of two sputtered Pt contacts (2-point setup, see scheme in Fig. 4.7a and the FESEM pictures therein). Before the measurement, the sensing chamber was rinsed and preheated at the desired temperature with an Eurotherm 3216-based temperature controller

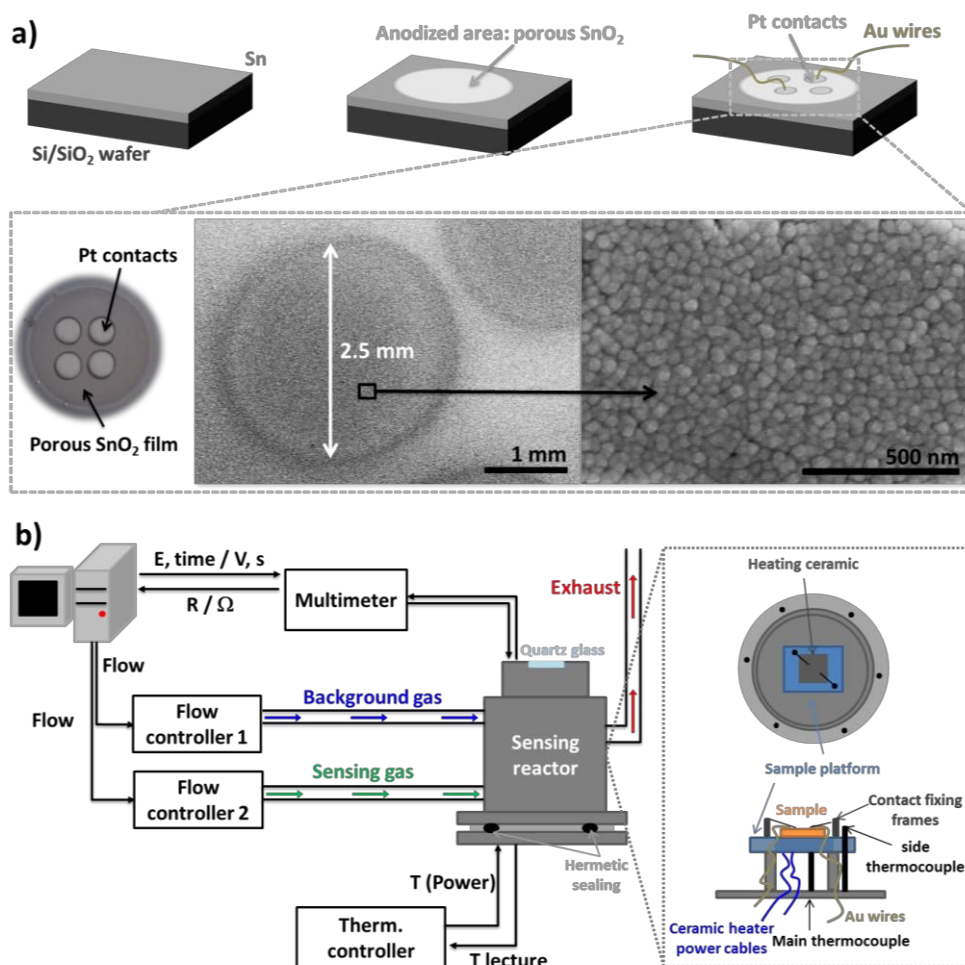


Figure 4.7 a) Scheme of the sensor build-up: anodization of evaporated Sn layers, annealing, sputtering of Pt contacts and disposition of the gold wires used for the two point measurement. A photograph of a sensor and detail of the Pt contacts from FESEM micrographs are also included. b) Scheme of the sensing setup.

(Invensys Eurotherm, USA). The sensing properties were assessed by measuring the changes in the resistance of the anodic films with a Keithley 2400 SourceMeter (Keithley Instruments, USA) when artificial air (background gas N₂+O₂; 80:20 vol%) or the latter along with injections of different volumes of a H₂+Ar (100ppm H₂ in Ar) mixture were alternately flowed through the sensing chamber (see Fig. 4.7b). Sensor response was calculated using the following expression:

$$\text{Sensor response (\%)} = \frac{R_0 - R_H}{R_0} \times 100 \quad (4.1)$$

where R_0 is the resistance measured when the reference gas is flowing in the chamber and R_H the resistance when the sample is exposed to H_2 . The magnitude of the response was defined as the ratio R_0/R_H .

I-V curves were recorded at room temperature and in ambient conditions using a 2-point measurement setup that consisted of a USMCO micromanipulator and an Agilent 4156C precision semiconductor parameter analyser. For this purpose, gold contacts were evaporated on the SnO_2 nanochanneled layer.

Chapter 5

Photoelectrochemical properties of self-ordered tin oxide structures

As seen in previous chapters, the as-formed anodic tin oxide porous structures are amorphous or poorly crystalline, and present a dark brown colour far from the white one expected for a stoichiometric SnO₂ layer ($E_g \sim 3.6$ eV). Due to this discrepancy between the obtained and predicted appearance, some researchers suggested that as-anodized layers might be composed by a black SnO layer [175,176], whose indirect band gap is located in the infrared range ($E_g \sim 0.7$ eV [215]). The exact nature of as-anodized porous tin oxide layers remains still uncertain. In a recent contribution, Long *et al.* showed that the enhancement in the visible absorption observed for co-precipitated SnO₂ nanoparticles using SnCl₂·2H₂O and K₂SnO₃·3H₂O may arise from Sn²⁺ doping [216]. Considering the high Sn²⁺ content determined by Mössbauer spectroscopy for as-anodized porous tin oxide films [183], it would be reasonable to attribute its characteristic colour to Sn²⁺ content.

From a theoretical point of view, SnO₂ is known to have a very rich defect nature [217–219] and, as a consequence, it is able to tolerate an enormous concentration of intrinsic vacancies violating the stoichiometry [217]. Oxygen vacancies can be easily compensated by substitutional self-doping with Sn²⁺ ions [217,220] with a minimal structural distortion, given the slight differences in the ionic radius of the two ions [218] (0.69 Å for hexacoordinated Sn⁴⁺ and 0.62 Å for hexacoordinated Sn²⁺ [218]). The presence of a high Sn²⁺ content, acting as an n-type dopant of n-SnO₂ [218,221], implies a high concentration of oxygen vacancies that change the nature of the O 2p states in the valence band [218]. The modification of these states in the valence band is responsible of the narrowing of the optical

band gap [216,218] and the extended absorption in the visible range. In this sense, controlled thermal annealing is a feasible way to tune the concentration of oxygen vacancies or Sn^{2+} defects and, consequently, modify the optical properties of SnO_2 [222]. SnO_2 -based materials with absorption in the visible range could have potential application in photocatalysis [216] or photoelectrochemical water splitting.

5.1 Specific goals of this chapter

- Study the effect of the annealing temperature in the structure and composition of nanochannelled tin oxide structures on Sn foils.
- Determine the effect of the annealing temperature (between 200 °C and 400 °C) and atmosphere (Ar, air, O_2) on the incident photon to charge carrier efficiency (IPCE) and optical band gap by means of photocurrent measurements.
- Test the films as anodes in photoelectrochemical water splitting using solar simulated light (AM 1.5, 100 mW cm^{-2}).

5.2 Results and discussion

5.2.1 Effect of annealing in morphology, structure and composition

Fig. 5.1a shows the top-view FESEM image for as-formed tin oxide nanochannels obtained after 10 min of anodization at 10 V in a 50 % acetonitrile and 50 % water electrolyte containing 0.2 M Na_2S and 0.1 M NH_4F . The top morphology clearly shows that pores are completely open. The corresponding cross-sectional view is presented in Fig. 5.1b together with the estimated thickness ($\sim 8 \mu\text{m}$). Details of the top and middle part of the channels are shown in Fig. 5.1c and 5.1d. Channels are vertically aligned and have a diameter of ~ 100 nm. The origin of this channelled structure, in analogy to other self-organized nanostructures, is the equilibrium between passivation, induced by the presence of Na_2S , and the dissolution of the growing oxide caused by both the alkaline medium and NH_4F [214], as discussed in detail in Chapter 3. The upper part of the channels (Fig. 5.1c), in close contact with the electrolyte, presents smooth walls most likely due to a more effective etching/dissolution process. On the contrary, several ripples can be found at the bottom of the channels (Fig. 5.1d).

Fig. 5.1e-g display the FESEM images of the top surface for films prepared in the same conditions and annealed at 200 °C, 300 °C and 400 °C. Although the metallic tin substrate has a low melting point ($T_{\text{m,Sn}} \sim 230$ °C), annealing up to 400 °C was feasible and the channel structure of the film was preserved for all temperatures. This is because when molten, tin forms a liquid pool confined by an outer oxide layer that protects it from further melting [219,223]. At $T > 400$ °C, annealing was not possible since the anodic oxide films

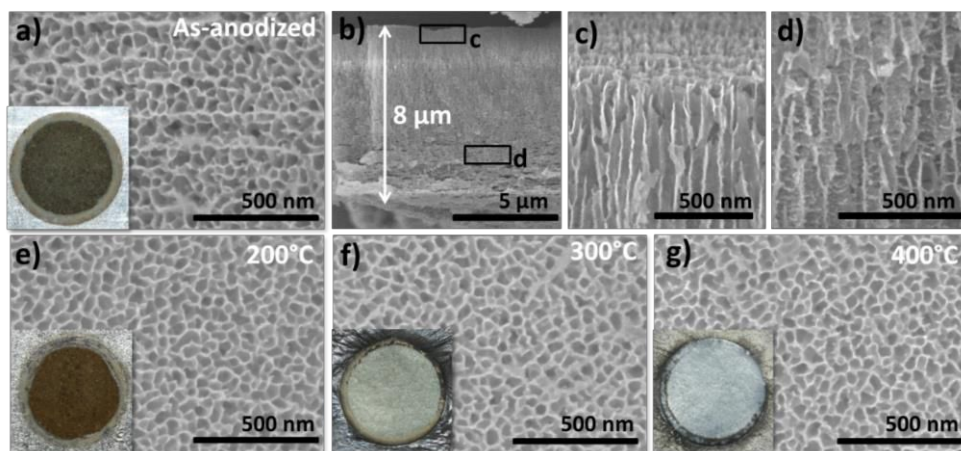
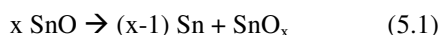


Figure 5.1 FESEM micrographs of a) top and b) cross-sectional view of an as-anodized nanochannelled tin oxide film prepared by applying a constant potential of 10 V to a tin foil immersed in an electrolyte solution composed of acetonitrile and water (volume ratio 50:50) and containing 0.2 M $\text{Na}_2\text{S}\cdot x\text{H}_2\text{O}$ and 0.1 M NH_4F . c) and d) correspond to details of the nanochannels taken in different regions of the cross-sectional view. FESEM images of the top view for samples prepared in the same conditions as a) but annealed at e) 200 °C, f) 300 °C and g) 400 °C in air conditions. Insets in the left corner correspond to photographs of the sample after the corresponding thermal treatment.

peeled off from the substrate. In the inset of Fig. 5.1a and 5.1e-g, photographs of the corresponding as-anodized and annealed samples are shown. Both the as-anodized and the sample annealed at 200 °C present a dark-brown colour, which seems to be more reddish for the thermally treated sample. Conversely, samples annealed at $T \geq 300$ °C become whiter, closer to the expected colour for a stoichiometric SnO_2 oxide. The identical morphology observed throughout all annealed samples (Fig.5.1a and 5.1e-g) suggests that the colour change is related either to the presence of defects or to the alteration of the crystalline phase.

Fig. 5.2a shows the XRD patterns of the as-anodized and annealed films. As-anodized layers do not present relevant peaks, just broad shoulders in the region of 2θ around 30° and 52°, where the main peaks of SnO_2 are located. The as-anodized films' crystallinity was further characterized by TEM-SAED (Fig. 5.3). The weak continuous ring patterns obtained are typical of low-ordered materials, amorphous or poorly crystalline. The interplanar distances calculated from the rings are consistent with the planes (110), (101) and (211) of tetragonal SnO_2 (see Table V.1). After annealing at 200 °C, the XRD pattern (Fig. 5.2) reveals the presence of three broad peaks at 26.4°, 34.4° and 52.3° in accord with the SnO_2 phase and also a peak at 30.6° related to metallic Sn. The presence of metallic Sn can arise from the decomposition of amorphous SnO or SnO_x (Sn_2O_3 or Sn_3O_4) domains in the sample following reactions (5.1) and (5.2) as described in the literature [224–226]:



The 200 °C annealed sample also presents better defined rings in the SAED pattern (Fig. 5.3b). The layers annealed at 300 °C show a similar pattern as compared to the films annealed at 200 °C, with an additional peak at 29.8° associated to crystalline SnO (see detail of the 2θ region between 20° and 40° in Fig. 5.2). Annealing at 400 °C, leads to an increase

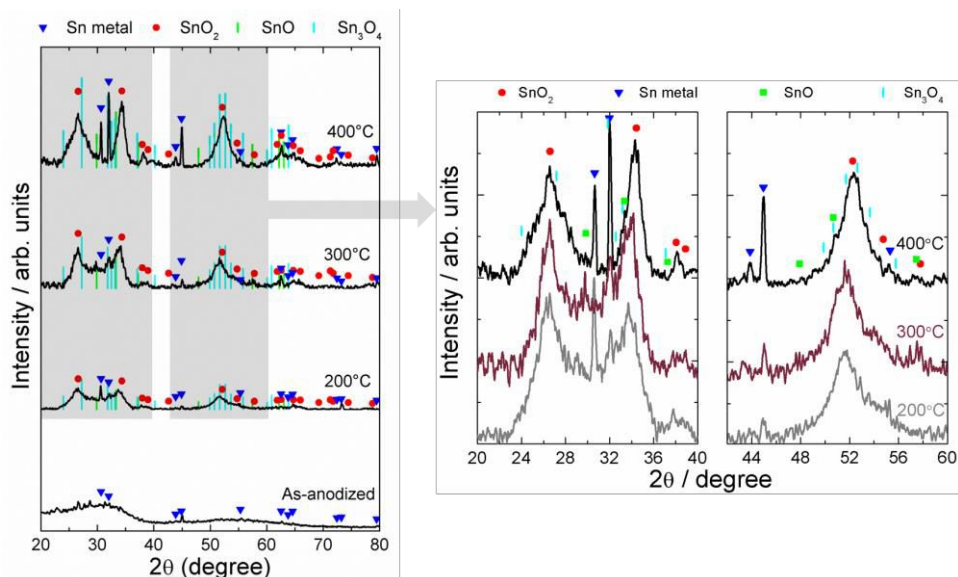


Figure 5.2 XRD patterns of as-formed nanochannelled tin oxide films prepared by applying a constant potential of 10 V to a tin foil immersed in an electrolyte solution composed of acetonitrile and water (volume ratio 50:50) containing 0.2 M $\text{Na}_2\text{S}\cdot x\text{H}_2\text{O}$ and 0.1 M NH_4F and subsequently annealed at 200 °C, 300 °C and 400 °C in air atmosphere. JCPDS cards: 040673 (Sn), 411445 (tetragonal SnO_2), 060395 (tetragonal SnO) and 160737 (Sn_3O_4). Figures on the right correspond to a zoom of the relevant regions of 2θ .

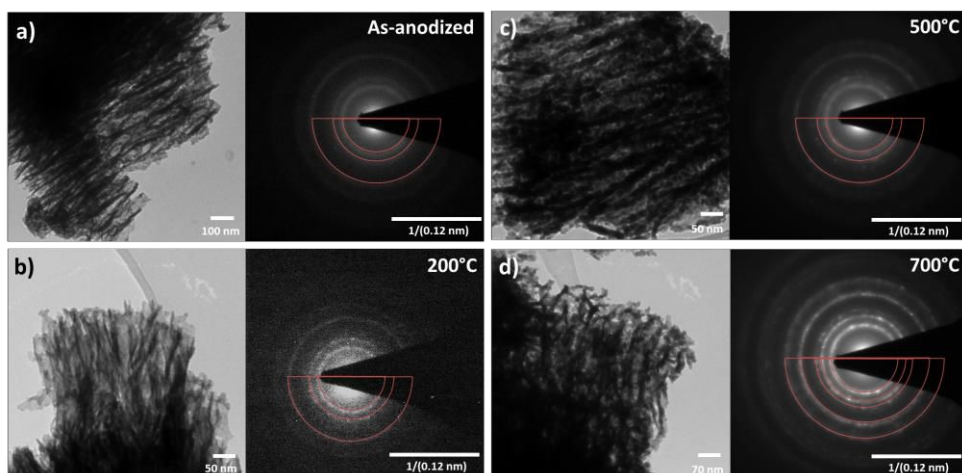


Figure 5.3 TEM image (left) and SAED pattern (right) of a fragment of an b) as-anodized and annealed in air conditions at b) 200 °C, c) 500 °C and d) 700 °C for 1 hour. Samples c) and d) were prepared by anodizing Sn films evaporated onto Si/SiO_2 wafers.

Table V.1. Interplanar distance (d) values obtained from SAED patterns shown in Fig. 5.3.

Thermal treatment	D_{hkl} from XRD*	D_{hkl} from SAED	Planes (hkl)
As-anodized, 200 °C and 500 °C	3.347	3.229	(110)
	2.643	2.547	(101)
	1.764	1.683	(211)
700 °C	3.347	3.231	(110)
	2.643	2.545	(101)
	2.369	2.211	(200)
	1.764	1.680	(211)
	1.416	1.354	(301)

* Values from tetragonal SnO₂ JCPDS card 411445.

in the intensity of Sn peaks and also to the formation of shoulders around the SnO₂ peaks where Sn₃O₄ reflections are expected. SAED patterns of samples annealed at $T > 400$ °C can be found in Fig. 5.3c and 5.3d to demonstrate the high crystallinity level achieved at 700 °C, where bright spots can be clearly distinguished.

Information of the chemical speciation of the oxide films was obtained from Raman spectroscopy measurements (Fig. 5.4a). The as-anodized samples and those annealed at 200 °C do not present strong Raman modes, as expected from their poorly crystalline nature [222]. A broad band can be seen in the 450-700 cm⁻¹ range, where the main SnO₂ Raman bands are located. Samples annealed at 300 °C exhibit also two Raman bands at 113 and 211

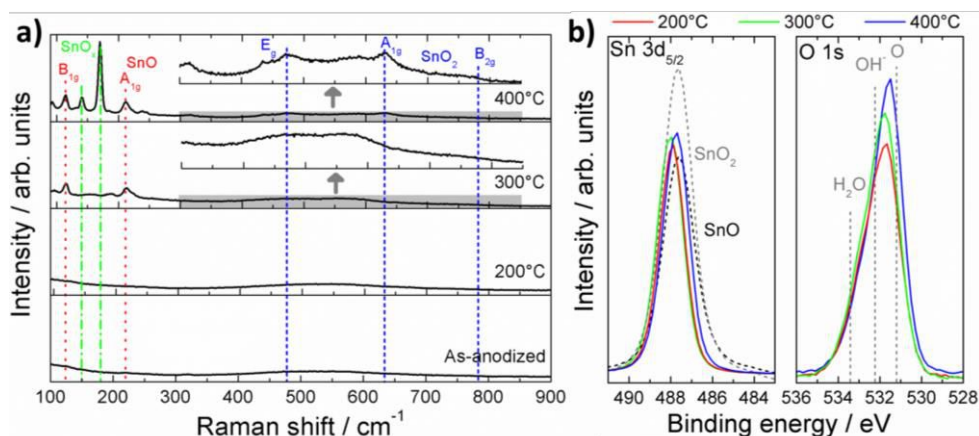


Figure 5.4. a) Raman spectra for nanochannelled tin oxide samples prepared by applying a constant potential of 10 V to a tin foil immersed in an electrolyte solution composed of acetonitrile and water (volume ratio 50:50) and containing 0.2 M Na₂S_xH₂O and 0.1 M NH₄F and subsequently annealed in air at 200 °C, 300 °C and 400 °C. b) XPS spectra of Sn 3d_{5/2} and O 1s peaks for tin oxide samples prepared in the same conditions as in panel a) and subsequently annealed at 200 °C, 300 °C and 400 °C. For sake of comparison, in the Sn 3d_{5/2} region the XPS spectra of SnO (Sigma Aldrich, 97 %) and SnO₂ (Sigma Aldrich, 99.9 %) reference powders is also presented.

cm^{-1} , associated to B_{1g} and A_{1g} bands of tetragonal SnO, respectively [215,224,225]. The results are in accord with the XRD data shown previously (Fig. 5.2). Films annealed at 400 °C still present the SnO-related bands together with other Raman modes at 141 and 170 cm^{-1} assigned to a SnO_x phase [224,225] and at 473, 632 and 776 cm^{-1} characteristic of SnO_2 [222,224,225]. The formation of crystalline SnO_x in this temperature range by crystallization of the amorphous matrix and the oxidation of SnO regions following reaction (5.1) is consistent with results reported in the literature [224]. Although weak SnO_2 bands can be distinguished in the spectrum, full conversion into SnO_2 is known to occur only at $T > 600$ °C [225,226].

XPS measurements were performed to distinguish Sn^{2+} and Sn^{4+} ratios but were not conclusive. As observed in Fig. 5.4b, discrimination between Sn^{2+} and Sn^{4+} could not be achieved even for the powder SnO and SnO_2 references. This is a common issue in tin oxide materials because the termination of the surfaces strongly depends on the preparation conditions and non-stoichiometric terminated surfaces are frequent in both SnO and SnO_2 [227]. This fact and their close binding energies [228] make it difficult to differentiate both species by XPS. The only effect worth to mention in this case is the increase in the oxygen content (O1s peak) as the annealing temperature is increased, which supports that the nanochannelled structure is further oxidized.

5.2.2 Photoelectrochemical characterization

5.2.2.1 Photocurrent at variable wavelength

Fig. 5.5b shows the incident photon to charge carrier efficiency (IPCE), calculated from photocurrent measurements, as a function of the incident wavelength. An example of a photocurrent measurement is given in Fig. 5.5a showing that, upon illumination, current density is increased to more positive values. This result confirms the n-type semiconductor behaviour for all films, even for as-formed films or after annealing at 200 °C, in contrast to stoichiometric p-type SnO [229]. This fact, as well as the XRD and Raman spectroscopy results, suggests that the as-anodized layer is formed by an amorphous SnO_x -based matrix with a high content of non-stoichiometric defects. This highly defective structure presents absorption in the visible range (onset at ~ 500 nm) [218], as observed in the IPCE results (Fig. 5.5b). The samples annealed at 200 °C show even larger IPCE response in the visible range, this owing to their improved crystallinity while keeping the Sn^{2+} content, as the annealing temperature is still low to promote further oxidation to Sn^{4+} . The band gap calculated from IPCE data is ~ 2.6 eV (see Experimental details at the end of the Chapter for information on how to calculate E_g from the IPCE data). When samples are annealed at 400 °C, we observe a shift in the IPCE absorption edge towards the UV, this meaning that the fundamental band gap is displaced to higher energies, 3.2 eV. This E_g value is closer to the expected values for stoichiometric SnO_2 (3.6 eV [175,212]), the difference probably being due to the presence of SnO_x observed in the Raman spectra. Complete oxidation to SnO_2 requires a thermal treatment at even higher temperatures ($T > 600$ °C) as discussed by other

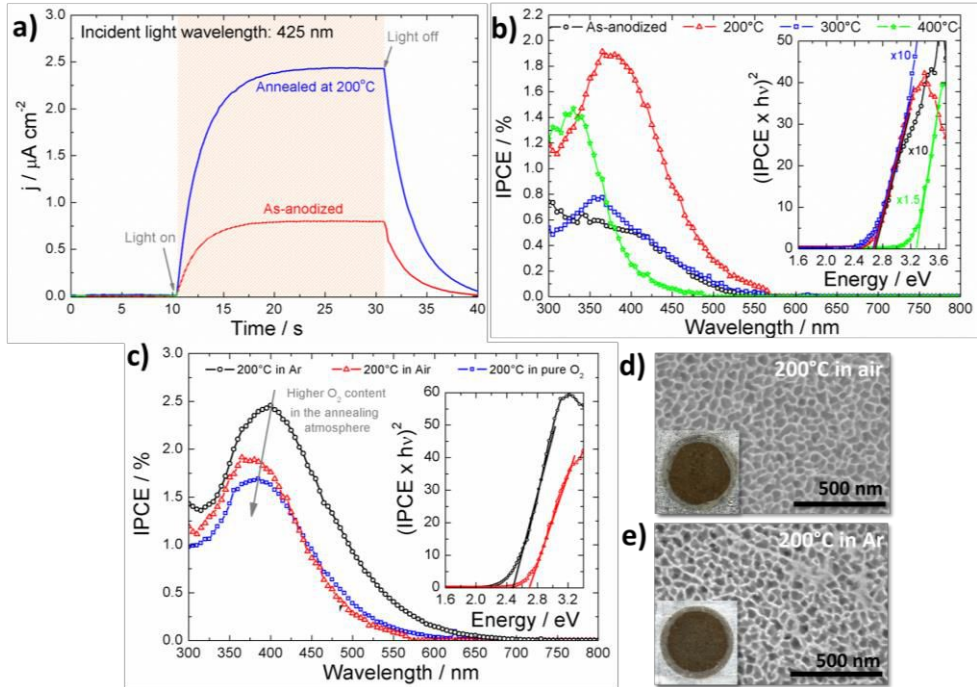


Figure 5.5 a) Photocurrent response at 425 nm for tin oxide samples prepared by applying a potential of 10 V to a tin foil immersed in an electrolyte solution composed of acetonitrile and water (volume ratio 50:50) and containing 0.2 M $\text{Na}_2\text{S}_x\text{H}_2\text{O}$ and 0.1 M NH_4F . Response of both as-formed and layer annealed at 200 °C are shown. Measurement was performed in a borate buffer solution at a constant potential of 0.5 V vs SSC. b) Incident photon to charge carrier efficiency (IPCE) as function of the incident wavelength and determination of the band gap from $(\text{IPCE} \times h\nu)^2$ vs $(h\nu)$ plots (inset) for nanochannelled tin oxide samples prepared in the same conditions as a). c) IPCE as function of the incident wavelength for anodic tin annealed at 200 °C in different atmospheres: Ar, air or pure O_2 . Top-view FESEM micrograph and photograph (inset) of nanochannelled tin oxide samples annealed at 200 °C in d) air and e) Argon atmosphere.

authors [225,226] or in accord with the SAED patterns given in Fig. 5.3 and the XRD patterns in Fig. 4.2 from Chapter 4.

As the Sn^{2+} and oxygen vacancies contents seem to play a key role in the optical properties, and especially on achieving visible photoresponse [216,218], we considered that the annealing atmosphere may also be an important parameter to control. For this purpose, we studied the photocurrent response of samples annealed at 200 °C, where the best photoresponse in the visible range was obtained, under different atmospheres, namely air, Ar and O_2 . In Fig. 5.10c the IPCE vs the incident wavelength of these samples is given together with the FESEM images and its photographs (Fig. 5.5d and 5.5e). By thermal treatment in Ar atmosphere, the efficiency of the material to absorb visible light is enhanced and the absorption edge suffers a red shift. The observed behaviour evidences that the Ar atmosphere prevents the oxidation of Sn^{2+} defects to Sn^{4+} , resulting in a highly doped material, *i.e.* high O vacancies concentration, which yields a lower band gap (~ 2.4 eV)

[216,218]. On the contrary, annealing in O_2 atmosphere lead to larger band gap values of ~ 2.6 eV, similar to what we obtained for air conditions.

5.2.2.2 Photoelectrochemical performance: measurements under simulated solar light

Photoelectrochemical performance of the tin oxide nanochannel structures was further studied by performing chopped light experiments under solar simulated light. First, the response of the samples annealed at different temperatures was evaluated in a 0.5 M Na_2SO_4 solution, as detailed in Fig 5.6a. An increase in the current density is observed upon illumination due to the increment of minority charge carriers, but the current rapidly drops once light is switched off. In as-anodized samples or samples treated at 100 °C, the amplitude of the photoresponse is very small, less than 0.1 mA cm^{-2} . The highest responses, ~ 0.2 mA cm^{-2} , were given by samples annealed at 200 °C, in agreement with the higher IPCE values observed previously in the visible range. Their superior response might arise from the appropriate matching of its band gap with the visible spectra together with its higher conversion efficiencies. However, it must be noticed that dark current values in this 0.5 M Na_2SO_4 solution are very high, especially for the films annealed at temperatures above 200 °C. This is indicative that additional reactions are taking place such as further oxidation or corrosion. The magnitude of this dark current seems to be proportional to the amplitude of the photoresponse, *i.e.* the higher the photoresponse is, the higher it is the dark current. Also, dark current was shown to be strongly dependent on how much time did the sample remain immersed and the number of potential scans performed.

The electrolyte can be a source of corrosion, thus, other electrolytes were explored such as borate buffer or sodium hydroxide. As shown in Fig. 5.6b, in both NaOH and Na_2SO_4 current profiles have a wavy behaviour indicating that other reactions occur whereas in borate buffer, the dark current is considerably minimized. In NaOH, reactivity can come

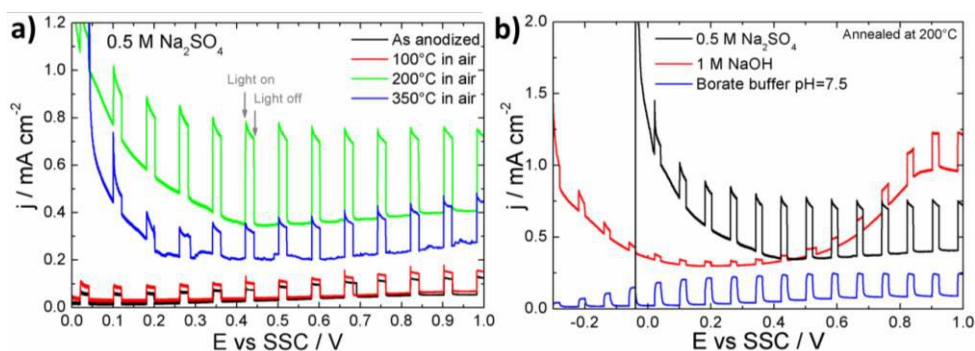


Figure 5.6 a) Current-potential characteristics with chopped light of nanochanneled tin oxide samples annealed at different temperatures. Measurements were performed in a 0.5 M Na_2SO_4 solution, and scanning the potential at 0.002 Vs^{-1} under chopped AM 1.5 (100 $mW\ cm^{-2}$) light. b) Current-potential characteristics under chopped light obtained in different electrolyte solutions (0.5 M Na_2SO_4 , 1 M NaOH and borate buffer) for a nanochanneled tin oxide film annealed at 200 °C.

from the strongly alkaline pH, as Sn(II)-related oxides are amphoteric and become less stable in such conditions [89,90]. XRD and Raman measurements confirmed the presence of SnO and intermediate oxides such as Sn₂O₃ for samples annealed at temperatures below 400°C. Although Na₂SO₄ solutions have a neutral pH, here corrosion might be induced by SO₄²⁻ ions as has been reported in the literature [230]. Taking into account the above-mentioned trends, additional characterization on the effect of the anodization time, the annealing atmosphere and the annealing time was assessed by using an annealing temperature of 200 °C and performing the photocurrent measurements in borate buffer solutions.

Fig. 5.7a displays the photocurrent response for nanochannelled tin oxide structures obtained using different anodization times. Anodization time is directly related to the film thickness as we discussed in Chapter 3. For the thinnest sample, anodized for 2 min, photoresponses lower than 0.1 mA cm⁻² are obtained. Increase in film thickness results in an improvement of the photoresponse but at the same time dark current is enhanced too. A compromise between both is obtained at an intermediate anodization time of 10 min, though the presence of dark current is an important drawback for the stability and long-term use of these electrodes in photoelectrochemical water splitting [203]. Annealing in Ar atmosphere heightened the

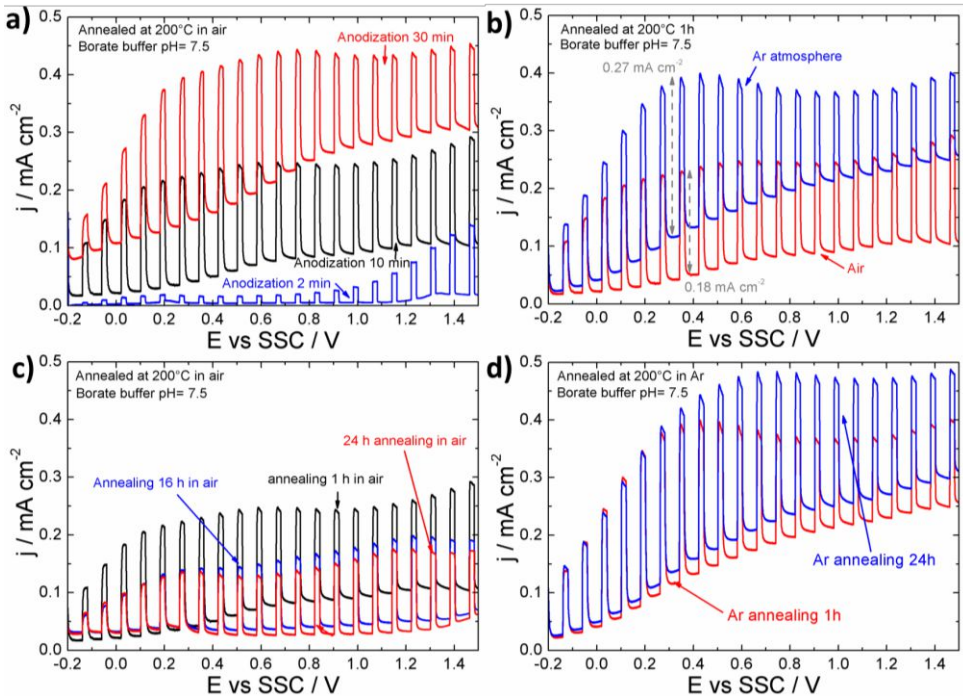


Figure 5.7 a) Current-potential characteristics with chopped light of nanochannelled tin oxide samples with different anodization times 2 min, 10 min and 30 min. b) Current-potential characteristics with chopped light of nanochannelled tin oxide samples annealed at 200 °C in argon and air atmosphere (anodization time: 10 min). Tin oxide nanochannelled structures annealed at 200 °C in c) air or b) argon for different times, ranging from 1 h to 24 h (anodization time 10 min). All measurements were performed in borate buffer solution at pH= 7.5 and scanning the potential at 0.002 Vs⁻¹ under chopped AM 1.5 (100 mW cm⁻²) light.

maximum amplitude of the photoresponse up to 0.27 mA cm^{-2} versus the 0.18 mA cm^{-2} achieved when annealing in air conditions. This is in accord with the enhanced IPCE observed in Fig. 5.7c upon Ar annealing. However, in Ar annealing the dark current is also superior. In both annealing atmospheres, prolonged annealing times were used (Fig. 5.7c and 5.7d). Longer annealing in air, as illustrated in Fig. 5.7c, has two effects: on one side it decreases the photoresponse probably because the amount of Sn^{2+} defects is reduced and, on the other, also the dark current. When prolonged annealing treatments are done in Ar, no significant changes are found (Fig. 5.7d). Overall, this suggests that oxygen vacancies or Sn^{2+} defects are responsible for the dark current observed.

5.1 Summary

In summary, nanochannelled tin oxide structures with thicknesses of $\sim 8 \text{ }\mu\text{m}$ were successfully prepared by anodizing tin foils in an acetonitrile-water mixture-based electrolyte, containing Na_2S and NH_4F . Samples were annealed at different temperatures up to $400 \text{ }^\circ\text{C}$. As-anodized layers (without annealing) are poorly crystalline and might correspond to a SnO_x defective phase with high Sn^{2+} and oxygen vacancies content. Upon annealing at $200 \text{ }^\circ\text{C}$ the crystallinity of the layers was improved but their Sn^{2+} defects persisted in the structure, giving rise to an enhancement in the photocurrent response in the visible range. This effect could be further improved by annealing in Ar conditions, where the E_g can reach values as low as $\sim 2.4 \text{ eV}$. Samples annealed at $300 \text{ }^\circ\text{C}$ present stoichiometric SnO phase, which we attribute either to the disproportionation of the SnO_x phase or to the crystallization of Sn^{2+} rich domains in the structure. Thermal treatment at $400 \text{ }^\circ\text{C}$ leads to a decrease in the SnO content, which is gradually oxidized to SnO_2 as observed in the Raman spectra. In this case, the absorption edge shifts to the UV range, 3.2 eV , in agreement with the expected reduction of oxygen vacancies and Sn^{2+} defects due to the formation of a more stoichiometric SnO_2 ($E_g = 3.6 \text{ eV}$).

The structures were tested for photoelectrochemical water splitting under solar illumination. The best response in terms of generated photocurrent was achieved for samples annealed at $200 \text{ }^\circ\text{C}$ in Ar conditions (0.27 mA cm^{-2}) but this value is far from the values reported in other water splitting systems such as TiO_2 ($\sim 1 - 1.5 \text{ mA cm}^{-2}$). Additionally, an important contribution of the dark current was found, suggesting that Sn^{2+} and vacancy states further react upon the application of an anodic potential.

5.2 Further work

- It is striking that the IPCE vs wavelength behaviour and the calculated band gap of as-anodized tin oxide structures and those annealed at $300 \text{ }^\circ\text{C}$ is quite similar, despite their notable discrepancy in appearance. Both samples show differences in crystallinity, composition, and overall presence of defects. In this situation it is difficult to balance

all the aspects contributing to the observed IPCE trends and it would be interesting to clarify this point.

- Photoluminescence measurements can provide information on the band gap, impurity levels, defects and recombination mechanisms. In the present work it would be of particular interest to corroborate the band gap values obtained by IPCE, confirm the presence of oxygen vacancies and determine its relative concentration.

5.3 Experimental Section

5.2.3 Sample preparation

Polycrystalline tin foils (99.95 %, Advent Ltd.) were ultrasonically cleaned in acetone, ethanol and deionized water ($\sim 18.2 \text{ M}\Omega\cdot\text{cm}$), and then dried in N_2 stream. Substrates were mounted in the bottom of a two-electrode electrochemical cell equipped with a Pt foil as counter electrode. Anodization was performed by applying a constant potential of 10 V with a LAB-SM1500 (ET System, Germany) potentiostat in an electrolyte solution composed of acetonitrile (99.8 %, Sigma Aldrich) and deionized water (volume ratio 50:50) containing 0.2 M $\text{Na}_2\text{S}\cdot x\text{H}_2\text{O}$ (Sigma-Aldrich) and 0.1 M NH_4F (≥ 98.0 %, Sigma-Aldrich). Anodization time for all samples was 10 minutes.

After anodization films were rinsed with deionized water and annealed in a tube-furnace (ZEW 1450-4, Heraeus, Germany) at 200 °C, 300 °C and 400 °C for 1h. Due to the low melting point of metallic tin ($T_{\text{m,Sn}} \sim 230$ °C), annealing at a temperature higher than 300 °C was carried out on top of a copper foil. This allowed us to have a stable support during the annealing process and also a good electrical contact for the subsequent photocurrent measurements. Annealing at $T > 400$ °C was not possible because it caused the delamination of the anodic oxide film from the tin substrate.

5.2.4 Characterization techniques

The morphology of the samples was characterized in a S4800 field-emission scanning electron microscope (FESEM, Hitachi Technologies Corporation, Japan). Transmission electron microscopy (TEM) images and selected area electron diffraction (SAED) patterns were taken with a Philips CM 30 T/STEM microscope. X-Ray diffraction measurements (XRD) were performed with a X'pert Philips MPD diffractometer equipped with a PANalytical X'celerator detector using the $\text{Cu K}\alpha$ ($\lambda = 1.5418 \text{ \AA}$) radiation in the Bragg-Brentano geometry. The phases were identified with the JCPDS database. X-ray photoelectron spectroscopy (XPS) measurements were performed in a PHI 5600 Multi-Technique System (Physical Electronics, USA) with a monochromatic X-ray source (Al $\text{K}\alpha$ line of 1486.6 eV). Raman scattering analysis was carried out in a LabRAM HR 800 (Horiba Jobin Yvon) microscope using the backscattering configuration and the 532 nm line of a

solid-state laser as excitation source. To avoid sample damage by laser heating, measurements were taken at the minimal power density of 0.5 mW.

Photocurrent measurements were performed in a three electrode electrochemical cell equipped with a quartz glass window to illuminate the sample surface, a Ag/AgCl/3M KCl reference electrode (SSC from herein, E vs SHE = +0.210 V) and a Platinum foil as counter electrode. A potential of 0.5 V. vs SSC was applied during the measurements with a Jaissle IMP83 PCT-BC potentiostat (Jaissle Elektronik, Germany). As electrolyte a borate buffer solution prepared by mixing a 0.35 M H₃BO₃ (Sigma Aldrich, 99.5 %) and 0.0375 M Na₂B₄O₇·10H₂O (Sigma Aldrich, ≥ 99.5 %) to reach a pH ~ 7.5 was utilized. A Xe lamp (Oriel 6356) and an Oriel Cornerstone 7400 1/8 m monochromator were used for the optical setup. Incident photon to charge carrier efficiency (IPCE) was calculated from the expression given in (5.3).

$$\text{IPCE}(\%) = \frac{I}{P} \times \frac{1240}{\lambda} \times 100 \quad (5.3)$$

where I is the photocurrent density (A cm⁻²), P de power of the lamp (W cm⁻²), and λ the wavelength (nm). For a direct band gap semiconductor, the band gap (E_g) can be obtained by plotting (IPCE x hv)² vs (hv) and extrapolating the linear region of the plot to the energy axis at (IPCE x hv)² = 0 [231].

The photoelectrochemical experiments were carried out under simulated AM 1.5 (100 mW cm⁻²) illumination provided by a solar simulator (300 W Xe with optical filter, Solarlight; RT) in borate buffer. The same three-electrode configuration than in the photocurrent measurements was employed. Photocurrent vs. voltage (I-V) characteristics were recorded by scanning the potential with a Jaissle IMP 88 PC potentiostat from open circuit potential to 1.5 V (vs Ag/AgCl) at a scan rate of 2 mV s⁻¹ under intermittent illumination.

Chapter 6

Self-ordered SnO₂ as hematite host for photoelectrochemical water splitting applications

The main parameters influencing the photoelectrochemical water splitting efficiency of a semiconducting oxide were discussed in section B.3 from the Introduction Chapter. According to them, SnO₂ is not the optimal semiconductor to be used as photoanode given its large band gap of ~3.6 eV located in the UV range. In Chapter 5, annealing conditions were tailored to achieve absorption in the visible range thanks to the presence of oxygen vacancies and Sn²⁺ defects. Nevertheless, these structures were found to be unstable under operating conditions because they tend to be further oxidized under anodic potential.

In 1976, Hardee and Bard first turned to hematite (α -Fe₂O₃) as a material for photoelectrochemical water splitting when seeking a photoanode that was both stable under anodic polarization and capable of absorbing light with wavelengths longer than 400 nm [232]. Hematite was shown to meet many of the requirements for the water oxidation half reaction: it has a suitable band gap of 2.0 - 2.1 eV, it is stable against photocorrosion, it is earth-abundant, contains nontoxic elements, and is relatively low-cost [202,203,233–248]. However, its poor conductivity and extremely short hole diffusion length (2-4 nm) hamper the charge transport and give rise to high recombination rates of the photo-generated charge carriers in the bulk [234,247]. Both limitations stem from the fact that holes are apparently located in the d orbitals that form very narrow bands [202]. Moreover, the charge transfer at the interface is limited by the mismatch in energy between the acceptor d orbitals of Fe₂O₃ and the donor p orbital of the oxygen or hydroxide redox couple in solution [202].

To improve these weaknesses of Fe_2O_3 , nanostructured electrodes including nanoparticles, nanowires, and nanonets have been proposed [233,236,240,245,247]. Nanostructured photoanodes offer an increased semiconductor | electrolyte interface area for water oxidation and substantially reduce the diffusion length for minority carriers [247]. For instance, nanonet-based hematite photoanodes achieved an excellent photocurrent of 1.6 mA cm^{-2} at 1.23 V versus RHE, which is four times higher than the value obtained for a planar sample with the same thickness [243,247]. Further improvement on the photoactivity of hematite can be achieved by doping. The role of dopants such as Ti, Si, Al, Mg, Zn, Pt, Mo, and Sn, has been investigated [234,236,237,240,245,247]. Recently, there is an increasing interest in developing Sn-doped hematite due to its enhanced electroconductivity. In 2010, Sivula *et al.* reported that the thermal treatment of solution-processed Fe_2O_3 films at a sufficiently high temperature (800 °C) induced the diffusion of tin atoms from a transparent fluorine-doped tin oxide (FTO) substrate [238,247] improving the overall water splitting performance.

Finally, another possible promising approach to tackle some of the inherent problems of hematite is to distribute the active light absorbing Fe_2O_3 nanostructures on a suitable transparent conductive/semiconductive scaffold [243,248,249]. This often called “host-guest approach” consists on providing a 3-dimensional (3D) support material for majority carrier conduction (“host”), into which the photoactive “guest” nanoscale material can readily inject photo-generated electrons. The use of such host-guest strategies significantly lowers the functional requirements of the photo-absorbing material but depends upon the availability of the “host” material and its characteristics. In general, good electronic transport properties, appropriate band alignment and low optical absorption in the visible light range are indispensable. In this view, SnO_2 offers the optical transparency and good conducting properties required, especially when doped with other elements like F, In, Nb, Sb, *etc.* [249–254]. So, upon suitable doping, our nanochannelled tin oxide structures would offer the high surface area needed for such 3D scaffolds. Stefik *et al.* [249] have recently reported a similar approach by depositing niobium doped tin oxide (NTO) onto high surface area templates, and subsequently coating the electrode with hematite. Peng *et al.* [253] reported also host-guest structures by coating a solution-processed antimony-doped tin oxide (nanoATO) nanoparticle film with a TiO_2 photo-absorber. The conductive nanoporous ATO film-supported TiO_2 electrode yielded a photocurrent density of 0.58 mA cm^{-2} .

6.1 Specific goals of this chapter

- Find the best conditions to obtain nanochannelled tin oxide structures on Sn/ITO substrates and successfully dope them with antimony.
- Build up a host-guest system by depositing Fe_2O_3 nanoparticles onto the Sb:SnO₂ nanochannelled matrix.
- Optimize the conditions that give the best water splitting efficiency (thickness of the SnO₂ layer, Sb doping content, hematite deposition time, *etc.*).

6.2 Results and discussion

6.2.1 Building-up the photoanode

To prepare the ATO/ α -Fe₂O₃ electrodes for photoelectrochemical water splitting applications, we follow the procedure described in Figure 6.1a. As starting point, we use evaporated Sn films on FTO substrates. The morphology and cross-sectional view of $\sim 1 \mu\text{m}$ thick Sn layer is given in Fig. 6.1b and 6.1c respectively. By self-ordering anodization of this Sn layer in an organic-based Na₂S and NH₄F electrolyte a porous SnO_x film, consisting of aligned nanochannels, is formed. Then, a Sb impregnation and annealing treatment is used to increase the conductivity and fully convert the oxide porous structure into SnO₂. Finally, FeOOH particles are deposited into the Sb-doped SnO₂ by an anodic electrodeposition treatment [244]. The FeOOH particles are transformed into hematite (Fe₂O₃) by an adequate thermal treatment in an Ar atmosphere, as previously described in the literature [246]. The overall process leads to the conformal coatings of Fe₂O₃ particles onto the SnO₂ scaffolds as illustrated in Fig. 6.1a.

6.2.2 Structure, morphology and composition

Fig. 6.2a and 6.2b show the typical morphology of the as-grown amorphous anodic SnO₂ layer obtained after anodizing the Sn/FTO in a sulphide-based organic electrolyte (ethylene glycol and water (20:80 vol. %) containing 0.2 M Na₂S·xH₂O and 0.1 M NH₄F). Here, an ethylene glycol-based electrolyte was used instead of the optimized acetonitrile solution because it allowed a better control of the anodization time before the film is detached and led to improved top-open structures [214]. The low magnification FESEM image (Fig. 6.2a)

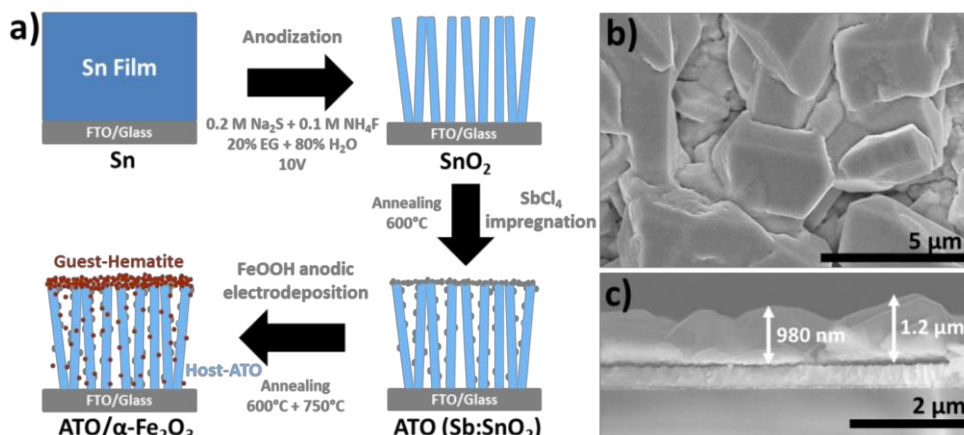


Figure 6.1 a) Schematic diagram of the process developed to obtain FTO-Sb doped porous SnO₂ (ATO) film supported α -Fe₂O₃ PEC electrodes by anodic electrodeposition. FESEM b) top and c) cross-sectional view of a $\sim 1 \mu\text{m}$ thick Sn film evaporated on FTO used for the preparation of porous SnO₂ films.

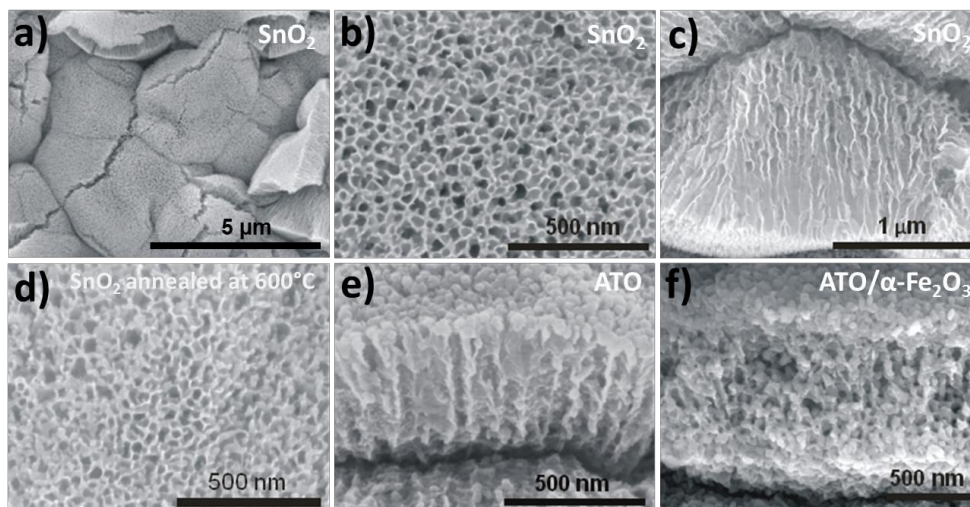


Figure 6.2 FESEM top (a and b) and c) cross-sectional view of anodized porous SnO₂ (Sn film thickness ~1500 nm). d) FESEM image of the same film after annealing at 600 °C during 1 h. e) Cross-sectional micrograph of the ATO film annealed at 600 °C for 1 h in air and (f) ATO/α-Fe₂O₃ annealed in 600 °C for 1 h and 750 °C for 20 min in Ar.

gives an overview of the sample surface. It has a faceted surface morphology with a long-range wave-like shape, due to the use of evaporated Sn layers on FTO (Fig. 6.1a). Despite this coarse inhomogeneity, the surface is fully covered with a continuous oxide layer that contains channels perpendicular to the surface as can be seen in the cross section image from Fig. 6.2c. The irregular porous oxide structure has a typical pore size of approximately 40 nm. Upon annealing at 600 °C, the porous structure is maintained and a slight thickening of the nanochannel walls is observed (Fig. 6.2d). Fig. 6.2e shows the corresponding FESEM image after Sb impregnation and subsequent annealing at 600 °C in air. Some round particles with a size of ~ 20 - 40 nm become apparent on the top surface and in the channel structure. After deposition of α-Fe₂O₃ and appropriate annealing treatment (Fig. 6.2f) the surface of ATO is homogeneously decorated by α-Fe₂O₃ nanoparticles of ~ 50 - 80 nm in size.

The successful SnO₂ doping achieved by Sb impregnation was evidenced by XPS (Fig. 6.3b) and the drastic improvement of the electrical conductivity (Fig. 6.3a). The average resistance of an undoped SnO₂ layer is ~ 1.5 KΩ while, when treated with Sb, its value can be decreased two orders of magnitude (~ 30 Ω). Good conductive properties are of great importance to obtain a suitable Fe₂O₃ support material. The effect of the Sb doping in the photoelectrochemical water splitting response will be later discussed. The distribution of Sn, O and Sb through the nanochannel structure is shown in the XPS sputter depth profiles in Fig. 6.3c. Here, a high Sb concentration can be appreciated at the surface and a tail throughout the whole SnO₂ film. The high resolution Sn 3d XPS spectrum for SnO₂ samples with various Sb contents is shown in Fig. 6.3d. A shift in the barycenter of the core level

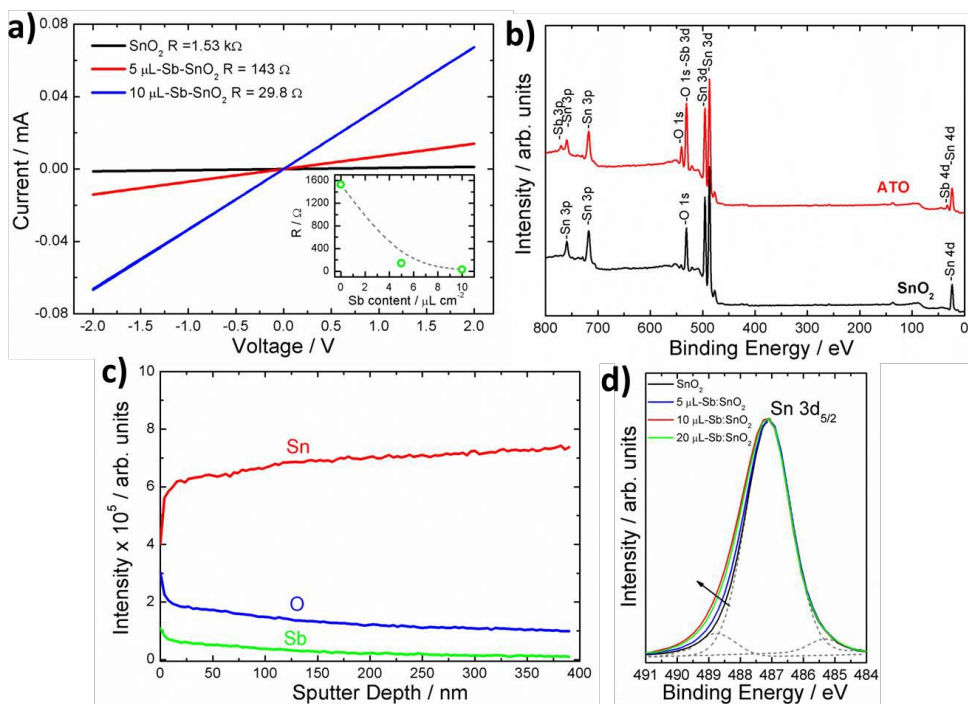


Figure 6.3 a) I-V curves for ATO samples with different Sb contents and comparison of their electrical resistance (inset). b) XPS survey spectrum of SnO₂ and Sb:SnO₂ (ATO) samples after annealing at 600 °C for 1 h in air. c) XPS depth profile for an ATO film (thickness Sn film ~ 500 nm) and high resolution Sn 3d_{5/2} spectra of ATO samples using different volumes of 0.125 M SbCl₄ solution for impregnation.

binding energy with the increasing Sb doping is observed. This asymmetric shape of the Sn 3d peak is typically observed for successfully Sb-doped SnO₂ where the asymmetry increases with increasing Sb-induced charge carrier concentration [227].

Figure 6.4a shows the XRD patterns of the ATO and ATO/ α -Fe₂O₃ samples. The ATO sample after annealing at 600 °C for 1 h in air shows the tetragonal rutile SnO₂ structure and a smaller SnO peak. After deposition of FeOOH and annealing in Ar, the sample shows α -Fe₂O₃ (JCPDS 86-0550) [244] and tetragonal SnO₂ signals. The elemental composition of ATO/ α -Fe₂O₃ was further studied by XPS. A representative survey spectrum is presented in Fig. 6.4b and the corresponding high-resolution XPS peaks of Fe 2p, Sb 3d, O 1s, and Sn 3d are shown in Fig. 6.4b and 6.4c. For the ATO/ α -Fe₂O₃ sample, the Sb 3d_{5/2} peak is overlapped with O 1s (Fig. 6.4c). In consequence, the Sb 3d_{3/2} transition was used to obtain the oxidation state of antimony. The peak at 540.0 eV can be separated into two contributions corresponding to Sb (V) and Sb (III) [250,252,254]. Analysis of the Sn 3d region shows two major peaks at 487.9 eV (3d_{5/2}) and 496.3 eV (3d_{3/2}) that confirm the presence of Sn⁴⁺ ions in the hematite sample. An in-depth XPS profile of the ATO/ α -Fe₂O₃ structure is shown in Fig. 6.4d. After the α -Fe₂O₃ deposition and high temperature annealing,

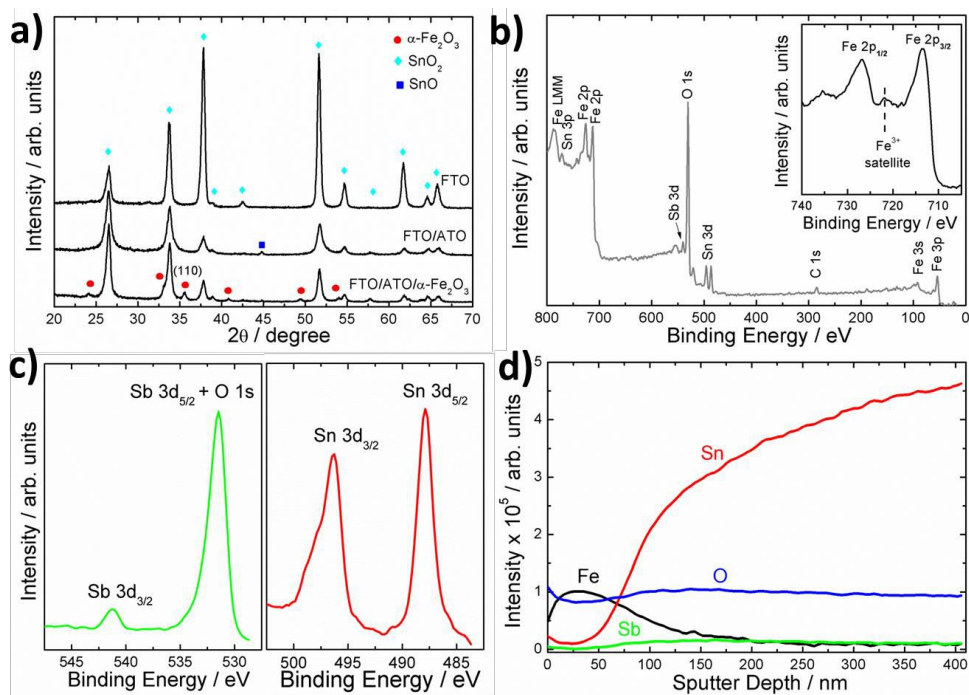


Figure 6.4 a) XRD patterns of the annealed ATO and ATO/ $\alpha\text{-Fe}_2\text{O}_3$ electrodes. b) XPS survey spectrum and high resolution Fe 2p spectrum (inset). c) XPS depth profile for Fe, Sn, Sb and O species and d) high resolution Sb 3d, O 1s and Sn 3d peaks.

the Sb distribution is homogenized over the SnO_2 thickness indicating diffusion penetration. At the same time, a Sn concentration tail throughout the $\alpha\text{-Fe}_2\text{O}_3$ is obtained. This phenomenon of Sn diffusion upon high temperature annealing is the so-called unintentional Sn doping and has been found to contribute positively to the photoelectrochemical performance of hematite films [247].

6.2.3 Photoelectrochemical performance

Photocurrent densities were measured in a shuttered mode as a function of an applied potential in a 1 M KOH electrolyte using AM 1.5 ($100 \text{ mW}\cdot\text{cm}^{-2}$) simulated solar illumination. The effect of the Sb doping is shown in Fig. 6.5a. For undoped electrodes, the photoelectrochemical performance is very low, below 0.1 mA cm^{-2} . Upon Sb incorporation the photoresponse is considerably improved and $10 \mu\text{L}$ of 0.125 M SbCl_4 was shown to be the optimum loading for a constant hematite deposition time. For the electrodes that were deposited with various amounts of FeOOH (Fig. 6.5b), the photocurrent increases dramatically as the deposition time is increased from 8 min to 15 min, due to the corresponding increase in photo-absorbing material and surface area of the films. It

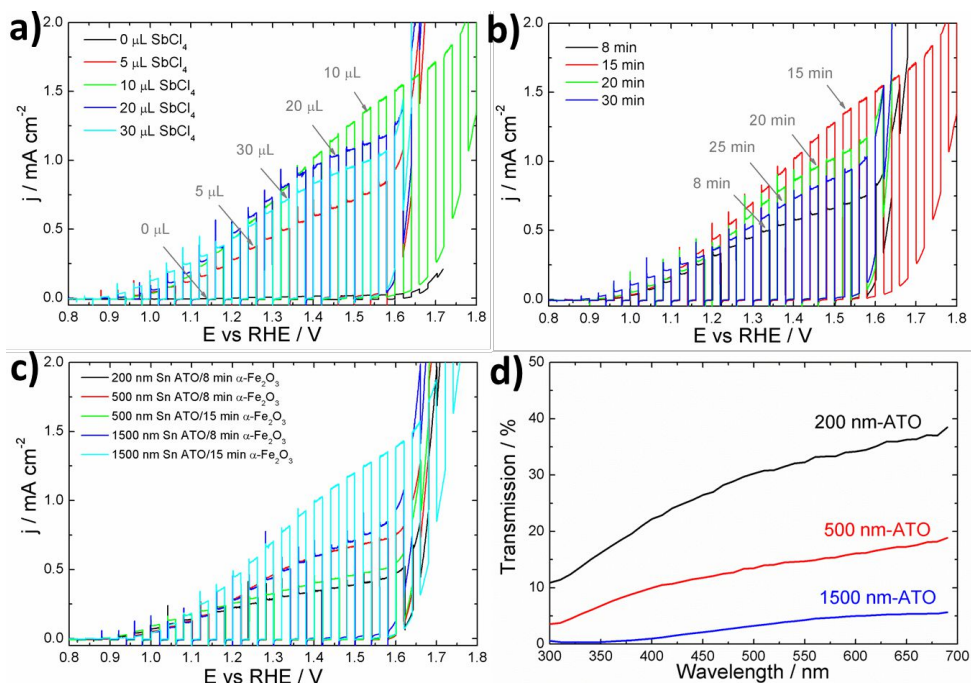


Figure 6.5 Current-potential characteristics with chopped light of ATO/ α -Fe₂O₃ electrodes: a) various Sb contents (deposition FeOOH for 15 min); b) various FeOOH deposition times (10 μ L of 0.125 M SbCl₄); c) different thickness of the Sn film. The measurements were performed in 1 M KOH solution (pH 13.6) at a scan rate of 0.002 Vs⁻¹. Photocurrents are excited with AM 1.5, 100 mW cm⁻² simulated sunlight. d) Transmission spectra in the UV-Vis region of ATO films of different thickness after annealing at 600 °C for 1 h.

gradually decreases for deposition times extended to 20 - 25 min. This decrease can be attributed to the large amount of hematite introduced into the channel structure, which leads to the reduction of porosity in the ATO/ α -Fe₂O₃ films (see FESEM images in Fig. 6.6). The optimum ATO/ α -Fe₂O₃ electrode with 15 min deposition time shows a plateau from 0.7 V to 1.5 V, and a maximum photocurrent density of 1.5 mA cm⁻² at 1.5 V vs RHE. The influence of the ATO layer thickness is analysed in Fig. 6.5c. ATO layers prepared by anodizing Sn layers of 1500 nm in thickness exhibit a photoresponse two times larger than those having 200 nm and 500 nm. Of course an increase in the Sn thickness is detrimental for the optical properties as shown in Fig. 6.5d, but probably larger exposed surface area and a better penetration of the hematite particles through the ATO nanochannels is achieved.

Fig. 6.7a shows the incident photon to current conversion efficiencies (IPCEs) as a function of incident light wavelength for the ATO/ α -Fe₂O₃ electrodes measured at the applied potential of 1.5 V (vs RHE) in 1 M KOH. The IPCE data are in line with the results obtained from the photoelectrochemical measurements under AM 1.5, illustrated in Fig. 6.5b. Over the entire range from 300 nm to 600 nm, Sb loading leads to an enhanced IPCE compared to

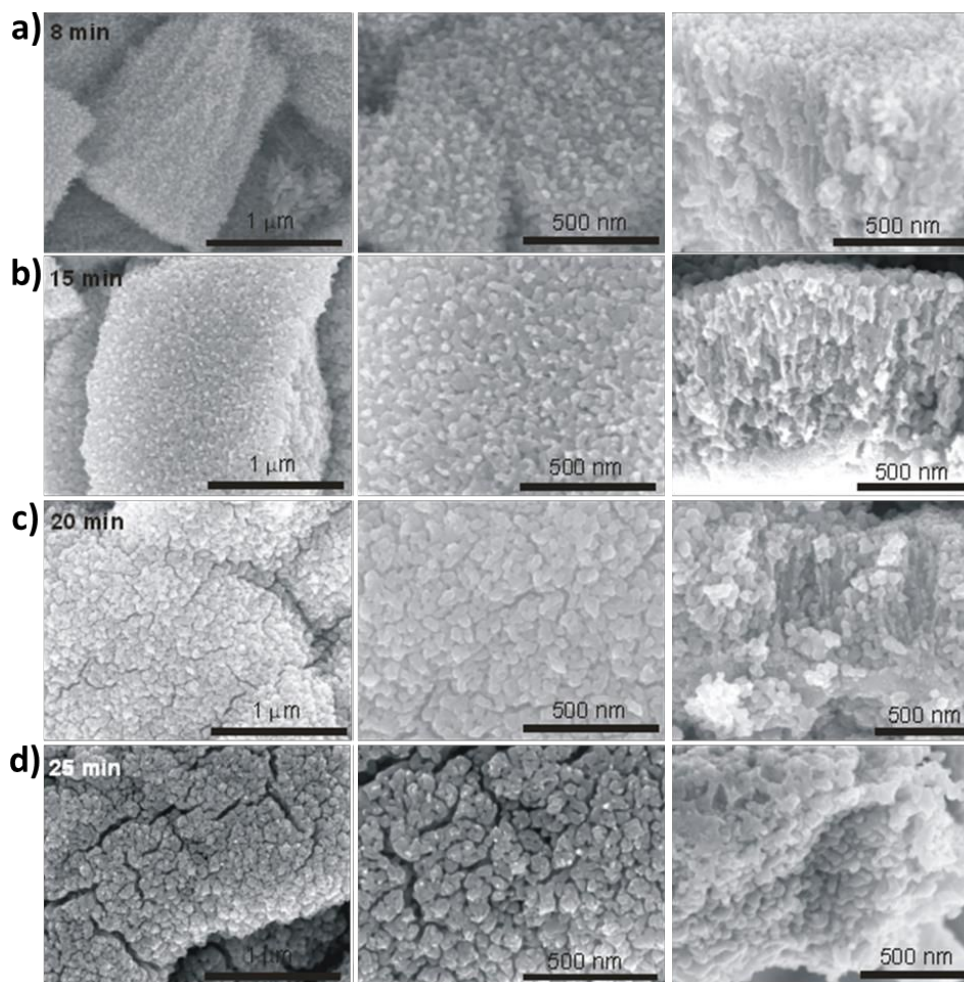


Figure 6.6 FESEM top view of ATO/ α -Fe₂O₃ electrodes with different FeOOH deposition times a) 8 min, b) 15 min, c) 20 min and d) 25 min and subsequently annealed in Ar at 600 °C and 750 °C for 20 min.

the Sb-free sample, and a maximum IPCE value of 19% at 330 nm is achieved for the ATO/ α -Fe₂O₃ electrode with 15 min FeOOH deposition. Replotting the data as $(\text{IPCE} \times h\nu)^{1/2}$ vs photon energy (see details in Experimental Section 6.5), the band gap was extracted. The indirect transition is located at ~1.9 - 2.0 eV (Fig. 6.7b). Usually, an indirect transition has been reported in hematite although few recent works report a direct band gap [238].

The effect of the Sb/Sn doping can also be evaluated from the transient photoresponse (Fig. 6.7c). In general, the transients have a very similar shape characterized by an initial spike followed by a gradual decay in current. This shape is associated to the accumulation of photogenerated holes at the semiconductor | electrolyte interface due to the slow oxygen

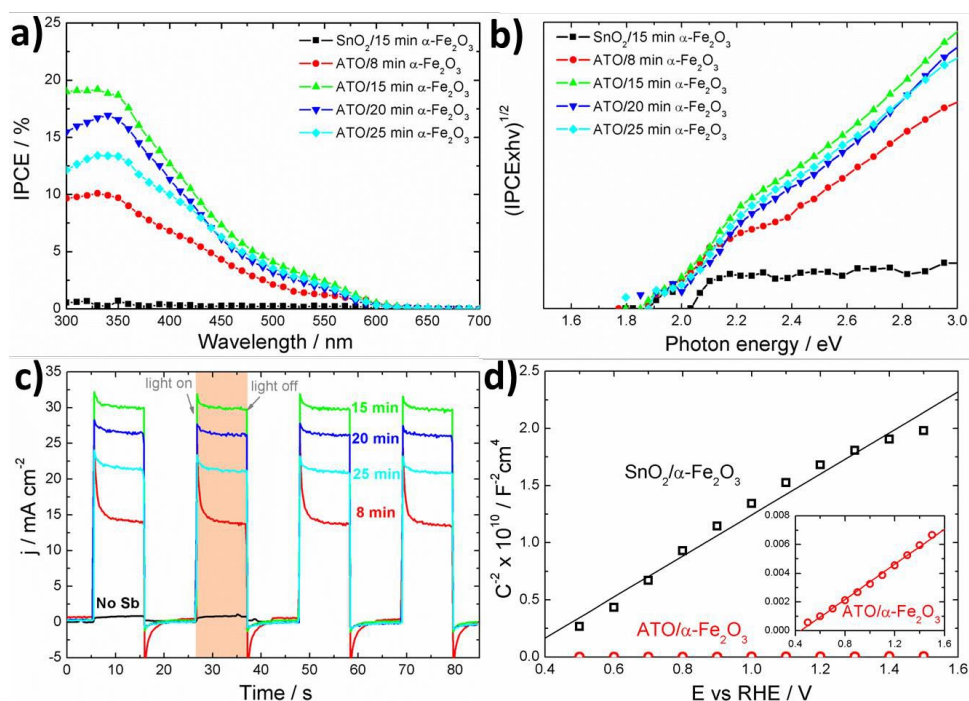


Figure 6.7 a) Incident photon to current conversion efficiency (IPCE) in 1 M KOH solution of ATO/α-Fe₂O₃ electrodes with different hematite deposition times and band gap determination from a b) (IPCE × λ)² vs photon energy (hν) plot assuming an indirect transition. c) Photocurrent at 360 nm at an applied potential of 1.5 V (vs RHE) in 1 M KOH for SnO₂/α-Fe₂O₃ and ATO/α-Fe₂O₃ electrodes. e) Mott-Schottky plots for SnO₂/α-Fe₂O₃ and ATO/α-Fe₂O₃ electrodes in 1 M KOH in dark, recorded at a frequency of 500 Hz.

evolution reaction kinetics near the onset potential. In such case, then, recombination in the bulk (or at grain boundaries) does not limit charge carrier transport [238]. Upon successful Sb/Sn treatment, the entire transient magnitude is increased, *i.e.* this is in line with bulk doping (conductivity) being the main beneficial effect of the Sb treatment.

To additionally substantiate the role of Sb doping on the electronic properties of SnO₂, Mott-Schottky measurements were performed for the SnO₂/α-Fe₂O₃ and ATO/α-Fe₂O₃ samples as presented in Figure 6.7d. From the Mott-Schottky expression in (6.2) of the Experimental details (see also Section A.2 from Introduction in Part A) the semiconductor type, the carrier density and the flat band potential at α-Fe₂O₃/electrolyte interface were estimated [245] (ϵ for hematite = 80 [236]). From positive slopes in Mott-Schottky plots, n-type character of hematite is confirmed. Moreover, donor densities for SnO₂/α-Fe₂O₃ and ATO/α-Fe₂O₃ were estimated to be $9.75 \times 10^{19} \text{ cm}^{-3}$ and $2.89 \times 10^{22} \text{ cm}^{-3}$, respectively, being clearly higher for the Sb doped sample. The flat band potential around ~ 0.3 - 0.4 V vs RHE is in agreement with other works [236].

6.3 Summary

Porous tin oxide films with nanochannel architecture were prepared on FTO substrates and successfully doped with antimony to improve their conducting properties. This conductive, transparent oxide structure was used as a host for α -Fe₂O₃ nanoparticles. Upon optimization of the hematite deposition time, the thickness of the SnO₂ layer and the Sb loading, the photoelectrochemical performance of this host-guest system showed photocurrents of up to 1.5 mA cm⁻² at 1.6 V (vs RHE) in 1 M KOH under AM 1.5 (100 mW cm⁻²) illumination. The significant improvement in photocurrent can be attributed to a successful Sb doping of the SnO₂ structure displaying a high surface area and a nanochannelled geometry.

6.4 Further work

- Try other possible applications of these transparent conductive porous antimony-doped tin oxide structures, for example, in dye-sensitized solar cells. Attempts with undoped samples were done but they lead to very low efficiencies probably due to its high resistance.

6.5 Experimental details

6.5.1 Sample preparation

Nanochannelled SnO₂ layers of different thicknesses were prepared by anodizing evaporated tin films of ~200 nm, ~500 nm, and ~1500 nm. Tin evaporation on fluorine-doped tin oxide substrates (FTO-15 Ω , Solaronix, Switzerland) was carried out with a PLS 500 evaporation system (Balzers-Pfeiffer, Germany) using 2-4 mm tin granules (99.999 %, Chempur) as metal source. Deposition was performed at a rate of 0.1 nm s⁻¹ and a pressure between 1 x 10⁻⁶ and 6 x 10⁻⁶ mbar.

Anodization was done at room temperature in a solution of ethylene glycol (Sigma Aldrich) and deionized water (20:80 vol. %) containing 0.2 M Na₂S_xH₂O (Sigma-Aldrich) and 0.1 M NH₄F (98 %, anhydrous, Sigma-Aldrich). A conventional electrochemical cell in the two-electrode configuration with a platinum foil as counter electrode was used. Under optimized conditions, anodization was conducted at 10 V for different durations (*i.e.* 0.5, 1, and 2 min for ~200 nm, ~500 nm, and ~1500 nm Sn films, respectively) using a LAB-SM 1500 power source (ET System, Germany). After anodization, samples were rinsed with ethanol and then dried in a N₂ stream.

Antimony-doped porous tin oxide (ATO) was prepared by dropping on top of the anodized SnO₂ layers (0.785 cm² surface area) a series of volumes (5 μ L, 10 μ L, 20 μ L, and 30 μ L) of

a freshly prepared solution of 0.125 M SbCl₄ (99 %, Sigma-Aldrich) in ethanol. Then samples were annealed in a furnace (Heraeus, TYP ROK 6.5/60) in air at 600 °C for 1 h.

In order to fabricate FeOOH nanoparticles, anodic electrodeposition was carried out using an aqueous acidic solution (pH = 4.1) containing 0.02 M FeSO₄·7H₂O (99 %, Sigma-Aldrich) according to literature [244,246]. The anodic deposition was done at ~ 70-80 °C by applying a constant potential of 1.2 V (Voltcraft VSP 2653) for 8, 15, 20, and 25 min. Subsequently, the samples were annealed in Ar atmosphere at 600 °C for 1 h and further annealed at 750 °C for 20 min. For the Ar annealing, the furnace (Heraeus, ZEW 1450-4, Germany) was purged with argon (99.9 %, Linde Gas, Germany) at least for 20 min in a flux of 300 mL min⁻¹ before the treatment.

6.5.2 Characterization techniques

The morphology of the samples was characterized in a field-emission scanning microscope (Hitachi FESEM S4800, Japan). X-ray diffraction measurements were performed with a X'pert Philips MPD diffractometer equipped with a Panalytical X'celerator detector using graphite monochromized Cu K α radiation (Wavelength 1.54056 Å). Chemical characterization was carried out by X-ray photoelectron spectroscopy in a PHI 5600 Multitechnique System (Physical Electronics, USA) using a monochromatic X-ray source (AlK α line of 1486.6 eV).

For the solid-state conductivity measurements, first, 300 nm thick Pt dots were evaporated onto the porous surface using a shadow mask (3 mm in diameter). Subsequently, electrical contact was established by connecting two Au wires on top of the Pt contacts (2-point measurements setup) [255]. Then, resistivity values were calculated from the I-V curves.

The photoelectrochemical experiments were carried out under simulated AM 1.5 (100 mW cm⁻²) illumination provided by a solar simulator (300 W Xe with optical filter, Solarlight; RT) in 1 M KOH solution. A three-electrode configuration was used in the measurement, with the α -Fe₂O₃ electrode serving as the working electrode (photoanode), a Ag/AgCl (3 M KCl) as the reference electrode, and a platinum foil as the counter electrode. Photocurrent vs voltage (I-V) characteristics were recorded by scanning the potential with a Jaissle IMP 88 PC potentiostat from -0.5 V to 0.9 V (vs Ag/AgCl) at a scan rate of 2 mV s⁻¹ under intermittent illumination. The measured potentials vs Ag/AgCl were converted to the reversible hydrogen electrode (RHE) scale using the relationship $E_{\text{RHE}} = E_{\text{Ag/AgCl}} + 0.059 \text{ pH} + E_{\text{Ag/AgCl}}^0$, where $E_{\text{Ag/AgCl}}$ is the experimentally measured potential and $E_{\text{Ag/AgCl}}^0 = 0.209 \text{ V}$ at 25 °C for a Ag/AgCl electrode in 3 M KCl.

Photocurrent measurements were performed also in the three-electrode configuration in a cell equipped with a quartz glass window to illuminate the sample. A 1 M KOH electrolyte and a potential of 0.5 V (vs Ag/AgCl) applied with a Jaissle IMP83 PTC-BC potentiostat (Jaissle Elektronik, Germany) was used for the measurements. A 150 W Xe lamp (Oriel

6356) and an Oriel Cornerstone 7400 1/8 m monochromator were employed to do 10 nm steps in the 300-700 nm wavelength range. Incident photon to charge carrier efficiency (IPCE) was calculated from the expression given in (6.1).

$$\text{IPCE}(\%) = \frac{I}{P} \times \frac{1240}{\lambda} \times 100 \quad (6.1)$$

where I is the photocurrent density (A cm^{-2}), P de power of the lamp (W cm^{-2}), and λ the wavelength (nm). For an indirect band gap semiconductor, the band gap (E_g) can be obtained by plotting $(\text{IPCE} \times h\nu)^{1/2}$ vs $(h\nu)$ and extrapolating the linear region of the plot to the energy axis at $(\text{IPCE} \times h\nu)^{1/2} = 0$ [231].

The Mott-Schottky curves were performed in a Zahner IM6 (Zahner Elektrik, Kronach, Germany). Measurements were obtained under dark conditions at a frequency of 500 Hz in 1 M KOH solution, amplitude +/-10 mV. The semiconductor type, the carrier density and the flat band potential were extracted from equation (6.2).

$$\frac{1}{C_{\text{Total}}^2} = \frac{2}{\epsilon\epsilon_0 e N_D} \left(E - E_{\text{FB}} - \frac{k_B T}{e} \right) \quad (6.2)$$

Conclusions

Conclusions

The study of the electrochemical oxidation behaviour of tin in alkaline media, the development of anodic self-ordered tin oxide nanostructures and its application to laboratory scale devices have been the main focus of this PhD Thesis.

In part A, the passivation process of Sn has been studied from an electrochemical approach covering the whole range from hydrogen evolution to the final passivation of the metal. In **Chapter 1**, the oxides formed in each relevant potential region have been characterized by *ex situ* techniques and a mechanism for the process has been proposed by correlating composition, morphology and electronic properties. In the potential region between -1.1 V and -0.9 V vs SSC, a first peak in the current response appears. Here, a white primary passive SnO·nH₂O film is formed by a dissolution-precipitation mechanism. At very high pH, this layer becomes unstable given the amphoteric nature of the Sn(II) species. This hydrated primary oxide is amorphous and porous, so it does not effectively passivate the electrode surface. At potentials between -0.9 V and -0.7 V vs SSC, the current increases again and the second peak composed of several contributions shows up. In this electrochemical range, black three-dimensional SnO crystals start to precipitate from the supersaturation of Sn²⁺ species generated as a result of a severe etching process. Surface etching is evidenced by the pyramidal pits found at the metal/SnO interface. The strong dependence of this etching process on the NaOH concentration, suggests the formation of soluble Sn(II) hydroxocomplexes of high coordination number. When potentials larger than -0.7 V vs SSC are attained the current starts to drop and both the SnO formation and the etching process cease. Here, the final electrode passivation takes place as a result of a n-type semiconducting Sn(IV)-based film formation. Results presented indicate that the SnO crystals do not play a role in the passivation process and that the actual Sn(IV)-based passive layer develops at the Sn/SnO interface.

Also, *in situ* techniques like EC-STM were used to gain more knowledge on the growth mechanism, especially for the first passivation process. The work described in this **Chapter 2** was one of the most challenging because of the inherent difficulties of the technique and the lack of references in the literature on this kind of studies for Sn surfaces. In fact, as this part corresponds to the last experiments carried out during this Thesis, there are still points that need to be clarified and the model is still under discussion. For instance, the nature of

the initial islands on the Sn surface is not clear. These regions have a positive apparent height of ~0.05 nm, are mainly located at the step edges and do not grow with the increase in the anodic potential. Three different possibilities have been suggested: OH islands like those reported for Ni or Cu, a surface reconstruction or localized impurities. The most straightforward explanation would be the OH islands but there are aspects that substantially differ from the behaviour observed in transition metals. For example, OH islands are usually located at the step edges, have a negative apparent height, and tend to grow and coalesce under the application of a higher voltage. Considering that reconstruction processes are also potential dependent, further experiments are required to know whether the bright islands might correspond to regions where impurities are accumulated or not. Additionally, these islands seem to favour the redeposition of metallic Sn dissolved from the step edges before the dissolution pits and oxide precipitation take place.

The second part of this PhD Thesis, the so-called part B, is more oriented to applied science. In this line, **Chapter 3** is aimed to find a proper electrolyte to grow self-ordered tin oxide structures without the actual limitations of those prepared in oxalic acid or NaOH: clogged pores and cracks on its cross-section. The opening of the pores provides a higher specific area whereas the continuity of the channels improves the conducting properties and the transference of electrons through the structure. Once proper structures are attained, in order to assess their value, applications such as gas sensing or photoelectrochemical water splitting were attempted in the successive Chapters 4, 5 and 6. At this point, the low melting point of Sn (230 °C) became an important issue to solve because for conversion into SnO₂ thermal treatment at temperatures higher than 500 °C was required. Here, the use of evaporated Sn layers on substrates such as Si wafers or FTO/glass was introduced.

In **Chapter 4**, the nanochanneled tin oxide structures were applied in H₂ gas sensing. Our layers proved to have superior characteristics by detecting H₂ concentrations as low as 9 ppm and by operating at relatively low temperatures (80 °C). The performance is comparable to that of noble-metal doped SnO₂ particles or single SnO₂ nanowires and superior to that of other self-ordered structures prepared in non-optimized conditions or oxalic acid.

Self-ordered tin oxide structures have a dark brown colour far from the white expected for SnO₂ ($E_g = 3.6$ eV) due to the high amount of Sn²⁺ and oxygen vacancies present in the structure. These defects are known to introduce states in the band gap. Taking advantage of them and by adjusting the annealing conditions, SnO₂ structures with absorption in the visible range can be achieved as shown in **Chapter 5**. A band gap of 2.4 eV was achieved for self-ordered tin oxide structures annealed at 200 °C in Ar due to the improved crystallinity, with respect to as-grown samples, together with the conservation of the Sn²⁺ defects and oxygen vacancies. Despite the enhancement in collecting visible light, the structures were found to be unstable in the photoanode working conditions. The further oxidation occurring during the photoelectrochemical performance seems to arise from the Sn²⁺ defects and vacancies themselves. In these sense, the use of our anodic tin oxide structures as absorber in photoanodes for efficient water splitting was discarded.

In **Chapter 6**, an alternative approach to build up photoanodes is proposed. The system combines the good conducting properties of antimony doped-SnO₂ and the high surface area of the nanochanneled structures with the stability and good visible absorption of hematite nanoparticles. By building up this host-guest system some of the limitations of hematite like its poor conductivity and extremely short hole diffusion length are overcome. Although the role of SnO₂ here is just as charge collector, the overall performance of the photoanodes was shown to be strongly dependent on its characteristics. Photocurrents up to 1.5 mA cm⁻² at 1.6 V (vs. RHE) in 1 M KOH under AM 1.5 (100 mW cm⁻²) conditions were achieved, in line with values reported for other reported hematite nanostructured electrodes.

To end up with this conclusions chapter we will provide a short list of goals achieved and final remarks:

1. Anodic behaviour of tin in alkaline solution has been revised. Three main processes have been identified: the formation of a SnO·nH₂O primary passive layer; the hydroxyl induced etching of tin and concurrent SnO precipitation; and the final passivation due to the growth of Sn(IV) based oxides.
2. The protocol for the preparation of atomically flat and oxide free Sn surfaces has been optimized. This stage was crucial for the posterior EC-STM observations.
3. The early stages of anodic oxidation were followed *in situ* at the nanometer scale. Before the onset of the first oxidation peak, the formation of islands and metal dissolution and redeposition phenomena were observed. The composition of these islands is still under study.
4. Self-ordering anodization has proved to be a cheap, straightforward, and valuable technique for the fabrication of nanostructured tin oxide layers. Nanochanneled films without inner cracks and top-open pores were attained in a Na₂S-based electrolyte. The structures have been successfully implemented in gas sensors or anodes for photoelectrochemical water splitting.
5. Self-ordered anodic layers are amorphous, so they need to be thermally treated at temperatures above 500 °C for its final application in devices. The problem with the low melting point of metallic tin has been solved by anodising evaporated Sn films on Si wafers or FTO/glass substrates.
6. H₂ gas sensors based on self-ordered SnO₂ films showed a fast response, a linear dependence with increasing target gas concentrations and sensitivity to H₂ contents as low as 9 ppm. Moreover, it showed good sensing response even when operating at relatively low temperatures.
7. SnO₂ layers with visible absorption were attained by adjusting the annealing conditions. The visible absorption is given by Sn²⁺ defects and oxygen vacancies

which makes them unstable during photoelectrochemical water splitting performance.

8. Host-guest anodes combining self-ordered SnO₂ and hematite have been built up for water splitting. The successful antimony doping of the SnO₂ structure is critical to achieve good photoresponse.

Appendices

Appendix a

SnO electrosynthesis: effect of electrochemical conditions on the growth of microcrystals

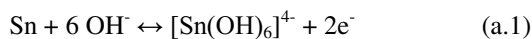
Introduction

In Chapter 1, tin anodization in alkaline media was described. For a specific region of electrochemical potentials, the development of SnO microcrystals by an etching and precipitation process was shown. SnO is an interesting material given its potential applications as anode in Li-ion batteries [256–259], catalyst for ethanol oxidation [260,261], p-type semiconductor in optoelectronic devices [229,262,263] or precursor to attain new SnO₂ morphologies [264]. The formation of the SnO platelet microcrystals during the passivation process could be exploited as a simple electro-synthetic alternative to wet-chemistry methods [91,113,256–260,265]. For this purpose, more knowledge on the effect of the electrochemical conditions and the possible morphologies that can be achieved is required.

Results and discussion

Effect of temperature and NaOH concentration

As discussed in Chapter 1, SnO crystals are formed by the decomposition of the high coordination Sn²⁺ complexes that result from the severe Sn etching process. The reactions involved are detailed in (a.1) and (a.2).



To study the effect of the temperature on the SnO crystal growth, a jacketed electrochemical cell was used to cool down or heat the 0.1 M NaOH solution. In this setup, the SnO crystals

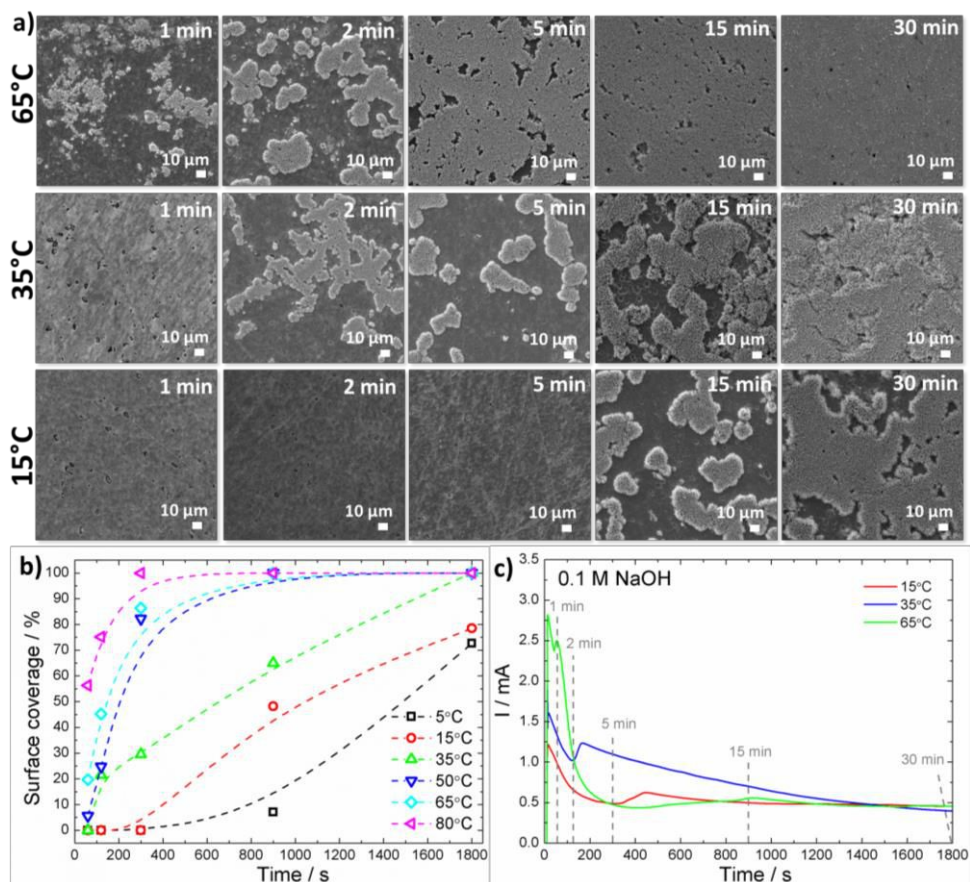


Figure a.1 a) Low magnification FESEM images of the SnO crystals developed on the Sn surface after stepping the electrode potential to -0.76 V when immersed in 0.1 M NaOH. Different deposition times of 1 min, 2 min, 5 min, 15 min and 30 min and temperatures (15, 35, 65 °C) were used. b) Average surface coverage vs the anodization time for the samples in prepared as in panel a. The surface coverage was determined by averaging the area of the regions covered by SnO crystals in the FESEM images (panel a). The area was calculated using the ImageJ software. c) Current vs time characteristics upon anodization of a tin electrode at -0.76 V in 0.1 M NaOH for 1800 s. The response at different temperatures is compared (15, 35 and 65 °C).

were developed by applying a potential step to -0.76 V. Temperatures in the range between 5 to 80 °C and anodization times of 1, 2, 5, 15 and 30 min were evaluated. The morphology of these samples was characterized by FESEM (Fig. a.1a) and from low magnification images the surface coverage for each temperature and anodization time was extracted. In Fig. a.1b the evolution of the SnO surface coverage with the time elapsed at the growth potential is given. It can be seen that at temperatures below 15 °C the appearance of the first SnO crystals is considerably retarded to anodization times larger than 300 s (5 min), whereas at temperatures above 65 °C first crystals are developed after 60 s (1 min) and complete coverage of the surface is achieved after 900 s (15 min). The faster surface covering

observed at high temperatures is related to enhancement of the Sn etching process that in turn speeds up the supersaturation at the electrode vicinity.

By comparing the current vs time response at different temperatures and the FESEM images, the behaviour of the curve can be related to the different stages of SnO development (Fig. a.1a and a.1c). For instance, if we take as reference the current response at 35 °C, first, a decrease in the current can be observed for the initial two minutes due to the formation of the primary passive layer. Subsequently, there is a slight increase in the current when the etching and dissolution process is initiated and the first SnO crystals on the surface appear (2 - 5 min). As the coverage of the surface increases (5 - 30 min), the current gradually decreases because the SnO crystals block the surface and hinder the arrival of more OH⁻ reactant species as well as the diffusion of the formed Sn²⁺ towards the bulk solution. At lower temperatures (15 °C), the local minimum in the current curve is retarded, because more time is required to develop the first passive layer and start the etching process. On the contrary, at higher temperatures (65 °C) this minimum occurs at times below 1 minute and the fast surface covering sharply decreases the current.

The effect of temperature on the crystal morphology was studied by high magnification FESEM images. Apparently at large anodization times, the typical microplatelet crystals with truncated bipyramidal shape are obtained and no special effect is observed on their morphology. However, the first nuclei formed at short anodization times present some differences, as shown in Fig. a.2. Their shape evolves from octagonal to squared with the increasing growth temperature. This phenomenon has been reported in the literature for SnO

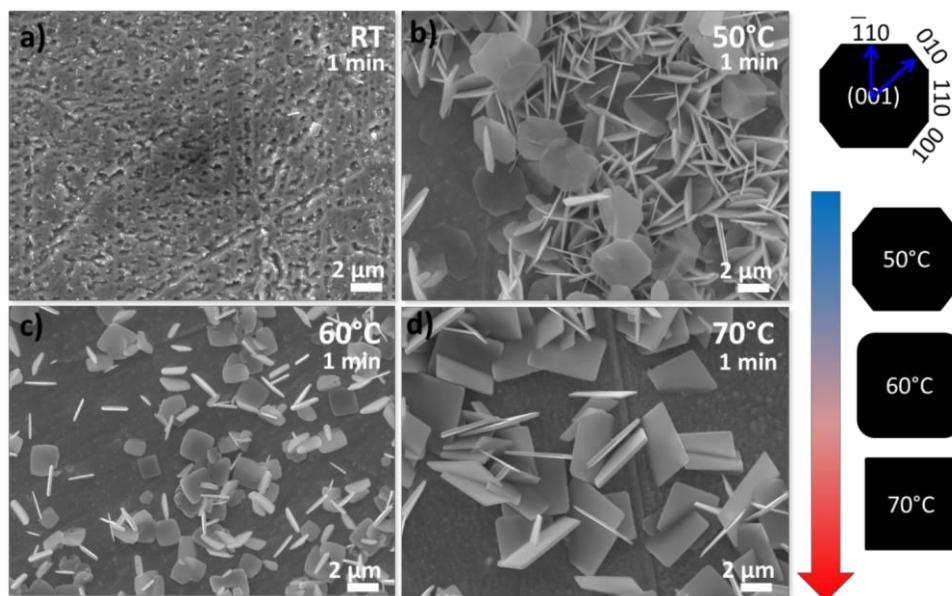


Figure a.2 FESEM image of the SnO crystals developed by after 1 min anodization at -0.75 V in 0.1 M NaOH at a) room temperature (RT), b) 50 °C, c) 60 °C and d) 70 °C. On the right side a scheme of the morphology evolution is given.

crystals grown by thermal evaporation [266] or solution chemical routes [265]. According to Wang *et al.*, the shape of the tetragonal SnO single crystal is mainly determined by the growth rates along the $\langle 001 \rangle$, $\langle 100 \rangle$ and $\langle 110 \rangle$ directions [265]. Owing to the slowest growth rate along the $\langle 001 \rangle$ direction, $\{001\}$ planes are always the most plentiful surfaces, while the shape of the (001) surface is determined by the relative ratio between the growth rates along the $\langle 100 \rangle$ and $\langle 110 \rangle$ as shown in the scheme in Fig a.2. Temperature seems to have an influence in this ratio between the growth rates; however, in our case we cannot discriminate which side of the octagon or the square correspond to each direction. For this TEM experiments would be required.

The morphology evolution was also followed for different NaOH concentrations in the range from 0.05 M to 8 M. For NaOH concentrations below 0.5 M, no SnO growth was observed after 1 minute of anodization (Fig. a.3a and a3.b). After 5 min, octagonal crystals appear for 0.05 M and 0.1 M solutions. At long anodization times (30 min), these first nuclei derive in the truncated bipyramids typically obtained in situations close to the equilibrium [91]. Similar structures have been reported by chemical solution routes [91,113]. For 0.05 M, even the stepped growth of (001) planes is observed in the surface due to the slow kinetics. When concentration is increased to 0.5 M NaOH (Fig. a.3c), the first nuclei present after 5 min have a slightly different shape: the short sides of the octagon are slightly longer. This

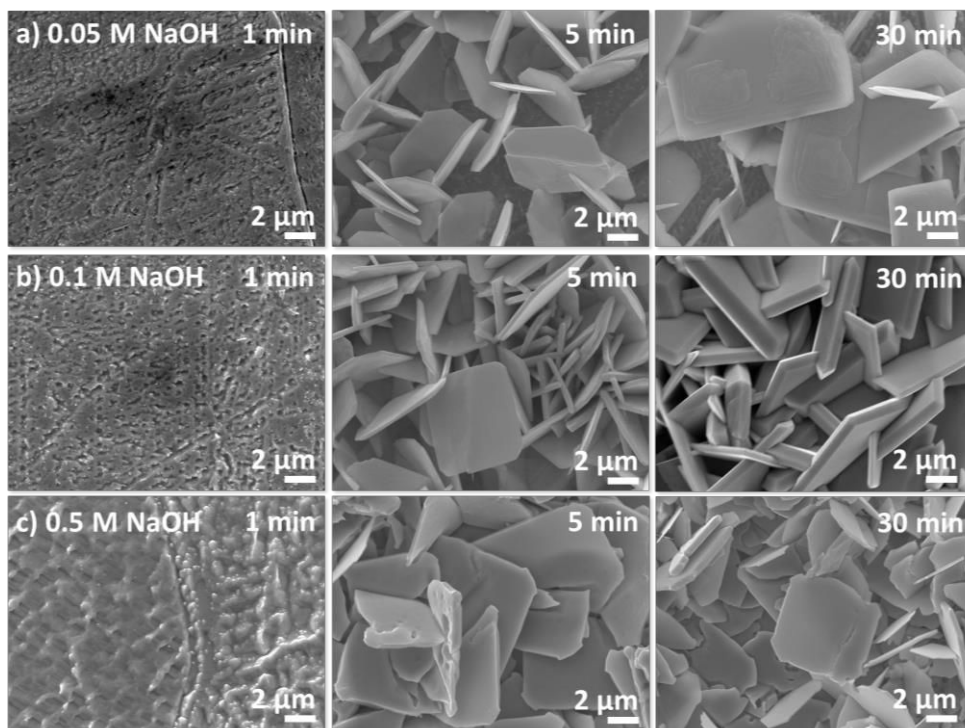


Figure a.3 FESEM images of the SnO microcrystals grown on Sn substrates by potential step to -0.77 V in a) 0.05 M, b) 0.1 M and c) 0.5 M NaOH solutions under room temperature conditions. Anodization times from left to right are 1 min, 5 min and 30 min.

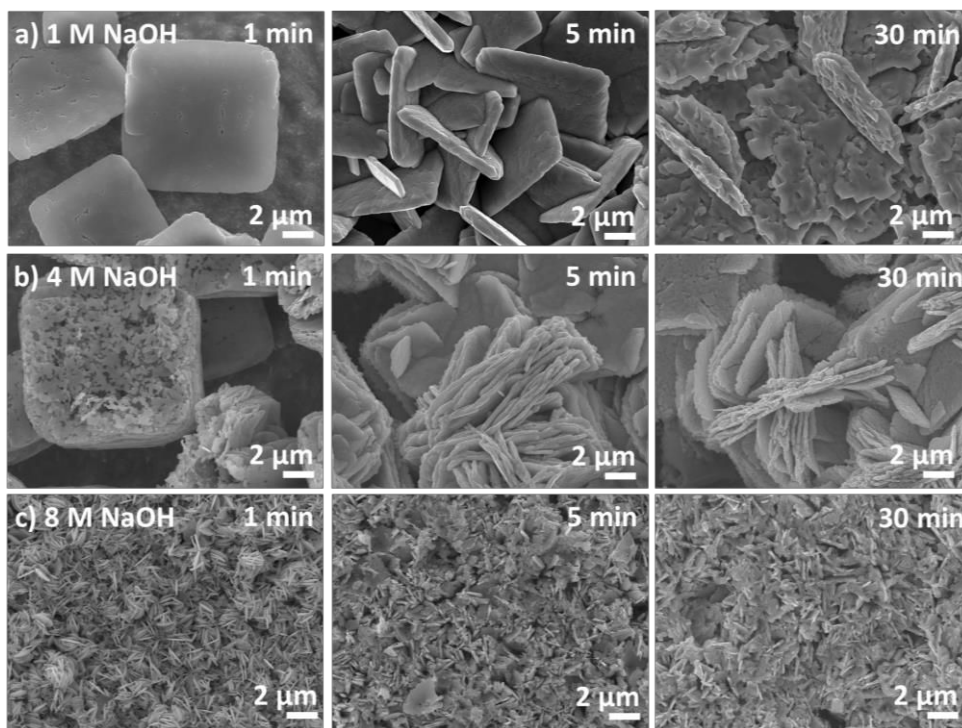


Figure a.4 FESEM images of the SnO microcrystals grown on Sn substrates by potential step to -0.77 V in a) 1 M, b) 4 M and c) 8 M NaOH solutions under room temperature conditions. Anodization times from left to right are 1 min, 5 min and 30 min.

effect might arise from an increase in the growth rate of that crystal direction or to an enhanced dissolution of the others provided by the higher OH concentration.

At concentrations above 1 M NaOH, the SnO nucleation is faster than in the previous cases and crystals are developed after only 1 min (Fig. a.4). For 1 M and 4 M NaOH (Fig. a.4a and a.4b), ~ 5 μm square crystals with evident defects in the surface are formed, especially for those prepared in 4 M NaOH (Fig. a.4b). These imperfections stem from the SnO dissolution occurring at such high NaOH concentration. The same effect has been reported in electrocrystallized SnO pompon-like structures [85]. The dissolution effect is especially notorious at large anodization times where dissolution affects the planes in (001) direction and they become separated into sheets. At 8 M NaOH, the case seems to be more dramatic (Fig. a.4c). Very small crystals are formed after 1 min with a completely rounded shape. Their smaller size compared to SnO crystals obtained in lower NaOH concentration and the rounded shape suggest that the strong dissolution at the edges does not allow them to grow and reach the typical squared shape. At larger growth times the disk-like morphology is completely lost and just random particles remain.

Effect of organic solvents: limiting the etching rate

Organic solvents can act as anodic dissolution or corrosion inhibitors. The hindering capacity of an organic solvent depends on its physical properties (density, viscosity, diffusion coefficient, *etc.*), its concentration in solution (water/organic content ratio) and the nature of the metal itself [108,267]. In order to control the rate of the hydroxyl-etching process voltammetric curves and growth of SnO crystals were performed at room temperature by incorporating an organic fraction into the 0.1 M NaOH solutions. The effect of three different solvents was studied: glycerol, ethylene glycol and acetonitrile.

In Fig. a.5 linear sweep voltammeteries at increasing glycerol contents are shown. For glycerol contents up to 10 % there are very little changes in the first anodization peak at ~ -

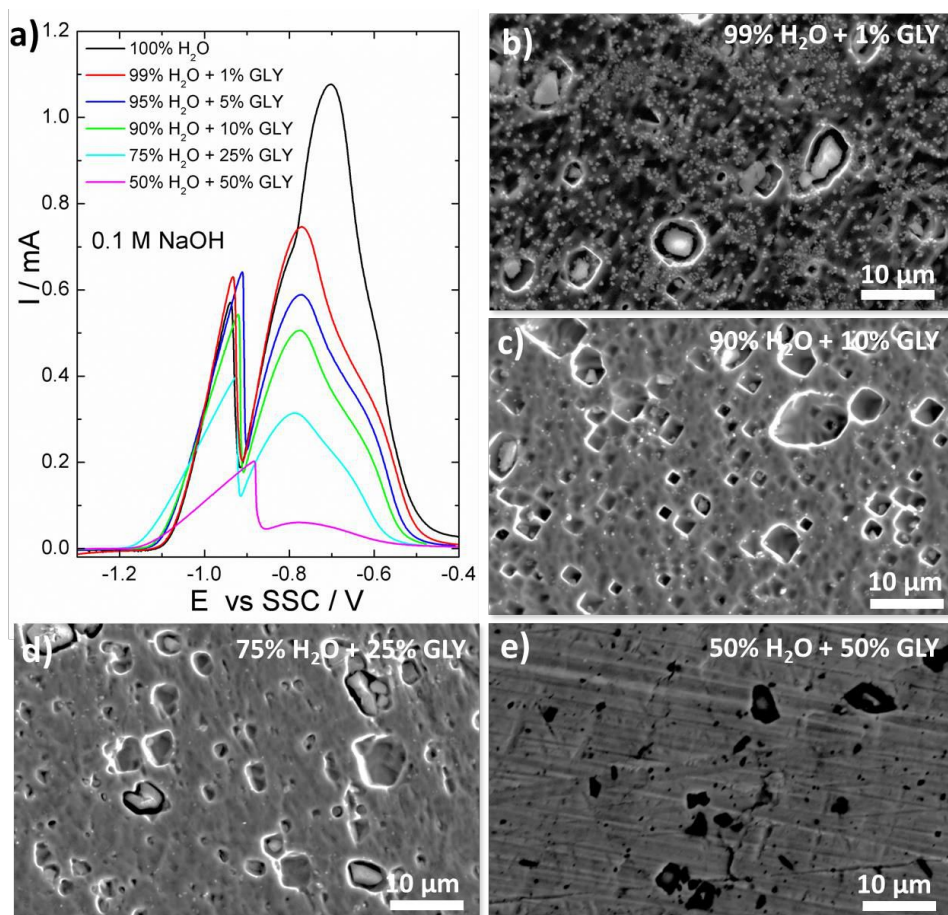


Figure a.5 a) Linear sweep voltammetry scans for a Sn electrode immersed in 0.1 M NaOH solutions containing different percentage of glycerol. (Scan rate= 0.001 Vs⁻¹). FESEM image of the Sn electrode after electrochemical oxidation by potential sweep and 1800 s hold at -0.75 V in 0.1 M NaOH solutions with b) 1% glycerol, c) 10% glycerol, d) 25 % glycerol and e) 50 % glycerol.

0.95 V, while the peak at -0.7 V seems to disappear completely. The peak located at -0.7 V, as discussed in Chapter 1, corresponds to the region of potentials where massive formation of SnO microplatelet crystals takes place. If the glycerol percentage is increased above 25 %, then the current response of all the anodic processes is decreased. FESEM images of the electrode surface after potential sweep and hold during 1800 s at -0.7 V are shown in Fig. a.5b-e. For 1% glycerol content, small white crystallites can be appreciated together with alumina incrustations from the polishing process (Fig. a.5b). These small crystallites correspond to SnO nuclei formed by the etching /dissolution process. Here, the $\sim 10 \mu\text{m}$ platelet-like SnO microcrystals are not formed due to inhibition effect of glycerol. The amount of these small SnO crystals is decreased upon increasing glycerol contents. At 10 % glycerol pyramidal pits from the etching process are visible on the Sn surface but very few SnO crystals precipitate (Fig. a.5c). Upon incorporation of 25 % glycerol, the surface is similar to that of the primary passive layer (Fig. a.5d) and finally at 50 % glycerol, only

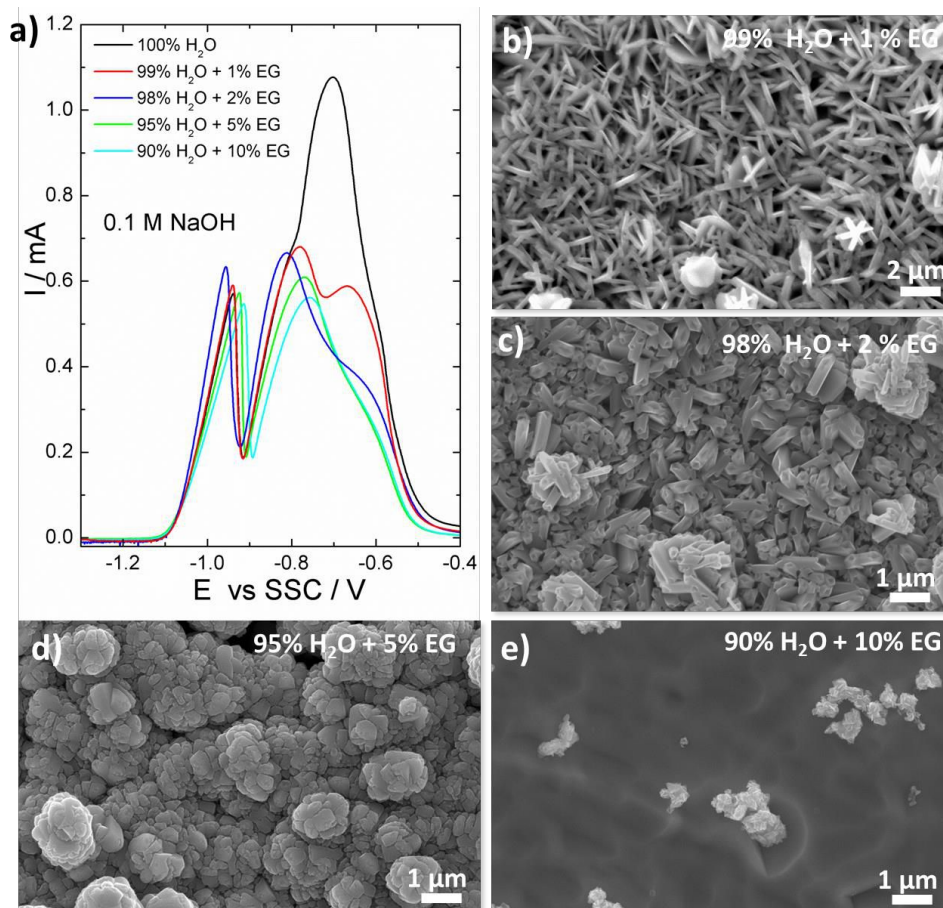


Figure a.6 a) Linear sweep voltammetry scans for a Sn electrode immersed in 0.1 M NaOH solutions containing different percentage of ethylene glycol. (Scan rate= 0.001 Vs⁻¹). FESEM image of the Sn electrode after electrochemical oxidation by potential sweep and 1800 s hold at -0.75 V in 0.1 M NaOH solutions with b) 1% ethylene glycol, c) 2% ethylene glycol, d) 2 % ethylene glycol and e) 10 % ethylene glycol.

polishing lines can be observed suggesting that the oxide layer must be very thin (Fig. a.5e). This is in line with the low current observed even for the primary passivation process in solutions with 50 % glycerol (Fig. a.5a).

The effect of ethylene glycol is analysed in Fig. a.6. The voltammetric scans show a similar behaviour to the one described previously for glycerol. The current contribution of the first peak, associated to the primary passivation, remains more or less constant upon ethylene glycol incorporation while a strong effect is evident for the peak at -0.7 V (Fig. a.6a). It must be noticed, however, that the decrease in current is lower than in the glycerol-based solutions (Fig. a.5a). For instance, for 1 % ethylene glycol in solution, a relevant contribution of the peak at -0.7 V can be inferred if the region between -0.9 and -0.4 V is deconvoluted in three peaks and SnO crystals of ~ 2 μm are formed as displayed in Fig a.6b. For ethylene glycol contents up to 10%, SnO crystals are developed in the electrode surface but their platelet morphology is gradually lost. At 2% ethylene glycol, the corners of the platelet crystals disappear and bend inwards (Fig. a.6c), while for 5 % round-shaped particles are obtained (Fig. a.6d). Very small nuclei are obtained in NaOH solutions having more than 10 % ethylene glycol (Fig. A.6e).

Finally, the other solvent under study was acetonitrile. The linear voltammetry scan and the FESEM images are given in Fig. a.7. Here, percentages of organic fraction of up to 50 % were achieved without a substantial decrease in the current associated to the formation of

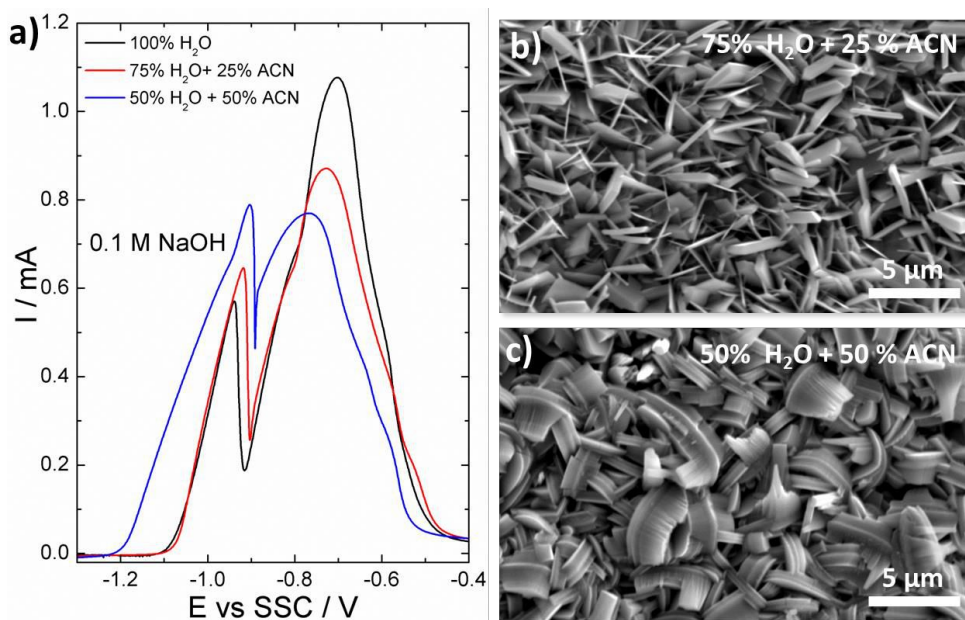


Figure a.7 a) Linear sweep voltammetry scans for a Sn electrode immersed in 0.1 M NaOH solutions containing different percentage of acetonitrile. (Scan rate = 0.001 V s^{-1}). FESEM image of the Sn electrode after electrochemical oxidation by potential sweep and 1800 s hold at -0.75 V in 0.1 M NaOH solutions with b) 25 % acetonitrile and c) 50 % acetonitrile.

SnO crystals at -0.7 V (Fig. a.7a). In fact, Fig. a.7b and a.7c evidence the formation of SnO for 25 % and 50 % acetonitrile. The morphology of the crystals at 50% is slightly different; they seem to be more rounded in shape and composed of stacked platelets. In some cases perpendicularly to the platelet plane other structures develop. Acetonitrile contents above 75 % could not be attempted as the organic and aqueous phases became immiscible.

The observed stronger or weaker inhibition effect of each organic solvent can be correlated to its properties. Those relevant characteristics for the present discussion are gathered in Table a.I [268]. In all cases, the solvents have lower dielectric constants as compared to the value for pure water (80.4 at 20°C), so when incorporated in the solution are supposed to lower the dielectric constant of the media. A decrease in the dielectric constant increases the degree of association of NaOH and decreases the basicity of the solution [267]. In tin anodization, a decrease in the OH concentration is manifested by a decrease in the current response as the oxidation products become more stable; this in agreement with the amphoteric nature of tin oxides [89,90]. Although the changes in the dielectric constant can play a role in decreasing the current response, there are other parameters like viscosity that are more relevant upon solvent incorporation. For instance, if the properties of glycerol and ethylene glycol are compared (see Table a.I) both correspond to protic solvents (can provide acidic protons) with similar dielectric constants but they have a considerably different viscosity. Then, the enhanced corrosion inhibition provided by glycerol can be attributed to its higher viscosity, which can limit the diffusion of reactant species to the electrode (OH^-) and the diffusion of the reacted ions towards the bulk solution (Sn^{2+}) [108]. As proposed in chapter 1, the etching at -0.7 V is mediated by hydroxyl ions and probably via high coordination number Sn^{2+} compounds. This could explain the stronger effect in the etching process as compared to the primary dissolution-precipitation process. Of course, surface adsorption effects at the metal surface cannot be neglected [269]. Actually, the changes in the morphology of the SnO crystals could arise from the distortion of the diffusion regime or the preferential adsorption of the solvents in different crystalline planes.

The behaviour of acetonitrile seems to be less straightforward. Acetonitrile is less viscous than ethylene glycol or even water (1 mPa s at 25°C), but aside from this, its properties are relatively similar to those of ethylene glycol. Both solvents have similar dielectric constants and viscosity change is not as relevant as between glycerol and ethylene glycol to justify the observed decrease on its inhibition effect. The only difference lies in the aprotic character of acetonitrile. Aprotic solvents cannot interact by hydrogen bonding, just by ion-dipole or

Table a.I. Properties of the solvents employed. Taken from reference [268].

Solvent	Polar / non-polar	Protic / Aprotic	Density / g mL^{-1} (25°C)	Dielectric constant (25°C)	Viscosity / mPa s (25°C)
Glycerol	Polar	Protic	1.261	46.53	934
Ethylene glycol	Polar	Protic	1.114	41.40	16.06
Acetonitrile	Polar	Aprotic	0.785	36.64	0.369

dipole-dipole interactions so they strongly solvate cations but are poor solvents for anions. This can have influence in the solubility of the species, both OH^- and Sn^{2+} , and decrease the current response with respect to the pure water solution. However, there might be other contributions to explain its relatively low inhibition effect. For all the solvents we discussed, solvent-metal surface interactions, structure of the electrolyte at the electrode vicinity (capacitance) or adsorption of the solvent molecules blocking the metal electrode should be considered. Further studies are required to fully understand the effect of organic solvents on Sn electrochemical behaviour.

Summary

We have studied the effect of both concentration and temperature on the rate of crystal formation and morphology of the SnO crystals. An increase in temperature and concentration accelerates the etching and supersaturation processes, and nucleation of the SnO phase takes place at shorter anodization times. For instance, first crystals can be observed after just 1 min when anodizing tin in a 0.1 M NaOH solution at temperatures above 50 °C or at room temperature but using 1 M NaOH. The temperature was found to have very little effect on the shape of the crystals and after long anodization times (> 30 min) and truncated bipyramidal crystals were always obtained. On the contrary, concentration could influence the shape given the reversible reaction that promotes the dissolution of the grown SnO at high NaOH concentrations.

In order to control the etching rate by OH species and achieve new morphologies, fractions of organic solvent were incorporated in our standard 0.1 M NaOH solution. The organic solvents considerably reduced the current at -0.7 V associated to the etching process, especially glycerol. In these conditions, just very small SnO crystals were formed. In ethylene glycol and acetonitrile different morphologies such as particles or platelets with truncated corners were attained.

Experimental details

Sample preparation

Polycrystalline Sn disks (99.999 %, Goodfellow) of 1 cm dia. were used as substrates. Prior to electrochemical studies and film growth, the substrates were mechanically polished down to 3 μm with Al_2O_3 polishing disks, rinsed with MilliQ water and N_2 blown. The experiments were performed in a jacketed electrochemical glass cell in a standard three-electrode configuration using an Ag/AgCl/KCl(sat) (SSC from herein, E^0 vs. NHE = 0.222 V) reference electrode and a platinum auxiliary electrode. The temperature was controlled with an ED-5 thermostatic bath (Julabo, Germany).

The voltammetric curves and the film growth were carried out using a PGSTAT302N Autolab potentiostat (Metrohm Autolab). The electrolyte was purged with Ar (99.999 %) prior to measurements to remove the dissolved oxygen. Solutions were prepared from NaOH (Riedel-de Haën, 99%), ethylene glycol (Sigma Aldrich, > 99%), glycerol (Sigma Aldrich > 99.5 %) and acetonitrile (99.8 %, Sigma Aldrich).

Characterization techniques

The morphology was characterized in a field-emission scanning microscope (Hitachi FESEM S4800, Japan). Surface coverage was analysed with the Image J software.

Appendix **b**

First steps towards the further improvement of self-ordered tin oxide structures: pulsed anodization and indented Sn surfaces

Introduction

In Chapter 3, we optimized the preparation of tin oxide self-ordered nanochannelled structures in an organic-based Na₂S and NH₄F electrolyte. Parameters like the applied potential, the concentration or the organic/water ratio were assessed. Here, more advanced strategies like the use of potential pulses or the anodization of indented/patterned surfaces following the procedure reported by Masuda *et al.* [270,271] will be explored.

Results and discussion

Potential pulses

As discussed in Section B.1.2 from the Introduction in Part B, the use of potential pulses is commonly employed to obtain advanced anodic self-ordered structures such as the bamboo tubes or the nanolaces reported for TiO₂. However, in our case the aim of using such potential pulses is totally different: we intend to avoid the presence of inner cracks by alternating the growth potential with a rest potential where no reaction occurs. During the growth stage, oxygen evolves at the Sn anode and if trapped can result in cracking of the film. By switching to a rest potential we let the oxygen go before the growth proceeds.

For this, Sn foils were anodized in a solution 50:50 volume ratio of H₂O and acetonitrile containing 0.2 M Na₂S and 0.1 M NH₄F using symmetric potential pulses. In Fig. b.1 the FESEM images of the top morphology and cross-sectional view are given in comparison to the one obtained at a constant potential (Fig. b1a). It can be seen that the use of potential pulses in Sn does not lead to different morphologies, and nanochannels similar to those

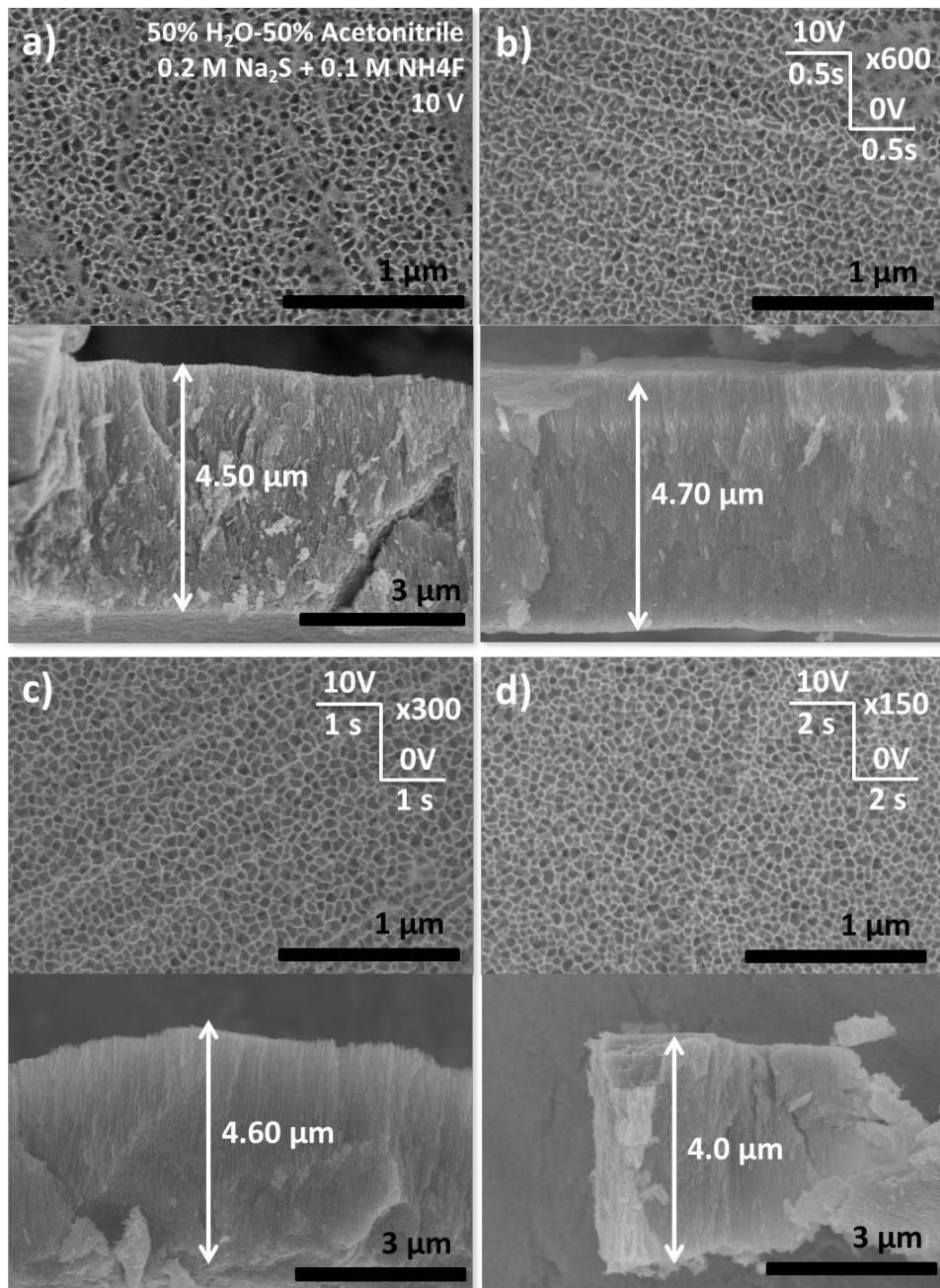


Figure b.1 FESEM images of the top morphology (top) and cross-sectional view (bottom) of self-ordered nanochannelled layers prepared by Sn anodization in a 50 % H₂O - 50 % acetonitrile mixture containing 0.2 M Na₂S and 0.1 M NH₄F at a) constant potential of 10 V for 5 min or by pulsing the potential b-d. In all cases the potential is stepped from 10 V to 0 V using symmetric pulses of b) 0.5 s, c) 1 s and d) 2 s. Anodization time was adjusted to be 5 min at the growth potential (10 V).

described in Chapter 3 or in Fig. b.1a are achieved. For pulses of 0.5 s (Fig. b.1b), the top morphology, the crack-free cross-section and the final thickness ($\sim 4.7 \mu\text{m}$) are comparable to the one obtained at constant potential. By increasing the time of the pulses to 1 s or 2 s, the top morphology seems to show more open pores (Fig. b.1c-d). In both cases, asymmetric pulses were attempted by doubling the time elapsed at the rest potential (0 V). FESEM images are shown in Fig. b.2. For asymmetric potential steps of 2 s (10 V) and 4 s (0 V) the top morphology is completely open yet the bottoms are not very well defined and thinning of the top channel walls is observed in the cross-sectional view (Fig. b.2a). The thinning of the channel walls in close contact with the electrolyte comes from the dissolution of the oxide during the time spent at the rest potential. If both times are reduced to 1 s (10 V) and 2 s (0V), completely open pores with more clear channels are achieved. Here, the presence of inner ripples is still evident as occurred in constant potential anodization (see details in Chapter 3).

Among all the pulsing conditions attempted, the best nanochannelled structures are attained using asymmetric pulses of 1s and 2s (10 V: 0 V). However, it must be noticed that just potential pulsing does not represent a big breakthrough in improving the overall morphology of the samples.

Patterning with Ni mould: indented Sn surfaces

Despite the improvement in the continuity of the channels reached by proper optimization of the electrolyte composition, the pores are still randomly distributed on the surface; they are not completely straight and even merge at some point. To enhance the ordered distribution

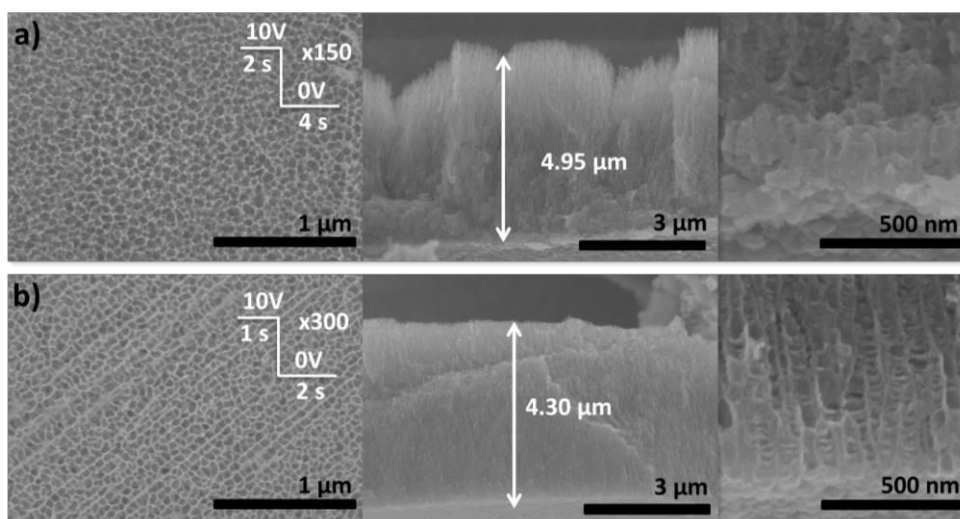


Figure b.2 FESEM images of the top morphology (left), cross-sectional view (middle) and detail of the channel bottoms (right) of self-ordered nanochannelled layers prepared by Sn anodization in a 50 % H_2O - 50 % acetonitrile mixture containing 0.2 M Na_2S and 0.1 M NH_4F by pulsing the potential between 10 V and 0 V. Here asymmetric pulses of a) 2 s at 10 V and 4 s at 0 V and b) 1 s at 10 V and 2 s at 0 V were used. The total time spent at the growth potential is 5 min.

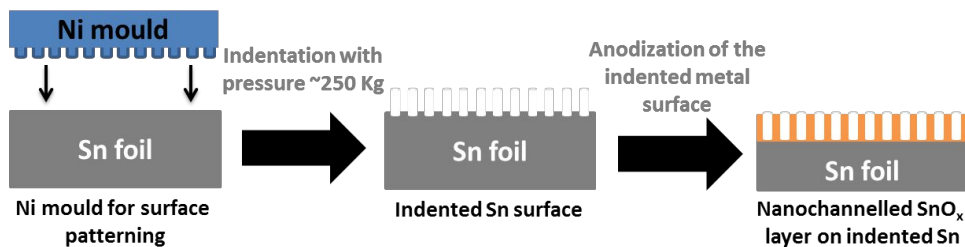


Figure b.3 Scheme of the indentation process on Sn foils and the subsequent anodization.

of the channels, the surface of the Sn foils was patterned before anodization by applying 250 Kg of pressure on a Ni mould. A scheme of the process is displayed in Fig. b.3. First attempts on surface indentation were carried out in our usual tin foils having 0.25 mm in thickness. As tin is a very soft material, when the pressure was applied the foils tended to bend and the patterning of the surface was inhomogeneous. Then, thicker tin sheets having 2 mm in thickness were employed.

First, indented surfaces were anodized using a constant potential of 10 V in an electrolyte composed of 50 % H₂O and 50 % 2-methyl-1,3-propanediol and containing 0.2 M Na₂S and 0.1 M NH₄F. This electrolyte offered similar results to the optimized acetonitrile one, but

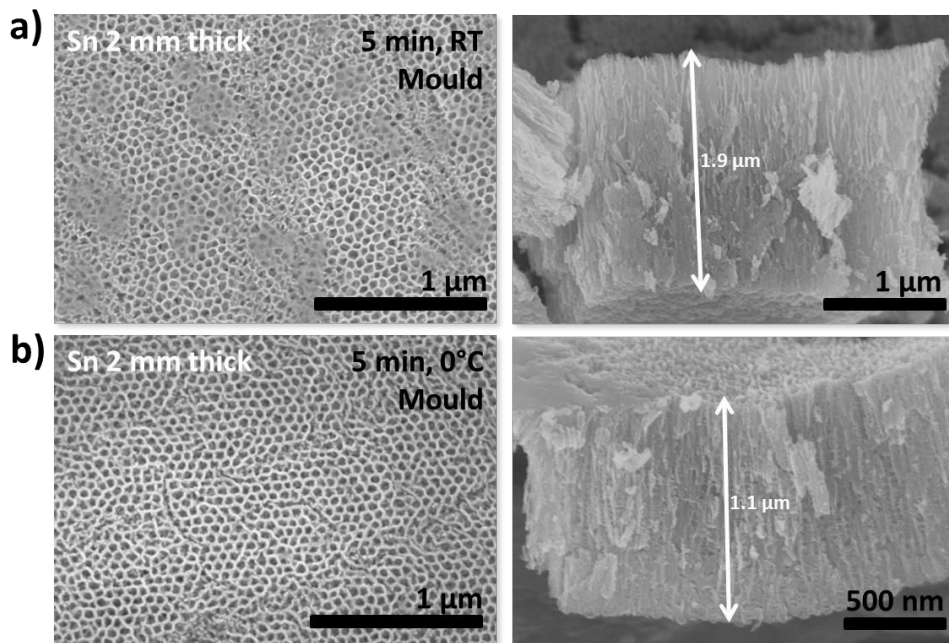


Figure b.4 FESEM images of the top (left) and cross-sectional view (right) of self-ordered nanochannelled layers prepared by anodization of indented Sn foils (2 mm thick) in a 50 % H₂O - 50 % 2-methyl-1,3-propanediol mixture containing 0.2 M Na₂S and 0.1 M NH₄F. Anodization was performed for 5 min at a constant potential of 10 V at a) room temperature and b) cooling down at 0 °C.

allows working at low temperatures. In Fig. b.4, the morphology of self-ordered Sn structures on previously indented Sn foils is shown. At the top, the pores present thicker walls and more regular pore structures. At room temperature, the final thickness achieved in this electrolyte was found to be $\sim 1.9 \mu\text{m}$ (Fig. b.4a), which is substantially less than in the acetonitrile-based electrolyte (Fig. b.1a, thickness $\sim 4.5 \mu\text{m}$). By decreasing the anodization temperature to 0°C , the regular top morphology is maintained and thicker pore walls are attained, as displayed in Fig. b.4b. Lowering the temperature also results in a slower development of the oxide and a final thickness of $\sim 1.1 \mu\text{m}$ is reached.

Finally, we decided to combine the effect of the patterned Sn surface and the potential pulses described in the previous section. In Fig. b5, samples prepared by asymmetric potential pulsing in patterned and non-patterned are given. A more regular pore arrangement is obtained by effect of the surface patterning prior to anodization. Besides, pulsing enables us to get well-defined channels.

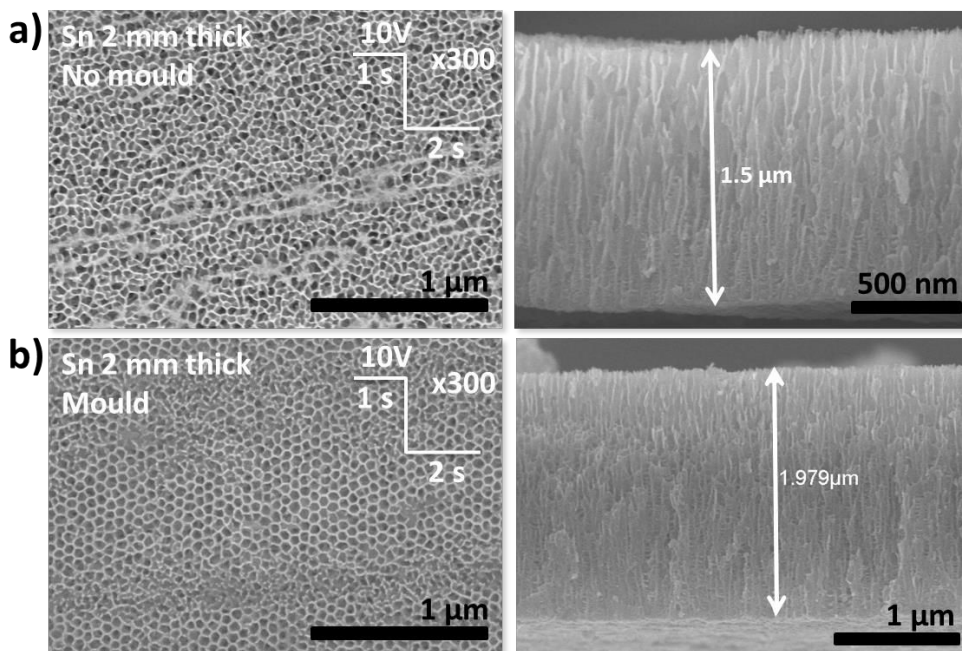


Figure b.5 FESEM images of the top (left) and cross-sectional view (right) of self-ordered nanochannelled layers prepared by anodization of 2 mm thick Sn foils a) as supplied or b) patterned with the Ni mould in a 50 % H_2O - 50 % 2-methyl-1,3-propanediol mixture containing 0.2 M Na_2S and 0.1 M NH_4F . Anodization was performed by using asymmetric potential pulses of 1 s and 2 s at the growth potential (10 V) and rest potential (0 V), respectively, with total anodization time of 5 min.

Summary

In the preliminary experiments shown in this appendix, the synergic effect of both potential pulses and surface patterning is evaluated. Self-ordered tin oxide structures with straight

channels showing a more regular pore distribution are attained. Nevertheless, further research on this issue is required. For example, the patterning procedure needs to be optimized (*e.g.* pressure required, influence of the Sn foil thickness, distance of the indented pattern, *etc.*) and more pulsing ratios or potential values should be considered.

Experimental details

Polycrystalline tin foils (99.95 %, Advent Ltd.) 0.25 mm and 2 mm were ultrasonically cleaned in acetone, ethanol and deionized water ($\sim 18.2 \text{ M}\Omega\cdot\text{cm}$), and then dried in N_2 stream. Substrates (working electrodes) were mounted at the bottom of a two-electrode electrochemical cell equipped with a Pt foil as counter electrode. Anodization was performed in a circular area of 1 cm in diameter by applying a constant potential with a LAB-SM1500 (ET System, Germany) potentiostat or potential pulses when indicated. Electrolyte was composed of 0.2 M $\text{Na}_2\text{S}\cdot x\text{H}_2\text{O}$ (Sigma-Aldrich) and 0.1 M NH_4F ($\geq 98.0\%$, Sigma-Aldrich) in 50:50 volume ratio deionized water and organic mixture. As organic solvents acetonitrile (99.8 %, Sigma Aldrich) and 2-methyl-1,3-propanediol (99%, Sigma Aldrich) were employed. Anodization at low temperatures was performed by cooling down the substrates using a Peltier element (quick cool, Conrad Electronics) and pumping out the heat with a thermostat (Huber Badthermostat-K6-NR, Germany). After anodization films were rinsed with deionized water and N_2 blown.

The morphology of was characterized with a S4800 field-emission scanning electron microscope (FESEM, Hitachi High-Technologies Corporation, Japan).

Appendix C

Symbols and acronyms

As far as possible, the recommendations of the International Union of Pure and Applied Chemistry (IUPAC) have been used for the units, symbols and acronyms employed through this PhD. Thesis. Hereby, a selection of the most frequent symbols and acronyms in the present work are provided for reference:

α	Absorption coefficient
ΔE_{ph}	Photovoltage
ΔG	Gibbs free energy
δ	Film thickness
ϵ	Dielectric constant
ϵ_0	Permittivity of vacuum
θ	Surface coverage
κ	Specific conductivity
λ	Reorganization energy of the solvation shell / wavelength
ν	Frequency (radiation)
χ	Electron affinity
ρ	Specific gravity or relative density / charge density
τ_p	Hole life-time
μ_p	Hole mobility
A	Area
C	Capacitance
C_d	Diffuse (Gouy) layer capacitance

C_{el}	Electrochemical (electrolyte) double layer capacitance
C_H	Helmholtz (compact) layer capacitance
C_{SC}	Semiconductor capacitance
C_{Total}	Total interface capacitance
e	Electron charge
e^-	Electron (charge carrier)
E	Applied potential
E_{bias}	Applied bias
E_{CB}	Conduction band energy
E_F	Fermi energy
E_F^*	Quasi-Fermi level
$E_{F,redox}$	Fermi energy in the electrolyte
E_{FB}	Flat band potential
E_g	Band gap energy
E_{ox}	Energy of the unoccupied state of the redox system
E_{ox}^0	Standard redox potential of the oxidation electrochemical reaction
E_{red}	Energy of the occupied state of the redox system
E_{red}^0	Standard redox potential of the reduction electrochemical reaction
E_{tip}	Tip potential
E_{vac}	Vacuum level
E_{VB}	Valence band energy
F	Faraday constant
f	Frequency
F_S	Field strength
h^+	Hole (charge carrier)
I / i	Current
i_p	Passivation current
i_{crit}	Critical current
I_M^n	Interstitial metal cation
I_{ph}	Photocurrent
I_T	Tunnelling current
j	Current density
k	Wave vector
k_B	Boltzmann constant
K_{sp}	Solubility product
L_D	Debye length
L_p	Diffusion length of holes
M	Molecular weight

N	Density of electronic states
N_A	Density of acceptor states
N_D	Density of donor states
P	Power
Q	Charge
Q_{el}	Charge stored at the interfacial electrolyte
Q_{SC}	Charge stored at the semiconductor
R	Resistance
T	Temperature
T_m	Melting point
v	Scan rate
V_M^{n'}	Metal vacancy
V_O	Oxygen vacancy
w	Width of the space charge layer
Z	Impedance
Z'	Real part of impedance
Z''	Imaginary part of impedance
ACN	Acetonitrile
AFM	Atomic force microscopy
ATO	Antimony doped tin oxide
CB	Conduction band
CPE	Constant phase element
CV	Cyclic voltammetry
DMSO	Dimethyl sulfoxide
EC-STM	Electrochemical scanning tunnelling microscopy
EDL	Electrical double layer
EG	Ethylene glycol
EIS	Electrochemical impedance spectroscopy
FESEM	Field emission scanning electron microscopy
FTO	Fluorine doped tin oxide
GLY	Glycerol
HER	Hydrogen electrode reaction
IHP	Inner Helmholtz plane
IPCE	Incident photon to current conversion efficiency
LPRM	Layer pore resistance model
NHE	Normal hydrogen electrode

OCP	Open circuit potential
OHP	Outer Helmholtz plane
PBR	Pilling-Bedworth ratio
PDM	Point defect model
PEC	Photoelectrochemical cell
RHE	Reversible hydrogen electrode
SAED	Selected area electron diffraction
SCL	Space charge layer
SEM	Scanning electron microscopy
SHE	Standard hydrogen electrode
SPM	Scanning probe microscopy
SSC	Silver / silver chloride reference electrode
STM	Scanning tunnelling microscopy
TEM	Transmission electron microscopy
UHV	Ultra high vacuum
VB	Valence band
XANES	X-ray absorption near edge spectroscopy
XPS	X-ray photoelectron spectroscopy
XRD	X-ray diffraction

Appendix d

Publications and Meetings (2010-2014)

Publications in journals

1. A. Palacios-Adrós, M. Altomare, K. Lee, I. Díez-Pérez, F. Sanz, P. Schmuki, Controlled thermal annealing tunes the photoelectrochemical properties of nanochanneled tin oxide structures, *ChemElectroChem* **1** (2014) 1133 - 1137.
2. L. Wang, A. Palacios-Adrós, R. Kirchgeorg, A. Tighineanu, P. Schmuki, Enhanced photoelectrochemical water splitting efficiency of a hematite-ordered Sb:SnO₂ host-guest system, *ChemSusChem* **7** (2014) 421 - 424.
3. A. Palacios-Adrós, M. Altomare, A. Tighineanu, R. Kirchgeorg, N. Shrestha, I. Díez-Pérez, F. Caballero-Briones, F. Sanz, P. Schmuki, Growth of ordered anodic SnO₂ nanochannel layers and their use for H₂ gas sensing, *Journal of Materials Chemistry A* **2** (2014) 915 - 920.
4. A. Palacios-Adrós, F. Caballero-Briones, I. Díez-Pérez, F. Sanz, Tin passivation in alkaline media: formation of SnO microcrystals as hydroxyl etching product, *Electrochimica Acta* **111** (2013) 837 - 845.
5. A. C. Aragonès, A. Palacios-Adrós, F. Caballero-Briones, F. Sanz, Study and improvement of aluminium doped ZnO thin films: limits and advantages, *Electrochimica Acta* **109** (2013) 117 - 124.
6. F. Caballero-Briones, A. Palacios-Adrós, O. Calzadilla, I. de P.R. Moreira, F. Sanz, Disruption of the chemical environment and electronic structure in p-type Cu₂O films by alkaline doping, *The Journal of Physical Chemistry C* **116** (2012) 13524 - 13535.
7. F. Caballero-Briones, A. Palacios-Adrós, F. Sanz, CuInSe₂ films prepared by three step pulsed electrodeposition. Deposition mechanisms, optical and photoelectrochemical studies, *Electrochimica Acta* **56** (2011) 9556 - 9567.

8. A. Palacios-Adrós, F. Caballero-Briones, F. Sanz, Enhancement in as-grown CuInSe₂ film microstructure by a three potential pulsed electrodeposition method, *Electrochemistry Communications* **12** (2010) 1025 - 1029.

Oral presentations in meetings

1. F. Caballero-Briones, A. Palacios-Adrós, O. Calzadilla, I. de P.R. Moreira, F. Sanz, Alkaline doping causes disruption through the chemical environment and electronic structure in anodic p-type Cu₂O films. 7th International Conference on Surfaces, Coatings and Nanostructured Materials (Nanosmat). September 18-21, 2012. Prague, Czech Republic.
2. F. Caballero-Briones, A. Palacios-Adrós, O. Calzadilla, I. de P.R. Moreira, F. Sanz, Películas delgadas de Cu₂O dopadas con iones alcalinos mediante anodización de Cu. Estudio experimental y teórico de sus propiedades optoelectrónicas. XXXIII Reunión del Grupo de Electroquímica de la Real Sociedad Española de Química. July 1-4, 2012. Miraflores de la Sierra, Spain.
3. A.C. Aragonès, A. Palacios-Adrós, F. Sanz, Electrodeposición y caracterización de películas delgadas de ZnO:Al. XXXIII Reunión del Grupo de Electroquímica de la Real Sociedad Española de Química. July 1-4, 2012. Miraflores de la Sierra, Spain.
4. J.A. Padilla, E. Xuriguera, A. Palacios-Adrós, M. Segarra, F. Caballero-Briones, F. Sanz, Estudio de la rugosidad superficial en láminas de cobre mediante microscopía interferométrica. Aplicación al estudio del crecimiento de óxido de cobre texturado para su aplicación en cintas superconductoras. BCNano'11. September 19-23, 2011. Barcelona, Spain.
5. A. Palacios-Adrós, F. Caballero-Briones, F. Sanz, Preparation of copper indium diselenide films by pulsed electrodeposition, Photovoltaic technical conference: thin film and advanced solutions. May 25-27, 2011. Aix-en-provence, France.

Poster presentations in meetings

1. A. Palacios-Adrós, M. Altomare, A. Tighineanu, R. Kirchgeorg, N. Shrestha, I. Díez-Pérez, F. Caballero-Briones, F. Sanz, P. Schmuki, Growth of ordered anodic SnO₂ nanochannel layers and their application for H₂ gas sensing. Electrochemistry 2014. September 22-24. Mainz, Germany.
2. A. Palacios-Adrós, F. Caballero-Briones, I. Díez-Pérez, F. Sanz, Tin electrochemistry in NaOH: SnO microcrystals as a result of hydroxyl etching. Electrochemistry 2014. September 22-24. Mainz, Germany.

3. A. Palacios-Adrós, M. Altomare, A. Tighineanu, R. Kirchgeorg, N. Shrestha, I. Díez-Pérez, F. Caballero-Briones, F. Sanz, P. Schmuki, Growth of ordered anodic SnO₂ nanochannel layers and their application for H₂ gas sensing. 65th Annual Meeting of the International Society of Electrochemistry. August 31-September 5, 2014. Lausanne, Switzerland.
4. A. Palacios-Adrós, F. Caballero-Briones, I. Díez-Pérez, F. Sanz, Tin passivation in alkaline media: formation of SnO microcrystals as a result of hydroxyl etching. 65th Annual Meeting of the International Society of Electrochemistry. August 31-September 5, 2014. Lausanne, Switzerland.
5. A. Palacios-Adrós, F. Caballero-Briones, F. Sanz, Optical and photoelectrochemical studies on CuInSe₂ films prepared by three step pulsed electrodeposition. 5th Gerischer Symposium, Photoelectrochemistry: from fundamentals to solar applications. June 22-24, 2011. Berlin, Germany.
6. F. Caballero-Briones, A. Palacios-Adrós, O. Calzadilla, I. de P.R. Moreira, F. Sanz, Alkaline doped p-type Cu₂O films prepared by Cu anodization: testing the band structure by optical, electrochemical and spectroscopic techniques. 5th Gerischer Symposium, Photoelectrochemistry: from fundamentals to solar applications. June 22-24, 2011. Berlin, Germany.
7. F. Caballero-Briones, A. Palacios-Adrós, O. Calzadilla, I. de P.R. Moreira, F. Sanz, Experimental and theoretical study of the optoelectronic properties of alkaline doped Cu₂O films. 2nd new trends in computational chemistry for industry applications. May 25-27, 2011. Barcelona, Spain.

Resum en català

Resum en català

PRÒLEG

L'anodització es pot definir com el procés electroquímic que es duu a terme per tal de produir una capa d'òxid estable sobre una superfície metàl·lica. El nom prové del procés en si mateix: el metall a oxidar actua com a ànode en la cel·la electroquímica i transmet els electrons al càtode a través del circuit extern [1].

La primera patent sobre el tractament anòdic de superfícies data de 1923, quan Bengough i Stuart van desenvolupar un procediment per tal de protegir contra la corrosió les parts d'alumini de l'hidroavió Duralumin [2,3]. D'ençà, l'ús de pel·lícules anòdiques s'ha estès sobretot en la indústria de l'acabat de metalls, ja que proporcionen una bona protecció contra la corrosió, augmenten la resistència al desgast, milloren l'adhesió de pintures o coles i fins i tot poden donar un acabat acolorit per a finalitats decoratives. Donada la seva capacitat protectora, aquestes capes d'òxids també reben el nom d'òxids passius. En metalls amb una vasta aplicació tecnològica com ara l'alumini, el titani, el magnesi o el zinc, l'anodització és un procés industrial molt estandarditzat. La majoria d'ells formen part de la nostra vida quotidiana, per exemple, l'alumini anoditzat s'empra per fabricar certes parts dels avions, elements arquitectònics com marcs de finestres o bé productes de consum (estris de cuina, telèfons mòbils, càmeres fotogràfiques, etc.) mentre que el titani anoditzat s'usa principalment en implants dentals o joieria.

A part d'aquesta finalitat essencialment protectora, els òxids anòdics han demostrat de llarg el seu gran potencial en dispositius biomèdics, fotoelectroquímics, elèctrics i sensors. En la majoria de condicions experimentals les capes d'òxid que es formen en una superfície metàl·lica són de tipus compacte o lleugerament porós. Tanmateix, l'any 1995, Fukuda i Masuda van descriure per primer cop la formació de nanopors perfectament alineats i ordenats mitjançant un procés que es va anomenar anodització autoorganitzada [4]. Uns quants anys més tard, al 1999, es va publicar el creixement autoorganitzat de nanotubs en

titani [5]. La possibilitat de desenvolupar nanoestructures com tubs, pors o canals amb millors propietats respecte al corresponent material compacte va obrir un ampli camp de recerca que ha generat un gran volum de contribucions científiques en els darrers anys. A més, recentment s'ha descrit la formació de capes anòdiques autoorganitzades en molts altres metalls (Ta, Nb, Fe, Sn, W, Hf o Zr) i aliatges (TiZr, TiAl, TiTa, etc.) [6].

Motivació: per què l'estany?

L'estany va ésser un dels primers metalls coneguts per l'home i històricament va tenir un paper clau en el desenvolupament de les primeres civilitzacions. El descobriment dels aliatges coure-estany va marcar l'inici de l'Edat de Bronze i va permetre als primers humans elaborar eines, armes o elements decoratius més duradors. Per tal d'afrontar la creixent demanda, l'estany va ser en un dels primers metalls explotat a les mines.

En l'actualitat, l'estany s'utilitza bàsicament en soldadures o bé com a recobriments per a prevenir la corrosió d'altres metalls. En aquest últim cas, l'exemple més evident són les llaunes d'acer estanyat que s'usen per a la conservació d'aliments. En general, l'estany resisteix bé la corrosió en medi aquós a pH neutre, però pot veure's fàcilment atacat per àcids o bases fortes. En ambdues aplicacions, doncs, els estudis de passivació i corrosió són de gran importància. Durant la dècada dels anys 80, molts treballs d'investigació es van adreçar a aclarir-ne aquests aspectes però la complexitat en la identificació de la composició exacta de la capa d'òxid passiu, la forta dependència de la seva estructura amb les condicions ambientals (electròlit, pH, potencial, etc.) i el gran nombre de possibles vies electroquímiques i espècies en solució va donar lloc a un conjunt de dades força disperses.

En el nostre grup de recerca, Raul Díaz va estudiar el comportament electroquímic del estany en solucions tampó d'àcid bòric i tetraborat sòdic a pH neutre i va aplicar per primera vegada a aquest sistema la tècnica de microscòpia d'efecte túnel amb control electroquímic (EC-STM) per tal de seguir-ne *in situ* el procés d'oxidació [7]. En medi neutre, l'estabilitat dels òxids d'estany és major i per tant les capes que s'obtenen són més primes i difícils de caracteritzar i els processos electroquímics menys evidents. Basats en aquesta experiència prèvia al grup en l'estudi del comportament electroquímic de l'estany així com en d'altres metalls com el coure o el ferro [7–14], es va decidir realitzar un estudi sistemàtic de la passivació de l'estany en medi alcalí. Amb aquesta finalitat, es van emprar eines electroquímiques clàssiques com la voltamperometria o la espectroscòpia d'impedància electroquímica, disponibles al nostre laboratori, juntament amb tècniques de caracterització *ex situ* com la microscòpia electrònica de rastreig, la microscòpia de forces atòmiques, la difracció de raigs X, l'espectroscòpia Raman i l'espectroscòpia de fotoelectrons emesos per raig X o bé *in situ* com el EC-STM. Combinant totes aquestes mesures i tècniques de caracterització vam poder detectar nous processos electròdics com ara l'atac preferencial mediat per ions hidroxil, la electrocristal·lització de SnO o les modificacions superficials prèvies al primer pic d'oxidació.

Malgrat que aportar una mica de llum en tot el procés de passivació de l'estany en medi alcalí és en sí una motivació, l'exploració de l'oxidació electroquímica o anodització per a la preparació de capes d'òxid funcionals és un repte encara més estimulant. D'acord amb els seus possibles estats d'oxidació, els òxids estequiòmètrics a què pot donar lloc l'estany són en SnO i el SnO₂. També pot formar fàcilment òxids intermedis amb una valència mixta gràcies a la quantitat de defectes que pot encabir en la seva estructura. Dins d'aquesta família d'òxids, el SnO₂ en particular ha estat definit com un material amb "una abundància d'usos" que poden anar des d'òxids transparents conductors a sensors de gasos, bateries de liti, supercapacitors, detectors de radiació UV, transistors d'efecte camp o cel·les solars. En moltes d'aquestes aplicacions, l'ús d'estructures de SnO₂ en forma de nanopors o nanotubs amb un elevada raó superfície/volum podria marcar realment una gran diferència.

Objectius

D'entrada hi ha dos grans objectius en aquesta Tesi: d'una banda es pretén entendre de manera quantitativa el comportament anòdic de l'estany en solucions alcalines i els processos que hi estan involucrats, i de l'altre desenvolupar nanoestructures anòdiques d'òxid d'estany amb aplicacions reals en dispositius.

Respecte a l'estudi fonamental de la passivació de l'estany, d'entrada es requereix una caracterització electroquímica bàsica, després créixer capes d'òxids tant en el règim actiu com passiu i finalment caracteritzar-ne la topografia i la composició. Amb això, es pot extreure una imatge global de com té lloc el procés. Per tal d'obtenir informació sobre com s'inicia el procés d'oxidació cal un estudi *in situ* a nivell atòmic mitjançant la microscòpia d'efecte túnel amb control electroquímic (EC-STM). Encara que el nostre grup té experiència en el camp del EC-STM, per aquesta part es va decidir col·laborar amb el grup del Professor Philippe Marcus, un dels laboratoris més importants en l'estudi EC-STM de processos d'oxidació.

Els coneixements adquirits per assolir aquest primer objectiu conformen un rerefons de coneixements fonamentals sobre el comportament dels òxids en solució i la seva estabilitat, i per tant tindran un paper destacat en el desenvolupament de les estructures autoorganitzades d'òxid d'estany. Per a créixer-les, es va col·laborar amb el laboratori del Professor Patrik Schmuki, expert en l'anodització autoorganitzada de titani i d'altres metalls i aliatges. Primerament es van optimitzar les condicions experimentals per obtenir les estructures poroses organitzades. Un cop obtinguda la nanoestructura desitjada, les mostres es van tractar tèrmicament per tal de millorar-ne la cristal·linitat i ajustar-ne les propietats abans de la seva aplicació en sensors de gasos i ànodes per a la fotòlisi de l'aigua. Els resultats finals demostren les possibilitats de les nostres pel·lícules en aplicacions reals. Amb tot, aquest objectiu és tan ambiciós que possiblement les dades que es recullen en aquesta tesi són només la punta de l'iceberg. Hi ha encara moltíssim treball en aconseguir estructures poroses més definides i ordenades i en provar noves aplicacions potencials.

Estructura de la memòria

Aquesta tesi s'ha estructurat en dues parts diferenciades per tal de discernir els capítols que tracten sobre l'estudi fonamental del comportament electroquímic de l'estany (Part A) dels que es concentren en desenvolupar les nanoestructures anòdiques d'òxid d'estany i la seva aplicació en sensors o ànodes per a la fotòlisi de l'aigua (Part B). A l'inici de cadascuna de les parts hi ha un capítol introductori on es proporcionen tots els conceptes necessaris per entendre els resultats.

PART A: ESTUDI FONAMENTAL

- **Introducció:** pretén definir conceptes indispensables com ara la passivació. També inclou una breu explicació sobre els mecanismes més habituals de creixement dels òxids passius i del coneixements sobre l'electroquímica de semiconductors necessaris per a interpretar els resultats dels capítols 1 i 2. A més, es subratlla la importància del EC-STM en els estudis de passivació i corrosió i es discuteixen els resultats obtinguts en altres metalls com el Cu, Fe i Ni. Finalment, s'inclou un resum sobre les conclusions més rellevants sobre el mecanisme de passivació de l'estany a què s'ha arribat fins ara, amb especial èmfasi en les reaccions proposades i la possible estructura de la capa passiva.
- **Capítol 1:** conté el resultat sobre l'estudi del comportament electroquímic de l'estany en medi alcalí. Es caracteritzen els òxids formats tant en el rang de potencials actiu com en el passiu i es proposa un mecanisme per als diferents processos i reaccions identificades. Dins aquest capítol cal destacar la detecció d'un procés que no ha estat descrit amb anterioritat en la literatura: la formació de cristalls de SnO micromètrics degut a l'atac del Sn metàl·lic per els grups OH. Els resultats aquí detallats es troben publicats a *Electrochimica Acta* 111 (2013) 837 - 845.
- **Capítol 2:** s'inicia amb l'optimització del procés de polí i atac químic per a revelar superfícies atòmicament planes en policristalls d'estany. Després, en aquestes terrasses atòmicament planes es segueixen els primers estadis de l'oxidació anòdica mitjançant EC-STM. L'estudi té lloc en medi alcalí i permet seguir els canvis que tenen lloc en la morfologia abans de l'inici del primer procés de passivació, que tal com es demostra segueix un mecanisme de dissolució-precipitació. Els resultats s'estan preparant per a la seva publicació.

PART B: APLICACIONS

- **Introducció:** inclou els principis bàsics de l'anodització autoorganitzada, una revisió sobre els treballs existents per al cas de l'estany i de les millores necessàries en

l'estructura per tal que aquesta es pugui implementar en dispositius. Les seccions posteriors contenen conceptes relacionats amb les aplicacions que es discutiran en els capítols 4, 5 i 6. Per exemple, es descriu el funcionament de sensors de gasos resistius i els millors resultats obtinguts fins ara en a la detecció de H_2 emprant SnO_2 , o en referència a les aplicacions fotoelectroquímiques, es descriuen els processos induïts per la llum en un semiconductor, en la corresponent interfície semiconductor | solució i els principals requisits per obtenir ànodes eficients en la fotòlisi de l'aigua.

- **Capítol 3:** mostra tot el rastreig d'electròlits i condicions electroquímiques que es duu a terme per assolir estructures anòdiques autoorganitzades d'òxid d'estany amb pors nanomètriques completament oberts i lliures de fractures en la seva secció transversal. Els resultats es poden trobar a *J. Mater. Chem. A 2 (2014) 915 - 920*.
- **Capítol 4:** les capes desenvolupades en el capítol 3 s'empren en sensors de H_2 . S'estudia l'efecte de la temperatura de recuit, la temperatura a la qual treballa el sensor o el gruix, en la sensibilitat i el límit de detecció del sensor. A més, es compara la resposta de les nostres capes d'òxid amb la que presenten capes preparades en condicions no optimitzades o bé en d'altres electròlits com l'àcid oxàlic. Els resultats dels sensors han estat publicats en *J. Mater. Chem. A 2 (2014) 915 - 920*.
- **Capítol 5:** està adreçat a estudiar l'efecte de la temperatura de recuit en la composició, l'estructura i les propietats fotoelectroquímiques de les pel·lícules d'òxid d'estany autoorganitzades. També s'avalua l'efecte de l'atmosfera de recuit. Gràcies a aquest tractament tèrmic en condicions controlades, s'obtenen estructures d'òxid d'estany amb absorció en la zona de la llum visible. Aquestes capes s'han aplicat en la fotòlisi de l'aigua. Part dels resultats aquí descrits es troben publicats a *ChemElectrochem 1 (2014) 1133-1137*.
- **Capítol 6:** descriu la preparació d'ànodes per a la fotòlisi de l'aigua que combinen dues estructures; d'una banda una pel·lícula anòdica d'òxid d'estany nanoporosa com a material matriu o suport i de l'altra nanopartícules de Fe_2O_3 que actuen com a absorbent de la llum. Per tal que el fotoànode sigui eficient cal millorar les propietats conductores de l'òxid d'estany dopant-lo eficaçment amb antimoni. Aquest pas és clau per a la eficiència global de l'elèctrode. També s'avaluen d'altres paràmetres rellevants com el temps de dipòsit del Fe_2O_3 o el gruix de la capa de SnO_2 . Els resultats estan recollits a *ChemSusChem 7 (2014) 421-424*.

CONCLUSIONS, APÈNDIXS I ALTRES

Les conclusions generals de la tesi van seguides de 4 apèndixs: l'**Apèndix a** mostra l'efecte de la temperatura, la concentració de NaOH i els dissolvents orgànics en la morfologia dels cristalls de SnO ; l'**Apèndix b** inclou experiments preliminars sobre la millora de les

estructures d'òxid d'estany autoorganitzades emprant estratègies avançades com els polsos de potencial o superfícies prèviament indentades; l'**Apèndix C** detalla els símbols i acrònims utilitzats en aquesta tesi; i finalment l'**Apèndix d** conté el llistat de publicacions i congressos durant el període 2010-2014.

PART A: estudi fonamental

Introducció

La passivació d'un elèctrode metàl·lic es pot definir com "l'obstaculització, en certes condicions, de la reacció de dissolució termodinàmicament favorable"[15]. Dit amb altres paraules, la passivació en un ànode metàl·lic en retarda cinèticament la seva dissolució espontània, i per tant esdevé químicament inactiu o inert respecte a factors ambientals com ara l'aire o l'aigua. La majoria de metalls com l'alumini, el titani o el mateix estany són auto-passivants i en una atmosfera determinada reaccionen immediatament formant una capa prima d'òxid. Per contra, el ferro o altres metalls pateixen una corrosió uniforme i necessiten estar recoberts o be aliats amb altres metalls per tal de crear una pel·lícula protectora.

L'estudi fonamental dels processos de passivació i corrosió en medi aquós s'ha abordat sempre a través de l'Electroquímica clàssica. Tècniques electroquímiques bàsiques han proporcionat informació sobre aspectes tant cinètics com termodinàmics per a una gran varietat d'elèctrodes metàl·lics en contacte amb diferents medis o solucions. Gran part dels esforços en aquest camp també s'han adreçat a entendre l'estructura química i cristal·lina de les capes d'òxid passiu, ja que la seva distribució atòmica o defectes estructurals determinen en gran mesura les seves propietats elèctriques i el seu caràcter protector.

Aspectes bàsics de la passivitat dels metalls

Un metall noble que es troba en contacte amb l'aire o una solució, és termodinàmicament estable perquè té un potencial de reducció elevat. Per contra, en els metalls no nobles la diferència entre el potencial redox entre el metall i l'altre fase actua com a força impulsora per la oxidació del metall ($\Delta G < 0$) [15]. Les condicions ambientals poden afavorir tant la dissolució del metall com la formació d'una capa insoluble d'òxid (passivació), per tant ambdós processos estan en certa manera competint. Com en tot procés químic, cal considerar els dos factors; l'equilibri (termodinàmic) i el cinètic.

L'estabilitat termodinàmica de les diferents espècies en funció del pH i el potencial electroquímic es sol donar en forma de diagrames de Pourbaix [15-17]. Aquests diagrames permeten predir les regions d'existència; per exemple, per a un combinació determinada de pH i potencial podem saber si és termodinàmicament més estable que un metall romangui inert (immunitat), es dissolgui activament (corrosió) o formi una capa d'òxid o hidròxid

(passivació). Aquests diagrames, però, no donen cap informació de tipus cinètic ni sobre la composició o estructura final de la capa passiva, per tant cal usar-los amb cura i només com a una eina orientativa. Per tal de tenir informació sobre aspectes termodinàmics i cinètics alhora són molt útils les corbes de polarització [16]. Podem extreure'n informació sobre els diferents estats d'oxidació del metall i les transicions entre la zona activa i passiva. A més, el corrent crític és una mesura de la facilitat amb què l'elèctrode metàl·lic es passiva i mentre que el corrent durant el règim passiu ho és de la seva capacitat protectora [15].

Mecanismes de formació de capes passives

Hi ha bàsicament dos models per a descriure la formació de capes passives:

- “Layer pore resistance model” o de dissolució-precipitació: aquest model va ser inicialment proposat per Müller i ampliat posteriorment per Calandra *et al.* [20,21]. Assumeix que la passivació de la superfície es dona a través d'un procés de dissolució-precipitació: el metall es dissol fins assolir una concentració crítica i després una pel·lícula d'òxid poc conductor precipita recobrint-ne la superfície. Inicialment els precipitats s'estenen per la superfície mantenint constant el gruix de la capa fins que només queden petits pors. Després, el gruix de la capa augmenta mantenint constant l'àrea dels pors. La corrent ve controlada per la resistència del sistema capa-pors. En general aquests òxids presenten estructures de tipus tridimensional (no epitaxials) i amb mala capacitat protectora.
- “High field mechanism” o de migració iònica: permet descriure la formació de capes barrera en la superfície d'un elèctrode metàl·lic. La pel·lícula d'òxid creix gràcies a la migració d'ions (M^{n+} o O^{2-}) a través de l'òxid. Per tant hi ha dos fronts on es pot desenvolupar: la interfase metall | òxid i la de l'òxid | solució. Les capes d'òxid que creixen seguint aquest mecanisme solen ser compactes (capes barrera) i impedeixen el pas de corrent a través seu en assolir un gruix determinat. Si el creixement té lloc a potencial constant, el corrent decau exponencialment. Hi ha diferents models que pretenen predir-ne el comportament i donar un mecanisme plausible per a la migració dels ions (Cabrera-Mott [27], Fehlner-Mott [28] i Macdonald, també conegut com a “Point Defect Model”[31,32]).

Propietats de les capes d'òxid passives

Els òxids passius solen ser amorfs o nanocristal·lins i no-estequiomètrics, per tant contenen una gran quantitat de defectes que poden actuar com a dopants. Hi ha molts paràmetres que poden influir notablement en el seu gruix i composició com ara el potencial de passivació, el temps d'anoditzat, la solució on es forma o la temperatura [15]. A més, les capes passives no s'han de considerar un sistema rígid, sinó un sistema en equilibri dinàmic que pot veure's afectat per factors ambientals. Per exemple, l'alteració amb el temps de la composició,

l'estructura, el grau d'hidratació i la conductivitat iònica o electrònica són fenòmens ben documentats [15].

Les propietats electròniques del òxids passius són molt importants perquè en alguns casos fins i tot poden determinar-ne el mecanisme de formació o el seu trencament transpassiu, donat que són processos que involucren la difusió de portadors de càrrega a través de la capa. La majoria d'òxids passius es comporten com a materials semiconductors. A diferència dels metalls, en els semiconductors els estats energètics que contenen electrons i els que es troben buits estan diferenciats en la banda de valència i la de conducció, respectivament. Ambdues bandes es troben separades per la banda prohibida (E_g). En presència de defectes, com és típic en les capes passives, s'introdueixen nous nivells dins de la banda prohibida que poden actuar com a donadors o acceptors d'electrons. Si un semiconductor conté un nivell acceptor prop de la banda de valència, els nombre de buits (h^+) supera al d'electrons a la banda de conducció i per tant el material es comporta com un semiconductor tipus p, per contra, si disposa d'un nivell donador a prop de la banda de conducció els electrons (e^-) seran els portadors de càrrega majoritaris i parlarem d'un semiconductor tipus n [12].

Interfície semiconductor | solució: efecte del potencial i mesures de capacitàcia

Les propietats electròniques de les capes passives es poden estudiar mitjançant tècniques derivades de l'electroquímica de semiconductors com ara la fotoelectroquímica o les mesures de capacitàcia Mott-Schottky. Per ambdues cal primer introduir el comportament de la interfície semiconductor | solució.

Quan s'introdueix un semiconductor en una solució, l'energia del nivell de Fermi (E_F) del semiconductor s'iguala a l'energia del parell redox de l'electròlit, $E_{F,Redox}$ (veure Fig. 1). Això, provoca una redistribució de la densitat de càrrega tant en el semiconductor com a la

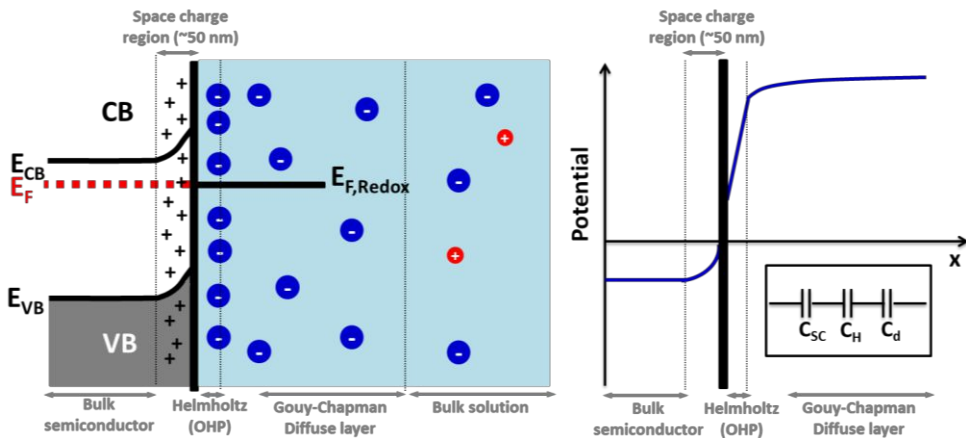


Figura 1 Esquema de la doble capa elèctrica formada en posar en contacte un elèctrode semiconductor i un electròlit.

interfície, donant lloc a la doble capa elèctrica. La doble capa elèctrica a la banda de l'electròlit es descriu com una capa rígida de Helmholtz acompanyada d'una regió difosa. Aquesta interfície (C_{el}) es pot descriure com a dos condensadors en sèrie de capacitats C_H i C_d , respectivament. En el cas dels metalls la densitat de càrrega es concentra a la superfície però en els semiconductors com que el nombre de portadors de càrrega es menor, la distribució de càrrega es pot estendre una distància considerable dins el semiconductor donant lloc a l'anomenada regió de càrrega espacial. Així doncs, la interfície es pot representar com un conjunt de condensadors en sèrie on cadascun representa una regió de la doble capa:

$$\frac{1}{C_{Total}} = \frac{1}{C_{SC}} + \frac{1}{C_{el}} = \frac{1}{C_{SC}} + \frac{1}{C_H} + \frac{1}{C_d}$$

En un semiconductor tipus n, típicament es transfereixen electrons de l'elèctrode a la solució, per tant la regió de càrrega espacial roman carregada positivament i les bandes es dobleguen cap amunt (Fig. 1). En un semiconductor tipus p, es transfereixen electrons de la solució a l'elèctrode, carregant negativament la regió de càrrega espacial i per tant les bandes es dobleguen cap avall. Com que en ambdós casos els portadors de càrrega majoritaris s'extreuen de la interfase, es diu que la regió de càrrega espacial es troba en depleció.

Modificant el potencial electroquímico, podem desplaçar la posició del E_F del semiconductor i per consegüent influir en l'extensió de la regió de càrrega espacial. Tal com es detalla a la Fig. 2 es poden donar les següents situacions:

- La càrrega dins el sòlid es compensa amb les càrregues en superfície i no hi ha una caiguda de potencial a través de la interfície. En aquestes circumstàncies, l'energia de les bandes a la superfície del semiconductor és la mateixa que en la resta del material i per tant les bandes es representen com a planes. Aquest potencial s'anomena de bandes planes (E_{FB}) i podríem dir que és anàleg al potencial de càrrega zero d'un metall.
- Regió de depleció: té lloc a potencials més positius a E_{FB} en un semiconductor tipus n i a potencials més negatius a E_{FB} en un semiconductor tipus p. En aquest cas s'extreuen els portadors majoritaris de la superfície i es forma una capa "aïllant".
- Acumulació: a potencials més negatius a E_{FB} en un semiconductor tipus n hi ha un excés de portadors majoritaris, e^- , a la regió de càrrega espacial, mentre que en un semiconductor tipus p calen potencials més positius al E_{FB} per tal d'acumular h^+ . En aquestes condicions el material semiconductor es comporta gairebé com un metall.

Les mesures d'impedància permeten determinar la capacitància de la regió de càrrega espacial d'un semiconductor. Representat aquests valors en funció del potencial electroquímico podem extreure, usant la raó de Mott-Schottky (Fig. 3), informació sobre les seves propietats electròniques: E_{FB} , tipus de semiconductor i nombre de portadors (N_D).

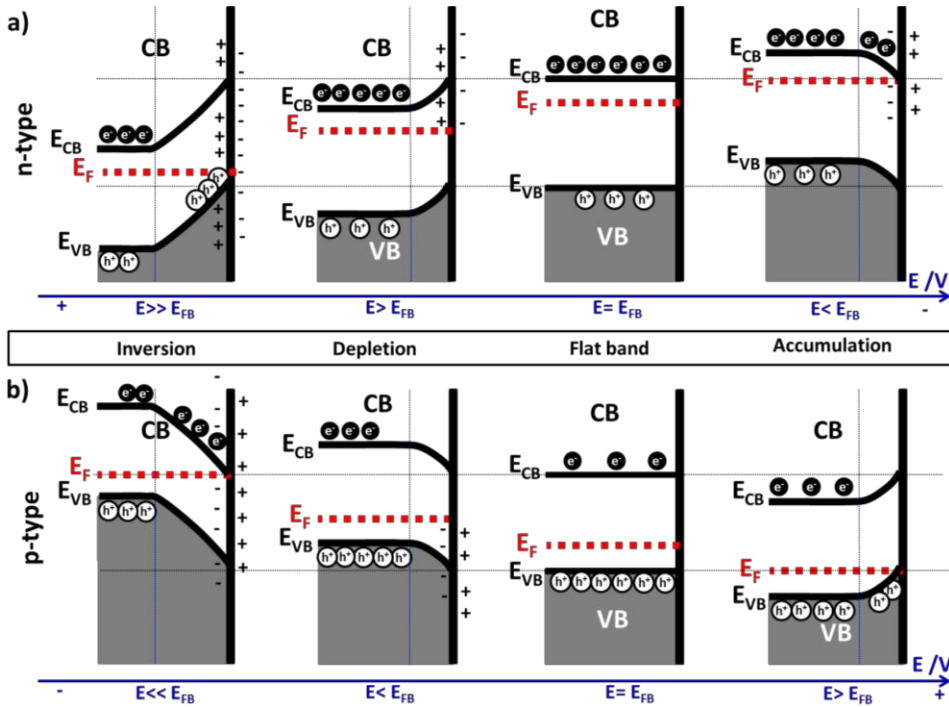


Figura 2 Diagrames de bandes mostrant la regió de càrrega espacial per a un semiconductor tipus a) n i b) tipus p en diferent potencial (E). Es descriuen quatre situacions: inversió, depleció, bandes planes i acumulació.

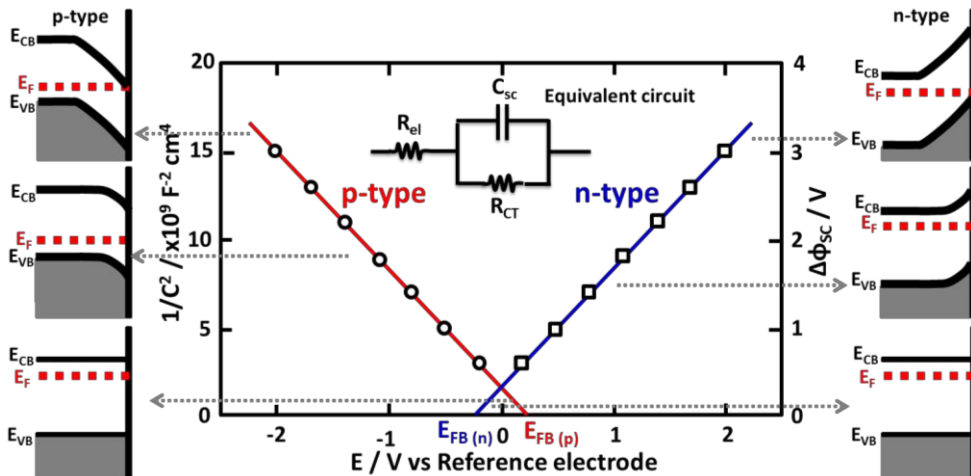


Figura 3 Representació Mott-Schottky de les dades de capacítància per a un semiconductor tipus n i tipus p en condicions de depleció. L'esquema lateral mostra el comportament seqüencial de les bandes la quan es modifica el potencial respecte a la condició de bandes planes (E_{FB}). Dins el gràfic es detalla el circuit equivalent utilitzat per simular les dades d'impedància: R_{el} és la resistència de la dissolució, R_{CT} la residència de l'òxid al pas de la càrrega i C_{sc} la capacítància del semiconductor.

$$\frac{1}{C_{\text{Total}}^2} = \frac{2}{\epsilon\epsilon_0 e N_D} \left(E - E_{\text{FB}} - \frac{k_B T}{e} \right)$$

on C_{Total} es la capacítància de la interfície semiconductor | solució, E el potencial aplicat, k_B la constant de Boltzmann, T la temperatura absoluta i e la càrrega de l'electró ($k_B T/e = 0.025$ V) [13]. La capacítància total es pot aproximar a la capacítància del semiconductor (C_{SC}). En aquest resum no s'inclou la derivació de l'equació però es pot trobar a la referència [49].

Passivació de l'estany: reaccions i estructura de la capa passiva

Tot i la gran quantitat de referències disponibles sobre la passivació [65-78] i corrosió [82-84] de l'estany, les possibles reaccions electroquímiques i la composició final de la capa passiva encara generen controvèrsia. Fins ara la majoria de treballs coincideixen en què el primer procés anòdic correspon a la dissolució activa de l'estany per a formar espècies divalents en solució que posteriorment donaran lloc a una primera capa passivant de $\text{Sn}(\text{OH})_2$ o SnO [7,65-76]. Independentment de la dissolució en què es realitza l'estudi, el procés té lloc seguint un mecanisme de dissolució-precipitació [7,65-72]. El segon procés anòdic, però, ha generat més discussió, perquè tot i que es considera que el SnO_2 és l'òxid final, la via per la qual es forma no està clara. S'ha proposat per exemple que pot provenir de l'oxidació de la capa prèvia [70], de l'oxidació directa del metall a $\text{Sn}(\text{OH})_4$ [86] o bé d'ambdós processos alhora [65,66,68,69]. Aquest $\text{Sn}(\text{OH})_4$ deshidrata i esdevé més estequiomètric en augmentar el potencial anòdic [68,71].

La composició final de la capa passiva tampoc acaba d'estar clara. Stirrup *et al.* proposen una estructura dual que conté una capa externa de $\text{Sn}(\text{OH})_2$ i/o SnO i una capa de $\text{Sn}(\text{OH})_4$ a la interfase òxid | metall [65]. Per contra, les mesures d'espectroscòpia de fotoelectrons emesos per raig X d'Ansell *et al.* mostren només la presència de SnO_2 o $\text{Sn}(\text{OH})_4$.

Capítol 1: Electroquímica de l'estany (Sn) en medi alcalí

Objectius

- Caracteritzar mitjançant tècniques microscòpiques i espectroscòpiques l'evolució en la composició química, l'estructura i les propietats electròniques de les capes d'òxid d'estany formades en la zona activa i passiva.
- Proposar un mecanisme complet per a la passivació electroquímica de l'estany en medi alcalí.

Resultats

S'ha estudiat el procés de passivació en medi alcalí per a un elèctrode metàl·lic de Sn. S'ha cobert un ampli rang de potencials que abasta des de la zona activa a la passivació final. Per

a estudiar en detall els processos i caracteritzar els diferents òxids, s'ha dividit el rang electroquímic en diferents regions de potencial d'acord amb els processos que hi tenen lloc (veure Fig. 4). A potencials inferiors a -0.9 V, es forma una primera capa passiva de $\text{SnO}\cdot n\text{H}_2\text{O}$ amb una coloració blanquinosa. Aquesta capa creix seguint un mecanisme de dissolució-precipitació. La formació d'aquesta capa es veu afavorida a pH neutres o moderadament alcalins gràcies al seu baix producte de solubilitat. A valors de pH fortament alcalins, la dissolució d'espècies que contenen Sn(II) té lloc donada la seva naturalesa amfòtera i per tant la capa perd estabilitat. Aquesta primera capa passiva és amorfa i porosa, en conseqüència, no passiva de forma efectiva la superfície de l'elèctrode.

A potencials superiors a -0.9 V (més anòdics), s'observa la formació d'uns cristalls negres de mida micromètrica a la superfície de l'elèctrode. Aquests cristalls tridimensionals corresponen a la fase tetragonal de SnO , i provenen de la descomposició de complexos d'estany Sn^{2+} en solució. Aquests complexos es deriven de l'atac preferencial de la superfície de Sn, clarament evidenciat per la presència de cavitats piramidals a la interfase metall/ SnO . El procés depèn fortament de la concentració de NaOH i el potencial es desplaça considerablement a valors més negatius en incrementar-ne la concentració. Finalment, a potencials més positius de -0.7 V s'observa una caiguda sobtada del corrent i es deté la formació de cristalls de SnO degut a la passivació final de l'elèctrode de Sn. Aquesta capa passiva està basada en Sn(IV) i té un caràcter semiconductor tipus n. Tot sembla indicar que els cristalls de SnO no tenen cap paper en la passivació i la capa passiva es desenvolupa a la interfase Sn/ SnO .

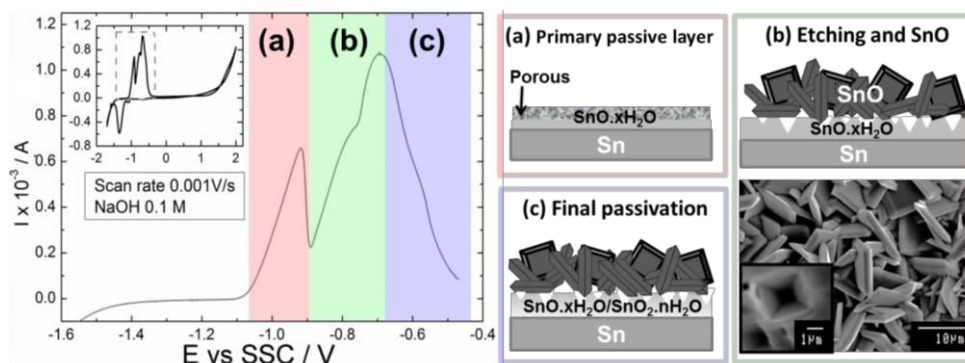


Figura 4 Resum de les regions de potencial electroquímic discutides en el Capítol 1 i esquema de la composició de les capes d'òxid en cadascuna d'aquestes regions.

Capítol 2: Estudi a nivell nanomètric dels primers estadis de l'oxidació electroquímica de l'estany

Objectius

- Optimitzar el procés de polí i atac preferencial químic per tal d'assolir superfícies de Sn atòmicament planes on poder realitzar les mesures de EC-STM.

- Seguir per EC-STM els canvis morfològics i les reaccions que tenen lloc durant els primers estadis de l'oxidació anòdica del Sn en una solució de NaOH 0.05 M.
- Relacionar els fenòmens observats amb els estudis previs en d'altres metalls o per al Sn en solució tampó d'àcid bòric i tetraborat sòdic.

Resultats

Per tal de seguir els primers estadis de l'anodització de l'estany primerament s'ha optimitzat el procediment per a preparar superfícies atòmicament planes combinant un procés de polítmic i un posterior revelat preferencial. Amb aquest mètode es formen estructures piramidals en els grans amb orientació (001) del policristall d'estany, que presenten cares perfectament llises en els plans {101}. En aquests plans, que contenen terrasses atòmicament planes, s'han dut a terme les mesures de EC-STM (Fig. 5a).

A potencials molt negatius (-1.3 V), on esperem que no hi hagi cap reacció, la superfície de l'elèctrode de Sn es troba recoberta per unes illes d'uns 20 - 50 nm d'amplada i una alçada de ~ 0.05 nm (Fig.5b i 5c). L'origen aquestes illes encara no es compren però es proposen diferents hipòtesis com la formació d'una capa de OH adsorbits, l'acumulació d'impureses o bé una possible reconstrucció superficial. Aquestes illes es troben localitzades preferentment a les vores de les terrasses, romanen estàtiques en augmentar el potencial i tenen una alçada aparent positiva. Tots aquests factors contradiuen les característiques habituals de les capes de OH adsorbides en metalls de transició com el Cu o el Ni . Els fenòmens de reconstrucció superficials també solen ser processos dependents del potencial, per tant les tendències observades no acaben de suportar aquesta teoria. D'altra banda la presència d'impureses està pendent de confirmació amb experiments complementaris com el XPS amb incidència rasant o el XANES. A potencials de -1.1 V una nova fase es desenvolupa sobre les illes. L'alçada d'aquesta sembla coincidir amb la distància interplanar del Sn, per tant sembla que té lloc un procés de dissolució i redeposició del metall. A potencials més anòdics s'inicia la dissolució de les terrasses i la formació de precipitats distribuïts aleatòriament per la superfície. Si el potencial s'augmenta fins a -0.94 V, la precipitació de la fase 3-D es veu accelerada i s'observen cavitats provinents de la dissolució del metall d'uns quants nanòmetres de

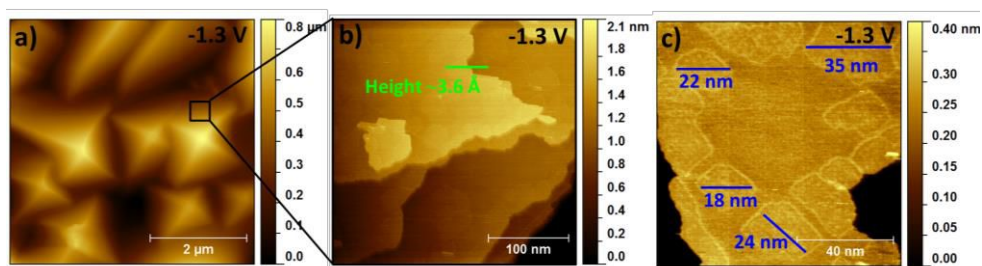


Figura 5 a) Imatge EC-STM ($5 \times 5 \mu\text{m}^2$) de les cares piràmides formades en els grans amb orientació (001) de la superfície policristal·lina d'estany, b) imatge de les terrasses en les cares {101} de les piràmides ($300 \times 300 \text{ nm}^2$) i c) imatge de les illes presents en les terrasses ($100 \times 100 \text{ nm}^2$) adquirides a un potencial de $E_S = -1.3 \text{ V}$ ($E_{\text{tip}} = -0.9 \text{ V}$, $E_{\text{bias}} = 0.4 \text{ V}$).

profunditat. L'aparició d'aquest precipitat d'òxid poc conductor provoca la pèrdua de la imatge de EC-STM.

PART B: Aplicacions

Introducció

Per tal d'entendre el creixement de nanotubs o nanopors mitjançant l'anodització autoorganitzada cal considerar primer la formació de capes compactes o barrera mitjançant la migració de ions. En aquests casos si l'òxid és molt poc soluble en l'electròlit es formarà una capa compacta però si es proporciona una concentració moderada de ions que n'afavoreixin la solubilitat, com H^+ en el cas de l'alumini o F^- en el del titani, llavors es pot establir un equilibri entre el creixement de l'òxid per migració i la seva dissolució a la interfase electròlit | òxid. Aquest equilibri entre les dues situacions és la clau per a la formació de nanotubs o nanopors tal com es mostra a la Fig. 6.

D'entrada es forma una capa compacta o barrera, anomenada capa d'iniciació. Aquesta capa conté defectes i imperfeccions on tendeix a acumular-se l'estrès i també localment el camp elèctric fent que s'iniciïn els primers pors. Els pors creixen i es combinen amb pors adjacents fins que s'igualen les mides de tots i comencen a créixer a una velocitat constant. Durant el creixement dels pors s'assoleix una situació d'equilibri entre la formació de l'òxid a la interfase òxid | metall i la seva dissolució a la interfase òxid | electròlit.

Control de la geometria en l'anodització autoorganitzada

L'anodització autoorganitzada és una tècnica amb un gran potencial ja que permet controlar acuradament la geometria (tubs o pors), el seu diàmetre o gruix final.

- Pors o tubs: ambdues estructures parteixen d'una capa inicial porosa, és la solubilitat de les fronteres entre els pors la que determinarà si s'obtindran estructures tubulars o no. Normalment aquestes zones són riques en ions de la dissolució. En el cas del Ti i l'Al, en igualtat de condicions la major solubilitat de les espècies Ti-F i Ti-O-F fa que el Ti doni lloc a la formació de tubs, mentre que per a l'Al s'obtenen pors. Per tant la separació entre tubs està estretament lligada a la concentració d'espècies que promouen la dissolució (F^- en l'exemple citat) i al contingut d'aigua, necessària per a la solubilització dels complexos.
- Diàmetre i gruix: el diàmetre dels tubs o pors depèn linealment del potencial per a un mateix electròlit i temperatura. El temps d'anoditzat determina el gruix de la capa fins que s'assoleix un estat estacionari entre el creixement de l'òxid i la seva dissolució a la part superior i per tant el procés s'atura. En medis aquosos la dissolució es veu

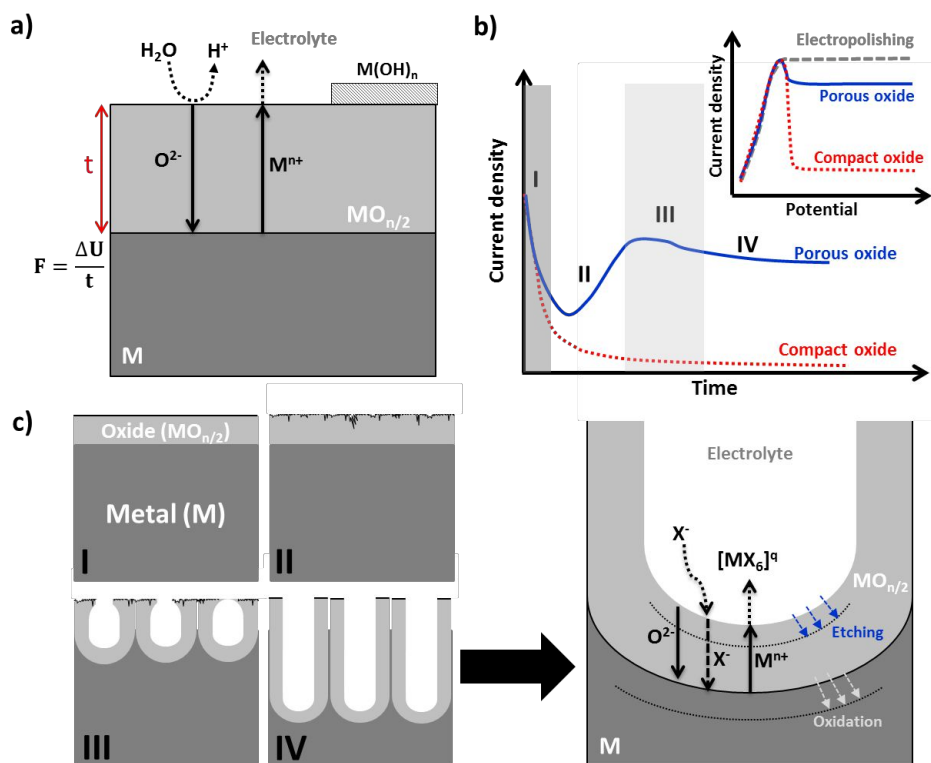


Figura 6 a) Esquema del creixement d'una capa compacta per mecanisme de migració de ions. Aquest procés es dona si la capa es desenvolupa en absència d'un agent que promogui la dissolució de l'òxid (X). b) Típica corba corrent-temps obtinguda en aplicar un esglaió de potencial per al creixement d'una capa compacta o porosa. El requadre indica el comportament de la corba potencial-corrent en augmentar la concentració de l'agent que afavoreix la solubilitat de l'òxid. c) Il·lustració de les diferents etapes involucrades en el creixement anòdic de capes poroses o nanotubulars en relació a les etapes indicades a la corba b). L'anodització es duu a terme en presència de X^- que dona lloc al complex soluble $[MX_6]^q$. Adaptat de les referències [6,25,123].

afavorida i el gruix de les estructures sol ser inferior a $1 \mu m$, per contra, en solucions amb un alt contingut orgànic es poden obtenir capes de fins a $\sim 70 \mu m$.

- **Estructures avançades (tubs ramificats, tubs en forma de bambú):** la geometria dels tubs o pors es pot alterar modificant el potencial durant el creixement ja sigui disminuint-lo, aturant-lo o fent esglaió de potencial. A més, es poden aplicar tractaments posteriors a l'anodització per promoure la dissolució.

L'anodització autoorganitzada de l'estany: treballs previs

L'anodització autoorganitzada de l'estany es troba encara en una fase molt preliminar si es compara amb d'altres metalls com el titani o l'alumini. Fins ara les nanoestructures de SnO_2

s'havien preparat seguint tècniques físiques com l'evaporació [181] o l'ablació làser [185], o per mètodes en solució com la síntesi hidrotermal [182] o l'electrodeposició en plantilles [188]. Al 2004, Shin *et al.* va descriure per primer cop la preparació d'estructures poroses de SnO₂ mitjançant l'anodització autoorganitzada en solucions d'àcid oxàlic [189]. Les estructures obtingudes presentaven discontinuïtats al llarg dels canals degut a la forta evolució d'oxigen i a l'elevada velocitat de creixement. Malgrat que inicialment aquestes estructures discontinües o multicapa poden semblar beneficioses per aplicacions catalítiques, per d'altres com els sensors de gasos o ànodes per a la fotòlisi de l'aigua calen capes més homogènies i robustes.

En treballs posteriors s'ha intentat minimitzar la presència d'aquestes fissures optimitzant la temperatura, el potencial, la concentració d'àcid oxàlic o fins i tot emprant polsos de potencial. Tanmateix, els resultats d'aquests estudis no són massa esperançadors; quan es redueix la temperatura o el potencial per disminuir la velocitat de formació de l'òxid s'obtenen capes amb pors totalment obstruïts. Recentment, Ono *et al.* ha proposat un electròlit alternatiu basat en NaOH però els resultats són similars als descrits per a l'àcid oxàlic [191].

Capítol 3: Desenvolupament d'estructures anòdiques d'òxid d'estany en forma de nanocanals

Objectius

- Trobar un electròlit alternatiu al NaOH o l'àcid oxàlic per a obtenir estructures autoorganitzades d'estany.
- Optimitzar les condicions experimentals per tal d'obtenir nanoestructures sense fissures en la seva secció transversal i amb pors perfectament oberts a la superfície.

Resultats

En primer lloc s'ha fet una prospecció de possibles electròlits i condicions electroquímiques per a l'obtenció de capes anòdiques d'òxid d'estany autoorganitzades. L'objectiu final era la preparació de pel·lícules amb les superfícies dels pors totalment obertes i sense esquerdes. Dels electròlits estudiats, el que proporciona uns resultats més prometedors és el basat en una solució de Na₂S i NH₄F en una mescla d'aigua i solvent orgànic. Optimitzant-ne la composició i utilitzant un potencial adequat és possible obtenir estructures amb nanocanals amb un gruix de fins a ~ 4.5 μm (Fig. 7a i 7b). Les estructures són inicialment de natura amorfa i contenen fins a un 3% d'impureses com ara fluorur, sulfur o carboni provinents de la dissolució.

Capítol 4: Aplicació de les estructures autoorganitzades de SnO₂ en sensors de H₂

Objectius

- Desenvolupar estructures autoorganitzades d'òxid d'estany sobre substrats de Si/SiO₂ per poder dur a terme el tractament tèrmic necessari a 700 °C.
- Aplicar les pel·lícules en la detecció de H₂ i ajustar-ne els paràmetres rellevants com la temperatura de recuit, la temperatura d'operació del sensor o el gruix.
- Comparar la resposta a la presència de H₂ de les capes nanoestructurades de SnO₂ preparades en condicions optimitzades, no optimitzades o emprant altres condicions descrites a la literatura (com ara àcid oxàlic).

Resultats

S'han preparat pel·lícules nanoestructurades d'òxid d'estany anoditzant, en les condicions optimitzades al Capítol 3, el metall evaporat sobre oblees de Si. Aquest substrat permet dur a terme el tractament tèrmic a 700 °C, necessari per a la cristallització del SnO₂. Amb aquestes capes s'han preparat sensors per a la detecció d'H₂. La millor resposta s'obté en capes de 600 nm de gruix treballant a una temperatura de 160 °C, malgrat que la seva resposta a temperatures de 80 °C és més que notable (Fig. 7c). En general, el sensor ofereix una resposta extremadament ràpida i que depèn linealment amb la concentració de H₂ en el rang de 9 a 50 ppm. El rendiment de les pel·lícules és millor que el de les capes anòdiques preparades utilitzant altres mètodes, especialment quan el sensor opera a temperatures baixes. La sensitivitat a baixes concentracions d'H₂ i la seva ràpida resposta es poden atribuir a l'elevada àrea específica que confereix l'estructura en forma de nanocanals.

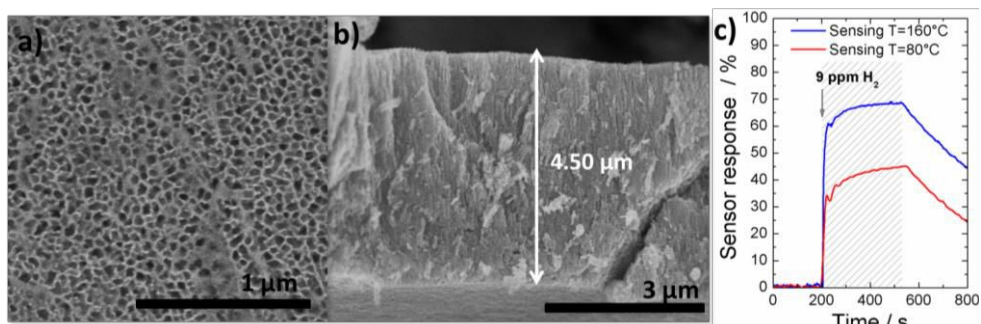


Figura 7 Imatge FESEM de a) la superfície i b) la secció transversal d'una capa d'òxid d'estany preparada per anodització autoorganitzada en una solució 0.2 M de Na₂S i 0.1 M de NH₄F dissolts en aigua i acetoni (50:50) (potencial = 10 V; temps d'anoditzat = 5 minuts). c) Resposta envers 9 ppm de H₂ d'una capa de anòdica de SnO₂ preparada en condicions optimitzades en substrats de Si/SiO₂ (gruix = 600 nm, tractament tèrmic a 700 °C). Es mostren dues temperatures de treball del sensor, 80 °C i 160 °C.

Capítol 5: Propietats fotoelectroquímiques de les capes autoorganitzades d'òxid d'estany

Objectius

- Estudiar l'efecte de la temperatura de recuit en l'estructura i composició de les pel·lícules d'òxid d'estany desenvolupades per anodització autoorganitzada.
- Determinar amb mesures de fotocorrent els canvis induïts per la temperatura del tractament tèrmic i l'atmosfera (Ar, aire, O₂) en l'eficiència de conversió dels fotons incidents en corrent elèctric (IPCE) i l'amplada de la banda prohibida (E_g).
- Aplicar les capes com a ànodes en la fotòlisi de l'aigua emprant llum solar simulada (AM 1.5, 100 mW cm⁻²)

Resultats

S'han preparat estructures d'òxid d'estany mitjançant l'anodització autoorganitzada de làmines d'estany. Per a l'anodització s'utilitza l'electròlit i les condicions optimitzades al capítol 3. Les mostres es sotmeten a un tractament tèrmic a diferents temperatures, totes elles inferiors als 400 °C. Les capes sense recuit són poc cristal·lines i es creu que poden correspondre a una fase de SnO_x amb un alt contingut de defectes de Sn²⁺ i vacants d'oxigen.

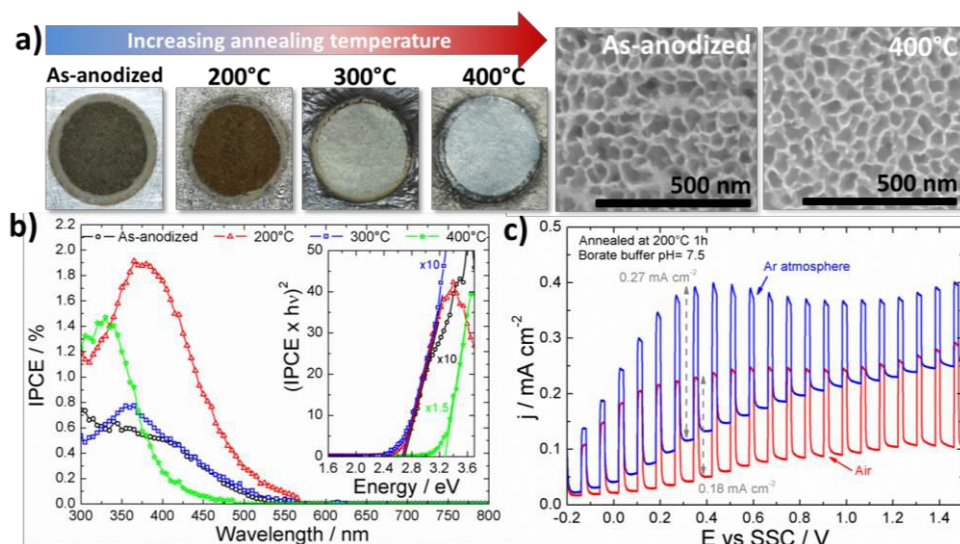


Figura 8 a) Fotografies de les capes d'òxid d'estany preparades per anodització autoorganitzada en una solució 0.2 M de Na₂S i 0.1 M de NH₄F dissolts en aigua i acetonitril (50:50) (potencial = 10 V; temps d'anoditzat = 10 minuts). A la dreta es mostren les imatges FESEM de la capa acabada d'anoditzar i tractada a 400 °C. b) Eficiència de conversió dels fotons incidents en corrent elèctric (IPCE) per a les mostres tractades a diferent temperatura i càlcul del Eg. c) Corba corrent-potencial sota il·luminació intermitent (AM 1.5, 100 mW cm⁻²) per una mostra tractada a 200 °C en Ar i aire.

En tractar-les a 200 °C, la seva cristal·linitat millora però els defectes de Sn^{2+} persisteixen, donant lloc a un augment de la resposta de fotocorrent en la regió visible de l'espectre (Fig. 8a i 8b). Aquest efecte es veu reforçat si el tractament tèrmic es realitza en atmosfera d'Ar, assolint un E_g de l'ordre de 2.4 eV. Les mostres sotmeses a temperatures de 300 °C mostren la presència de SnO provinent o bé de la desproporció de la fase SnO_x o de la cristal·lització de dominis rics en Sn^{2+} . Com s'observa en els espectres Raman, el tractament tèrmic a 400 °C disminueix el contingut de SnO, ja que s'oxida gradualment a SnO_2 , i desplaça l'absorció cap a la regió UV d'acord amb el E_g del SnO_2 estequiomètric (3.6 eV).

Aquestes estructures s'han emprat com a ànodes en la fotòlisi de l'aigua. La millor resposta en referència a la fotocorrent generada s'obté en les capes tractades a 200 °C en atmosfera d'Ar (0.27 mA cm^{-2}), d'acord amb la seva major absorció en el rang visible (Fig. 8c). Aquest valor, però, es troba lluny de l'eficiència d'altres materials com ara el TiO_2 ($\sim 1 - 1.5 \text{ mA cm}^{-2}$). A més, cal destacar que en les mesures hi ha una contribució important del corrent en condicions de foscor que suggereix que les vacants d'oxigen i els estats de Sn^{2+} segueixen reaccionant durant l'aplicació del potencial necessari per a realitzar la fotòlisi.

Capítol 6: Estructures autoorganitzades de SnO_2 com a suport de partícules Fe_2O_3 per a la fotòlisi de l'aigua.

Objectius

- Trobar les millors condicions per anoditzar pel·lícules d'estany evaporades en substrats transparents conductors com el FTO i dopar-les amb antimoni.
- Construir un elèctrode compost per una matriu de canals de $\text{Sb}:\text{SnO}_2$ amb bones propietats conductores i unes nanopartícules de Fe_2O_3 que actuïn com a absorbent de la llum visible.
- Optimitzar les condicions experimentals com ara el gruix de la capa de SnO_2 , contingut de Sb o temps de deposició de les partícules de Fe_2O_3 , per tal d'assolir una elevada eficiència en la fotòlisi de l'aigua.

Resultats

S'han preparat capes poroses d'òxid d'estany sobre substrats de FTO/vidre i s'han dopat amb antimoni per tal de millorar-ne les seves propietats conductores. Aquestes capes d'òxid transparent i conductor s'han utilitzat com a matriu suport de nanopartícules de $\alpha\text{-Fe}_2\text{O}_3$ (Fig. 8a). Gràcies a la optimització de condicions com el temps de dipòsit de les nanopartícules de $\alpha\text{-Fe}_2\text{O}_3$, el gruix de la capa de SnO_2 o la càrrega d'antimoni, s'han aconseguit fotocorrents de fins a 1.5 mA cm^{-2} a 1.6 V (respecte RHE) com mostra la Fig. 8b. Un dels paràmetres clau per obtenir aquesta bona resposta en la fotòlisi de l'aigua és la incorporació de Sb, que redueix la resistència de les estructures fins a dos ordres de magnitud, i l'elevada àrea

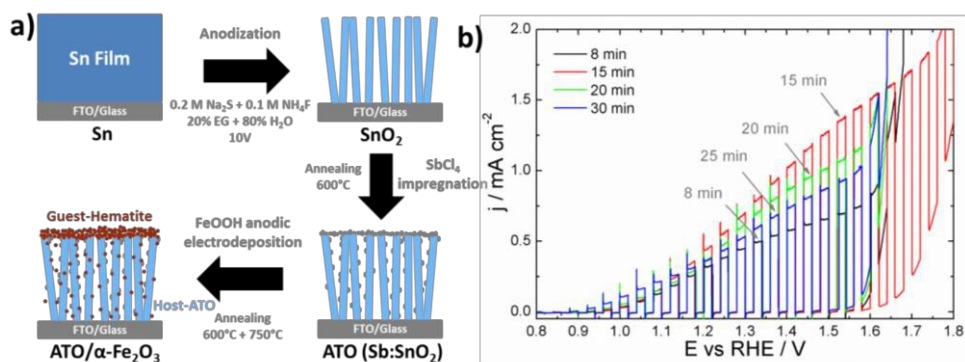


Figura 8 a) Esquema del procés de fabricació dels fotoànodes. b) Corba corrent-potencial sota il·luminació intermitent (AM 1.5, 100 mW cm⁻²) per una mostra ATO/α-Fe₂O₃ a diferents temps de deposició de FeOOH (10 μL of 0.125 M SbCl₄). La mesura es realitza en una solució 1 M de KOH a una velocitat de 0.002 V s⁻¹.

superficial dels canals que afavoreix el contacte entre les partícules absorbents i la matriu conductora.

Conclusions

A continuació es presenten les conclusions generals d'aquesta tesi:

1. S'ha revisat el comportament anòdic de l'estany en medi alcalí. S'han identificat tres processos principals: la formació d'una primera capa passiva de SnO₂.nH₂O; l'atac preferencial promogut per els ions OH i la precipitació de SnO; i la passivació final de l'electrode degut al creixement d'òxids de Sn(IV).
2. S'ha optimitzat el protocol per a la preparació de superfícies d'estany atòmicament planes i lliures d'òxid. Aquesta etapa és clau per als posteriors estudis de EC-STM.
3. S'han seguit *in situ* a nivell nanomètric les primeres etapes de l'oxidació de l'estany. Abans de l'inici del primer pic anòdic, s'observa la formació d'illes i la dissolució i redeposició del metall. Calen més experiments per determinar la composició de les illes.
4. L'anodització autoorganitzada ha demostrat ser un mètode barat, directe i molt valuós per a l'obtenció de capes nanoestructurades d'òxid d'estany. Es van obtenir capes compostes per nanocanals totalment oberts i sense ruptures en la seva secció emprant una solució basada en Na₂S i NH₄F. Aquestes estructures es van implementar en sensors de gasos i ànodes per a la fotòlisi de l'aigua.

5. Les capes nanoestructurades d'òxid d'estany són amorfes i requereixen un tractament tèrmic a temperatures superiors als 500 °C per a la seva aplicació final en dispositius. El punt de fusió de l'estany és molt baix comparat amb d'altres metalls i representa un problema evident. Això es va solucionar evaporant-lo sobre oblees de silici o substrats FTO/vidre i després anoditzant aquestes capes en lloc de les làmines.
6. Els sensors de H₂ basats en nanoestructures anòdiques de SnO₂ mostren una resposta ràpida, lineal amb l'augment de concentració de H₂ i una bona sensibilitat a concentracions de fins a 9 ppm. A més la resposta obtinguda a temperatures relativament baixes és molt bona.
7. Es poden aconseguir capes nanoestructurades de SnO₂ amb absorció en la zona de la radiació visible ajustant les condicions del tractament tèrmic. L'absorció a la zona del visible ve proporcionada per els defectes de Sn²⁺ i les vacants d'oxigen en l'estructura. Tanmateix, aquests mateixos defectes són els que després fan que la capa no sigui estable com a fotoànode.
8. Sistemes compostos per nanoestructures de SnO₂ i nanopartícules de Fe₂O₃ s'han emprat en la fotòlisi de l'aigua. El dopatge de l'estructura de SnO₂ amb antimoni es crític i essencial per obtenir una bona fotoresposta.

Acknowledgements

Agraïments

Esta tesis ha sido financiada por el Programa de Becas de Formación de Profesorado Universitario (FPU) del Ministerio de Educación Cultura y Deporte (Referencia AP2009-0941), el programa de Estancias Breves FPU (Convocatoria 2012) y los proyectos de investigación CTQ2007-68101-C02-01 y CTQ2011-25156 del Ministerio de Ciencia e Innovación.

El procés d'elaboració i escriptura d'una tesi no és mai un procés que es dugui a terme en solitari, sinó que hi ha un munt de gent que hi contribueix aportant el seu granet de sorra ja sigui petit o gran, a nivell científic o bé simplement personal. Així que totes aquestes línies que venen a continuació són per vosaltres!

En primer lloc, vull agrair als meus directors Fausto Sanz i Ismael Díez el seu suport al llarg de tot aquest temps, i no em refereixo només a aquests quatre anys de tesi sinó també als anys que vaig passar al grup com a alumne intern i masterand. Al Fausto donar-li les gràcies per les facilitats que m'ha donat, la seva confiança, les hores de discussió que m'ha dedicat i la llibertat de moviments que sempre m'ha concedit (potser a vegades massa i tot per a una estudiant una mica dispersa com jo). A l'Isma, dir que li dec gran part d'aquesta tesi. Ell va adoptar una estudiant de primer any completament desorientada que tenia un munt de voltamogrames i molt pànic a les mesures d'impedància. Gràcies per posar ordre en tot aquell garbuix de resultats que tenia i posar-me les piles en els moments de “palles mentals”. Et desitjo molta sort en el món de la recerca, que tinguis molts estudiants amb “esterilla i plàtans” (ja saps que a mi els plàtans mai m'han agradat).

I would like to express my deepest gratitude to Prof. Patrik Schmuki for his warm welcome in such a top research group, his motivation and guidance during all my stay in Erlangen. I will always admire his smartness and scientific perspective.

Je tiens tout d'abord à remercier Philippe Marcus d'avoir accepté ma visite dans son laboratoire de recherche, ainsi que pour son accueil chaleureux. Je tiens également à remercier Vincent Maurice et Lorena Klein pour toute l'aide qu'ils m'ont apportée à travers les discussions techniques ou les conseils sur le fonctionnement du microscope. Cela a été un énorme plaisir de travailler avec vous.

També vull expressar el meu reconeixement als tècnics dels CCiT-UB que d'alguna manera han contribuït a les mesures que s'han inclòs en aquesta tesi: Gerard i Jordi

(Tècniques Nanomètriques); Tariq (Espectroscòpia Molecular); Anna, Aranzazu i Eva (Microscòpia Electrònica); Lorenzo (Anàlisi de Superfícies); Pep i Xavier (Difracció de Raig X).

Als companys de grup, moltes mercès per tots els anys compartits treballant colze amb colze i els bons moments al laboratori: Nadim, Felipe (gràcies per despertar la meva curiositat científica i tots els coneixements transmesos), Lorena, Aleix, Javier (Mr. Hole!), Montse, Marta, Juan Ma, Andrés, Kay i Marina. I direu... no et deixes algú? Doncs sí i els deixo a part perquè crec que mereixen una menció especial: Albert (brother of steel) i Pepi. Vosaltres a més de companys heu estat bons amics sempre disposats a ajudar i/o escoltar en els moments difícils. A més, no puc passar per alt la introducció gradual al heavy metal que va fer l'Albert i que va ser la meva salvació a Alemanya!

I ja que em passejo per la 4a planta, això em porta als companys de departament amb qui he compartit hores de dinar, de festa, de jocs (Bang!), pràctiques, gimcanes de nadal, escalada, etc.: Javi, Estefi, Sergi (Vela), Maria, Sergi (Heavy/ Dinamita Hernández), Oriol (Güell), Fransis, Alex (Trapote), Alba, Núria, Laura, Marc (Caballero), Hector, Elena, Quim, Jordi (Gómez), Jordi (Ribas), Marçal, Bruix, Oriol (Lamiel), Noe, Almu, Sergey, Gian, Alex (Rodríguez), Meri, Anna (Amell), Marc (Belenguer) i no se si em dec estar deixant algun nom...si es així em sap moltíssim greu i prometo pagar-ho en cafès, cerveses o el que preferiu (en espècies no val, eh!). També afegir en aquest llistat gent d'altres departaments, facultats i alguns fins i tot a hores d'ara ja països com el Carlos Heras, Carme (Menchu! Oh là là!), Padi, Robert, Carlos (Fan!), Guillem, Natàlia i Xavi (moltíssimes gràcies per els ànims des de la city). A més voldria incloure en aquesta gran família a tots els professors del departament de Química Física i en especial a: Jordi Ignès, Francesc Sagués, Jaime de Andrés i Nacho Sirés amb qui vaig compartir hores de pràctiques; Juan Carlos Paniagua (Pani) perquè no conec ningú millor que m'asseguri quan escalo; Ibério per les hores de treball compartides i els savis consells; Francesc Illas (Xino) per donar un cop de mà quan se'l necessita; i finalment a la Elvira per perseguir-me sempre que no entregava la memòria de seguiment del doctorat i per ajudar-me en tantíssims tràmits. A tots moltíssimes gràcies!

De tot aquest gran llistat vull fer menció especial a l'Estefi (Jamelgaaa!!!) que sempre té una paraula d'ànim, un elogi, un consell, una cançó (encara que sigui el "potorro contento"...) quan es necessita. Guapa, guapa i guapa! Al Javi que darrere la seva màscara de "gañanisme" amaga un enorme fons i al Fran per el seu sentit del humor estrambòtic i per oferir-se a revisar alguns capítols de la tesi, quan siguem

sincers...sent teòric el que pugui dir aquesta tesi t'importa un rave i no tenies per què fer-ho. A l'Oriol per rebre sempre amb bon humor les infinites vegades que l'he molestat amb els retocs de la portada. Ah i no em puc deixar a la Meri!!! L'altre Jamelga, companya d'escalada i també de pis a Paris! Encara no sé com em vas enredar perquè llogués aquella habitació però tot i el horrible pis sempre tindrè un gran record del caos que hi regnava i de les nits de converses a la cuina (tampoc oblidaré aquell terra negra...).

Also I want to thank all the colleagues of the WW4 in Erlangen with whom I shared soooo many hours (coffee breaks, lunch time, dinners, seminars, parties, barbecues, microscope sessions...): Marco, Anca (and Alex), Alexei (and Katie), Raul (are you kidding?), Selda, Manuela, Robin, Victoria, Ferdinand, Christian, Damian, JeongEun, Sabina, Truong, Seulgui, Ning, Nabeen, Yanis (I'll come back to you later, don't worry), Simon, Bastien, Jyotsna, Chong-Yong, Hameed, Mukta, Veeda, Dagmar, Kiyong, Martin, Micael and Rob, and the technicians Helga Hildebrand, Martin Kolacyak and Ulrike Marten-Jahns. It is mandatory, though, considering their effort and contribution to this PhD thesis to especially thank Marco and Alexei, the first for his good job as mentor, his enthusiasm and super appreciated English corrections (my battle with prepositions is absolutely lost...) and the second for all the sensing measurements and his long-lasting friendship (I hope to see you back in Barcelona!). Also I cannot forget Luis from WW7 for all the jokes and crazy philosophical discussions and my friend Júlia (quina alegria haver-nos retrobat encara que hagi estat a quilòmetres de casa nostra! Gràcies per acollir-me a Nuremberg i per les genials nits de teatre!). Danke schön! Alles Gute!

Pour leurs encouragements et leur assistance aussi bien matérielle que morale je remercie tous mes collègues du Laboratoire de Physico-Chimie des Surfaces: Marion (pour ton éternelle bonne humeur et pour être toujours là pour aider), Toni, Nawel, Shadi (pour tout le temps que nous avons passé dans la salle de polissage), Zuzana (toutes ces heures dans la salle de STM!), Omaïma, Rémi (pour tes blagues), Emna, Hu (pour ton introduction à la technique STM et parce que je crois que tu vas certainement réussir dans ta thèse), Bing Bing (tu es grand!), Ha, Slava et Hao (pour toute ton aide et tous les week-ends où je t'ai dérangé pour accéder au bâtiment). Merci beaucoup à tous! Mais mon séjour à Paris n'aurait pas été le même sans Yanis (le meilleur guide touristique) et tous ses amis. Alors, merci beaucoup à Mathieu, Grégoire, Jacky, Alexandra, Loïc, Gaëlle, Louis, Hehzi, Sara, Miguel, Anaïs, Adrien, et toutes les autres personnes que j'ai probablement oublié de mentionner. Bisous à tous!

També no poden faltar en aquesta secció tota la colla d'amics de la universitat amb qui he compartit caps d'any, nits de Sant Joan (bé els dos últims he estat fora...però per al proper no m'escapo!), excursions, esquiades, manifestacions, "Corominas", etc. Una abraçada molt forta a tots per el vostre suport tot aquest temps, per proporcionar-me l'oxigen que necessito de tant en tant a la muntanya i per aguantar dignament la xarrera amb què us torturo a vegades: Albert (AP Foundation power!), Núria (des de P3! Qui ho havia de dir!), Wake, Laia, Gal·li, Àlex, Lorena, Ivan, Anna, Guerrero, Dañi, Sandra i Carlos (gràcies per els anys que has compartit amb mi d'aquesta tesi, que no van ser precisament els més senzills...i per tots els bons moments!). També vull incloure, tot i que són d'un àmbit totalment diferent, a la Saray, el Marc, la Natàlia, l'Anna Tallada, la Marta Bertran, la Yolanda, el Max i el meu amic de quatre potes Vigo.

Per acabar, vull donar les gràcies a tota la meva família perquè sempre em recolza incondicionalment en tot. M'han empès a seguir endavant quan els experiments es resistien o les forces em fallaven. Per ells no deixo de caminar! Sou els millors (i no cal que digui que us estimo amb bogeria)!



References

- [1] H. Terryn, J. Vereecken, Surface engineering of aluminium and its alloys, in: EMC' 91: Non-ferrous Metallurgy-Present and Future, Springer, Netherlands, 1991, 473–480.
- [2] G.D. Bengough, J.M. Stuart, Anodic coatings for aluminium and aluminium Alloys, UK patent 223994, 1923.
- [3] G.D. Bengough, J.M. Stuart, Process of protecting surfaces of aluminium or aluminium alloys, US patent 1771910, 1930.
- [4] H. Masuda, K. Fukuda, Ordered metal nanohole arrays made by a two-step replication of honeycomb structures of anodic alumina, *Science*, **268** (1995) 1466–1468.
- [5] V. Zwillling, E. Darque-Ceretti, A. Boutry-Forveille, D. David, M.Y. Perrin, M. Aucouturier, Structure and physicochemistry of anodic oxide films on titanium and TA6V alloy, *Surf. Interface Anal.* **27** (1999) 629–637.
- [6] P. Roy, S. Berger, P. Schmuki, TiO₂ nanotubes: synthesis and applications, *Angew. Chemie Int. Ed.* **50** (2011) 2904–2939.
- [7] R. Díaz, S. Joiret, Á. Cuesta, I. Díez-Pérez, P. Allongue, C. Gutiérrez, P. Gorostiza, F. Sanz, Electrochemically grown tin oxide thin films: in situ characterization of electronic properties and growth mechanism, *J. Phys. Chem. B* **108** (2004) 8173–8181.
- [8] I. Díez-Pérez, P. Gorostiza, F. Sanz, Direct evidence of the electronic conduction of the passive film on iron by EC-STM, *J. Electrochem. Soc.* **150** (2003) B348–B354.
- [9] I. Díez-Pérez, C. Vericat, P. Gorostiza, F. Sanz, The iron passive film breakdown in chloride media may be mediated by transient chloride-induced surface states located within the band gap, *Electrochem. Commun.* **8** (2006) 627–632.
- [10] I. Díez-Pérez, P. Gorostiza, F. Sanz, C. Müller, First stages of electrochemical growth of the passive film on iron, *J. Electrochem. Soc.* **148** (2001) B307–B313.
- [11] I. Díez-Pérez, F. Sanz, P. Gorostiza, Electronic barriers in the iron oxide film govern its passivity and redox behavior: effect of electrode potential and solution pH, *Electrochem. Commun.* **8** (2006) 1595–1602.
- [12] F. Caballero-Briones, J.M. Artés, I. Díez-Pérez, P. Gorostiza, F. Sanz, Direct observation of the valence band edge by in situ ECSTM-ECTS in p-type Cu₂O layers prepared by copper anodization, *J. Phys. Chem. C* **113** (2008) 1028–1036.
- [13] F. Caballero-Briones, A. Palacios-Adrós, O. Calzadilla, I. de P.R. Moreira, F. Sanz, Disruption of the chemical environment and electronic structure in p-type Cu₂O films by alkaline doping, *J. Phys. Chem. C* **116** (2012) 13524–13535.
- [14] F. Caballero-Briones, A. Palacios-Adrós, O. Calzadilla, F. Sanz, Evidence and analysis of parallel growth mechanisms in Cu₂O films prepared by Cu anodization, *Electrochim. Acta* **55** (2010) 4353–4358.
- [15] P. Schmuki, From Bacon to barriers: a review on the passivity of metals and alloys, *J. Solid State Electrochem.* **6** (2002) 145–164.
- [16] H.-H. Strehblow, V. Maurice, P. Marcus, Passivity of metals, in: Corrosion Mechanisms in Theory and Practice, 3rd ed., CRC Press, USA, 2012, 235–326.
- [17] J. Kruger, Passivity of metals- a materials science perspective, *Int. Mater. Rev.* **33** (1988) 113–130.

- [18] M. Pourbaix, Atlas of Electrochemical Equilibria in Aqueous Solutions, 2nd ed., Nace International, USA, 1974.
- [19] N. Sato, Anodic breakdown of passive films on metals, *J. Electrochem. Soc.* **129** (1982) 255–260.
- [20] W.J. Müller, On the passivity of metals, *Trans. Faraday Soc.* **27** (1931) 737–751.
- [21] A.J. Calandra, N.R. Tacconi, R. Pereiro, A.J. Arvia, Potentiodynamic current/potential relations for film formation under ohmic resistance control, *Electrochim. Acta* **19** (1974) 901–905.
- [22] D. Kowalski, D. Kim, P. Schmuki, TiO₂ nanotubes, nanochannels and mesosponge: self-organized formation and applications, *Nano Today* **8** (2013) 235–264.
- [23] W. Lee, S.-J. Park, Porous anodic aluminum oxide: anodization and templated synthesis of functional nanostructures, *Chem. Rev.* **114** (2014) 7487–7556.
- [24] A. Ghicov, P. Schmuki, Self-ordering electrochemistry: a review on growth and functionality of TiO₂ nanotubes and other self-aligned MO_x structures, *Chem. Commun.* (2009) 2791–2808.
- [25] J.M. Macak, H. Tsuchiya, A. Ghicov, K. Yasuda, R. Hahn, S. Bauer, P. Schmuki, TiO₂ nanotubes: self-organized electrochemical formation, properties and applications, *Curr. Opin. Solid State Mater. Sci.* **11** (2007) 3–18.
- [26] E.J.W. Verwey, Electrolytic conduction of a solid insulator at high fields: the formation of the anodic oxide film on aluminium, *Physica* **2** (1935) 1059–1063.
- [27] N. Cabrera, N.F. Mott, Theory of the oxidation of metals, *Reports Prog. Phys.* **12** (1949) 163.
- [28] F.P. Fehlner, N.F. Mott, Low-temperature oxidation, *Oxid. Met.* **2** (1970) 59–99.
- [29] A. Seyeux, V. Maurice, P. Marcus, Oxide film growth kinetics on metals and alloys: I. Physical model, *J. Electrochem. Soc.* **160** (2013) C189–C196.
- [30] B.M. Marx, Exploring the mechanisms of passivity on iron: experimental methods for characterizing and developing models to describe nano-oxide growth, PhD Thesis, The Pennsylvania State University, 2006.
- [31] C.Y. Chao, L.F. Lin, D.D. Macdonald, A Point Defect Model for anodic passive films: I. Film growth kinetics, *J. Electrochem. Soc.* **128** (1981) 1187–1194.
- [32] D.D. Macdonald, The Point Defect Model for the passive state, *J. Electrochem. Soc.* **139** (1992) 3434–3449.
- [33] S.M. Wilhelm, N. Hackerman, Photoelectrochemical characterization of the passive films on iron and nickel, *J. Electrochem. Soc.* **128** (1981) 1668–1674.
- [34] Z. Szklarska-Smialowska, W. Kozłowski, Electrochemical and ellipsometric investigations of passive films on iron in borate solutions: II. Cathodic reduction of passive films on Iron, *J. Electrochem. Soc.* **131** (1984) 499–505.
- [35] J.C. Rubim, J. Dünwald, Enhanced Raman scattering from passive films on silver-coated iron electrodes, *J. Electroanal. Chem. Interfacial Electrochem.* **258** (1989) 327–344.

- [36] L.J. Oblonsky, S. Virtanen, V. Schroeder, T.M. Devine, Surface Enhanced Raman Spectroscopy of iron oxide thin films: comparison with the passive film on iron, *J. Electrochem. Soc.* **144** (1997) 1604–1609.
- [37] B.X. Huang, P. Tornatore, Y.-S. Li, IR and Raman spectroelectrochemical studies of corrosion films on tin, *Electrochim. Acta* **46** (2001) 671–679.
- [38] J.C. Rubim, In situ Raman and reflectance spectra of iron electrodes in borate buffer solution containing 2,2-Bipyridine, *J. Electrochem. Soc.* **140** (1993) 1601–1606.
- [39] V. Schroeder, T.M. Devine, Surface Enhanced Raman Spectroscopy study of the galvanostatic reduction of the passive film on Iron, *J. Electrochem. Soc.* **146** (1999) 4061–4070.
- [40] H.Y.H. Chan, C.G. Takoudis, M.J. Weaver, Oxide film formation and oxygen adsorption on copper in aqueous media as probed by Surface-Enhanced Raman Spectroscopy, *J. Phys. Chem. B* **103** (1998) 357–365.
- [41] C.A. Melendres, G.A. Bowmaker, J.M. Leger, B. Beden, In-situ synchrotron far infrared spectroscopy of surface films on a copper electrode in aqueous solutions, *J. Electroanal. Chem.* **449** (1998) 215–218.
- [42] L.J. Oblonsky, A.J. Davenport, M.P. Ryan, H.S. Isaacs, R.C. Newman, In Situ X-Ray Absorption Near Edge Structure study of the potential dependence of the formation of the passive film on Iron in borate buffer, *J. Electrochem. Soc.* **144** (1997) 2398–2404.
- [43] A.J. Davenport, L.J. Oblonsky, M.P. Ryan, M.F. Toney, The structure of the passive film that forms on iron in aqueous environments, *J. Electrochem. Soc.* **147** (2000) 2162–2173.
- [44] M.F. Toney, A.J. Davenport, L.J. Oblonsky, M.P. Ryan, C.M. Vitus, Atomic structure of the passive oxide film formed on iron, *Phys. Rev. Lett.* **79** (1997) 4282–4285.
- [45] O.M. Magnussen, J. Scherer, B.M. Ocko, R.J. Behm, In situ X-ray scattering study of the passive film on Ni (111) in sulfuric acid solution, *J. Phys. Chem. B* **104** (2000) 1222–1226.
- [46] R. Lindsay, F. Sanz, I. Díez-Pérez, A. Garcia-Güell, J.F.W. Mosselmans, J. Zegenhagen, Chemical and structural characterization of tin oxide films: an in situ XAS study, European Synchrotron Facility, Report SI-1010, 2005.
- [47] N. Sato, *Electrochemistry at Metal and Semiconductor Electrodes*, Elsevier, Netherlands, 1998.
- [48] S.R. Morrison, *Electrochemistry at Semiconductor and Oxidized Metal Electrodes*, Plenum Press, USA, 1980.
- [49] K. Gelderman, L. Lee, S.W. Donne, Flat-band potential of a semiconductor: using the Mott-Schottky equation, *J. Chem. Educ.* **84** (2007) 685–688.
- [50] R. Lindström, V. Maurice, L.H. Klein, P. Marcus, *The use of electrochemical scanning tunneling microscopy (EC-STM) in corrosion analysis: reference material and procedural guidelines*, CRC Press, USA, 2007.
- [51] J. Kunze, V. Maurice, L.H. Klein, H.-H. Strehlow, P. Marcus, In situ STM study of the effect of chlorides on the initial stages of anodic oxidation of Cu (111) in alkaline solutions, *Electrochim. Acta* **48** (2003) 1157–1167.

- [52] A. Seyeux, V. Maurice, L.H. Klein, P. Marcus, In situ STM study of the effect of chloride on passive film on Nickel in alkaline solution, *J. Electrochem. Soc.* **153** (2006) B453–B463.
- [53] V. Maurice, P. Marcus, Passive films at the nanoscale, *Electrochim. Acta* **84** (2012) 129–138.
- [54] G. Binnig, H. Rohrer, C. Gerber, E. Weibel, (111) facets as the origin of reconstructed Au (110) surfaces, *Surf. Sci. Lett.* **131** (1983) L379–L384.
- [55] A.K. Yagati, J. Min, J.-W. Choi, Electrochemical Scanning Tunneling Microscopy (ECSTM) – From Theory to Future Applications, in: *Modern Electrochemical Methods in Nano, Surface and Corrosion Science*, InTechOpen, 2014.
- [56] H.-H. Strehblow, V. Maurice, P. Marcus, Initial and later stages of anodic oxide formation on Cu, chemical aspects, structure and electronic properties, *Electrochim. Acta* **46** (2001) 3755–3766.
- [57] V. Maurice, H.-H. Strehblow, P. Marcus, In situ STM study of the initial stages of oxidation of Cu (111) in aqueous solution, *Surf. Sci.* **458** (2000) 185–194.
- [58] J. Kunze, V. Maurice, L.H. Klein, H.-H. Strehblow, P. Marcus, In situ STM study of the anodic oxidation of Cu (001) in 0.1 M NaOH, *J. Electroanal. Chem.* **554-555** (2003) 113–125.
- [59] V. Maurice, H.-H. Strehblow, P. Marcus, In situ scanning tunneling microscope study of the passivation of Cu (111), *J. Electrochem. Soc.* **146** (1999) 524–530.
- [60] J. Kunze, V. Maurice, L.H. Klein, H.-H. Strehblow, P. Marcus, In situ STM study of the duplex passive films formed on Cu (111) and Cu (001) in 0.1 M NaOH, *Corros. Sci.* **46** (2004) 245–264.
- [61] A. Seyeux, V. Maurice, L.H. Klein, P. Marcus, Initiation of localized corrosion at the nanoscale by competitive dissolution and passivation of nickel surfaces, *Electrochim. Acta* **54** (2008) 540–544.
- [62] A. Seyeux, V. Maurice, L.H. Klein, P. Marcus, In situ scanning tunnelling microscopic study of the initial stages of growth and the structure of the passive film on Ni (111) in 1 mM NaOH (aq), *J. Solid State Electrochem.* **9** (2005) 337–346.
- [63] J. Kunze, H.-H. Strehblow, G. Staikov, In situ STM study of the initial stages of electrochemical oxide formation at the Ag (111) / 0.1 M NaOH(aq) interface, *Electrochem. Commun.* **6** (2004) 132–137.
- [64] V. Maurice, L.H. Klein, H.-H. Strehblow, P. Marcus, In Situ STM study of the surface structure, dissolution, and early stages of electrochemical oxidation of the Ag (111) electrode, *J. Phys. Chem. C* **111** (2007) 16351–16361.
- [65] B.N. Stirrup, N.A. Hampson, Anodic passivation of tin in sodium hydroxide solutions, *J. Electroanal. Chem. Interfacial Electrochem.* **67** (1976) 45–56.
- [66] P.E. Alvarez, S.B. Ribotta, M.E. Folquer, C.A. Gervasi, J.R. Vilche, Potentiodynamic behaviour of tin in different buffer solutions, *Corros. Sci.* **44** (2002) 49–65.
- [67] V.S. Muralidharan, K. Thangavel, K.S. Rajagopalan, The triangular potential sweep voltammetric studies on pure tin in concentrated sodium hydroxide solutions, *Electrochim. Acta* **28** (1983) 1611–1618.

- [68] S.D. Kapusta, N. Hackerman, Anodic passivation of tin in slightly alkaline solutions, *Electrochim. Acta* **25** (1980) 1625–1639.
- [69] S.H. Bonilla, B.F. Giannetti, Early stages of film formation and surface growth on tin electrodes at bicarbonate medium: a modelistic approach, *Eitschrift Für Phys. Chemie/International J. Res. Phys. Chem. Chem. Phys.* **218** (2004) 837–856.
- [70] V. Brunetti, M. López Teijelo, Oxide / hydroxide films on tin. Part I: Kinetic aspects of the electroformation and electroreduction of the films, *J. Electroanal. Chem.* **613** (2008) 9–15.
- [71] M. Šeruga, M. Metikoš-Huković, T. Valla, M. Milun, H. Hoffschultz, K. Wandelt, Electrochemical and X-ray photoelectron spectroscopy studies of passive film on tin in citrate buffer solution, *J. Electroanal. Chem.* **407** (1996) 83–89.
- [72] V. Brunetti, M. López Teijelo, Oxide/hydroxide films on tin. II: Characterization of the anodic growth in alkaline solutions, *J. Electroanal. Chem.* **613** (2008) 16–22.
- [73] M. Metikoš-Huković, A. Rešeti'c, V. Gvozdić, Behaviour of tin as a valve metal, *Electrochim. Acta* **40** (1995) 1777–1779.
- [74] R.O. Ansell, T. Dickinson, A.F. Povey, P.M.A. Sherwood, X-ray photoelectron spectroscopic studies of Tin electrodes after polarization in sodium hydroxide solution, *J. Electrochem. Soc.* **124** (1977) 1360–1364.
- [75] A. Vértes, H. Leidheiser, M.L. Varsányi, G.W. Simmons, L. Kiss, Mössbauer studies of the passive film formed on tin in borate buffer, *J. Electrochem. Soc.* **125** (1978) 1946–1950.
- [76] C.A. Gervasi, P.A. Palacios, M.V. Fiori Bimbi, P.E. Alvarez, Electrochemical studies on the anodic behavior of tin in citrate buffer solutions, *J. Electroanal. Chem.* **639** (2010) 141–146.
- [77] C.A. Gervasi, P.E. Alvarez, M.V. Fiori Bimbi, M.E. Folquer, Comparative cyclic voltammetry and SEM analysis of tin electrodes in citrate buffer solutions, *J. Electroanal. Chem.* **601** (2007) 194–204.
- [78] M. Wang, Y. Liu, D. Zhang, H. Yang, Anodization process of Sn in oxalic acid at low applied voltages, *Electrochim. Acta* **59** (2012) 441–448.
- [79] V.I. Birss, M.T. Shevalier, The lead anode in alkaline solutions: I. The initial oxidation processes, *J. Electrochem. Soc.* **134** (1987) 802–808.
- [80] V.I. Birss, M.T. Shevalier, The lead anode in alkaline solutions: III. Growth of thick films, *J. Electrochem. Soc.* **137** (1990) 2643–2647.
- [81] E.R. Crandall, Factors governing tin whisker growth, PhD Thesis, Auburn University, 2012.
- [82] H.H. Hassan, S.S. Abd El Rehim, N.F. Mohamed, Role of ClO_4^- in breakdown of tin passivity in NaOH solutions, *Corros. Sci.* **44** (2002) 37–47.
- [83] M. Jafarian, F. Gopal, I. Danaee, R. Biabani, M.G. Mahjani, Electrochemical studies of the pitting corrosion of tin in citric acid solution containing Cl^- , *Electrochim. Acta* **53** (2008) 4528–4536.
- [84] S.A.M. Refaey, The corrosion and passivation of tin in borate solutions and the effect of halide ions, *Electrochim. Acta* **41** (1996) 2545–2549.

- [85] Y. Yang, J. Liu, C. Li, L. Fu, W. Huang, Z. Li, Fabrication of pompon-like and flower-like SnO microspheres comprised of layered nanoflakes by anodic electrocrystallization, *Electrochim. Acta* **72** (2012) 94–100.
- [86] M. Metikoš-Huković, S. Omanović, A. Jukić, Impedance spectroscopy of semiconducting films on tin electrodes, *Electrochim. Acta* **45** (1999) 977–986.
- [87] T. Dickinson, S. Lotfi, The anodic dissolution of tin in sodium hydroxide solutions, *Electrochim. Acta* **23** (1978) 513–519.
- [88] S. Nakayama, T. Sugihara, J. Matsumoto, T. Notoya, T. Osakai, Chemical state analysis of tin oxide films by voltammetric reduction, *J. Electrochem. Soc.* **158** (2011) C341–C345.
- [89] W.-W. du Mont, B. Neudert, A new variant of the amphoterism of tin(II) hydroxide: Sn(OH)₂ as stannio complex ligand, *Angew. Chemie Int. Ed.* **19** (1980) 553–554.
- [90] N. Wiberg, Inorganic Chemistry, Academic Press, USA, 2001.
- [91] Y.Q. Guo, R.Q. Tan, X. Li, J.H. Zhao, Z.L. Luo, C. Gao, W.J. Song, Shape-controlled growth and single-crystal XRD study of submillimeter-sized single crystals of SnO, *CrystEngComm*. **13** (2011) 5677–5680.
- [92] X. Wang, F.X. Zhang, I. Loa, K. Syassen, M. Hanfland, Y.-L. Mathis, Structural properties, infrared reflectivity, and Raman modes of SnO at high pressure, *Phys. Status Solidi* **241** (2004) 3168–3178.
- [93] A. Hedoux, D. Le Bellac, Y. Guinet, J.M. Kiat, I. Noiret, P. Garnier, Raman spectroscopy and X-ray diffraction studies on PbO and (PbO)_{1-x}(TiO₂)_x, *J. Phys. Condens. Matter* **7** (1995) 8547.
- [94] I. Abrahams, S.M. Grimes, S.R. Johnston, J.C. Knowles, Tin(II) oxyhydroxide by X-ray powder diffraction, *Acta Crystallogr. Sect. C.* **52** (1996) 286–288.
- [95] M. Büchler, P. Schmuki, H. Böhni, Iron passivity in borate buffer: formation of a deposit layer and its influence on the semiconducting properties, *J. Electrochem. Soc.* **145** (1998) 609–614.
- [96] E. Sikora, D.D. Macdonald, Nature of the passive film on nickel, *Electrochim. Acta* **48** (2002) 69–77.
- [97] J. Pan, D. Thierry, C. Leygraf, Electrochemical impedance spectroscopy study of the passive oxide film on titanium for implant application, *Electrochim. Acta* **41** (1996) 1143–1153.
- [98] J. Baszkiewicz, D. Krupa, J. Mizera, J.W. Sobczak, A. Biliński, Corrosion resistance of the surface layers formed on titanium by plasma electrolytic oxidation and hydrothermal treatment, *Vacuum* **78** (2005) 143–147.
- [99] C.R. Magaña-Zavala, M.E. Angeles-San Martín, F.J. Rodríguez-Gómez, D.R. Acosta, R. Ávila-Godoy, B. Hidalgo-Prada, Electrochemical impedance spectroscopy (EIS) modelling of different behaviours of Ni and Ni oxide thin films for corrosion prevention in sour media, *Anti-Corrosion Methods Mater.* **57** (2010) 118–125.
- [100] S.L. de Assis, I. Costa, The effect of polarization on the electrochemical behavior of Ti-13Nb-13Zr alloy, *Mater. Res.* **10** (2007) 293–296.
- [101] M. Metikoš-Huković, S. Omanović, Kinetics of anodic oxide-film growth on tin: ionic transport across a barrier in the high-field limit, *Mater. Chem. Phys.* **38** (1994) 55–62.

- [102] J. Liu, D.D. Macdonald, The passivity of iron in the presence of ethylenediaminetetraacetic acid. II. The defect and electronic structures of the barrier layer, *J. Electrochem. Soc.* **148** (2001) B425–B430.
- [103] T. Hirokawa, K. Yomogita, K. Honda, Observations of dislocation motion by etch hillocks in white Tin single crystals, *Jpn. J. Appl. Phys.* **9** (1970) 1210.
- [104] J.A. Dean, Lange's Handbook of Chemistry, MacGraw-Hill, USA, 1999.
- [105] F.A. Cotton, G. Wilkinson, Advanced Inorganic Chemistry: a comprehensive text, John Wiley & Sons, USA, 1980.
- [106] H.H. Hassan, M.A.M. Ibrahim, S.S. Abd El Rehim, M.A. Amin, Comparative study of the electrochemical behaviour of silver electrode in chloride, bromide and iodide aqueous solutions, *Int. J. Electrochem. Sci.* **5** (2010) 278–294.
- [107] V. Lehmann, The physics of macropore formation in low doped n-type silicon, *J. Electrochem. Soc.* **140** (1993) 2836–2843.
- [108] M.A. Shaker, H.H. Abdel-Rahman, Corrosion of copper metal in presence of binary mixtures, *Am. J. Appl. Sci.* **4** (2007) 554–564.
- [109] M. Lundström, Chalcopyrite dissolution in cupric chloride solutions, PhD Thesis, Helsinki University of Technology, 2009.
- [110] C.P. Thurgood, D.W. Kirk, F.R. Foulkes, W.F. Graydon, Activation energies of anodic gold reactions in aqueous alkaline cyanide, *J. Electrochem. Soc.* **128** (1981) 1680–1685.
- [111] A.S. Tselesh, Anodic behaviour of tin in citrate solutions: The IR and XPS study on the composition of the passive layer, *Thin Solid Films* **516** (2008) 6253–6260.
- [112] I. Horcas, R. Fernández, J.M. Gómez-Rodríguez, J. Colchero, J. Gómez-Herrero, A.M. Baro, WSXM: A software for scanning probe microscopy and a tool for nanotechnology, *Rev. Sci. Instrum.* **78** (2007) 013705.
- [113] H. Uchiyama, H. Imai, Matrix-mediated formation of hierarchically structured SnO crystals as intermediates between single crystals and polycrystalline aggregates, *Langmuir* **24** (2008) 9038–9042.
- [114] K. Honda, Step structure of dislocation boundaries in white tin single crystals. Part I. Observations, *Jpn. J. Appl. Phys.* **27** (1988) 1599–1603.
- [115] T. Hirokawa, K. Ojima, The dislocation movement in the pre-yield region in white tin single crystals by using the etch hillock technique, *Jpn. J. Appl. Phys.* **18** (1979) 729–734.
- [116] K. Honda, T. Hirokawa, Dislocation etch hillock formation in white tin single crystals, *Jpn. J. Appl. Phys.* **11** (1972) 1763–1774.
- [117] X. Gao, A. Hamelin, M.J. Weaver, Potential-dependent reconstruction at ordered Au (100)-aqueous interfaces as probed by atomic-resolution scanning tunneling microscopy, *Phys. Rev. Lett.* **67** (1991) 618–621.
- [118] H. Matsushima, C. Haak, A. Taranovskyy, Y. Grunder, O.M. Magnussen, In situ video STM studies of the hydrogen-induced reconstruction of Cu (100): potential and pH dependence, *Phys. Chem. Chem. Phys.* **12** (2010) 13992–13998.

- [119] H. Matsushima, A. Taranovskyy, C. Haak, Y. Gründer, O.M. Magnussen, Reconstruction of Cu (100) electrode surfaces during hydrogen evolution, *J. Am. Chem. Soc.* **131** (2009) 10362–10363.
- [120] S. Iijima, Helical microtubules of graphitic carbon, *Nature* **354** (1991) 56–58.
- [121] F. Krumeich, H.-J. Muhr, M. Niederberger, F. Bieri, B. Schnyder, R. Nesper, Morphology and topochemical reactions of novel vanadium oxide nanotubes, *J. Am. Chem. Soc.* **121** (1999) 8324–8331.
- [122] T. Kasuga, M. Hiramatsu, A. Hoson, T. Sekino, K. Niihara, Formation of titanium oxide nanotube, *Langmuir* **14** (1998) 3160–3163.
- [123] G.D. Sulka, Highly ordered anodic porous alumina formation by self-organized anodizing, in: *Nanostructured Materials in Electrochemistry*, Wiley-VCH, 2008, pp. 1–116.
- [124] H. Masuda, M. Ohya, H. Asoh, M. Nakao, M. Nohtomi, T. Tamamura, Photonic crystal using anodic porous alumina, *Jpn. J. Appl. Phys.* **38** (1999) L1403.
- [125] C.R. Martin, Nanomaterials: A membrane-based synthetic approach, *Science* **266** (1994) 1961–1966.
- [126] Y. Sui, B. Cui, R. Guardián, D. Acosta, L. Martínez, R. Perez, Growth of carbon nanotubes and nanofibres in porous anodic alumina film, *Carbon* **40** (2002) 1011–1016.
- [127] L. Li, S. Pan, X. Dou, Y. Zhu, X. Huang, Y. Yang, G. Li, L. Zhang, Direct electrodeposition of ZnO nanotube arrays in anodic alumina membranes, *J. Phys. Chem. C* **111** (2007) 7288–7291.
- [128] S. Berger, F. Jakubka, P. Schmuki, Self-ordered hexagonal nanoporous hafnium oxide and transition to aligned HfO₂ nanotube layers, *Electrochem. Solid-State Lett.* **12** (2009) K45–K48.
- [129] H. Tsuchiya, P. Schmuki, Self-organized high aspect ratio porous hafnium oxide prepared by electrochemical anodization, *Electrochem. Commun.* **7** (2005) 49–52.
- [130] W. Wei, J.M. Macak, N.K. Shrestha, P. Schmuki, Thick self-ordered nanoporous Ta₂O₅ films with long-range lateral order, *J. Electrochem. Soc.* **156** (2009) K104–K109.
- [131] W. Wei, J.M. Macak, P. Schmuki, High aspect ratio ordered nanoporous Ta₂O₅ films by anodization of Ta, *Electrochem. Commun.* **10** (2008) 428–432.
- [132] I. Sieber, B. Kannan, P. Schmuki, Self-assembled porous tantalum oxide prepared in H₂SO₄/HF electrolytes, *Electrochem. Solid-State Lett.* **8** (2005) J10–J12.
- [133] K. Lee, P. Schmuki, Highly ordered nanoporous Ta₂O₅ formed by anodization of Ta at high temperatures in a glycerol/phosphate electrolyte, *Electrochem. Commun.* **13** (2011) 542–545.
- [134] W. Wei, R. Kirchgeorg, K. Lee, S. So, P. Schmuki, Nitrates: a new class of electrolytes for the rapid anodic growth of self-ordered oxide nanopore layers on Ti and Ta, *Phys. Status Solidi Rapid Res. Lett.* **5** (2011) 394–396.
- [135] H. Tsuchiya, J.M. Macak, I. Sieber, L. Taveira, A. Ghicov, K. Sirotna, P. Schmuk, Self-organized porous WO₃ formed in NaF electrolytes, *Electrochem. Commun.* **7** (2005) 295–298.
- [136] W. Wei, S. Shaw, K. Lee, P. Schmuki, Rapid anodic formation of high aspect ratio WO₃ layers with self-ordered nanochannel geometry and use in photocatalysis, *Chem. Eur. J.* **18** (2012) 14622–14626.

- [137] I. Sieber, H. Hildebrand, A. Friedrich, P. Schmuki, Formation of self-organized niobium porous oxide on niobium, *Electrochem. Commun.* **7** (2005) 97–100.
- [138] R. Kirchgeorg, W. Wei, K. Lee, S. So, P. Schmuki, Through-hole, self-ordered nanoporous oxide layers on titanium, niobium and titanium-niobium alloys in aqueous and organic nitrate electrolytes, *ChemistryOpen*. **1** (2012) 21–25.
- [139] S. Berger, J. Faltenbacher, S. Bauer, P. Schmuki, Enhanced self-ordering of anodic ZrO₂ nanotubes in inorganic and organic electrolytes using two-step anodization, *Phys. Status Solidi Rapid Res. Lett.* **2** (2008) 102–104.
- [140] Y. Yang, S.P. Albu, D. Kim, P. Schmuki, Enabling the anodic growth of highly ordered V₂O₅ nanoporous/nanotubular structures, *Angew. Chemie Int. Ed.* **50** (2011) 9071–9075.
- [141] A. Ghicov, S. Aldabergenova, H. Tsuchiya, P. Schmuki, TiO₂-Nb₂O₅ nanotubes with electrochemically tunable morphologies, *Angew. Chemie Int. Ed.* **45** (2006) 6993–6996.
- [142] M. Yang, H. Jha, N. Liu, P. Schmuki, Increased photocurrent response in Nb-doped TiO₂ nanotubes, *J. Mater. Chem.* **21** (2011) 15205–15208.
- [143] A. Ghicov, M. Yamamoto, P. Schmuki, Lattice widening in niobium-doped TiO₂ nanotubes: efficient ion intercalation and swift electrochromic contrast, *Angew. Chemie Int. Ed.* **47** (2008) 7934–7937.
- [144] K. Yasuda, P. Schmuki, Formation of self-organized zirconium titanate nanotube layers by alloy anodization, *Adv. Mater.* **19** (2007) 1757–1760.
- [145] K. Yasuda, P. Schmuki, Electrochemical formation of self-organized zirconium titanate nanotube multilayers, *Electrochem. Commun.* **9** (2007) 615–619.
- [146] H. Tsuchiya, S. Berger, J.M. Macak, A. Ghicov, P. Schmuki, Self-organized porous and tubular oxide layers on TiAl alloys, *Electrochem. Commun.* **9** (2007) 2397–2402.
- [147] S. Berger, H. Tsuchiya, P. Schmuki, Transition from nanopores to nanotubes: self-ordered anodic oxide structures on titanium–aluminides, *Chem. Mater.* **20** (2008) 3245–3247.
- [148] W. Wei, S. Berger, N. Shrestha, P. Schmuki, Ideal hexagonal order: formation of self-organized anodic oxide nanotubes and nanopores on a Ti–35Ta alloy, *J. Electrochem. Soc.* **157** (2010) C409–C413.
- [149] H. Masuda, Y. Kouichi, A. Osaka, Self-ordering of cell configuration of anodic porous alumina with large-size pores in phosphoric acid solution, *Jpn. J. Appl. Phys.* **37** (1998) L1340–L1342.
- [150] J.M. Macak, S.P. Albu, P. Schmuki, Towards ideal hexagonal self-ordering of TiO₂ nanotubes, *Phys. Status Solidi Rapid Res. Lett.* **1** (2007) 181–183.
- [151] O.E. Linarez Pérez, V.C. Fuertes, M.A. Pérez, M. López Teijelo, Characterization of the anodic growth and dissolution of oxide films on valve metals, *Electrochem. Commun.* **10** (2008) 433–437.
- [152] J.P. O’Sullivan, G.C. Wood, The morphology and mechanism of formation of porous anodic films on aluminium, *Proc. R. Soc. London. A. Math. Phys. Sci.* **317** (1970) 511–543.

- [153] K. Yasuda, J.M. Macak, S. Berger, A. Ghicov, P. Schmuki, Mechanistic aspects of the self-organization process for oxide nanotube formation on valve metals, *J. Electrochem. Soc.* **154** (2007) C472–C478.
- [154] G. Thompson, Porous anodic alumina: fabrication, characterization and applications, *Thin Solid Films* **297** (1997) 192–201.
- [155] K. Shimizu, K. Kobayashi, G.E. Thompson, G.C. Wood, Development of porous anodic films on aluminium, *Philos. Mag. A.* **66** (1992) 643–652.
- [156] W. Lee, R. Scholz, U. Gösele, A continuous process for structurally well-defined Al₂O₃ nanotubes based on pulse anodization of aluminum, *Nano Lett.* **8** (2008) 2155–2160.
- [157] J.S.L. Leach, P. Neufeld, Pore structure in anodic Al₂O₃ films, *Corros. Sci.* **9** (1969) 413–416.
- [158] P. Chowdhury, A.N. Thomas, M. Sharma, H.C. Barshilia, An approach for in situ measurement of anode temperature during the growth of self-ordered nanoporous anodic alumina thin films: Influence of Joule heating on pore microstructure, *Electrochim. Acta* **115** (2014) 657–664.
- [159] S. Berger, J. Kunze, P. Schmuki, D. LeClere, A.T. Valota, P. Skeldon, G.E. Thompson, A lithographic approach to determine volume expansion factors during anodization: Using the example of initiation and growth of TiO₂-nanotubes, *Electrochim. Acta* **54** (2009) 5942–5948.
- [160] N.B. Pilling, R.E. Bedworth, The oxidation of metals at high temperatures, *J. Inst. Met.* **29** (1923) 529–591.
- [161] S.J. Garcia-Vergara, P. Skeldon, G.E. Thompson, H. Habazaki, A flow model of porous anodic film growth on aluminium, *Electrochim. Acta* **52** (2006) 681–687.
- [162] J.E. Houser, K.R. Hebert, The role of viscous flow of oxide in the growth of self-ordered porous anodic alumina films, *Nat. Mater.* **8** (2009) 415–420.
- [163] P. Skeldon, G.E. Thompson, S.J. Garcia-Vergara, L. Iglesias-Rubianes, C.E. Blanco-Pinzon, A tracer study of porous anodic alumina, *Electrochem. Solid-State Lett.* **9** (2006) B47–B51.
- [164] K.R. Hebert, J.E. Houser, A model for coupled electrical migration and stress-driven transport in anodic oxide films, *J. Electrochem. Soc.* **156** (2009) C275–C281.
- [165] S.P. Albu, D. Kim, P. Schmuki, Growth of aligned TiO₂ bamboo-type nanotubes and highly ordered nanolace, *Angew. Chemie Int. Ed.* **47** (2008) 1916–1919.
- [166] S.P. Albu, A. Ghicov, S. Aldabergenova, P. Drechsel, D. LeClere, G.E. Thompson, J.M. Macak, P. Schmuki, Formation of double-walled TiO₂ nanotubes and robust anatase membranes, *Adv. Mater.* **20** (2008) 4135–4139.
- [167] Z.L. Xiao, C.Y. Han, U. Welp, H.H. Wang, W.K. Kwok, G.A. Willing, J.M. Hiller, R.E. Cook, D.J. Miller, G.W. Carbtrees, Fabrication of alumina nanotubes and nanowires by etching porous alumina membranes, *Nano Lett.* **2** (2002) 1293–1297.
- [168] Y.F. Mei, X.L. Wu, X.F. Shao, G.S. Huang, G.G. Siu, Formation mechanism of alumina nanotube array, *Phys. Lett. A.* **309** (2003) 109–113.
- [169] K. Yasuda, P. Schmuki, Control of morphology and composition of self-organized zirconium titanate nanotubes formed in (NH₄)₂SO₄/NH₄F electrolytes, *Electrochim. Acta* **52** (2007) 4053–4061.

- [170] J.M. Macak, H. Hildebrand, U. Marten-Jahns, P. Schmuki, Mechanistic aspects and growth of large diameter self-organized TiO₂ nanotubes, *J. Electroanal. Chem.* **621** (2008) 254–266.
- [171] S. Bauer, S. Kleber, P. Schmuki, TiO₂ nanotubes: tailoring the geometry in H₃PO₄/HF electrolytes, *Electrochem. Commun.* **8** (2006) 1321–1325.
- [172] J.M. Macak, H. Tsuchiya, L. Taveira, S. Aldabergerova, P. Schmuki, Smooth anodic TiO₂ nanotubes, *Angew. Chemie Int. Ed.* **44** (2005) 7463–7465.
- [173] Y.-Y. Song, P. Schmuki, Modulated TiO₂ nanotube stacks and their use in interference sensors, *Electrochem. Commun.* **12** (2010) 579–582.
- [174] Y.-Y. Song, F. Schmidt-Stein, S. Bauer, P. Schmuki, Amphiphilic TiO₂ nanotube arrays: an actively controllable drug delivery system, *J. Am. Chem. Soc.* **131** (2009) 4230–4232.
- [175] J.-H. Jeun, S.-H. Hong, CuO-loaded nano-porous SnO₂ films fabricated by anodic oxidation and RIE process and their gas sensing properties, *Sensors Actuat. B-Chem.* **151** (2010) 1–7.
- [176] J.-H. Jeun, H.-S. Ryu, S.-H. Hong, Nanoporous SnO₂ film gas sensor formed by anodic oxidation, *J. Electrochem. Soc.* **156** (2009) J263–J266.
- [177] B. Wang, L.F. Zhu, Y.H. Yang, N.S. Xu, G.W. Yang, Fabrication of a SnO₂ nanowire gas sensor and sensor performance for hydrogen, *J. Phys. Chem. C* **112** (2008) 6643–6647.
- [178] E. Comini, G. Faglia, G. Sberveglieri, Z. Pan, Z.L. Wang, Stable and highly sensitive gas sensors based on semiconducting oxide nanobelts, *Appl. Phys. Lett.* **81** (2002) 1869–1871.
- [179] Y. Wang, X. Jiang, Y. Xia, A solution-phase, precursor route to polycrystalline SnO₂ nanowires that can be used for gas sensing under ambient conditions, *J. Am. Chem. Soc.* **125** (2003) 16176–16177.
- [180] S. Shao, X. Qiu, D. He, R. Koehn, N. Guan, X. Lu, N. Bao, C.A. Grimes, Low temperature crystallization of transparent highly ordered nanoporous SnO₂ thin films: application to room-temperature hydrogen sensing, *Nanoscale* **3** (2011) 4283–4289.
- [181] Y. Liu, E. Koep, M. Liu, A highly sensitive and fast-responding SnO₂ sensor fabricated by combustion chemical vapor deposition, *Chem. Mater.* **17** (2005) 3997–4000.
- [182] N. Baik, G. Sakai, N. Miura, N. Yamazoe, Hydrothermally treated sol solution of tin oxide for thin-film gas sensor, *Sensors Actuators B Chem.* **63** (2000) 74–79.
- [183] G.F. Ortiz, P. Lavela, P. Knauth, T. Djenizian, R. Alcántara, J.L. Tirado, Tin-based composite materials fabricated by anodic oxidation for the negative electrode of Li-ion batteries, *J. Electrochem. Soc.* **158** (2011) A1094–A1099.
- [184] K. Rajendra Prasad, N. Miura, Electrochemical synthesis and characterization of nanostructured tin oxide for electrochemical redox supercapacitors, *Electrochem. Commun.* **6** (2004) 849–852.
- [185] Z. Liu, D. Zhang, S. Han, C. Li, T. Tang, W. Jin, X. Liu, B. Lei, C. Zhou, Laser ablation synthesis and electron transport studies of tin oxide nanowires, *Adv. Mater.* **15** (2003) 1754–1757.

- [186] Y. Cheng, P. Xiong, C.S. Yun, G.F. Strouse, J.P. Zheng, R.S. Yang, Z.L. Wang, Mechanism and optimization of pH sensing using SnO₂ nanobelt field effect transistors, *Nano Lett.* **8** (2008) 4179–4184.
- [187] H.J. Snaith, C. Ducati, SnO₂-based dye-sensitized hybrid solar cells exhibiting near unity absorbed Photon-to-Electron Conversion Efficiency, *Nano Lett.* **10** (2010) 1259–1265.
- [188] H.S. Shin, S.G. Jeon, J. Yu, J.Y. Song, Transformation of Sn nanowires to oxide nanotubes by a localized corrosion process, *Mater. Lett.* **82** (2012) 22–25.
- [189] H.-C. Shin, J. Dong, M. Liu, Porous tin oxides prepared using an anodic oxidation process, *Adv. Mater.* **16** (2004) 237–240.
- [190] J.-W. Lee, S.-J. Park, W.-S. Choi, H.-C. Shin, Well-defined meso- to macro-porous films on tin oxides formed by an anodization process, *Electrochim. Acta* **56** (2011) 5919–1525.
- [191] S. Ono, Y. Kobayashi, R. Kobayashi, H. Asoh, Fabrication of self-organized nanoporous oxide semiconductors by anodization, *ECS Trans.* **16** (2008) 353–358.
- [192] S. Das, V. Jayaraman, SnO₂: A comprehensive review on structures and gas sensors, *Prog. Mater. Sci.* **66** (2014) 112–255.
- [193] G. Heiland, Zum Einfluß von adsorbiertem Sauerstoff auf die elektrische Leitfähigkeit von Zinkoxydkristallen, *Z. Physik.* **138** (1954) 459–464.
- [194] A. Bielanski, J. Deren, J. Haber, Electric conductivity and catalytic activity of semiconducting oxide catalysts, *Nature* **179** (1957) 668–669.
- [195] T. Seiyama, A. Kato, K. Fujiishi, M. Nagatani, A new detector for gaseous components using semiconductive thin films, *Anal. Chem.* **34** (1962) 1502–1503.
- [196] C. Wang, L. Yin, L. Zhang, D. Xiang, R. Gao, Metal oxide gas sensors: sensitivity and influencing factors, *Sensors* **10** (2010) 2088–106.
- [197] S.H. Jeong, S. Kim, J. Cha, M.S. Son, S.H. Park, H.-Y. Kim, M.H. Cho, M.-H. Whangbo, K.-H. Yoo, S.-J. Kim, Hydrogen sensing under ambient conditions using SnO₂ nanowires: synergetic effect of Pd/Sn codeposition, *Nano Lett.* **13** (2013) 5938–5943.
- [198] H. Huang, Y.C. Lee, O.K. Tan, W. Zhou, N. Peng, Q. Zhang, High sensitivity SnO₂ single-nanorod sensors for the detection of H₂ gas at low temperature, *Nanotechnology* **20** (2009) 115501.
- [199] J. Zhao, W. Wang, Y. Liu, J. Ma, X. Li, Y. Du, G. Lu, Ordered mesoporous Pd/SnO₂ synthesized by a nanocasting route for high hydrogen sensing performance, *Sensors Actuat. B-Chem.* **160** (2011) 604–608.
- [200] N. Shirahata, W. Shin, N. Murayama, A. Hozumi, Y. Yokogawa, T. Kameyama, Y. Masuda, K. Koumoto, Reliable monolayer-template patterning of SnO₂ thin films from aqueous solution and their hydrogen-sensing properties, *Adv. Funct. Mater.* **14** (2004) 580–588.
- [201] J.O. Bockris, A.K.N. Reddy, M. Gamboa-Aldeco, Modern electrochemistry, Kluwer Academic / Plenum Publishers, USA, 2000.
- [202] C.A. Grimes, O.K. Varghese, S. Ranjan, Light water, hydrogen. The solar generation of hydrogen by water photoelectrolysis, Springer, USA, 2008.

- [203] R. van de Krol, M. Grätzel, Photoelectrochemical hydrogen production, Springer, USA, 2012.
- [204] W. Schmickler, E. Santos, The semiconductor-electrolyte interface, 2nd ed., Springer, USA, 2010.
- [205] K. Rajeshwar, Fundamentals of Semiconductor Electrochemistry and Photoelectrochemistry, in: Encyclopedia of Electrochemistry, John Wiley & Sons, 2002, 1–53.
- [206] T. Hisatomi, J. Kubota, K. Domen, Recent advances in semiconductors for photocatalytic and photoelectrochemical water splitting, *Chem. Soc. Rev.* **43** (2014) 7520–7535.
- [207] Y. Li, J.Z. Zhang, Hydrogen generation from photoelectrochemical water splitting based on nanomaterials, *Laser Photon. Rev.* **4** (2010) 517–528.
- [208] A. Fujishima, K. Honda, Electrochemical photolysis of water at a semiconductor electrode, *Nature* **238** (1972) 37–38.
- [209] K.S. Raja, M. Misra, K. Paramguru, Formation of self-ordered nano-tubular structure of anodic oxide layer on titanium, *Electrochim. Acta* **51** (2005) 154–165.
- [210] X.Y. Han, W.Z. Shen, Improved two-step anodization technique for ordered porous anodic aluminum membranes, *J. Electroanal. Chem.* **655** (2011) 56–64.
- [211] N.K. Shrestha, K. Lee, R. Hahn, P. Schmuki, Anodic growth of hierarchically structured nanotubular ZnO architectures on zinc surfaces using a sulfide based electrolyte, *Electrochem. Commun.* **34** (2013) 9–13.
- [212] L. Zaraska, N. Czopik, M. Bobruk, G.D. Sulka, J. Mech, M. Jaskuła, Synthesis of nanoporous tin oxide layers by electrochemical anodization, *Electrochim. Acta* **104** (2013) 549–557.
- [213] M. Wang, Y. Liu, D. Xue, D. Zhang, H. Yang, Preparation of nanoporous tin oxide by electrochemical anodization in alkaline electrolytes, *Electrochim. Acta* **56** (2011) 8797–8801.
- [214] A. Palacios-Padrós, M. Altomare, A. Tighineanu, R. Kirchgeorg, N.K. Shrestha, I. Díez-Perez, F. Caballero-Briones, F. Sanz, P. Schmuki, Growth of ordered anodic SnO₂ nanochannel layers and their use for H₂ gas sensing, *J. Mater. Chem. A* **2** (2014) 915–920.
- [215] X. Wang, F.X. Zhang, I. Loa, K. Syassen, M. Hanfland, Y.-L. Mathis, Structural properties, infrared reflectivity, and Raman modes of SnO at high pressure, *Phys. Status Solidi* **241** (2004) 3168–3178.
- [216] J. Long, W. Xue, X. Xie, Q. Gu, Y. Zhou, Y. Chi, W. Chen, Z. Ding, X. Wang, Sn²⁺ dopant induced visible-light activity of SnO₂ nanoparticles for H₂ production, *Catal. Commun.* **16** (2011) 215–219.
- [217] Ç. Kılıç, A. Zunger, Origins of coexistence of conductivity and transparency in SnO₂, *Phys. Rev. Lett.* **88** (2002) 95501.
- [218] H. Wang, K. Dou, W.Y. Teoh, Y. Zhan, T.F. Hung, F. Zhang, J. Xu, R. Zhang, A.L. Rogach, Engineering of facets, band structure, and gas-sensing properties of hierarchical Sn²⁺-doped SnO₂ nanostructures, *Adv. Funct. Mater.* **23** (2013) 4847–4853.
- [219] M. Fang, L. Zhang, X. Tan, X. Hu, W. Yan, P. Liu, Fabrication and photoluminescence property of SnO₂ microtowers with interstitial tin ions, *J. Phys. Chem. C* **113** (2009) 9676–9680.

- [220] M. Fang, X. Tan, B. Cheng, L. Zhang, SnO₂ hierarchical nanostructure and its strong narrow-band photoluminescence, *J. Mater. Chem.* **19** (2009) 1320–1324.
- [221] A. Palacios-Adrós, F. Caballero-Briones, I. Díez-Pérez, F. Sanz, Tin passivation in alkaline media: formation of SnO microcrystals as hydroxyl etching product, *Electrochim. Acta* **111** (2013) 837–845.
- [222] Y. Li, W. Yin, R. Deng, R. Chen, J. Chen, Q. Yan, B. Yao, H. Sun, S.-H. Wei, T. Wu, Realizing a SnO₂-based ultraviolet light-emitting diode via breaking the dipole-forbidden rule, *NPG Asia Mater.* **4** (2012) e30.
- [223] A. Kolmakov, Y. Zhang, M. Moskovits, Topotactic thermal oxidation of Sn nanowires: intermediate suboxides and core–shell metastable structures, *Nano Lett.* **3** (2003) 1125–1129.
- [224] J. Geurts, S. Rau, W. Richter, F.J. Schmitte, SnO films and their oxidation to SnO₂: Raman scattering, IR reflectivity and X-ray diffraction studies, *Thin Solid Films* **121** (1984) 217–225.
- [225] L. Sangaletti, L.E. Depero, B. Allieri, F. Pioselli, E. Comini, G. Sberveglieri, M. Zocchi, Oxidation of Sn thin films to SnO₂. Micro-Raman mapping and X-ray diffraction studies, *J. Mater. Res.* **13** (1998) 2457–2460.
- [226] M.S. Moreno, R.C. Mercader, A.G. Bibiloni, Study of intermediate oxides in SnO thermal decomposition, *J. Phys. Condens. Matter.* **4** (1992) 351–355.
- [227] M. Batzill, U. Diebold, The surface and materials science of tin oxide, *Prog. Surf. Sci.* **79** (2005) 47–154.
- [228] C.L. Lau, G.K. Wertheim, Oxidation of tin: An ESCA study, *J. Vac. Sci. Technol.* **15** (1978).
- [229] Y. Ogo, H. Hiramatsu, K. Nomura, H. Yanagi, T. Kamiya, M. Hirano, H. Hosono, p-channel thin-film transistor using p-type oxide semiconductor, SnO, *Appl. Phys. Lett.* **93** (2008) 032113.
- [230] S.S. Abd El-Rehim, F. Taha, M.B. Saleh, S.A. Mohamed, On the pitting corrosion of tin by sulphate anion, *Corros. Sci.* **33** (1992) 1789–1796.
- [231] G.K. Boschloo, A. Goosens, J. Schoonman, Photoelectrochemical study of thin anatase TiO₂ films prepared by metallorganic chemical vapor deposition, *J. Electrochem. Soc.* **144** (1997) 1311–1317.
- [232] K.L. Hardee, A.J. Bard, Application of chemically vapor-deposited iron-oxide films to photosensitized electrolysis, *J. Electrochem. Soc.* **123** (1976) 1024.
- [233] N. Beermann, L. Vayssieres, S. Lindquist, A. Hagfeldt, Photoelectrochemical studies of oriented nanorod thin films of hematite, *J. Electrochem. Soc.* **147** (2000) 2456–2461.
- [234] K. Sivula, F. Le Formal, M. Grätzel, Solar water splitting: progress using hematite (α -Fe₂O₃) photoelectrodes, *ChemSusChem* **4** (2011) 432–449.
- [235] S.D. Tilley, M. Cornuz, K. Sivula, M. Grätzel, Light-induced water splitting with hematite: improved nanostructure and iridium oxide catalysis, *Angew. Chemie Int. Ed.* **49** (2010) 6405–6408.
- [236] Y. Ling, G. Wang, D.A. Wheeler, J.Z. Zhang, Y. Li, Sn-doped hematite nanostructures for photoelectrochemical water splitting, *Nano Lett.* **11** (2011) 2119–2125.

- [237] Y.-S. Hu, A. Kleiman-Shwarscstein, A.J. Forman, D. Hazen, J.-N. Park, E.W. McFarland, Pt-doped α -Fe₂O₃ thin films active for photoelectrochemical water splitting, *Chem. Mater.* **20** (2008) 3803–3805.
- [238] K. Sivula, R. Zboril, F. Le Formal, R. Robert, A. Weidenkaff, J. Tucek, M. Grätzel, Photoelectrochemical water splitting with mesoporous hematite prepared by a solution-based colloidal approach, *J. Am. Chem. Soc.* **132** (2010) 7436–7444.
- [239] L. Wang, C.-Y. Lee, P. Schmuki, Solar water splitting: preserving the beneficial small feature size in porous α -Fe₂O₃ photoelectrodes during annealing, *J. Mater. Chem. A* **1** (2013) 212–215.
- [240] L. Wang, C.-Y. Lee, A. Mazare, K. Lee, J. Müller, E. Spiecker, P. Schmuki, Enhancing the water splitting efficiency of Sn-doped hematite nanoflakes by flame annealing, *Chem. Eur. J.* **20** (2014) 77–82.
- [241] K. Itoh, J.O. Bockris, Stacked thin-film photoelectrode using iron oxide, *J. Appl. Phys.* **56** (1984) 874.
- [242] K. Itoh, J.O. Bockris, Thin film photoelectrochemistry: iron oxide, *J. Electrochem. Soc.* **131** (1984) 1266–1271.
- [243] Y. Lin, G. Yuan, S. Sheehan, S. Zhou, D. Wang, Hematite-based solar water splitting: challenges and opportunities, *Energy Environ. Sci.* **4** (2011) 4862.
- [244] R.L. Spray, K.-S. Choi, Photoactivity of transparent nanocrystalline Fe₂O₃ electrodes prepared via anodic electrodeposition, *Chem. Mater.* **21** (2009) 3701–3709.
- [245] I. Cesar, K. Sivula, A. Kay, R. Zboril, M. Grätzel, Influence of feature size, film thickness, and Silicon doping on the performance of nanostructured hematite photoanodes for solar water splitting, *J. Phys. Chem. C* **113** (2008) 772–782.
- [246] L. Wang, C.-Y. Lee, P. Schmuki, Influence of annealing temperature on photoelectrochemical water splitting of α -Fe₂O₃ films prepared by anodic deposition, *Electrochim. Acta* **91** (2013) 307–313.
- [247] Y. Ling, Y. Li, Review of Sn-doped hematite nanostructures for photoelectrochemical water splitting, *Part. Part. Syst. Charact.* **31** (2014) 1113–1121.
- [248] L. Wang, A. Palacios-Adrós, R. Kirchgeorg, A. Tighineanu, P. Schmuki, Enhanced photoelectrochemical water splitting efficiency of a hematite-ordered Sb:SnO₂ host-guest system, *ChemSusChem* **7** (2014) 421–424.
- [249] M. Stefik, M. Cornuz, N. Mathews, T. Hisatomi, S. Mhaisalkar, M. Grätzel, Transparent, conducting Nb:SnO₂ for host-guest photoelectrochemistry, *Nano Lett.* **12** (2012) 5431–5435.
- [250] F. Montilla, E. Morallón, A. De Battisti, J.L. Vázquez, Preparation and characterization of antimony-doped tin dioxide electrodes. Part 1. Electrochemical Characterization, *J. Phys. Chem. B* **108** (2004) 5036–5043.
- [251] J. Zhang, L. Gao, Synthesis and characterization of antimony-doped tin oxide (ATO) nanoparticles, *Inorg. Chem. Commun.* **7** (2004) 91–93.
- [252] C. Terrier, J.P. Chatelon, R. Berjoan, J.A. Roger, Sb-doped SnO₂ transparent conducting oxide from the sol-gel dip-coating technique, *Thin Solid Films* **263** (1995) 37–41.

- [253] Q. Peng, B. Kalanyan, P.G. Hoertz, A. Miller, D.H. Kim, K. Hanson, L. Alibabaei, J. Liu, T.J. Meyer, G.N. Parsons, J.T. Glass, Solution-processed, antimony-doped tin oxide colloid films enable high-performance TiO₂ photoanodes for water splitting, *Nano Lett.* **13** (2013) 1481–1488.
- [254] C. Terrier, J.P. Chatelon, J.A. Roger, R. Berjoan, C. Dubois, Analysis of antimony doping in tin oxide thin films obtained by the sol-gel method, *J. Sol-Gel Sci. Technol.* **10** (1997) 75–81.
- [255] C. Fàbrega, F. Hernández-Ramírez, J.D. Prades, R. Jiménez-Díaz, T. Andreu, J.R. Morante, On the photoconduction properties of low resistivity TiO₂ nanotubes, *Nanotechnology* **21** (2010) 445703.
- [256] K. Sakaushi, Y. Oaki, H. Uchiyama, E. Hosono, H. Zhou, H. Imai, Synthesis and applications of SnO nanosheets: parallel control of oxidation state and nanostructure through an aqueous solution route, *Small* **6** (2010) 776–781.
- [257] H. Uchiyama, E. Hosono, I. Honma, H. Zhou, H. Imai, A nanoscale meshed electrode of single-crystalline SnO for lithium-ion rechargeable batteries, *Electrochem. Commun.* **10** (2008) 52–55.
- [258] J. Ning, T. Jiang, K. Men, Q. Dai, D. Li, Y. Wei, B. Liu, G. Chen, B. Zou, G. Zou, Syntheses, characterizations, and applications in lithium ion batteries of hierarchical SnO nanocrystals, *J. Phys. Chem. C* **113** (2009) 14140–14144.
- [259] D. Aurbach, A. Nimberger, B. Markovsky, E. Levi, E. Sominski, A. Gedanken, Nanoparticles of SnO produced by sonochemistry as anode materials for rechargeable lithium batteries, *Chem. Mater.* **14** (2002) 4155–4163.
- [260] Z. Han, N. Guo, F. Li, W. Zhang, H. Zhao, Y. Qian, Solvothermal preparation and morphological evolution of stannous oxide powders, *Mater. Lett.* **48** (2001) 99–103.
- [261] S. Axnanda, W.-P. Zhou, M.G. White, Z. Zhu, Z. Liu, Unique properties of reduced SnO_x: CO oxidation on nanostructured SnO_x/Pt(111), *ECS Meet. Abstr.* **MA2012-02** (2012) 3757.
- [262] L.Y. Liang, Z.M. Liu, H.T. Cao, Y.Y. Shi, X.L. Sun, Z. Yu, A.H. Chen, H.Z. Zhang, Y.Q. Fang, Improvement of phase stability and accurate determination of optical constants of SnO thin films by using Al₂O₃ capping layer, *ACS Appl. Mater. Interfaces* **2** (2010) 1565–1568.
- [263] F.-S. Tsai, S.-J. Wang, Y.-C. Tu, Y.-W. Hsu, C.-Y. Kuo, Z.-S. Lin, R.-M. Ko, Preparation of p-SnO/n-ZnO heterojunction nanowire arrays and their optoelectronic characteristics under UV illumination, *Appl. Phys. Express* **4** (2011) 025002.
- [264] K.-M. Li, Y.-J. Li, M.-Y. Lu, C.-I. Kuo, L.-J. Chen, Direct conversion of single-layer SnO nanoplates to multi-layer SnO₂ nanoplates with enhanced ethanol sensing properties, *Adv. Funct. Mater.* **19** (2009) 2453–2456.
- [265] S. Wang, S. Xie, H. Li, S. Yan, K. Fan, M. Qiao, Solution route to single crystalline SnO platelets with tunable shapes, *Chem. Commun.* (2005) 507–509.
- [266] Z.R. Dai, Z.W. Pan, Z.L. Wang, Growth and structure evolution of novel tin oxide diskettes, *J. Am. Chem. Soc.* **124** (2002) 8673–8680.
- [267] B.A. Abd-El-Nabey, N. Khalil, E. Khamis, Alkaline corrosion of aluminium in water-organic solvent mixtures, *Surf. Technol.* **22** (1984) 367–376.

-
- [268] D.R. Lide, CRC Handbook of Chemistry and Physics, 90th ed., CRC Press, USA, 2009.
- [269] M.M. Al-Abdallah, M.K. Hammouri, Electrochemical measurements on aluminium electrodes in acidic water/dimethylsulphoxide and acetonitrile solutions, *Anti-Corrosion Methods Mater.* **42** (1995) 3–5.
- [270] Y. Matsui, N. Kazuyuki, H. Masuda, Highly ordered anodic porous alumina by imprinting using Ni molds prepared from ordered array of polystyrene particles, *Jpn. J. Appl. Phys.* **44** (2005) 7726–7728.
- [271] H. Masuda, M. Yotsuya, M. Asano, K. Nishio, M. Nakao, A. Yokoo, T. Tamamura, Self-repair of ordered pattern of nanometer dimensions based on self-compensation properties of anodic porous alumina, *Appl. Phys. Lett.* **78** (2001) 826–828.